Scouring Around Multiple Structures in Extreme Flow Conditions

By

Philippe April LeQuéré

Thesis submitted to the University of Ottawa

In partial fulfillment of the requirements for the

Doctorate in Philosophy in Civil Engineering

Academic advisors:

Dr. Ioan Nistor and Dr. Majid Mohammadian

uOttawa

Department of Civil Engineering

Faculty of Engineering

University of Ottawa

Abstract

As world population increases, coastal areas experience an increase in human occupancy. These community locations come with a greater risk of impacts due to extreme natural events. Tsunami, being one of the most unpredictable and most devastating types of extreme hydrodynamic events, received significant attention over the past decades due to the recent extreme events (2004 Indian Ocean, 2010 Chile, 2011 Japan, 2018 Indonesia). The focus of this thesis is on investigating scour around structures generated by tsunami. Scouring was found to be one of the greatest sources of building damage during the 2011 Tohoku Japan Tsunami and, at the date of the redaction of this thesis, this phenomenon is still little understood by the scientific community. The main objective of this thesis is to study the change in scouring when multiple buildings are constructed in close proximity, as opposed to individual elements such as in the case of all previous studies focussed on tsunami-induced scour. This topic was first investigated by the candidate with the use of a numerical model, FLOW-3D, using the large eddy simulation approach and the Nielsen (1992) bed load sediment transport model. The model results showed a significant increase in scouring when a second building was located along the same transversal plane as the building investigated. Then, three structure arrangements were investigated in a comprehensive physical experiment conducted in the new Dambreak Flume of Hydraulic Laboratory of the University of Ottawa, Canada, to study the effects of (1) upstream constriction, (2) lateral spacing and (3) sheltering on tsunami-induced scour. All three structure arrangements showed a significant effect on tsunami-induced scour. A secondary project was conducted in collaboration with the Technical University of Braunschweig, Germany, and the Leibniz University Hannover, Germany. This large-scale physical experiment, performed in the Large Wave Flume of the Leibniz Institute Hannover, Germany, was used to investigate three different research phenomenon that influence tsunami scouring: (1) the wave drawdown on scour around structures, (2) the evolution of flow eddies and (3) the change in the soil's pore pressure.

Acknowledgements

First, I would like to thank my supervisors, Ioan Nistor and Majid Mohammadian. They have guided me throughout this research, and financially supported this research. They allowed me to gather amazing international research experience and sharing contacts that were key in my development as an engineer and a researcher. They were very proactive by proposing new project avenues when outside factors hindered my research.

I would like to thank people that supported in many different ways my PhD thesis. Sanaz Mehrzad, PhD student at the University of Ottawa for sharing experimental results that were used for the calibration exercise of the numerical model. Nils Goseberg, who, with funding support from my academic supervisors and the Faculty of Engineering at uOttawa, for provided me two research opportunities in Germany, which were very helpful to learn various work techniques and ways of approaching research problems. Stefan Schimmels who, in collaboration with Nils Goseberg and others, made the organization of the Large Wave Flume experiment possible within the restrictions of Covid-19. I would like to thank all the support I got for my experimental work, for contributing to my articles and for teaching me efficient work practices: Pierrick Edgard Fokou Zotegouon, Alex Schendel, Mario Welzel, Jessica Wilson, Clemens Krautwald, Jacob Stolle.

Finally, I would like to thank the support of my family who was always there when I needed support. I would also like to thank Dave Heinbuch for being besides me for most of my University career. Through our collaborative project of improving the GeeGees swimming team, he helped me keep sane and improve different aspects of my person.

I would like to acknowledge the Ontario Graduate Scholarship (OGS) program, Flow Science for generously providing a full access license to the program FLOW-3D through their academic program, and to the support of the Natural Science and Engineering Council (NSERC) through the Discovery Grants held by Ioan Nistor and Majid Mohammadian.

Philippe April-LeQuéré

December 2021

Table of Contents

Abstract ii
Acknowledgements iii
List of Figures vi
List of Tables x
List of Acronyms xi
List of Symbols xii
Chapter 1: Introduction 1
1.1 Background 1
1.2 Research objectives 2
1.3 Scope and limitations 3
1.4 Novelty and motivation 4
1.5 Publications 5
1.6 Thesis outline 6
Chapter 2: Literature review 7
2.1 Steady flow scouring 7
2.2 Tsunami scouring 11
2.3 Tsunami design code 18
2.4 Discussion and Research Needs 22
Chapter 3: Numerical Modeling of Tsunami Induced Scouring around a Square Column: Performance Assessment of FLOW-3D and Delft3D 24
3.1 Abstract 24
3.2 Introduction 24
3.3 Methods 26
3.4 Results 34
3.5 Discussion 41
3.6 Conclusions 44
Chapter 4: Effect of Lateral Spacing of Structures on Tsunami-Induced Scour 45
4.1 Abstract 45
4.2 Introduction 45
4.3 Methods 48
4.4 Results 58
4.5 Discussion 64
4.6 Conclusions 66

Chapter 5: Hydrodynamics and associated scour around a free-standing structure due to turbulent bores 67
5.1 Abstract 67
5.2 Introduction 67
5.3 Methodology 69
5.4 Results 76
5.5 Discussion 89
5.6 Conclusions 91
Chapter 6: Influence of Macroroughness on Tsunami Scour of Coastal Structures 92
6.1 Abstract 92
6.2 Context and research needs 92
6.3 Methodology 94
6.4 Results 100
6.5 Discussion 113
6.6 Conclusions 114
Chapter 7: Structures Sheltering and Lateral Spacing Effects on Tsunami-Induced Scour 115
7.1 Abstract 115
7.2 Introduction 115
7.3 Methodology 118
7.4 Repeatability 124
7.5 Results 124
7.6 Discussion 135
7.7 Conclusions 138
Chapter 8: Conclusions and Recommendations for Future Work 140
8.1 Conclusions 140
8.2 Recommendation for Future Work 141
References 143

List of Figures

Figure 2.1: Schematic of the vortices structures responsible for scour at a pier in steady flow (Arneson et al., 2012) 7
Figure 2.2: Temporal evolution of live-bed and clear-water scour (Kothyari et al., 1992) 8
Figure 2.3: Variation of scour depth with respect to pier spacing (Beg, 2010) 9
Figure 2.4: Sketch of idealized long constriction scour (Sturm et al., 2011) 10
Figure 2.5: Types of scour mechanisms (Tonkin et al., 2013) 12
Figure 2.6: Local scour during the 2004 Indian Tsunami. (a) 1.4m Deep.(b) 1.5m Deep (Yeh and Li, 2008) 12
Figure 2.7: Scour evolution around a square column subjected to a long wave. (a) Longshore side; (b) offshore facing side. Measurements taken every 0.04 t/T (time over wave period) (D. J. McGovern et al., 2019) 14
Figure 2.8: Visualization of numerically generated turbulent structures generated by a solitary wave around a standing square structure (Arabi et al., 2019) 15
Figure 2.9: Difference in bed elevation after the 2011 Japan Tsunami (Wilson et al., 2012) 16
Figure 2.10: Channelized between two tsunami resistant critical infrastructures (a) View from shore side (b) Areal view of the affected area (Yeh et al., 2013) 17
Figure 2.11: Instantaneous vortical structures around a monopile subjected to a tsunami-like wave (Larsen et al., 2017) 18
Figure 2.12: Estimation of local scour depth with respect to flow depth (Tonkin et al., 2013) 20
Figure 2.13: Estimation of vertical extent of scour to projected pier width with respect to the Froude number 21
Figure 2.14: (a): Flow speed amplification factor vs wake clearance angle (β) (b): Diagram of the effective wake clearance angle (Thomas et al., 2015) 22
Figure 3.1: Experimental setup from Merzhad et al. (2016) 27
Figure 3.2: Final scour bathymetry generated by a hydraulic bore created by an impoundment depth of 0.25m for the case of a column with a 0.2m side square cross section (reproduction with permission of Mehrzad et al. (2016)) 27
Figure 3.3: Numerical Model Mesh for Delft3D 29
Figure 3.4: Numerical Model Mesh for FLOW-3D 30
Figure 3.5: Numerical Model's Bore Profile against Chanson (2009) Idealized Bore Profile 35
Figure 3.6: XZ Plane Velocity Vectors after 12s at the middle of the structure's front side using the a) FLOW-3D with LES Turbulence Model model and b) Delft3D model 36
Figure 3.7: a) Top: Difference between Experimental Results and Delft3D Results Bottom: Delft3D Results using Standard k-ε Turbulence Model b) Transversal Profile of the Final Bed Elevation at Cross-section 3 c) Longitudinal Profile of the Final Bed Elevation at Cross-section 4 37
Figure 3.8: a) FLOW-3D standard k-ε turbulence model results b) FLOW-3D k-ω turbulence model results c) FLOW-3D RNG k-ε turbulence model results d) FLOW-3D LES turbulence model results // top: difference between experimental results (Mehrzad et al., 2016) and FLOW-3D results // bottom: FLOW-3D results 39
Figure 3.9: Comparison of numerical and experimental data (Mehrzad et al., 2016): a) transversal profile of the final bed elevation at cross-section 3 b) longitudinal profile of the final bed elevation at cross-section 4 40

Figure 3.10: Nielsen (1992) and Van Rijn (1984) sediment transport model comparison in FLOW-3D using LES turbulence model a) plan view of bed elevation results of Nielsen (1992) sediment transport model b) plan view of bed elevation results of Van Rijn (1984) sediment transport model c) transversal profile of the final bed elevation at cross-section 3 d) longitudinal profile of the final bed elevation at cross-section 4 41
Figure 3.11: Comparison of FLOW-3D and Delft3D a) transversal profile of the final bed elevation at cross-section 3 b) longitudinal profile of the final bed elevation at cross-section 4.....43
Figure 4.1: Deep scour hole between two hospital buildings in Oganawa caused by the 2011 Great Japan Tsunami 47
Figure 4.2: Experimental flume setup.....49
Figure 4.3: Numerical Model Mesh in FLOW-3D 50
Figure 4.4: FLOW-3D calibration results with b = 0.2m and a bore generated by a h_0=0.25m impoundment depth; a) top plate: plan view of the experimental final bed surface) and bottom plate: plan view of the numerical model final bed surface; b) bed elevation at cross-section 1; c) bed elevation at cross-section 2 54
Figure 4.5: Numerical model verification using a 30 cm column and a bore generated by a 20 cm impoundment depth; top: FLOW-3D results // bottom: experimental results.....55
Figure 4.6: Maximum scour depth comparison for varying impoundment depths (h_0) and column widths (b).....56
Figure 4.7: Plan view of the laterally-spaced columns setup in the numerical model.....57
Figure 4.8: Plan view of the relative scour bed elevation for a single column (a) and for spacing ratios varying from 0 (b) to 2 (d); due to a bore generated by an impoundment depth, h_0 = 0.25m and a column width, b = 0.10m 59
Figure 4.9: Transversal vertical cross-section of the final bed elevation upstream of the columns; centered on the midpoint of the right column due to a bore generated by an impoundment death, with h_0 = 0.25m and a column width, b = 0.10m.....60
Figure 4.10: Maximum scour depth variation with the lateral spacing ratio (S/b) and the bore-generating impoundment depth (h_0).....61
Figure 4.11: Maximum scour depth increase as a function of the adjusted spacing ratio (S'=(S+b)/(by)) 62
Figure 4.12: Horseshoe vortex and vorticity at the midpoint of the column(s) upstream face at t = 30s with column width, b = 0.1m and the impoundment depth, h_0 = 0.25m; a), b): single column b) to e) and g) to j): spacing ratio varying from 0 to 3.....63
Figure 4.13: Schematic representation of the flow structures creating scour around the columns 65
Figure 4.14: Vertical extent of pile scour to projected element width ratio (d_s/b) 66
Figure 5.1: Experimental setup with side and plan view, waves propagating from left to right - Large Wave Flume, Hannover, Germany, a joint research facility run between Technische Universität Braunschweig and Leibniz University Hannover.....70
Figure 5.2: (a) Location of the measuring instrumentation; (b) location of the pore pressure sensors on the column faces; (c) photograph of the measuring instrumentation around the column; (d) photograph of the exposed pore pressure sensors during the bed construction.....73
Figure 5.3: Computational domain showing the four regions and their specific grid dimensions 75
Figure 5.4: Time-history of the water surface displacement caused by the solitary wave at WG1 77

Figure 5.5: Comparison of the numerical model and experimental results of the flow depth at the three ultrasonic sensors: (a) US1 (b) US2 (c) US3 79
Figure 5.6: Comparison of the flow velocity results in the numerical model and in the experiment at (a) ECM1 and (b) ECM2 81
Figure 5.7: Time-history of the Froude number variation at the US2 location (Numerical results) and the ECM2 location (Experimental results) 82
Figure 5.8: Evolution of the numerically-calculated turbulence structures (a,b) and sketches of the turbulence structures (c,d) around the column during the runup phase at 4.0 s (a,c) and the drawdown phase at 10.0 s (b,d) 83
Figure 5.9: GoPro video stills from inside the column showing the front and side faces (a,b,c,d) and the side and back face (e,f,g,h) at 4.0 s (a,e), at 7.0 s (b,f) at 10.0 s (c,g) and at 18.0 s (d,h). 84
Figure 5.10: Comparison of the final bed topography: (a) experimental results, (b) numerical results and (c) the difference between the experimental results and the numerical ones (red – larger erosion of numerical calculation, blue – larger erosion of experimental 85
Figure 5.11: Final bed elevation comparison between the numerical and the experimental results at the (a) front face (b) side face (c) back face 86
Figure 5.12: Temporal evolution of the bed elevation and the pore pressure at the center of the (a,b) front face (c,d) side face (e,f) back face 88
Figure 6.1: Plan and side view sketch of the dambreak flume, Hydraulic Laboratory of the University of Ottawa, Canada 95
Figure 6.2: Pictures of experiment installation: a) swing gate system; b) false floor installation; c) measurement equipment and column support system 96
Figure 6.3: Plan view of the three columns' arrangement and the relevant measurements 97
Figure 6.4: Repeatability of dambreak bore water surface elevations at US2, comparing 3 tests for 3 different impoundment depths 100
Figure 6.5: The time series data of the single column tests: (a) the runup at the upstream face of the column (US4); (b) the water surface elevation of the flow approaching the column (US3); (c) the water surface elevation just upstream of the sand bed (US2); (d) the surface flow velocity at US2; (e) the Froude number at US2 101
Figure 6.6: Water surface time histories from US2 compared to the bore surface solution proposed by Ritter (1892) 103
Figure 6.7: Comparison of the bore front velocity along the horizontal section of false floor with the theoretical solution proposed by FEMA P-646 (2012) 104
Figure 6.8: Images of flow surface reaction to the presence of the three vertical structures at t = 10 s: a) side view; b) angled view from upstream; c) in-flume top view (test: C_h2_w4_L4). Blue circles indicate surface rollers and red arrows indicate flow direction 105
Figure 6.9: Influence of upstream constriction on the runup at the design column (US4) 106
Figure 6.10: Post-bore passage sand topography: (a) h_0 = 0.15 m, L = 2; (b) h_0= 0.25 m, L = 2; (c) h_0= 0.25 m, L = 3; (d) h_0 = 0.25 m, L = 4; (e) h_0 = 0.35 m, L = 2 // (A) single column; (B) W_c = 0; (C) W_c = 1; (D) W_c = 2; (E) W_c = 3; (F) W_c = 4 108
Figure 6.11: Relative maximum scour depth with varying macroroughness spacing 109
Figure 6.12: Relative maximum scour depth increase with varying of angle β 110
Figure 6.13: Maximum scour depth at design structure with respect to the flow depth at US2 . 111
Figure 6.14: Maximum scour depth to column width ratio against the Froude number at US2 . 112
Figure 6.15: Single column results compared with the results from the experiments by Mehrzad et al. (2016) and Lavictoire et al. (2014) 113

Figure 7.1: Post-tsunami examples of sheltering and spacing effects, 2011 Great Japan Tsunami, Onagawa (Yeh et al., 2013) 116
Figure 7.2: Flume setup and equipment location: (a) plan view; (b) side view 119
Figure 7.3: (a) Column and ultrasonic sensor disposition; (b) the piston-activated swing gate.. 120
Figure 7.4: Plan view of sheltering setup column arrangements tested 121
Figure 7.5: Plan view of lateral spacing setup column arrangements tested 122
Figure 7.6: Scour repeatability of Sp_h2_S3 test 124
Figure 7.7: Hydraulic properties of flow at US2: (a) flow depth; (b) flow surface velocity; (c) Froude number 125
Figure 7.8: Turbulent flow structures around two structures placed in a sheltering setup (Sh_h3_L2_b1 at t = 7 s) 126
Figure 7.9: Relative maximum runup (maximum runup of the test (R_i) divided by the maximum runup of the single-column test (R_0)) with respect to the longitudinal distance between columns 127
Figure 7.10: Post-bore topographies 129
Figure 7.11: Relative maximum scour depth (maximum scour depth of the test (d_{si}) divided by the maximum scour depth of the single column test (d_{s0})) with respect to the longitudinal distance between columns (L_D/b) 130
Figure 7.12: Relative maximum scour depth with respect to distance between columns (b_{sh}/b) 131
Figure 7.13: Turbulent flows around two laterally spaced structures (Sp_h1_S2) 132
Figure 7.14: Spacing setup post-bore topographies (includes single columns) 133
Figure 7.15: Cross-section of bed 0.01m upstream of columns, centered on the left column 134
Figure 7.16: Relative maximum scour depth variation (maximum scour depth of the test (d_{si}) divided by the maximum scour depth of the single column test (d_{s0})) with the lateral spacing ratio and the bore-generating impoundment depth (h_0) 135
Figure 7.17: Comparison of present study to previous studies numerical results and steady flow results (a) h_0 = 0.15 m (b) h_0 = 0.25 m (c) h_0 = 0.35 m 137

List of Tables

Table 2.1: Approximate scour depth as a percentage of flow depth (Dames and Moore, 1980) ..19
Table 3.1: Scour RMSE for the regions defined in Figure 3.8 38
Table 4.1: Hydraulic properties of the dambreak bore at prototype scale following an 80:1 Froude similarity 58
Table 5.1: Sand slope sediment properties 70
Table 5.2: Solitary wave bore and sediment parameters at prototype scale following a 1:20 Froude scale and Dean's scale 71
Table 6.1: Detailed list of the experimental program tests 98
Table 6.2: Flow speed and scour depth amplification factors with respect to β 111
Table 7.1: Sheltering setups utilized 122
Table 7.2: Lateral spacing setups utilized 123
Table 7.3: Single column setups utilized 123

List of Acronyms

ADV	Acoustic Doppler Velocimeters
ASCE	American Society of Civil Engineering
CFD	Computational Fluid Dynamics
ECM	Electromagnet Current Meter
FEMA	Federal Emergency Management Agency
LES	Large Eddy Simulation
LiDAR	Light Detection And Ranging
KC	Keulegan-Carpenter
RANS	Reynold-Averaged Navier Stokes
RNG	Renormalization Group
RMSE	Root Mean Square Error
SWL	Still Water Level
TUB	Technical University of Braunschweig
US	Ultrasonic scanner
USD	United States Dollar
VOF	Volume-Of-Fluid
2D	Two Dimensional
3D	Three Dimensional

List of Symbols

a	Van Rijn's reference height
α_i	entrainment coefficient
$AKSFAC$	User defined proportionality factor in Delft3D
A	half of the runup maximum vertical reach
Al	Alignment of pier
b	Column or structure element width (m)
B_1	Channel width upstream of a contracted reach (m)
B_2	Width of a contracted reach (m)
b_{Sh}	Width of sheltering column (macroroughness) (m)
c	wave celerity
$c_a^{(l)}$	Sediment concentration at the reference height (kg/m^3)
c_s	Smagorinsky coefficient;
d	Still water depth (m)
D	downward sediment flux
d_{50}, D_{50}	Sediment's median grain size (mm)
D_*	Dimensionless grain size
d_s	Depth of scour hole (m)
D_{SM}	Sediment size at model scale (mm)
D_{SM}	Sediment size at prototype scale (mm)
E	upward sediment flux;
e_{ij}	Strain rate tensor components
f	Coriolis parameter
F_i	External forces (N)
Fr	Froude number
g	Gravitational acceleration (m/s^2)
G	Source term due to the gravitational forces
h	Water depth (m)

H	Wave height (m)
h_0	Impoundment depth (m)
h_{max}	maximum flow depth;
k	Turbulent kinetic energy
K	hydraulic conductivity;
k_s	Effective roughness height (mm)
L	Distance between column and still water level (m)
L_c	Length of embankment transition (m)
L_D	Distance between upstream constriction and test column (m)
L_M	Length at model scale (m)
L_P	Length at prototype scale (m)
L_s	length scale;
M_i	External hydraulic forces contribution to momentum
M_L	Momentum magnitude
n_s	outward pointing normal to the packed bed interface;
P	Pressure (kPa)
p'	sediment packing fraction;
P_k	Turbulent energy production term
$q_{b,i}$	bed load transport rate;
Re	Reynolds number;
S	Structure or structure element spacing (m)
S_b	Bed load transport (kg/s)
Sh	Parameter describing the shape of pier
t	Time (s)
T	Wave or inundation period (s)
t^*	time zeroed at the instant when the bore collapsed;
$T_a^{(l)}$	Non-dimensional bed-shear stress
t_M	Time at model scale (s)
t_P	Time at prototype scale (s)

t_e	Time to scour depth equilibrium (s)
u	x-direction velocity (m/s)
u_{*1}	Shear velocity of the flow upstream of a contracted reach (s/m1/3)
u_{*c}	Critical shear velocity for the initiation of sediment movement (s/m1/3)
u_i'	ith component of the fluctuation velocity
$u_{lift,i}$	entrainment lift velocity of sediment;
v	y-direction velocity (m/s)
V	Mean approach flow velocity (m/s)
V_1	Mean approach flow velocity upstream of a contracted reach (m/s)
V_c	Movable bed critical velocity for initiation of movement (m/s)
V_M	Velocity at model scale (m/s)
V_P	Velocity at prototype scale (m/s)
w	z-direction velocity (m/s)
Wc	Upstream constriction spacing (m)
x	longitudinal position;
x_i and x_j	position vectors;
x^*	longitudinal location with respect with the location of the bore collapse;
Y	Mean approach flow depth (m)
Y_1	Flow depth upstream of a contracted reach (m)
Y_2	Flow depth in a contracted reach (m)
z	vertical position
Z_b	bed elevation
β	Effective wave clearance angle (^{o})
B_w	wave number
δx, δy and δz	mesh's cell dimensions
Δ	numerical domain cell size
Δ_r	Wave-induced ripple height (m)
ε	Dissipation of turbulent kinematic energy
ζ	Height of free water surface elevation above the horizontal plane of reference (m)

η	free surface displacement
θ	angle of the bed slope
$\theta'_{b,c}$	local Shields parameter
$\theta_{b,cr}$	critical Shields parameter
μ	Fluid dynamic viscosity (N*s/m²)
$\mu_c^{(l)}$	Efficiency factor current
ν	Fluid dynamic viscosity (N*s/m²)
ν_V	Vertical eddy viscosity coefficient
ν_T	eddy viscosity coefficient
ρ	Fluid density (kg/m³)
ρ_s	Density of particle (kg/m³)
σ	Vertical coordinate in a
σ_g	Geometric standard deviation of the sediment particle distribution
$\tau'_{b,c}$	Bed shear stress due to current (N/m²)
$\tau'_{b,cr}$	Critical bed-shear stress (N/m²)
υ	Fluid kinematic viscosity (m²/s)
ω	Specific dissipation rate

Chapter 1: Introduction

1.1 Background

Tsunamis are long period waves generated by earthquakes, landslides or other type of water surface disturbance (Di Risio et al., 2009). Over the last two decades, many coastal communities have been impacted by this phenomenon. In 2004, an earthquake of moment magnitude $M_L = 9.0$ generated extremely large tsunami waves along the coastal areas of the Indian Ocean that caused 230,000 deaths (Synolakis et al., 2005), which made it the deadliest tsunami in recorded history and the second larger natural disaster ever recorded in humankind history. In order to mitigate the effects of such catastrophes, countries have proposed and/or implemented coastal defenses against such waves. The one country that led the world with its ambitious efforts to cope with tsunami risks is Japan. In 1992, a total of 9,400 km of Japan's coast was protected by coastal structures, 3,000 of which were dykes (Koike, 1996). Also, multiple evacuation routes and tsunami-resistant buildings were built to evacuate the population in case of extreme hydrodynamic events. These measures led to great success in protecting the coast from erosion, but, most importantly, from tsunamis. An example of this success was in the tsunami of 1993. A tsunami with a significant wave height of 6.6 m impacted the coasts of Japan. The death toll was of 230 casualties, a relatively low number compared to previous similar tsunami events (Satake and Tanioka, 1995).

However, in 2011, the Tohoku East Japan earthquake, generated waves with runups reaching 40 m (Tang, 2011). Due to this tsunami size, the majority of the coastline protection reached by this tsunami failed (Jayaratne et al., 2016), and over 19,000 people died as a result (Kawachi et al., 2020). The damages were estimated at 360 billion USD and 1.5 million tons of floating debris were released in the Pacific Ocean (Lebreton and Borrero, 2013). This tsunami exposed the limited knowledge of the devastating effects of such extreme hydrodynamic event. Therefore, research into the field are greatly needed to reduce similar impacts in the future.

In more recent post-tsunami investigations, multiple mechanisms of structure failure were observed, which helped inform future research (Chock et al., 2013; Fritz et al., 2011b; Palermo et al., 2013; Shibayama et al., 2013). Infrastructures failures and damage observed included overturning, scouring, displacement, dam core entrainment and debris impacts (Jayaratne et al., 2016; Palermo et al., 2013; Saatcioglu et al., 2005). Therefore, the level of details of many design guidelines and standards must be enhanced to help the design of structures capable of withstanding the impact of tsunami waves. This thesis focusses on the scouring induced by tsunami inundations and, more precisely, the factors enhancing this scouring. The results of this study is also applicable to other extreme hydrodynamic events such as fast moving storm surges and dam breaks. At present, current design standards for tsunami resistant infrastructure only account for three factors when prescribing scour depth around a structure: inundation flow depth, the structure width and the Froude number. However, the proposed methods of estimating scour depth fails to capture the complexity of the phenomenon. In fact, multiple parameters, such as the flow velocity, soil properties, flow direction, structure shape, etc., considered in steady flow conditions, are not factored in the scour predictions. This is most likely due to the lack of research in the field and the complexity of the phenomenon of tsunami-induced scour.

The main goal of the thesis is to better inform the scientific community on three factors that may influence tsunami-induced local scouring: flow obstruction/focusing, sheltering and the influence of structures' lateral spacing. Previous research performed with tsunami-like waves proved that flow is locally accelerated by obstructions placed upstream of that particular location (Nouri et al., 2010; Thomas et al., 2015). This flow acceleration may lead to greater scouring around structures located downstream of the obstruction since flow velocity and scouring are strongly related (Melville and Chiew, 1999). Upstream sheltering and lateral spacing, on the other hand, have never been researched in tsunami-type flows. However, it is well known that these structure arrangements can significantly influence local scouring in steady flow conditions (Arneson et al., 2012). These three factors are further discussed in this thesis.

Additional investigations in this thesis consisted of replicating tsunami waves and subsequent inundation using numerical models. The flow patterns around a square column and the subsequent scour were investigated. With the collaboration of researchers from the Technical University of Braunschweig and Leibniz Hannover University, the author further investigated the mechanisms that lead to tsunami-induced scour, including the formation of turbulent eddies around the column and the soil's pore pressure spatio-temporal variation.

1.2 Research objectives

The primary objective of the thesis is to better inform the scientific community on the different factors influencing scouring caused by tsunami-like flows and, based on those findings, provide new practical tools to design engineers to assist with designing infrastructure located in areas at risk of impact from extreme hydrodynamic events. The three main objectives and their associated secondary objectives are described below.

- Investigate scouring caused by a dam-break bore around multiple columns using state-of-the-art numerical models:
  - Evaluate the performance of two numerical models (FLOW-3D and Delft3D) to simulate scouring induced by tsunami-like flows.
  - Conduct a performance assessment of different turbulence models incorporated in these numerical models, including RANS and LES, and sediment transport models to find the optimal combination to be used to simulate local scouring at a square column induced by tsunami-like flows.
  - Investigate numerically the scour changes associated with the difference in spacing between two columns.
- Investigate factors influencing scouring around a single column using a combination of physical and numerical experimentations:
  - Investigate scour patterns caused by broken solitary waves around a square column at large scale.
  - Study the importance of inundation drawdown, typical for tsunami inundation, in the scouring process and in the variation of the pore pressure at the interface with the column.
  - Investigate the spatio-temporal formation of flow structures around a square column using a numerical model.
  - Investigate the correlation between pore pressure and evolution of flow patterns over time, and the scour patterns forming around a square column.

- Investigate scouring caused by a dam-break bore around multiple columns arranged in a pre-determined manner using physical modeling:
  - Investigate the scour change at a column when additional structures are placed upstream of it to constrict the flow.
  - Investigate the scour change at a column when an additional structure is placed upstream of it, generating a sheltering effect.
  - Investigate the scour change at a column when an additional structure is placed on the same flow-transversal section at various lateral spacing.
  - Develop a simple method to calculate scouring amplification effects associated with the close proximity of multiple structures. This will hopefully help engineers predict scour induced by flow constrictions.
  - Develop a comprehensive experimental database to compare with and validate the results of numerical models.

1.3 Scope and limitations

This study employs a combination of numerical modeling and physical experiments. Due to physical, time and numerical constraints, the study has some inherent limitations in the evaluation of the effect of multiple structure arrangements on tsunami-induced scour:

- Due to facility size constraints, the experiments were performed at a relatively small scale (between 1:10 (Hannover - Chapter 5) and 1:80 (Numerical model and University of Ottawa experiments – Chapters 3, 4, 6, 7)). The geometric scale of the experiment was maximized while remaining below sizes that would induce wall effects.
- In the experimental tests performed at the University of Ottawa (Chapters 6, 7), the width of flume limited the lateral spacing between columns at the scale the tests were performed.
- A lack of field data prevented a direct validation of the numerical model and an assessment of the results of the physical experiments. However, the candidate confirmed some of the prescriptions of ASCE7 Chapter 6 on scour due to flow concentration, which were derived from a limited field data. Further investigation into the scale effects should be conducted before any definitive conclusions are drawn.
- Due to time constraints, only a limited number of experimental tests and numerical simulations were performed. The full extent of two- and three-column arrangements has not been fully investigated.
- In both the physical experiments and numerical models, only one sediment size and column shape (square) were employed. Some scale effects, column shape and sediment size effect on the scour mechanisms discussed herein was not fully explored by the candidate.
- The models employed an idealized topography and simple columns' arrangements. The influence of complex topographies, non-symmetric column position and different bed slopes have not investigated in this study. However, these idealized cases provide novel benchmarking data to calibrate numerical models.
- In the numerical models and the physical experiments conducted at the University of Ottawa, Canada, (Chapters 3, 4, 6, 7), the tsunami-like inundation propagated over a horizontal bed, which did not allow for the phenomenon of drawdown to occur. This prevented the investigation of some physical phenomena, such as variation of the pore

pressure gradient during the drawdown phase, to influence the scour hole forming around the columns.

- In the physical experiment conducted in the Large Wave Flume in Hannover, Germany, (Chapter 5), a solitary wave was utilized to simulate a tsunami wave. However, the short period of solitary waves could not properly scale the period of a real tsunami wave. Therefore, the scour depth was, most likely, not adequately reproduced in this experiment. However, the mechanisms of the scour evolution are relatively close
- A numerical model was employed to simulate tsunami flows and the resulting scour around columns. The results of numerical models have inherent limitation because they are an approximation of the reality based on previously developed equations.

1.4 Novelty and motivation

The main novelties and motivations for this study are enumerated and explained in this subsection:

- Numerical modeling of inundation generated by tsunami-like waves have been performed by previous researchers by using similar flows, such as dambreak bores. Most of those investigations only studied hydrodynamic features or scouring near horizontal structures. Very few studies have attempted to numerically simulate the generation of scour by dam-break flows around a vertical structure, and most of these were performed using a circular column. The present study is one of the first to successfully apply a numerical model to study the dam-break bore scour around a square column. In addition, it is the first study to investigate the effect of columns spacing on dam-break flow behaviors and its resulting scouring. (Chapters 3, 4)
- In most cities, the proximity of buildings was shown to generate flow concentrations and flow decelerations depending on the building arrangement, which may increase or decrease scouring around these buildings. The increase in scour can be investigated by constricting the flow advancing onto the vertical structure of interest with the use of additional structures placed in the testing area. To the knowledge of the candidate, the present study is the first to research tsunami-induced scouring around an arrangement of multiple columns, using both a numerical model and a physical model. (Chapters 4, 6, 7)
- Flow amplification due to upstream constriction is included in the ASCE7 Chapter 6 *Tsunami Loads and Effects*. However, the effect of this flow amplification on scour is not discussed. The experimental program conducted at the University of Ottawa is the first study to investigate the phenomenon of tsunami scour amplification caused by upstream constriction. (Chapter 6)
- In steady flow, the lateral proximity between structures (lateral spacing) and upstream flow constrictions is already recognized by the scientific community as being a risk for scour amplification around a structure. Also, in steady flow, when a structure is located directly upstream of another structure, the former is reducing the scour forming at the latter because of an effect of sheltering. These phenomena may be similar in tsunami flows. By better predicting the scour risk of a given structure located in a tsunami prone area, the location of a structure relative to the others around it can be optimized to minimize the risk of a scouring-type failure of that given structure. The result of this study will help increase the precision of tsunami scour predictions for designing tsunami resistant structures. (Chapters 4, 6, 7)

- As part of the experimental program in the Large Wave Flume in Hannover, Germany, the candidate combined the results of the experimental program and the results of a numerical simulation to further investigate the mechanisms that drives tsunami-induced scour. This experimental program was unique in its largeness of scale. In addition, this study was the first to link the spatio-temporal evolution of turbulent eddies forming around a square column, the scour patterns forming around a square column and pore pressure measurements. (Chapter 5)

1.5 Publications

Journal articles:

1) April Le Quéré, P., Nistor, I. and Mohammadian, A. (2020). Numerical Modeling of Tsunami-Induced Scouring around a Square Column: Performance Assessment of FLOW-3D and Delft3D. *Journal of Coastal Research*, 36(6), 1278–1291. doi: 10.2112/JCOASTRES-D-19-00181.1.

   The author (Philippe April-LeQuéré) was responsible for applying the numerical models used in this study and writing the manuscript. This manuscript is presented in Chapter 3.

2) Le Quéré, P. A., Nistor, I., and Mohammadian, A. (2021). Effect of Lateral Spacing of Structures on Tsunami-Induced Scour. *Journal of Coastal Research*, 37(4), 813–826.

   The author was responsible for conducting the numerical models used in this study and writing the manuscript. This manuscript is presented in Chapter 4.

3) April Le Quéré, P., Nistor, I., Mohammadian A., Schimmels S., Schendel A., Goseberg N., Welzel M., Krautwald C., Stolle J. (2021). Hydrodynamics and associated scour around a free-standing structure due to turbulent bores. *Journal of Waterways, Port, Coastal, and Ocean Engineering*. Under review

   The author was responsible for designing and planning the physical experiment and applying the numerical models used in this study and writing the manuscript, which is presented in Chapter 5.

4) April Le Quéré, P., Nistor, I. and Mohammadian, A. (2022). Influence of Macroroughness on Tsunami Scour of Coastal Structures. In submission process

   The author was responsible for planning and conducting the physical experiment program discussed in this manuscript. The author also wrote the manuscipt, which is presented in Chapter 6.

5) April Le Quéré, P., Nistor, I. and Mohammadian, A. (2022). Structures Sheltering Effects and Lateral Spacing on Tsunami-Induced Scour. In submission process

   The author was responsible for planning and conducting the physical experiment program discussed in this manuscript. The author also wrote the manuscipt, which is presented in Chapter 7.

1.6 Thesis outline

This thesis is organized as follows:

- Chapter 2 presents a literature review of the most recent research related to tsunami-induced scouring. Four main topics are discussed: Steady flow scouring, Tsunami scouring, Tsunami design code and a brief discussion summarizing its finding is presented.
- Chapter 3 is two numerical models were applied with four different turbulence models and two sediment transport models were compared to asses their performance in terms of simulating the scour induced by tsunami-like flows.
- Chapter 4 outlines the application of one of the models employed in Chapter 3 to a two-column setup. These two columns were laterally spaced, and located transversal to the direction of the flow. Different lateral spacing and incoming flow conditions were tested to investigate their influence on the lateral spacing effect on scour.
- In Chapter 5, a combined numerical and physical study was performed to investigate flow patterns forming around a square column as well as the pore pressure variation during the broken wave flows.
- Chapter 6 presents the design and results of a comprehensive experimental program to study the effects of upstream flow constriction on scour forming around column. Various spacing between columns and various incoming flow conditions were tested to investigate the effect of the upstream constriction on scour.
- Chapter 7 presents the design and results of an experimental used to investigate scour formation around two-column setups. The two columns were placed on the central longitudinal flume axis and, then, on the same the transversal flume axis to investigate the sheltering and spacing effects, respectively, on scour induced by tsunami-like inundation.
- Chapter 8 summarizes the main conclusions of this study. The candidate's recommendations to further investigate gaps in knowledge in future works are also included.

Chapter 2: Literature review

In this section, an overview of the literature related to the topic of tsunami scour is presented. The chapter ends with a discussion of the findings from the literature review and the possible research avenues.

2.1 Steady flow scouring

Steady flow scouring is the phenomenon of mobile bed transport caused by a constant flow. A first look at the factors that influence scouring in steady flow condition will give clues into the potential factors that govern the process of tsunami scouring.

2.1.1 Local scouring

Local scouring is the phenomenon of bed material transport due to the local change of flow conditions, which is the case when a vertical obstruction is present in the flow (e.g. bridge piers). When the flow encounters an obstacle, the water piles up at the upstream face of the pier which redirects the flow vertically. The downward flow acceleration creates a vortex that undermines the bed material at the toe of the structure, creating the horseshoe vortex (Figure 2.1). Over time, the scour hole deepens and the horseshoe vortex increases in size. The vortex also diminishes in strength until the resulting shear stress on the soil becomes lower than the bed's critical shear stress (Melville and Raudkivi, 1977).

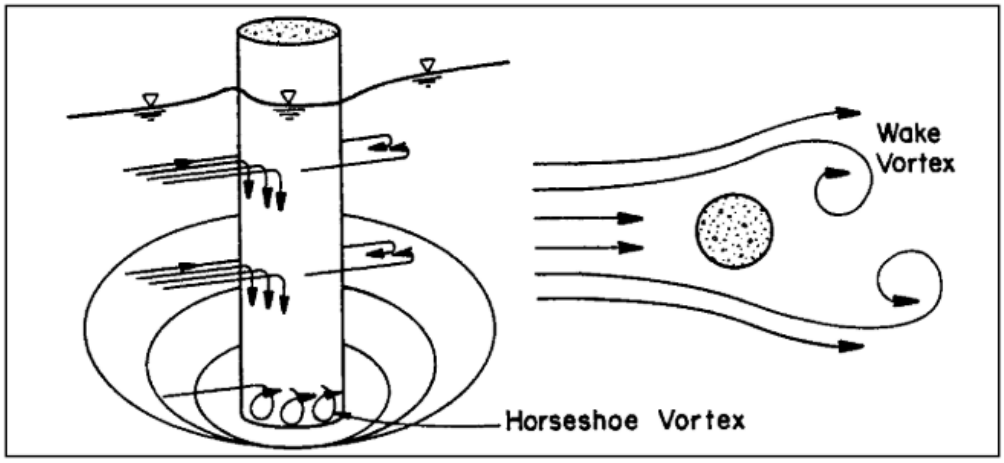

Figure 2.1: Schematic of the vortices structures responsible for scour at a pier in steady flow (Arneson et al., 2012)

Local scouring in steady flow is defined as clear-water scouring when the approach flow velocity is lower than the critical velocity for the initiation of bed material movement ($V<V_c$). Therefore, the bed is stable except for the bed near the obstruction where the local change in flow condition leads to sediment transport. Over time, the scour hole develops and reaches equilibrium once the maximum scour depth is attained. In cases where the approach flow velocity is exceeding the critical velocity for bed movement ($V>V_c$), the sediment transport condition is defined as live-bed scouring. In this type of condition, the movable bed, across the whole channel reach, is being transported with greater material transport near the obstruction. In addition, sediment dunes and

ripples are formed in the channel and are moving streamwise. These bed forms enter and exit the scour hole forming around the vertical obstruction, causing variation in scour depth after the equilibrium scour depth was reached (Guan et al., 2015). *Figure* 2.2 compares the temporal evolution of live-bed and clear-water scour depth. Due to the high velocities produced by a tsunami wave, the sediment transport condition can be considered as live-bed. However, the hydrodynamic features of a tsunami changes depending on the type of coastal slope (Takahashi et al., 2011), which means that, in some cases where the velocities are lower, the tsunami wave results in clear-water scour. Also, the equilibrium scour depth is normally not reached in tsunami flows because of the limited time span of the flow. The time dependency of tsunami flows is further discussed in section 2.1.4: Temporal evolution of bed scour

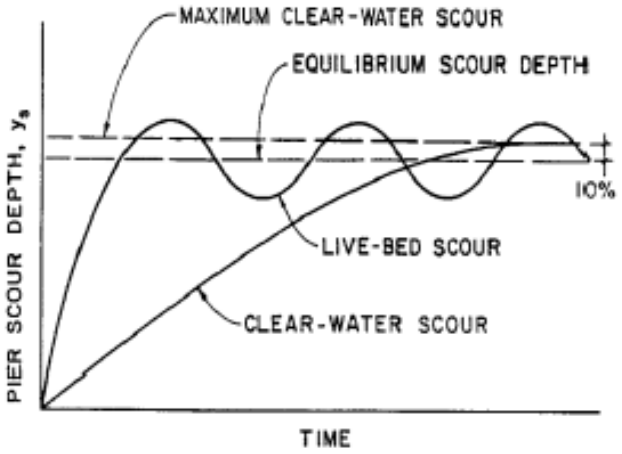

Figure 2.2: Temporal evolution of live-bed and clear-water scour (Kothyari et al., 1992)

The equilibrium scour depth (d_s) is a crucial measure in civil engineering design since it informs the engineer on multiple design decisions (Arneson et al., 2012). After reviewing over 20 passed physical experiments, Melville and Chiew (1999) concluded that the equilibrium scour depth is dependent on the following variables:

$$d_s = f(Flood\ flow, Bed\ sediment, Bridge\ pier\ geometry, Time) \qquad (2.1)$$

- Flood flow: Fluid density (ρ), kinematic viscosity (υ), mean approach flow velocity (V), mean approach flow depth (Y), acceleration of gravity (g)
- Bed sediment: Median grain size (d_{50}), geometric standard deviation of the sediment particle distribution (σ_g), density of particle (ρ_s), and critical mean approach flow velocity for entrainment of bed sediment (V_c)
- Bridge pier geometry: pier width (b), parameter describing the shape of pier (Sh), alignment of pier (Al)
- Time: time elapsed (t), time to scour depth equilibrium (t_e)

2.1.2 Spacing effects

In addition to the variables included in Equation 2.1, Kothyari et al. (1993) mentioned that the spacing between piers influences the equilibrium scour depth and temporal variation of the scour.

Spacing (S) is the distance, perpendicular to the flow direction, between two adjacent structures or structure elements. Spacing between two piers influences multiple properties of the scour hole forming around them. The decrease of the ratio between the pier spacing and the pier width (S/b) was found to be resulting in an increase of (Beg, 2010):

- the scour depth,
- the scour hole length,
- the scour hole slopes,
- the total scour area.

The link between the relative scour depth and pier spacing is shown in Figure 2.3. Beg (2010) found that pier spacing affected the scour depth up to a relative spacing of 6. However, Breusers et al. (1977) observed no effect of spacing on scouring passed a spacing of 4.3. The difference between the two results may be due to the dependency of the spacing effect on the approach flow condition (Elliott and Baker, 1985), which was different in the two cases.

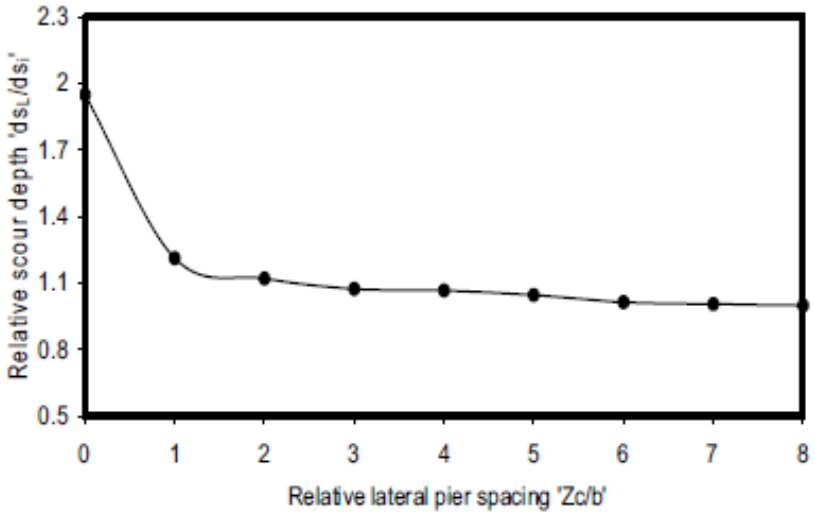

Figure 2.3: Variation of scour depth with respect to pier spacing (Beg, 2010)

Numerical modeling of transversal column arrangements showed that the reason for the increase in scour depth is the greater strength of the horseshoe vortex compared to the single column cases (Kim et al., 2014). The investigations of Zhang et al. (2017), and Vasquez and Walsh (2009) confirmed that state-of-the-art numerical models (FLOW-3D with k-ε turbulence model and Van Rijn (1984a) bed load sediment transport in these specific cases) can be used to accurately calculate the scouring around laterally spaced columns, and other complex columns configurations.

2.1.3 Constriction scouring

Constriction scouring is caused by flow acceleration ($V_1 < V_2$) due to the reduction in channel width ($B_1 > B_2$) in a particular reach of a channel (Figure 2.4). This type of scour can occur due to the natural bank topography or the construction of abutments, which reduces the channel width over the reach. The localized flow acceleration increases the flow intensity (V/V_c) over the contracted reach, which results in the lowering of the bed if the channel bed is comprised of movable material. When the length of transition (L_c) between the two different channel widths is too short, uneven

scouring occurs at the transition, which is attributed to local scouring instead of constriction scouring. In the idealized cases, it is assumed that the flow is one dimensional and the transition is long enough to allow no head loss and no local scour (Sharma, 2017).

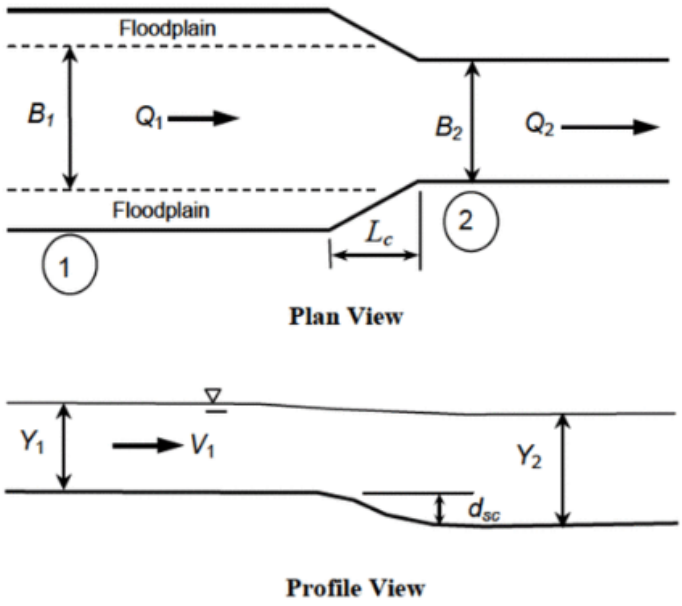

Figure 2.4: Sketch of idealized long constriction scour (Sturm et al., 2011)

The following parameters were found to influence constriction scouring (Sturm et al., 2011):

$$\frac{Y_2}{Y_1} = f\left(\frac{u_{*1}}{u_{*c}}, \frac{(V_1)^2}{gY_1}, \frac{\rho V_1 Y_1}{\mu}, \frac{B_1}{d_{50}}, \frac{B_1}{Y_1}, \frac{B_1}{B_2}, \sigma_g\right) \tag{2.2}$$

Where Y_2 is the maximum flow depth after the contraction, Y_1 is the upstream approach flow depth, B_1 is the width of the approach flow channel, B_2 is the width of the contracted section, d_{50} is the median grain size, μ is the viscosity of the fluid, V_1 is the approach velocity, u_{*1} and u_{*c} are the shear velocity of the approach flow and the critical shear velocity, g is the gravitational acceleration and σ_g is the geometric standard deviation of the sediment size distribution.

From this relationship, it is apparent that the approach flow properties, the sediment bed properties and the channel geometry are influencing the scouring in the contracted reach. When studying the phenomenon of constriction (channelization) scour caused by tsunami flows, these variables should be varied in order to fully comprehend their link to this scour mechanism in a tsunami context.

2.1.4 Temporal evolution of bed scour

Up to this point in the thesis, only the equilibrium scour depth has been discussed. However, in cases where the approach flow velocity is low, several days may be necessary to reach the equilibrium scour depth. In real-life hydrodynamic events, the time span of the event is often not long enough to reach the equilibrium scour depth (Kothyari et al., 1993; Melville and Chiew,

1999). During events such as floods, the maximum flow velocity may only last for a few hours before reducing. Extreme hydrodynamic events, such as rapid storm surges, dam breaks and tsunamis, only last a few minutes and can generate a large amount of scour (Tonkin et al., 2013; Wilson et al., 2012; Yeh et al., 2013). Due to the time dependency of the flow characteristics in the above mentioned hydrodynamic events, the flow is considered as unsteady.

Linking the temporal evolution of scour to the variation of flow may be the most appropriate way to predict the maximum scour depth in those cases, which means that the factors influencing the maximum scour depth attained in such events may be different than the ones dictating the equilibrium scour depth in steady flow. Therefore, the observations made in steady flow condition should be re-evaluated for these unsteady flows.

2.2 Tsunami scouring

2.2.1 Field observations of tsunami scouring

In recent decades, multiple tsunami events have caused building failures and the loss of lives. The recent post tsunami field investigations helped the researchers to better understand the modes of failures of buildings and the scour processes when these buildings are subjected to tsunami flows. Following their post-tsunami surveys of the 2011 Great Japan Tsunami, Tonkin et al. (2014) separated the observed scour mechanisms in 4 different categories:

- Overtopping scour: The water level increases up to a point where it overtops seawalls or breakwaters. Then, the flow plunges downward and scours the onshore toe of the structure.
- Local scour: This scour formation is smaller in diameter and is created by shear stresses at the surface of the soil interface. The scour hole forms at the bottom of the structures. This scour process is often associated with a loss in pore pressure in the soil, which can cause the liquefaction of the soil.
- General scour: This is the scouring of the soil over a large span of the inundation area. This scour mechanism is often associated with a loss in the soil's pore pressure.
- Channelization scour: The flow is locally concentrated due to constrictions or changes of flow direction. This type of scour can occur in the runup phase of the flow, but is more often associated with the drawdown phase.

Figure 2.5: Types of scour mechanisms (Tonkin et al., 2013)

Overtopping and local scour have frequently been observed in post-tsunami surveys and some data is available for the development of scour estimation models. To the contrary, data for channelized and general scour is lacking and not many studies have documented these scour processes. Local scour and channelized scour are discussed in this literature review as they are the processes that are susceptible to be responsible for the scour increase in multi-structure systems.

2.2.2 Local Scour

Local scour holes have been frequently observed around structures in post-tsunami surveys. During the 2004 tsunami, scour holes were responsible for the failure of many structures far inland (Figure 2.6), even exceeding the tsunami scour design standards of the time (Dames and Moore, 1980; FEMA, 2008). During the field investigations following the 1993 Hokkaido Tsunami and the 2011 Great Japan Tsunami, numerous scour holes were measured to be exceeding depths of 4m (Tang, 2011; Tonkin et al., 2013; Yeh et al., 2013), and one scour hole was documented to be 10m deep (Tonkin et al., 2003).

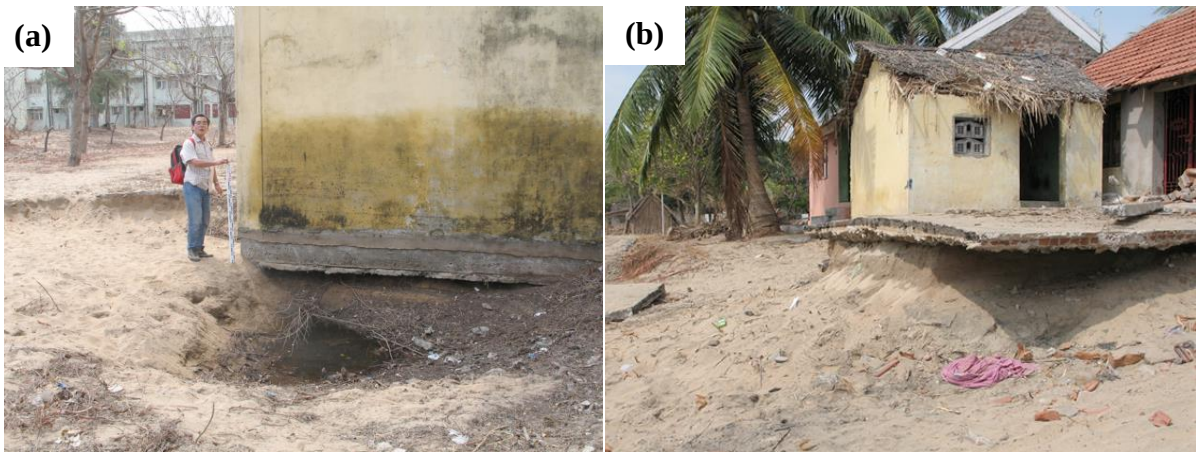

Figure 2.6: Local scour during the 2004 Indian Tsunami. (a) 1.4m Deep.(b) 1.5m Deep (Yeh and Li, 2008)

To study the phenomenon of local scour in laboratories, engineers and scientists have resorted to mimicking tsunami waves with different methods. Solitary waves, Cnoidal waves and N-waves

are often chosen because they can properly replicate the shape of a tsunami wave (Antuono and Brocchini, 2011; Chacón-Barrantes, 2018; Nakamura et al., 2008). The use of these short-period waves also allow for a test column to easily be installed on a sloped beach, which permits the drawdown flow to occur. In the large scale physical experiment conducted by Kato et al. (2000), and Tonkin et al. (2003), the drawdown phase of the wave generated the greatest scouring along the inshore and longshore faces of the structure. This was explained by the loss in pore water pressure inside the soil. When a lag is created between the pore pressure variation and the surface water pressure reduction, a negative vertical effective stress is created in the soil, which creates an upward pressure on the grain particles. At this point, the soil can experience liquefaction and is easily transported by the shear stresses imposed by the moving fluid. Therefore, allowing the drawdown phase of the wave to occur is crucial in the study of the processes governing tsunami scour.

When using the above-mentioned short-period waves, the method of wave generation limits the wave period (T), which results in waves that are often much shorter than that of an equivalent prototype-scale tsunami (Madsen et al., 2008). McGovern *et al.*, (2019) argued that the KC number (VT/b), defined by Sumer, et al. (1992), is an important proportion to respect when predicting scouring caused by tsunami-like waves because of the importance of the inundation time. Having a wave period that is too short will lead to an under prediction of the scour depth, since the scour depth at a structure is time dependent (Equation 2.1). It is recognized by the scientific community that dambreak bores replicate well tsunami waves since the appropriate scale of the wave period can be easily produced in laboratory and the bore front is hydraulically similar to an advancing tsunami bore on a flat coastal plain (Chanson, 2009, 2006, 2005).

The scour hole pattern resulting from the use of a dambreak bore is different from the use of the short-period waves in part because the drawdown is usually not simulated when using the former. A dambreak bore is typically simulated by impounding a large quantity of water and suddenly releasing it onto the test area with the use of a rapidly opening gate. The experiment of Lavictoire et al (2014) showed that the dambreak waves are resulting in greater scour depth than solitary wave and long wave tests, and the scouring resulting from this type of wave mainly occurs on the longshore sides and on the offshore side of a cylindrical structure with little scour onshore of the structure. When a square-shaped structure is used, the scouring mainly occurs at the offshore face and offshore corners of the column, with smaller scour on the longshore sides (Mehrzad et al., 2016). Therefore, the shape of the structure is influencing the pattern of the scour hole developing around the vertical structure. The approach wave properties, structure size and sediment size were all found to influence the scour depth resulting from a dambreak-type bore (Lavictoire et al., 2014; Mehrzad et al., 2016).

The scour hole forming at square structures generated by a dambreak bore begins at the upstream corners and extends to meet in the middle of the square column's offshore face (Mehrzad et al., 2016). A similar pattern of scour development was observed when a long period wave was used, which was attributed to lateral vortices forming at the structure's offshore corners (D. McGovern et al., 2019) (Figure 2.7b). With the use of a numerical model, Arabi et al. (2019) investigated the hydrodynamic interaction between a solitary wave and a standing structure (Figure 2.8). In their setup, the bed was non-erodible and flat, and an initial water depth was modeled throughout the domain. They observed some cylindrical turbulence structures at all corners of the square structures. These turbulent eddies were similar to the ones noted by D. J. McGovern et al. (2019)

and are most likely leading to scour in the above-mentioned two physical experiments (D. J. McGovern et al., 2019; Mehrzad et al., 2016).

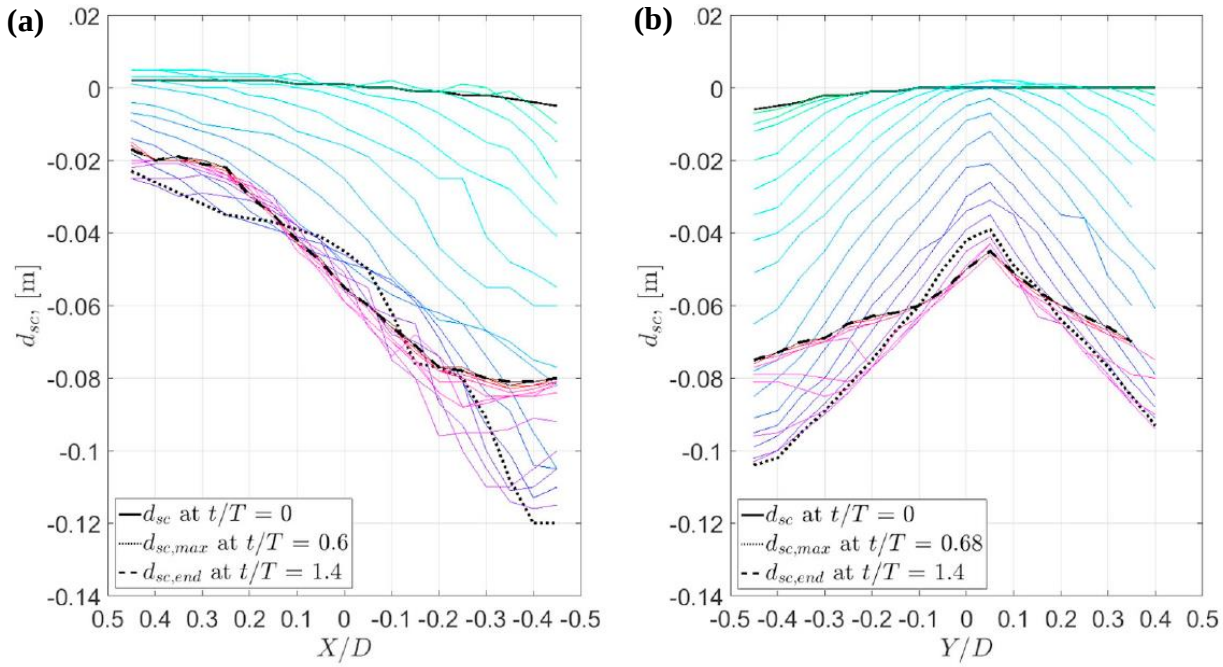

Figure 2.7: Scour evolution around a square column subjected to a long wave. (a) Longshore side; (b) offshore facing side. Measurements taken every 0.04 t/T (time over wave period) (D. J. McGovern et al., 2019)

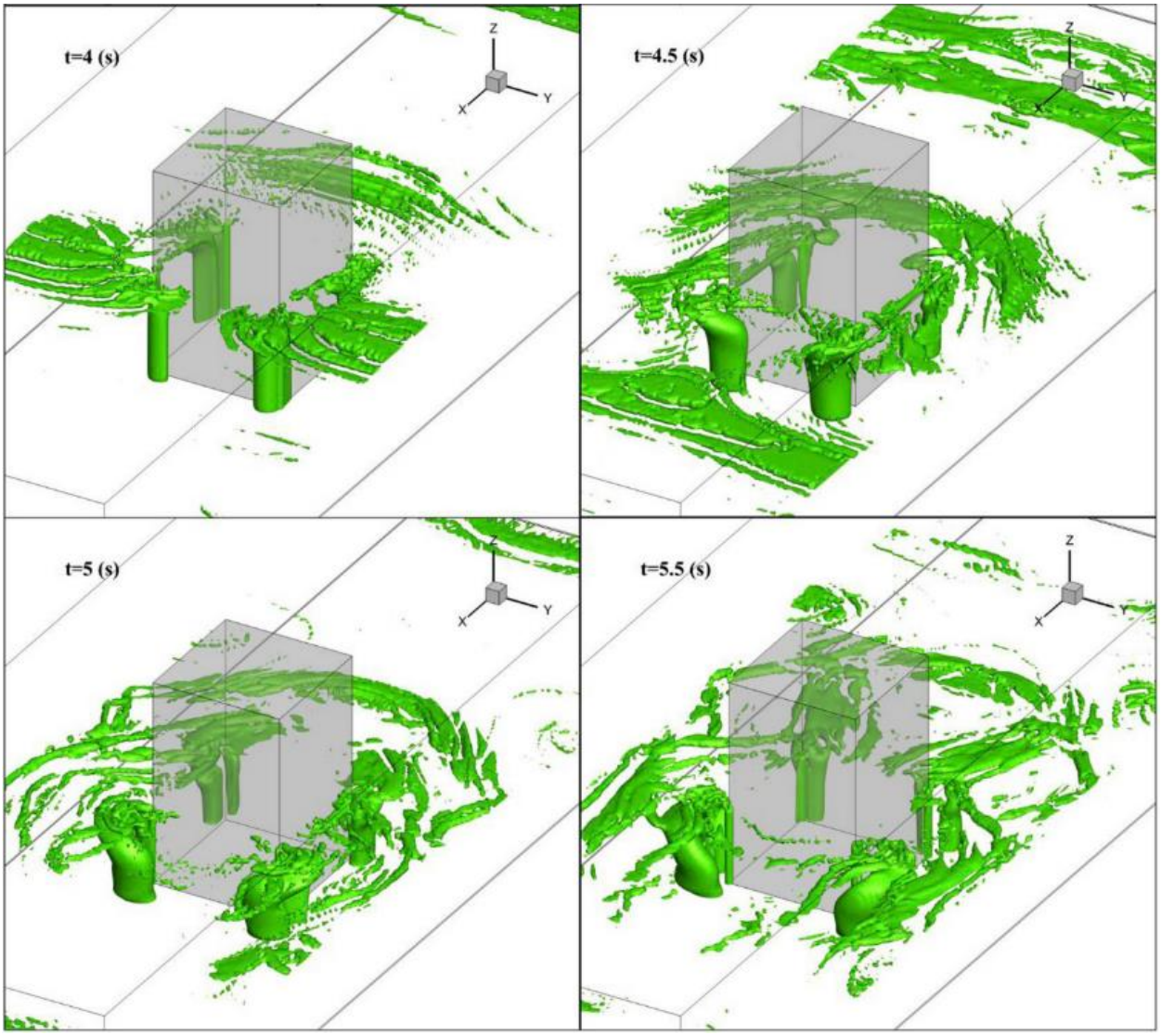

Figure 2.8: Visualization of numerically generated turbulent structures generated by a solitary wave around a standing square structure (green shows Q-criterion = 2) (Arabi et al., 2019)

2.2.3 Channelized Scour

Channelized scour has been observed in post tsunami surveys, but very little documentation on the subject is available. In the aftermath of the 2011 Great Japan Tsunami, the tsunami waves crossed the Pacific Ocean and impacted the Western American coast. Wilson et al. (2012) documented the erosion and deposition of sediments in two harbors in California, US, following the passage of the tsunami waves. Using the NOAA, USGS and USACE data base, they were able to estimate the difference in bed elevation caused by the tsunami waves at the two harbors (Figure 2.9).

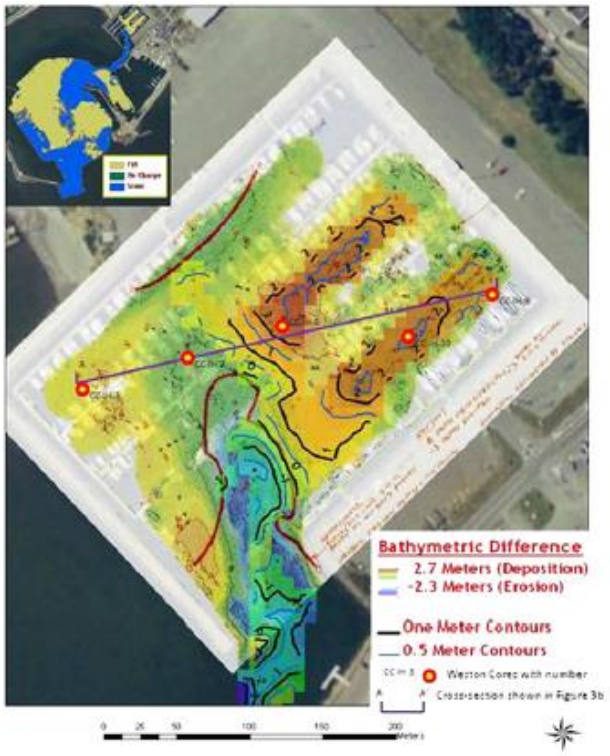

Figure 2.9: Difference in bed elevation in the Crescent City Harbour, United States, after the 2011 Japan Tsunami (Wilson et al., 2012)

They observed that the scouring occurred close to obstacles and where the flow was constricted. These scour holes were attributed to local scour and channelized scour respectively. Figure 2.9 shows a deep scour hole at the entrance of a harbor, which was caused by the concentrated flow resulting from the small opening in the seawalls. Wilson et al. (2012) estimated the surface water velocity from surveillance footage. A clear link was noted between the areas where surface water velocity was higher and the locations of channelized scouring. Therefore, constricted areas locally focussed the flow, which resulted in greater flow velocity and channelized-type scouring.

In their post-tsunami survey of the 2011 Great Japan Tsunami, Yeh, Sato and Tajima (2013) observed a deep scour hole between two tsunami-resistant hospital buildings. The scour hole, located exactly between the two buildings, was over 3.5 m deep (Figure 2.10a). Only a small amount of soil transport can be observed upstream or downstream of the buildings. The scour hole was attributed to the process of channelized scour since the buildings proximity locally accelerated the flow between them.

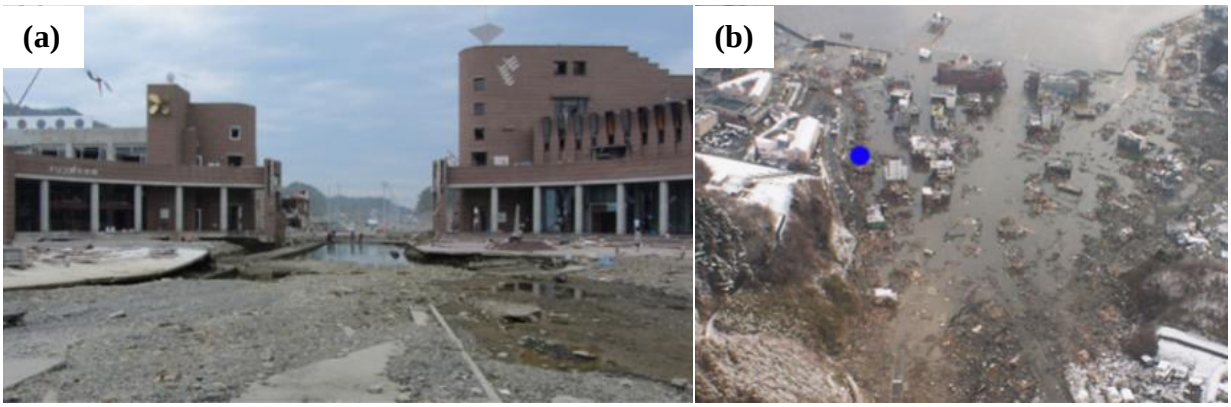

Figure 2.10: Channelized between two tsunami resistant critical infrastructures (a) View from shore side (b) Areal view of the affected area (Yeh et al., 2013)

In addition to the channelized scour, the phenomena of sheltering and flow amplification were noted (Figure 2.10b). First, the hospital buildings protected the weaker buildings that were located exactly onshore of them. Second, all the buildings, formerly situated onshore of the gap between the hospital buildings, were destroyed. A strong jet flow was generated by the narrow gap and caused greater than normal loads and/or scour at the downstream building, resulting in the failure of those structures.

2.2.4 Numerical modeling of tsunamis

With the development of reliable numerical modeling techniques, many researches have turned to using this tool to investigate different hydrodynamic characteristics of tsunamis and their associated scouring potential. Using numerical models comes with the advantage of easily changing the model's parameter and these parameters have no physical limitations, like in the case of physical experiments. However, the governing equations and the solving methods were built with inherent assumptions, which makes them only an approximation of the reality and is limiting the situations that can be accurately reproduced by the model. Therefore, these models need to be validated and calibrated for the tsunami-like flows before being used. At present, most studies involving numerical models in the field of tsunami research have used the numerical model to reproduce the results from a physical, which validates the numerical model. These studies have mostly focussed on the hydrodynamic features of tsunamis due to the complexity of modeling scour caused by any type of flows.

Numerical investigations of tsunami-like waves impacting a vertical structure have been performed successfully with the use of various numerical models. St-Germain et al. (2014) were successful at representing the complex hydrodynamic interaction between a dambreak bore and a square structure through the use of the Lagrangian model SPHysics in combination with the large eddy simulation (LES) turbulence model. Similarly, Sarjamee et al. (2017) modeled the dambreak-bore-structure interaction with the Eulerian model OpenFOAM, using LES. Sarjamee et al. (2017) included a mitigation wall upstream of the structure, which added to the complexity of the transient flow.

Authors have utilized numerical models to modeled overtopping scour (Chen et al., 2016; Sulianto and Murakami, 2015; Wang et al., 2016) and the morphological change of a flat beach (Liu et al.,

2019) caused by tsunami waves. These investigation were performed with vertical two-dimensional numerical models, because shear stresses caused by the cross-shore movement of water and vertical vortices are responsible for the bed material transport in those cases. In the case of vertical structures, the resolution of the flow in the two horizontal directions is necessary to replicate the vortices forming around a structure (Figure 2.1, Figure 2.8, and Figure 2.11).

Pan and Huang (2012) used a horizontal 2D numerical model to reproduce the physical experiment results of Tonkin et al. (2003). The experiment consisted of a solitary wave impacting a cylindrical vertical structure installed on a sloped movable bed. Their results showed that, although the model replicated well certain hydrodynamic features of the wave-column interactions, the 2D model was not detailed enough to accurately calculate the scour process around the column. 3D numerical models were found to be a lot more accurate for the calculation of wave-induced scouring around vertical structures caused by tsunami-like waves (Jayaratne et al., 2018; Nakamura and Mizutani, 2014). Larsen et al. (2017) studied the scour induced by a tsunami wave around an offshore cylindrical monopile using a 3D OpenFOAM model, with the Reynold-averaged Navier-Stokes (RANS) equations and the k-ω turbulence model. They found that the vortex formation responsible for the local scour (horseshoe vortex) was similar to that in steady current (Figure 2.11). The results of this numerical investigation were later compared to experimental results, which confirmed the validity of the numerical results (Larsen et al., 2018).

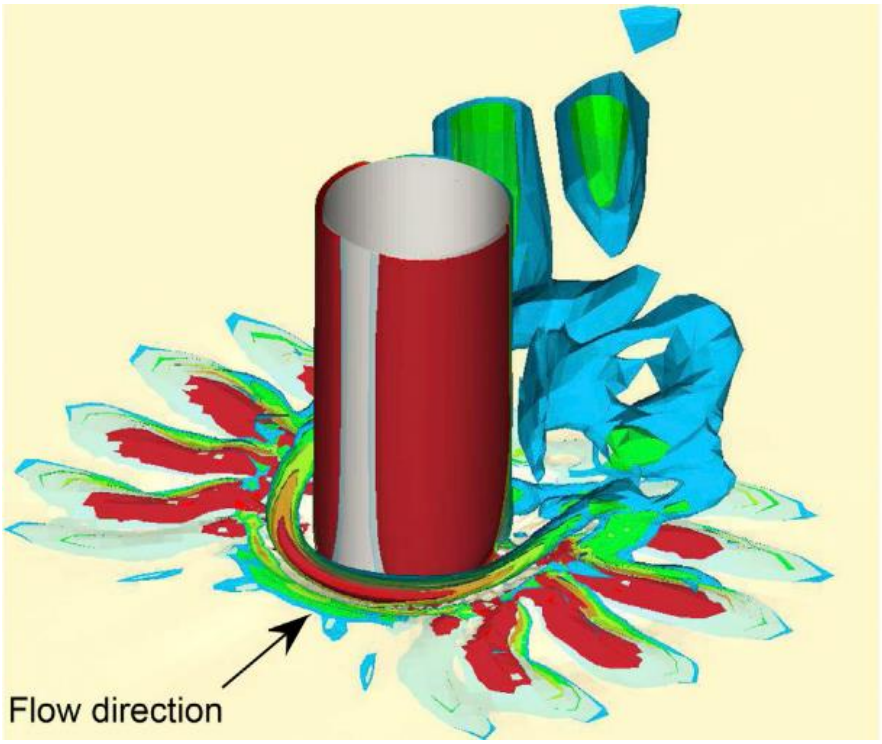

Figure 2.11: Instantaneous vortical structures around a monopile subjected to a tsunami-like wave (Larsen et al., 2017)

2.3 Tsunami design code

Since tsunamis were found to be responsible for the destruction of numerous buildings, design standards were developed to help engineers properly design buildings to withstand tsunami events.

Forces imposed by hydrostatic pressure, hydrodynamic pressure and debris impact must be considered when designing a tsunami-resistant building. In addition, requirements for scour design are now provided in some design standards. The latest provisions for local scouring, channelized scour and flow amplification are presented in this section.

2.3.1 Local scour design

Scouring has led to multiple structure failure during major tsunamis. Scouring around shallow foundation removes the support from under some structure elements, making the structure more vulnerable to failure. Therefore, adequate standards are required to ensure reliable designs. However, standards for tsunami scouring have only been recently added to construction standards (Yeh et al., 2005).

The Federal Emergency Management Agency (FEMA) standard requires designing a building's shallow foundation deeper than the predicted scour depth caused by a tsunami wave at the building location. The pile foundation must be able to resist the design loads after the scouring has exposed parts of the foundation. FEMA P-646 requires following the table developed by Dames and Moore (1980). This design scour depth prediction is related to the distance from the shoreline, flow depth and the soil type (Table 2.1).

Table 7-1 Approximate Scour Depth as a Percentage of Flow Depth, *d* (Dames and Moore, 1980)

Soil Type	*Scour depth (% of d) (Shoreline Distance < 300 feet)*	*Scour depth (% of d) (Shoreline Distance > 300 feet)*
Loose sand	80	60
Dense sand	50	35
Soft silt	50	25
Stiff silt	25	15
Soft clay	25	15
Stiff clay	10	5

Table 2.1: Approximate scour depth as a percentage of flow depth (Dames and Moore, 1980)

The ASCE 7-16 code is currently suggesting to follow the recommendations proposed by Tonkin et al. (2014) for local scour at a structure. Their curve was created based on field observations of tsunami scour in the aftermath of the 2011 Great Japan Tsunami (Figure 2.12). In this standard, only the local flow depth is used to estimate design scour depth. For a flow depth below 2.5 m, the design scour depth is equal to 1.2 times the flow depth. After this point, the design local scour depth remains at 3 m. This maximum was defined because only a single local scour hole was deeper than 3 m in the field observations of Tonkin et al. (2014).

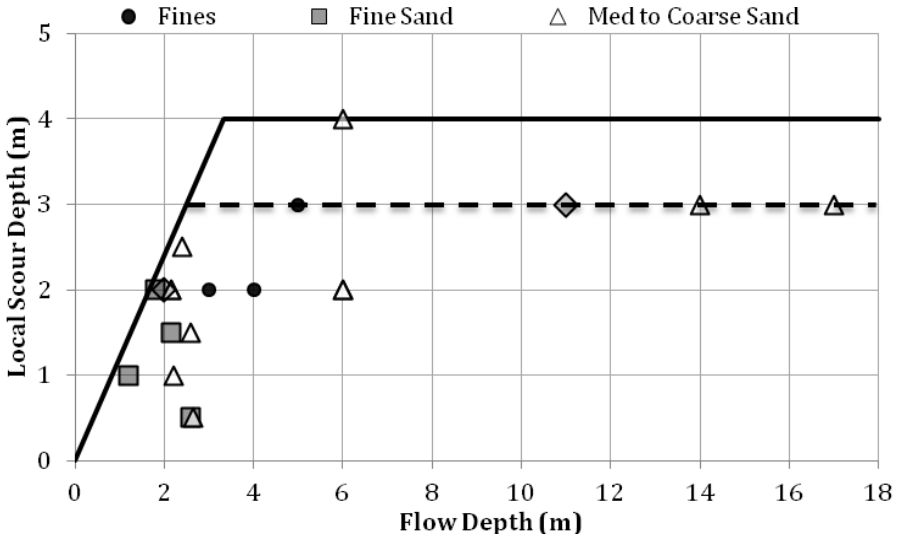

Figure 2.12: Estimation of local scour depth with respect to flow depth (Tonkin et al., 2013)

Two exceptions are included in the ASCE 7-16 standard. (1) If the soil is stable when subjected to flows velocities reaching 30 ft/s (9.14 m/s) or is non-erodible strata. Then, there is no need to design the building for tsunami scour. (2) When the estimated Froude number for the building location is less than 0.5. In those cases, a reduction factor based on the estimated Froude number can be applied.

The latest ASCE7 provisions for column scour design is to consider a vertical scouring to projected element width ratio of 1.3 times the Froude number ($d_s/b = 1.3Fr$) up to a Froude number of 1. The ratio of scour depth over pile width (d_s/b) remains at 1.3 for flows with a Froude number above 1 (Figure 2.13).

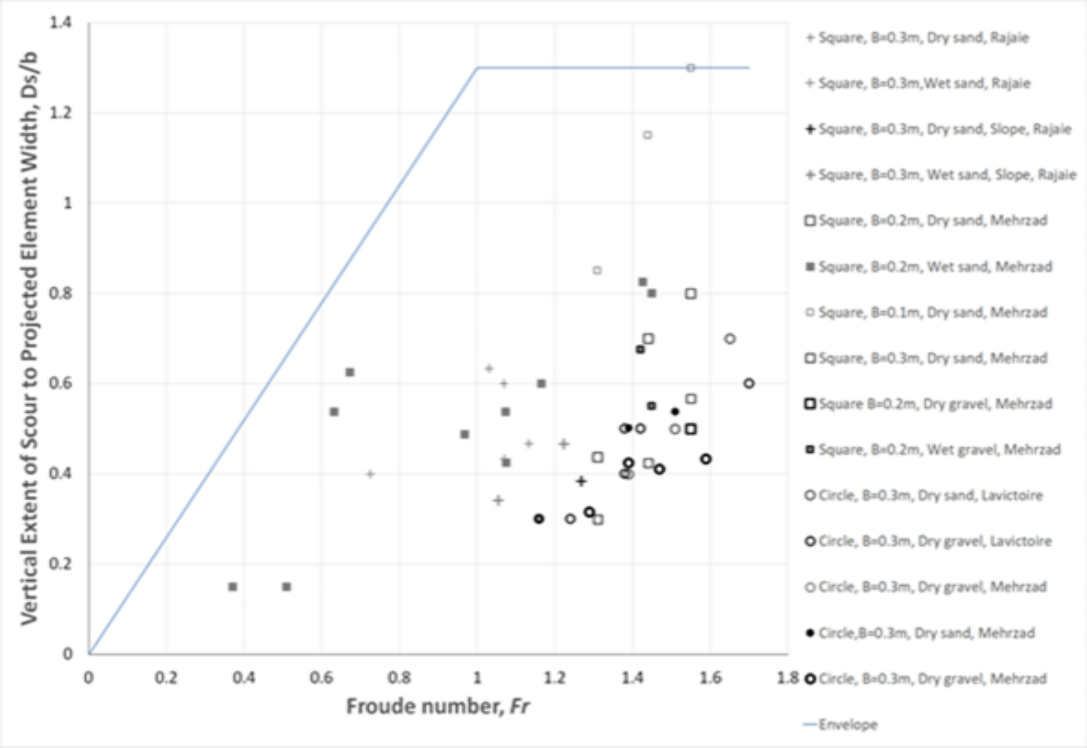

Figure 2.13: Estimation of vertical extent of scour to projected pier width with respect to the Froude number

2.3.2 Channelized and generalized scour

The ASCE 7-16 states that when designing a structure in a tsunami prone area, general and channelized scour should be considered. The scour depth is greater in areas where the returning flow can be concentrated, which is associated with channelized scour (example: along seawalls or in a pre-existing streambed). If the site has clues indicating that channelized scour is a risk, then analysis of this scour process should be carried out. Pore pressure softening should be ignored because soil liquefaction is associated with rapid changes in water level, as opposed to channelized scour that occurs over a longer time scale. It is recommended to use dynamic numerical modeling, physical modeling or empirical methods to determine the depth of scour generated by those mechanisms. However, no further guidance is provided for this type of analysis.

2.3.3 Flow velocity amplification

In the ASCE 7-16 standard, flow constriction must be considered because it amplifies the flow velocity and the associated hydrodynamic forces at a structure installed downstream of the constriction. Three experimental studies are mentioned in the standard's commentary for guidance (Nouri, 2008; Nouri et al., 2010; Thomas et al., 2015). Based on these studies, the ASCE 7-16 requires that the considered flow velocity be increased by 25% when the effective wake clearance angle (β) is $20^o < \beta < 35^o$ (Figure 2.14a). When β is lower than 10^o or greater than 55^o, no amplification factor needs to be applied to the flow velocity (Figure 2.14a). The effect of upstream obstruction on flow factor shall be considered only if enclosed structures are present within 500ft (152m) of the site.

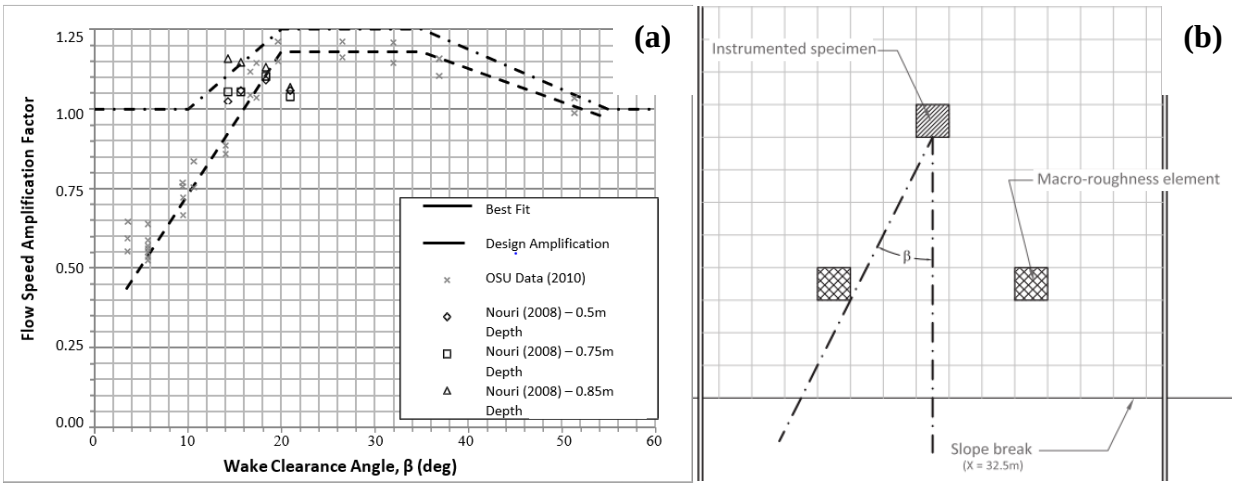

Figure 2.14: (a): Flow speed amplification factor vs wake clearance angle (β) (b): Diagram of the effective wake clearance angle (Thomas et al., 2015)

2.4 Discussion and Research Needs

Tsunami research contains many gaps, which present many research opportunities. As experienced during the large tsunamis of the 21st century, the lack of appropriate methods to cope with such a destructive hydraulic phenomenon makes the coastal communities vulnerable to any such future events. At present, only a very limited number of parameters are used to predict scouring caused by tsunamis. Only the flow depth, the Froude number, the structure width and the grain size are considered for tsunami scour design in construction standards. However, the standards fail to predict accurately the complex process of tsunami scour, because many factors that were found to influence scour induced by tsunami-like flows are not yet considered and many scour holes were found to exceed the construction standards' requirements. Additional factors, which are considered in steady flow scouring, could be studied in a tsunami context and included in the tsunami design standards in the future. Those factors include, but are not limited to: structure geometry, sediment properties, the presence of additional structures that concentrate the flow, flow velocity, shore slope and inundation time.

The influence of structure arrangements and their distance from one another on scour is still yet to be researched in tsunami flow conditions. Studies performed in steady flow showed that the addition of a similar sized structure placed on the same transversal plane can increase the scour depth by 21% when the distance between the structures is equal to the structures' width. The ASCE7 standard requires planning for flow velocity amplification due to upstream obstructions, but nothing is mentioned on the influence of this setup, nor on the effect of transversally spaced buildings, on the associated scour. Sheltering effects may also be occurring when two buildings are placed on the same longitudinal line. Further research on the effect of various structure arrangements on scouring is needed.

Several methods of analogizing tsunami waves have been used in previous studies. The use of dambreak bores and solitary waves have been the two most common ways to simulate a tsunami wave. Several authors have discussed theoretically their validity (Chacón-Barrantes, 2018; Chanson, 2009, 2006, 2005; Madsen et al., 2008). Both methods of simulating tsunami waves offer different advantages and disadvantages for the study of scouring. However, to this day, no

experimental research has been performed to directly compare the two tsunami mimicking waves, and discuss the importance of the drawdown phase, inundation period and beach slope when studying tsunami-induced scouring. Studies have previously varied the height of the incoming wave and column size and showed their importance on scour, but none have tested the scale effect by simultaneously changing the size of wave, structure and movable bed particles. Studying the scale effect would test the assumptions that the scaling rules that applies to scouring in steady flow conditions also applies for tsunami-like flows.

Few studies have used numerical models to study tsunami flows, and tsunami-induced scouring, which means that few situations have been modeled (Chen et al., 2016; Larsen et al., 2017; Liu et al., 2019; Pan and Huang, 2012; Sarjamee et al., 2017; St-Germain et al., 2014, 2012; Sulianto and Murakami, 2015). At present, all numerical studies in the field of tsunami, with only a few exceptions, have been performed with non-erodible soil or were studying the phenomenon of overtopping scour using a two-dimensional vertical model. To the candidate's knowledge, the morphological changes caused by local scour induced by a tsunami-like wave have only been discussed by two studies, and they both used a cylindrically shaped vertical structure. Scouring around a square column caused by tsunami has yet to be numerically investigated. These studies have utilized long waves and solitary waves to mimic tsunami waves and to study its associated local scour. Dambreak wave-structure interaction was investigated over a stable bed, but the resulting scour has not been numerically tested so far (St-Germain et al., 2014).

With the exception of flat beach numerical investigations, all the sediment transport numerical investigations were performed at laboratory scale. A prototype scale investigation of local scour induced by a tsunami wave has yet to be done. A study at this scale could help confirm the scaling methods used in small scale experiments to study the phenomenon of tsunami scour. In addition, a numerical model may be used to study the changes in turbulence patterns associated with multiple structures compared to a singular structure, which would help explain the reason for the change in scour.

Chapter 3: Numerical Modeling of Tsunami Induced Scouring around a Square Column: Performance Assessment of FLOW-3D and Delft3D

3.1 Abstract

In the recent years, tsunamis have caused considerable damage to coastal infrastructures and inflicted numerous casualties in coastal communities in the impacted regions. The information, which the design requirements for tsunami resistant infrastructures is based on, is still in its preliminary stages. The focus of the study is to investigate, by means of a numerical model, the scouring occurring around a single square column subjected to tsunami floods. A 3D hydrostatic numerical model (Delft3D) and a 3D non-hydrostatic model (FLOW-3D) were used to replicate a series of physical tests conducted at the University of Ottawa, which consisted of a dam-break wave impacting onto a single square column installed over a movable sediment bed. These experimental tests were conducted in the Dambreak Flume at the University of Ottawa. A total of four different turbulence models and two different sediment transport models were tested to find the most appropriate combination, which could model the complex flow characteristics associated with a dambreak-type bore. An extensive review of the hydrodynamic and scouring performance of various numerical models was also included in this study.

3.2 Introduction

Tsunamis are catastrophic events that affect highly populated coastlines along many regions of the world. They cause immense damage and have caused hundreds of thousands of deaths in the past two decades alone (Fritz *et al.*, 2011; Nistor, and Palermo, 2015; Palermo *et al.*, 2013; Samarajiva, 2005; Takahashi *et al.*, 2011; Tang, 2011; Tonkin, Francis, and Bricker, 2013). Although tsunamis have been observed to cause structural failure in buildings/infrastructure, very little information is available on scouring around buildings when exposed to tsunami-induces coastal inundation (Jayaratne *et al.*, 2016; Yeh, and Li, 2008).

In the latest version of the newest code, elaborated by the American Society of Civil Engineering (ASCE) and entitled *Minimum Design Loads and Associated Criteria for Buildings and Other Structures; Tsunami Loads and Effects ASCE7-Chapter 6*, only tsunami flow depth as a factor for designing to protect against scouring effects was taken into consideration (ASCE, 2016; Tonkin, Francis, and Bricker, 2013). This provision was developed based only on limited field observations and it may lead to inaccurate predictions of the scour around structures in extreme overland flow events. Recent physical experiments on extreme flood events suggest that flow properties, the structures' position relative to the shore, and the structures geometry and dimensions are significantly influencing the development of the scour and its final depth (Kato, Sato, and Yeh, 2000; Lavictoire, Nistor, and Rennie, 2014; Mehrzad, Nistor, and Rennie, 2016).

In order to physically model tsunamis, various wave generation modes have been previously employed to account for modifications to the waves as they advance inland in the form of either a surge or a highly turbulent bore (Fritz et al., 2011a; Takahashi et al., 2011). Solitary waves

(Nakamura, Kuramitsu, and Mizutani, 2008; Nistor *et al.*, 2017; Nistor, Goseberg, and Stolle, 2017), N-waves (Yeh, and Li, 2008), Cnoidal waves (Antuono, and Brocchini, 2011), and dam break waves (Lavictoire, Nistor, and Rennie, 2014; Mehrzad, Nistor, and Rennie, 2016; Nouri *et al.*, 2010; St-Germain *et al.*, 2014; St-Germain, Nistor, and Townsend, 2012) have been used by various scientists to study tsunami behavior. However, Madsen et al. (2008) have argued that the fact that a tsunami has a long period minimizes the energy loss due to friction, and tsunami-replicating models should follow the same logic. A dam break-type wave, in the form of a broken bore, has become a scientifically accepted method to model tsunami-induced inundation due to its ability to produce long period waves and to closely represent a tsunami wave advancing on a flat coastal plain (Chanson, 2009, 2006). In the present study, the authors employed the use of a dam break wave.

This paper focuses on simulating the impact of tsunami bores on scour around structures under extreme flow conditions. Physically-based numerical models are efficient and allow users to assess the effect of the specified parameters without the need to perform extensive experimental modeling work. Despite experimental modelling being extremely valuable to calibrate and validate numerical models, it tends to be expensive and time-consuming. In the particular case of tsunamis, the rapidly transient flows and the associated strong eddies in both the horizontal and vertical planes represent significant challenges. Presently, various computational fluid dynamic (CFD) models have been developed and are available both commercially and as open-source. As part of this study, two different numerical models were applied in an attempt to mimic tsunami-like flows: FLOW-3D (Flow Science, 2018) and Delft3D (Deltares, 2011). Both have their own set of assumptions leading to different strengths and weaknesses. FLOW-3D is a fully non-hydrostatic numerical model package developed to solve complicated flow structures. Delft3D is a quasi-3D numerical model designed to solve riverine and coastal processes. Although Delft3D was developed for larger scales, it was chosen in this study to evaluate to what extent this model can simulate the problems of the present study. The hydrostatic assumption for vertical accelerations is the main difference between the models. Additional open source CFD models, such as SPHysics (Fourtakas and Rogers, 2016; Saghatchi, Ghazanfarian, and Gorji-bandpy, 2014), OpenFOAM (Liu *et al.*, 2019; Yan, Mohammadian, and Rennie, 2020b), SSIM (Alemi and Maia, 2018; Ehteram and Mahdavi, 2015) and Fluent (Omara et al., 2019), could be used for this task. These models have proven to perform well at predicting scouring around a structure.

Numerical models have been applied for decades to represented tsunami waves and their complex interactions with the nearshore and infrastructure located in the vicinity of the shoreline. Reynolds Averaged Navier Stokes (RANS) (Chen et al., 2016; Larsen et al., 2018, 2017) and spatially-averaged models (Sarjamee, Nistor, and Mohammadian, 2017; St-Germain *et al.*, 2014; St-Germain, Nistor, and Townsend, 2012) were shown to correctly replicate the hydrodynamic properties of tsunami-like waves impacting a vertical structure.

Few numerical models have modeled tsunami-induced scouring around vertical structures. Larsen et al. (2017, 2018) were able to achieve realistic scouring around a circular mono-pile by applying RANS with k-ω as the closure model. Researchers have investigated some parameters influencing tsunami-induced scouring using numerical models, but the investigation of bed profile changes around a single column has been virtually unstudied (Jiang et al., 2015; Liu et al., 2019; Nakamura et al., 2008; Yeh and Li, 2008).

The objective of this study is to study the performance of the previously mentioned numerical models (FLOW-3D and Delft3D) in reproducing the tsunami-induced scour around. The model, which would prove most adequate to reproduce the spatio-temporal evolution of the experimental results, will be used for the authors' future work on tsunami-induced scour around multiple structures.

The remainder of this paper is organized as follows: Section 2 presents the methodology and details of each of the two numerical models investigated. Section 3 presents the results of the study while they are further discussed in Section 4. Finally, the conclusions stemming from this study are presented.

3.3 Methods

In order to find the most suitable numerical model for the authors' tsunami scouring study, the following steps were undertaken:

- The two numerical models were calibrated using Chanson (2009) analytical solution for a dambreak profile.
- Variables were defined as calibration variables in each sediment transport model and were adjusted to match the experimental results found by Merhzad et al. (2016). These results were used for the models' validation.
- The hydrodynamic field around the bore-building interaction, as well as scouring results, for Delft3D and FLOW-3D, were compared.
- The performance of four turbulence models (standard k-ε, RNG k-ε, k-ω and LES) were compared by comparing their effect on the final scour profile.
- Finally, two different sediment transport models, Van Rijn (1984) and Nielsen (1992), were tested in combination with the best performing turbulence model from the previous step.

3.3.1 Experimental data

The numerical models were developed to reproduce an experimental test by Mehrzad et al. (2016). This experiment was conducted in the Dambreak Flume at the University of Ottawa, Canada. The flume used for this experiment was 30 m long, 1.5 m wide and 0.5 m deep. Mehrzad et al (2016) studied the spatio-temporal evolution of scouring around vertical square structural models due to dam break-waves. Figure 3.1 shows the experimental set up. The dambreak wave was generated by the sudden release of a specified volume of water impounded behind a rapidly opening swinging gate. Only one of Mehrzad et al. (2016) tests was used for comparison purposes with the results from the numerical models investigated in this study. In this test run, Mehrzad et al. (2016) used water with an impoundment depth of 0.25 m, which generated a hydraulic bore that impacted a square column possessing a width of 0.2 m. The square column was installed in a 0.2 m deep by 3.3m long sediment bed (with a median diameter grain size (D_{50}) of 0.001 m). A false floor was installed upstream and downstream of the sediment bed. The same sand, as specified above, was glued onto the false floor to ensure uniform bed roughness over the entire section of propagation of the hydraulic bore. A 0.15 m wide gabion bed was installed at the upstream end of the sediment bed to reduce local erosion at the interface between the erodible bed and the false floor.

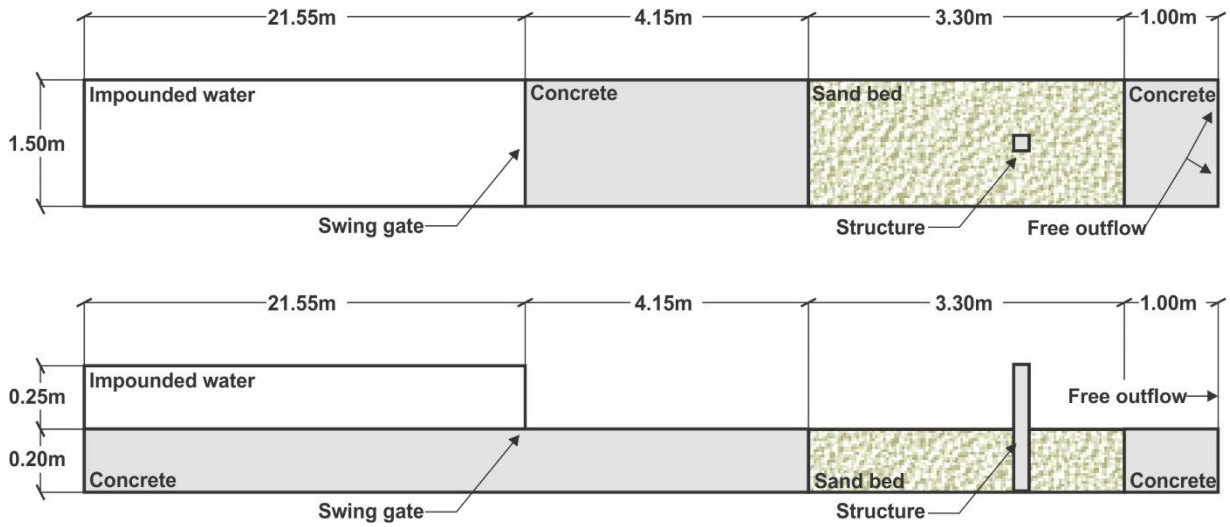

Figure 3.1: Experimental setup from Merzhad et al. (2016)

At the end of each test, the scour around the column was measured using a Leica Disto TM laser altimeter which was reported to have a distance measuring accuracy of ± 0.001 m. The results of the laser altimeter measurements are an accurate 3D representation of the final bed profile. In Mehrzad et al. (2016), wave gauges and video cameras were used to observe the time history of the bore velocity and of the sediment bed evolution. When analyzing their results, an apparent bowl-shaped deep scour hole, with a maximum depth of 160 mm, was observed to have formed at the upstream face of the column (Figure 3.2). A strong vertical vortex was observed to have occurred at the front of the model structure and the authors inferred that this was most likely responsible for much of the upstream scour hole development. Some minor scouring extended at a 45-degree angle downstream from the column. Cone shaped accumulation was observed directly behind the column. In their paper, additional information is available on the spatio-temporal scouring evolution for different structural models cross sections, size and upstream impoundment depths.

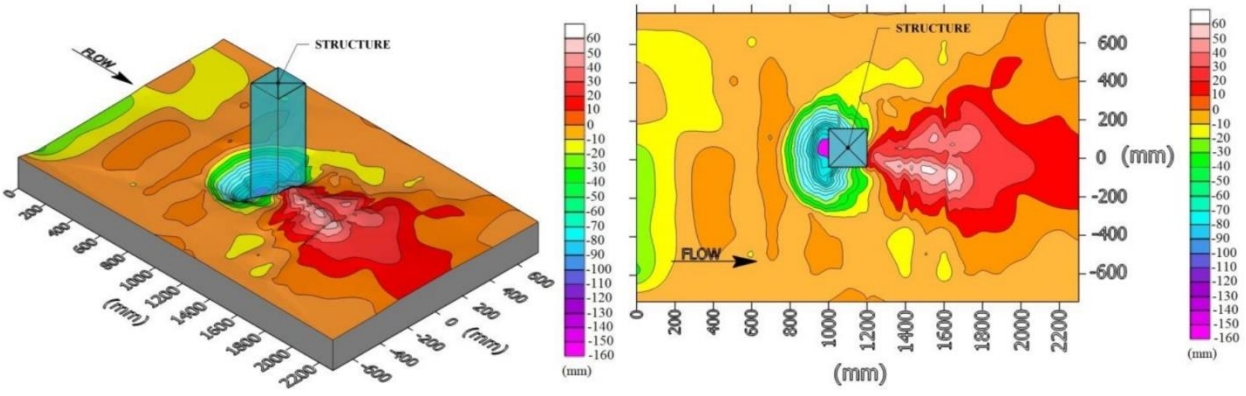

Figure 3.2: Final scour bathymetry generated by a hydraulic bore created by an impoundment depth of 0.25m for the case of a column with a 0.2m side square cross section (reproduction with permission of Mehrzad et al. (2016))

3.3.2 Numerical Models

As mentioned, the objective of this study is to compare the performance of two numerical models: FLOW-3D and Delft3D, and to assess their suitability to further investigate scouring around a structure induced by a dam-break wave. The first software discussed is Delft3D in its open source option (Briere, Giardino, and Van der Werf, 2011; Deltares, 2011). The second numerical model used in this study is FLOW-3D, for which a research license was granted to the authors. Their features and setups are discussed in this section.

3.3.2.1 Governing Equations

Delft3D does not allow the use of both the sediment transport module and its non-hydrostatic solver. Therefore, a hydrostatic simulation was performed instead. Due to the shallow water assumption, the vertical acceleration is only caused by the hydrostatic pressure:

$$\frac{\partial P}{\partial z} = -\rho g h \tag{3.1}$$

where P is the pressure, ρ is the density, g is the gravitational acceleration and h is the water depth. The continuity equations and the momentum equations for the two horizontal directions i (for both x- and y-direction) are as follows:

$$\frac{\partial u_i}{\partial x_i} = 0 \tag{3.2}$$

$$\frac{\partial u_i}{\partial t} + \frac{\partial u_i u_j}{\partial x} + \frac{\partial u_i u_j}{\partial y} + \frac{\partial u_i u_j}{\sigma \partial z} - f u_i = \frac{1}{\rho_0} P_i + F_i + M_i + \frac{1}{h^2}\frac{\partial}{\partial z}\left(\nu_V \frac{\partial u_i}{\partial z}\right) \tag{3.3}$$

where u_i and u_j are the velocity vectors, t is the time, x_i is the position vector, f is the Coriolis parameter, F_i are the external forces, M_i is the external hydraulic forces contribution to momentum and ν_V is the vertical eddy viscosity coefficient. The horizontal pressure terms (P_x and P_y) are provided by the Boussinesq assumptions. In the pressure equation, the horizontal pressure gradient is derived in the transformed vertical coordinate (σ) and ζ is the height of free water surface elevation above the horizontal plane of reference.

$$\frac{1}{\rho_0} P_i = g\frac{\partial \zeta}{\partial x_i} + g\frac{h}{\rho_0}\int_{\sigma}^{0}\left(\frac{\partial \rho}{\partial x_i} + \frac{\partial \sigma}{\partial x_i}\frac{\partial \rho}{\partial \sigma'}\right) d\sigma' \tag{3.4}$$

With FLOW-3D, four different turbulence models were employed and their performance was assessed to determine the optimal one: (1) the standard k-ε model (used to compare the performance of both models), (2) the RNG k-ε model; (3) the k-ω model and (4) the LES model. In contrast to Delft3D, FLOW-3D solves the Reynolds-averaged Navier-Stokes momentum equation in the vertical direction, allowing the simulation to be fully non-hydrostatic. This feature helps capturing the vertical vortices generated by the advancing bore. However, this comes with greater computational cost. Although FLOW-3D uses a structured orthogonal grid, it can model complex geometries by the application of the fractional area/volume method (FAVOR). This method allows a rectangular computational cell to be partially blocked by an obstacle, or, in the present case, the presence of a non-uniform bed. Sharp free surface (e.g. hydraulic jumps, free jets in air) are modeled using the Volume-of-Fluid (VOF) method (Vasquez, and Walsh, 2009). The following equation is the momentum equation which is solved for all axis:

$$\frac{\partial u_i}{\partial t} + \frac{\partial u_i u_j}{\partial x_j} = -\frac{1}{\rho}\frac{\partial P}{\partial x_i} + \frac{\partial}{\partial x_j}\left[(\nu)\left(\frac{\partial u_i}{\partial x_j} + \frac{\partial u_j}{\partial x_i}\right)\right] + F_i \qquad (3.5)$$

3.3.2.2 Boundary Conditions

In Delft3D and FLOW-3D, all boundaries were defined as symmetric pressure-type, except for the downstream one. In FLOW-3D, the downstream boundary was defined as a negative pressure boundary of z = -10m. This boundary definition allowed the flow to freely exit the computational domain and, as such, no flow reflection at the downstream boundary was observed, replicating the dambreak flume outlet. In the case of Delft3D, no boundary condition reflection was achieved by including a 10 m long, 3 m deep, 1.5 m wide reservoir, starting at x = 30 m, to allow the water to escape the flume's testing area. This setup replicates the downstream outflow of the University of Ottawa flume used during the physical model test (Mehrzad et al. 2016). No effect of this setup was observed on the time-history of the water surface near the structural model (column).

3.3.2.3 Computational Grids

In the case of Delft3D, simulations were performed using a curvilinear grid with maximum refinement of 0.02 m in the x-direction, a uniform grid size of 0.02 m in the y-direction, and 20 equal proportion σ-type cells in the z-direction (see Figure 3.3). The grid and time steps were optimized through a sensitivity analysis performed by the authors until the model was found to be grid and time insensitive.

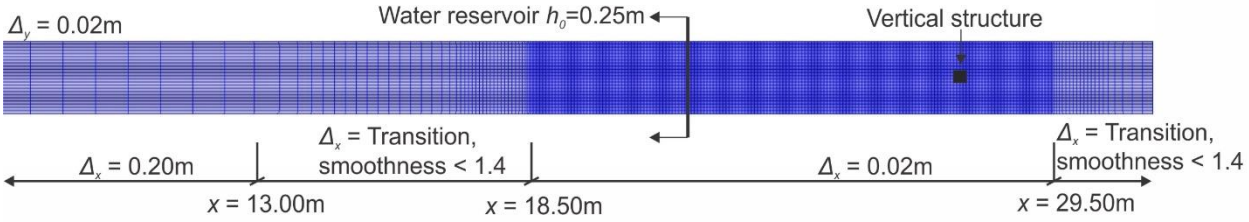

Figure 3.3: Numerical Model Mesh for Delft3D

For FLOW-3D, the computational domain consisted of four nested grids with uniform, prism-shaped cells. Their sizes varied from 0.02 m for most of the domain of the flume to 0.0075 m in the close vicinity of the structural model for a total of just over 2.5 million cells (see Figure 22). Sensitivity analysis showed no scouring change when additional finer grids were added. The time step was variable and optimized throughout the simulation to ensure convergence. Convergence is assessed based on the acceleration components. If the Courant number is larger than 1.0, then the time step is automatically reduced to achieve convergence. As such, the same computational domain setup was used for all numerical tests.

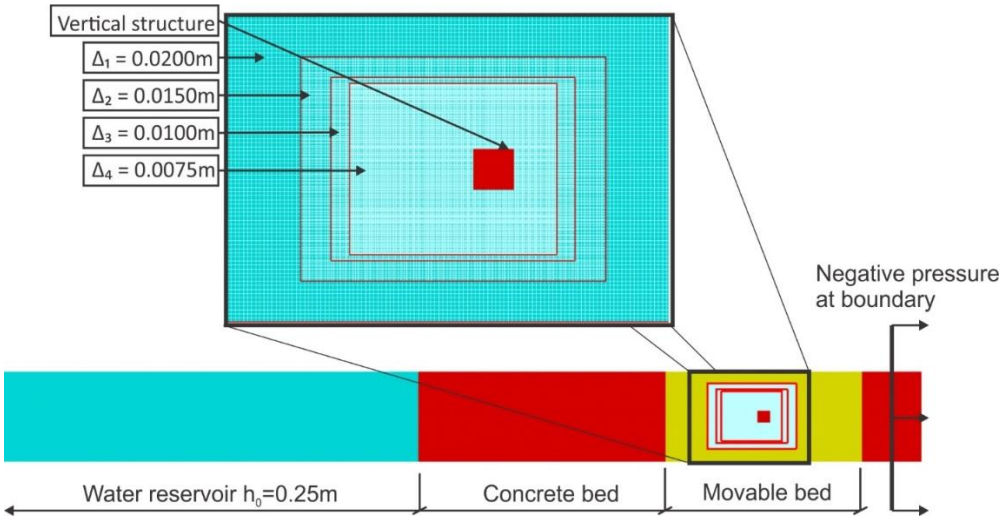

Figure 3.4: Numerical Model Mesh for FLOW-3D

3.3.2.4 Sediment Transport Model

The sediment transport model used in both Delft3D and FLOW-3D was the one developed by Van Rijn (1984), originally developed for coastal-type models. The model calculates separately the bedload and suspended sediment transport. According to reference height a determined by Equation 3.6, the sediment is considered as bedload and is suspended when above that height.

$$a = min\left[max\left(AKSFAC * k_s, \frac{\Delta_r}{2}, 0.01h\right), 0.2h\right] \tag{3.6}$$

where a is Van Rijn's reference height, *AKSFAC* is a proportionality factor (defined by the model user), k_s is the current related effective roughness height, Δ_r is the wave-induced ripple height, set as constant of 0.025m, and h is the water depth. The bedload transport equation is based on the principle of sediment motion such that when a certain shear stress is exceeded the sediment becomes entrained. The critical shear stress is based on Shield's diagram (van Rijn, 1984a,b). The following equation describes the bed load transport rate under reference height, a:

$$|S_b| = 0.25\alpha D_{50} D_*^{-0.3}\left[\tau'_{b,c}/\rho\right]^{0.5}\left[\left(\tau'_{b,c} - \tau_{b,cr}\right)/\tau_{b,cr}\right]^{2.1} \tag{3.7}$$

where, S_b is the bed load transport, D_{50} is the median grain size, $\tau'_{b,c}$ bed shear stress due to current, $\tau_{b,cr}$ is the critical bed-shear stress according to Shields, D_* and α are the non-dimensional particle diameter and a calibration factor (taken as 1.0 in both models), respectively. D_* is defined as:

$$D_* = D_{50}\left[\frac{\left(s^{(l)} - 1\right)g}{\nu^2}\right]^{1/3} \tag{3.81}$$

where ν is the dynamic viscosity and s is the sediment specific gravity. The total suspended sediment transport is found with Equation 3.8 which is the summation, from the reference height to the water surface, of the suspended sediment concentration (c) multiplied by the velocity (u):

$$q_s = \int_a^h u * c * dz \tag{3.9}$$

The reference sediment concentration is calculated using the following equation:

$$c_a^{(l)} = 0.015\rho_s^{(l)} \frac{D_{50}\left(T_a^{(l)}\right)^{1.5}}{a\left(D_*^{(l)}\right)^{0.3}} \tag{3.10}$$

where $c_a^{(l)}$ is the mass concentration at the reference height a, $T_a^{(l)}$ is the non-dimensional bed-shear stress, $\mu_c^{(l)}$ is the efficiency factor current, u_* is the friction velocity due to currents, and $\tau_{cr}^{(l)}$ is the critical bed shear stress. The following equations are used to determine the above-mentioned variables.

$$T_a^{(l)} = \frac{\left(\mu_c^{(l)}\tau_{b,c}\right) - \tau_{cr}^{(l)}}{\tau_{cr}^{(l)}} \tag{3.11}$$

$$\mu_c^{(l)} = \max\left(0.6/D_*^{(l)}, 0.06\right) \tag{3.12}$$

$$\tau_{cr}^{(l)} = (\rho_s^{(l)} - \rho_w) g D_{50} \theta_{cr}^{(l)} \tag{3.13}$$

A second sediment transport model, the diffusion model developed by Nielsen (1992), was tested, however only in the case of FLOW-3D. This model was developed for coastal-type conditions and was shown to perform well when the median diameter of the sediment is around 0.001 m (Nielsen, 1992). In FLOW-3D, only the formulation of bedload differs between the application of Van Rijn (1984) and Nielsen (1992). Also, both models are based on the Shield's parameter. The bedload transport rate is determined with the following equation:

$$|S_b| = 12\left[g\left(\frac{\rho_s - \rho_w}{\rho_w}\right){D_{50}}^3\right]^{1/2}\left[\tau'_{b,c}\right]^{0.5}\left(\tau'_{b,c} - \tau_{b,cr}\right) \tag{3.14}$$

3.3.2.5 Turbulence models

Four different numerical models were tested during this study. (1) The standard *k-ε* model was tested in both Delft3D and FLOW-3D since it was the only turbulence common to the two of them. It was also successfully used to model scouring in complex cases (Yan, Mohammadian, and Rennie, 2020a, 2020b) (2) The RNG *k-ε* model was tested in FLOW-3D since it has been used in similar cases (Chen et al., 2016). (3) Similarly, the *k- ω* model was used to measure scouring in comparable flows (Larsen et al., 2018). (4) The LES model was tested in FLOW-3D because it is recognized to perform well in highly turbulent flows and was previously proven to mimic well dambreak flows interacting with structures (Escue, and Cui, 2010; St-Germain *et al.*, 2014).

The *k-ε* and *k-ω* turbulence models are RANS (Reynolds-averaged Navier Stokes) closure models. To solve for turbulence, these models emulate energy losses due to turbulence as local viscosity increases following the Boussinesq assumption. The *k-ε* model, as well as all other RANS turbulence closure models applied in this study, is a two-equation-type model developed for fully turbulent flows: *k* is the turbulent kinetic energy and *ε* is the turbulence dissipation rate (Jones, and Launder, 1972). This model uses two main assumptions: (1) the fluid and its Reynold stresses are isotropic, and (2) the turbulence is only related to the local flow velocity. These assumptions reduce the model's accuracy in specific scenarios. For instance, the isotropic assumption may be erroneous close to walls, where the wall proximity changes fluid properties under certain circumstances (Nisizima, and Yoshizawa, 1987). In addition, this assumption removes the possibility to accurately model non-Newtonian fluids, which are anisotropic by definition and can often be the case for tsunami flows with high sediment or debris concentration (Chanson, 2005). The second assumption limits the model's capabilities as it pertains to highly mixed fluids. In such

cases, heavy turbulence from surrounding eddies will most likely affect local turbulence. The standard *k-ε* model is available on both Deflt3D and FLOW-3D and it was the common turbulence model used to compare the importance of the hydrostatic assumption on the numerical models' results. The two governing equations for the standard *k-ε* model are:

$$\frac{\partial k}{\partial t} + \frac{\partial k u_i}{\partial x_i} = \frac{\partial}{\partial x_j}\left[\left(\frac{\nu + \nu_t}{\sigma_k}\right)\frac{\partial k}{\partial x_j}\right] + P_k - G - \varepsilon \tag{3.15}$$

$$\frac{\partial \varepsilon}{\partial t} + \frac{\partial \varepsilon u_i}{\partial x_i} = \frac{\partial}{\partial x_j}\left[\left(\frac{\nu + \nu_t}{\sigma_\varepsilon}\right)\frac{\partial \varepsilon}{\partial x_j}\right] + C_{1\varepsilon}\frac{\varepsilon}{k}\left[P_k + (1 - C_{3\varepsilon})G\right] + C_{2\varepsilon}\frac{\varepsilon^2}{k} \tag{3.16}$$

where k is the turbulent kinetic energy calculated as follows:

$$k = \frac{1}{2}\overline{u_\iota{}' u_\iota{}'} \tag{3.17}$$

and ε is the dissipation of turbulent kinetic energy:

$$\varepsilon = \nu\,\overline{\frac{\partial u_\iota{}'}{\partial x_j}\frac{\partial u_\iota{}'}{\partial x_j}} \tag{3.18}$$

While $u_i{}'$ is the i^{th} component of the fluctuation velocity, P_k is a turbulent energy production term, G is a source term due to the gravitational forces, and ν_t is the eddy viscosity:

$$\nu_t = C_\mu \frac{k^2}{\varepsilon} \tag{3.19}$$

and σ_k, σ_ε, $C_{1\varepsilon}$, $C_{2\varepsilon}$ and $C_{3\varepsilon}$ are constants with the following empirically determined values:

$$C_\mu = 0.09 \qquad \sigma_k = 1.00 \qquad \sigma_\varepsilon = 1.30 \qquad C_{1\varepsilon} = 1.44 \qquad C_{2\varepsilon} = 1.92 \qquad C_{3\varepsilon} = -0.33$$

RNG *k-ε* is a more recent version of the standard *k-ε* model. It was derived from the instantaneous Navier-Stokes equations using a statistical method termed renormalization group (RNG) (Fluent Inc., 2001; Yakhot, and Orszag, 1986). This method uses a combination of dynamic scaling and invariance together with iterated perturbation methods to evaluate the transport coefficients and transport equations for low Reynolds flows and large-scale modes. This mathematical procedure resulted in a modification of some parameters and constant values from the standard *k-ε* model equations for turbulent dissipation rate (*ε*). *ε* is integrated to obtain an accurate description of the effective turbulent transport variation with respect to the effective Reynolds number (or eddy scale), allowing the model to better handle low-Reynolds-number and near-wall flows. RNG *k-ε* also includes a swirl modification factor in the eddy viscosity equation. The outcome of this addition is that swirling effects are included and are not dependent on the flow behavior. The equations for *k* and *ε* after the RNG modifications are:

$$\frac{\partial (\rho k)}{\partial t} + \frac{\partial (\rho k u_i)}{\partial x_i} = \frac{\partial}{\partial x_j}\left[\left(\nu + \frac{\nu_t}{\sigma_k}\right)\frac{\partial k}{\partial x_j}\right] + P_k - \rho\varepsilon \tag{3.20}$$

$$\frac{\partial (\rho \varepsilon)}{\partial t} + \frac{\partial (\rho \varepsilon u_i)}{\partial x_i} = \frac{\partial}{\partial x_j}\left[\left(\nu + \frac{\nu_t}{\sigma_\varepsilon}\right)\frac{\partial \varepsilon}{\partial x_j}\right] + C_{1\varepsilon}\frac{\varepsilon}{k}\,P_k + C_{2\varepsilon}\rho\frac{\varepsilon^2}{k} \tag{3.21}$$

Constants for RNG *k-ε* are also different from the standard *k-ε*:

$$C_\mu = 0.0837 \quad \sigma_k = 0.7179 \quad \sigma_\varepsilon = 0.7179 \quad C_{1\varepsilon} = 1.063 \quad C_{2\varepsilon} = 1.7215$$

The k-ω model was developed to cope with the accuracy problem of turbulence models when simulating boundary layers with adverse pressure gradient (Wilcox, 1988). Wilcox (1988) modified the previous two-equation models by introducing the specific dissipation rate term (ω). This term represents the ratio of turbulent dissipation rate (ε) to the turbulent mixing energy (k). This allowed for modelling with improved accuracy of the more significant turbulence occurring near walls (Bardina, Huang, and Coakley, 1997). The next two equations, Equation 3.22 and 3.23 describe the turbulent mixing energy and specific dissipation rate, respectively:

$$\frac{\partial(\rho k)}{\partial t} + \frac{\partial(\rho k u_j)}{\partial x_j} = \tau_{ij}\frac{\partial u_i}{\partial x_j} - \beta^*\rho\omega k + \frac{\partial}{\partial x_j}\left[(\nu + \nu_t\sigma^*)\frac{\partial k}{\partial x_j}\right] \tag{3.22}$$

$$\frac{\partial(\rho\omega)}{\partial t} + \frac{\partial(\rho\omega u_j)}{\partial x_j} = (\gamma\omega/k)\tau_{ij}\frac{\partial u_i}{\partial x_j} - \beta\rho\omega^2 + \frac{\partial}{\partial x_j}\left[(\nu + \nu_t\sigma)\frac{\partial \omega}{\partial x_j}\right] \tag{3.23}$$

where τ_{ij} is the Reynolds stress tensor. Invoking the Boussinesq approximation, Wilcox (1988) approximated that the Reynolds stress tensor is proportional to the mean strain-rate tensor:

$$\tau_{ij} = 2\nu_t\left[S_{ij} - \frac{1}{3}\frac{\partial u_k}{\partial x_k}\,\delta_{ij}\right] - \frac{2}{3}\rho k\delta_{ij} \tag{3.24}$$

The closure constants in the above equations have the following values:

$$\beta = 3/40, \quad \beta^* = 9/100, \quad \gamma = 5/9, \quad \sigma = \sigma^* = 1/2$$

LES is defined as a spatially averaged model, compared to time averaged model in the case of RANS. It approximates the Navier-Stokes equations by removing (filtering) the small-scale eddies in order to reduce the computational time. The base assumption of this model is that eddies can be separated into two categories: large eddies (larger than the computational grid cell size) which are solved directly and small eddies (smaller than the grid cell size) which are approximated by increasing local viscosity. Large eddies are believed to carry more energy and have greater influence on the flow. Therefore, they are the main contributors to the energy transport. However, this becomes a problematic issue near walls and in cases where multiple flows are interacting. In those cases, small-scale turbulence becomes relevant for the overall flow. Since LES does not average flow over time, it allows rapid fluctuations to occur, making the model better for simulation of flow separation and strong flow curvature (Pope, 2004; Spalart et al., 2006). To apply LES, the length scale is found using a geometric mean of the grid cell dimensions: δx, δy and δz (Smagorinsky, 1963):

$$L_s = (\delta x \delta y \delta z)^{\frac{1}{3}} \tag{3.25}$$

LES scales velocity fluctuation by the magnitude of L_s multiplied by the mean shear stress. The LES kinematic eddy viscosity is:

$$\nu_T = (cL_s)^2\sqrt{2e_{ij}2e_{ij}} \tag{3.26}$$

where c is a constant with typical values varying between 0.1 and 0.2 (0.1 was used) and e_{ij} is the strain rate tensor components. The kinematic eddy viscosity is added to the fluid's viscosity similarly to the other turbulence models used.

3.4 Results

The results from the two numerical models are presented in the following section, including both the resulting scour and the hydrodynamic features of the flow.

3.4.1 Hydrodynamic Results

Given that the flow is the driving force behind the scouring, it is first discussed. The hydrodynamic results of both models to model the non-obstructed flow and the flow-structure interaction are presented.

3.4.1.1 Bore Profile

First, the numerical results time history of the bore profiles from the two models were compared to Chanson's (2009) analytical solution and then calibrated to ensure that the models could reproduce near-theoretical profiles. In Delft3D, calibration was conducted by varying the fluid's minimum eddy viscosity, which resulted in defining the background eddy viscosity constants as $1x10^{-3}$ Pa*s in both *x* and *y* directions. In FLOW-3D, no calibration was needed to match the bore profile. Chanson's (2009) analytical solution has two components consisting of: (1) an ideal bore profile where the bottom friction does not affect the profile, and (2) a bore front that slows because of the bottom friction, such that its front and profile changes in shape. The following two equations are the idealized and friction-affected bore profile equations (Chanson, 2009, 2006, 2005).

$$\sqrt{\frac{d}{d_0}} = \frac{1}{3}\left(2 - \frac{x}{t * \sqrt{g * d_0}}\right) \tag{3.27}$$

$$\frac{d}{d_0} = \sqrt{\frac{f}{4} * \frac{U^2}{g * d_0} * \frac{x_s - x}{d_0}} \tag{3.28}$$

In Figure 3.5, the bore profile generated by the two numerical models at four different moments in time were compared to Chanson's (2009) analytical solutions. Both Delft3D's and FLOW-3D's profiles closely match the idealized profile of Chanson after the passage of the bore front. However, results of both numerical models showed discrepancies for the region of the tip of the bore. For FLOW-3D, only the very tip of the bore front differs from the theoretical solution of Chanson. The profile is advancing a little slower than the theoretical front. Delft3D also had difficulties replicating the tip of the front, predicting a slightly steeper and earlier (in terms of arrival and location) front in comparison to the analytical solution. However, the speed of the bore front and general profile were well represented. Delft3D's capacity to replicate the bore profile indicates that the hydrostatic assumption did not hinder the model's capability to replicate these conditions.

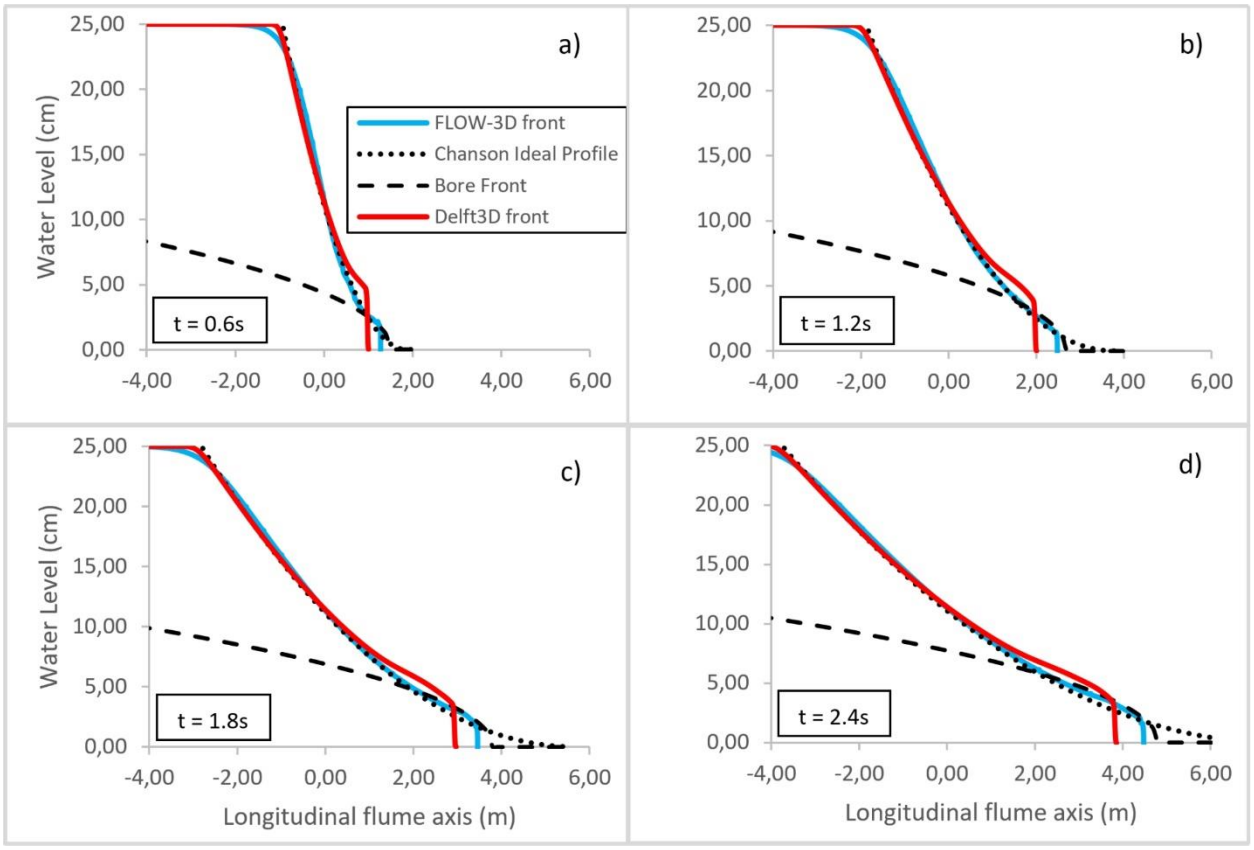

Figure 3.5: Numerical Model's Bore Profile against Chanson (2009) Idealized Bore Profile

3.4.1.2 Vertical Vortex

Previous studies on scouring around vertical structures due to rapidly transient flow concluded that the vertical vortex at the structure front is responsible for flow-induced scouring (Arneson et al., 2012; Chen et al., 2016; Istiarto, 2001; Tonkin et al., 2003). Therefore, the ability of a numerical model to reproduce such vortices is important to accurately reproduce scouring. All FLOW-3D simulations evidentiated the formation of a strong vertical vortex at the structure toe (Figure 3.6a)). The velocity magnitude of the vertical vortex generated when LES was utilized was larger than the other three turbulence models. The vertical vortex's maximum vertical velocity calculated was -1.76 m/s, -0.89 m/s, -0.72 m/s and -0.95 m/s for LES, k-ω, standard k-ε and RNG k-ε, respectively. Due to the vertical vortex, the flow plunged downwards at the front of the structure and then around the sides, thus increasing scour. As the bed started to erode, the vortex began to develop causing it to grow in size and velocity. This continued until the flow slowed and its energy decreased as a result of the reduction in the level of impounded water.

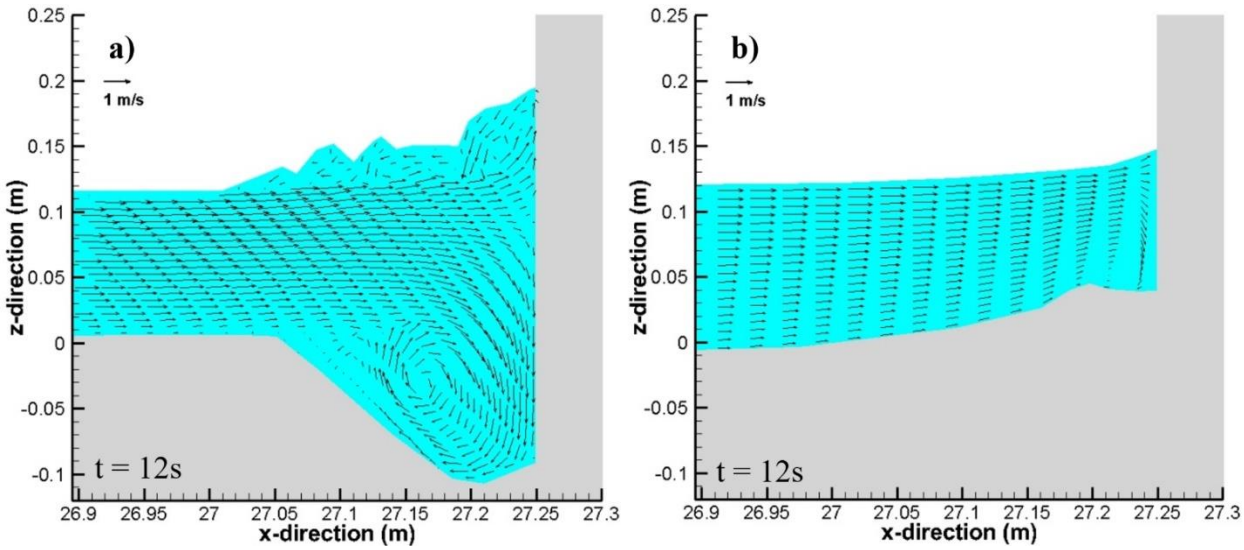

Figure 3.6: XZ Plane Velocity Vectors after 12s at the middle of the structure's front side using the a) FLOW-3D with LES Turbulence Model model and b) Delft3D model.

The flow velocity field for Delft3D in Figure 3.6b) as for the same location and time (time = 12 s) as the one for FLOW-3D. Flow never plunged downward, even when grid resolution near the column was increased to match that of FLOW-3D's. The only negative vertical velocities were found in the cells next to the structure. Sediment deposition at the structure toe, instead of scouring, was observed. This further forces the flow sideways, instead of downwards in a circular motion to create the vertical vortex. At the structure's corners, a stronger downward flow was observed, but no vortex formation. Also, the water surface elevation did not increase significantly in the case of Delft3D comparing to that of FLOW-3D. Both the absence of the vertical vortex and the lack of upward forcing of flow are possibly consequences of the hydrostatic assumption used by Delft3D which prevented the simulation from accurately reproducing the complex hydrodynamic field around the pier.

3.4.2 Scouring Results

In this section, the resulting scouring from the dambreak wave is discussed. The scouring results from Delft3D are first discussed, followed by the different turbulence models used in FLOW-3D and, finally, the comparison between van Rijn (1984) and Nielsen (1992) sediment transport performances in FLOW-3D

3.4.2.1 Delft3D Results

Both numerical models were calibrated by matching the maximum scour depth to that measured in the physical model by Mehrzad et al. (2016). In Delft3D, the calibration was performed using a morphological scale factor by varying its value from 0.5 to 15. The final value was 10. For FLOW-3D, the maximum scour depth was calibrated by increasing the entrainment coefficient to 0.15, 0.3, 0.3 and 0.6 for LES, *k-ω*, standard *k-ε* and RNG *k-ε* turbulence models, respectively (Ciofalo, 1996; Flow Science, 2018). Although the default value, 0.018, is quite low compared to the final values used by the authors, there is no physically-based reasoning for choosing this value (Mastbergen, and Van Den Berg, 2003). Both, the entrainment coefficient and the morphological

scale factor, are recommended by the model developers to be used for calibration. In the two models, they are used to enhance the pickup rate.

All simulations were run until the bed had reached equilibrium. This took around 60 seconds, which took less than 20 hours of computational time for Delft3D and in the order of 70 hours for the FLOW-3D simulations. The computer used to conduct all computational work was a server with an Intel Xeon CPU X5690 @ 3.47 GHz with 3.46 GHz (2 processors), 12 cores/24 threads and 96 GB of RAM. The reasons for this difference in computational time is because the number of cells necessary to obtain a cell-size-insensitive mesh was greater in the case of FLOW-3D. The increase in cells was necessary to solve the momentum equation in the vertical direction, as more calculations and the use of FAVOR for the computation of the geometry, was required.

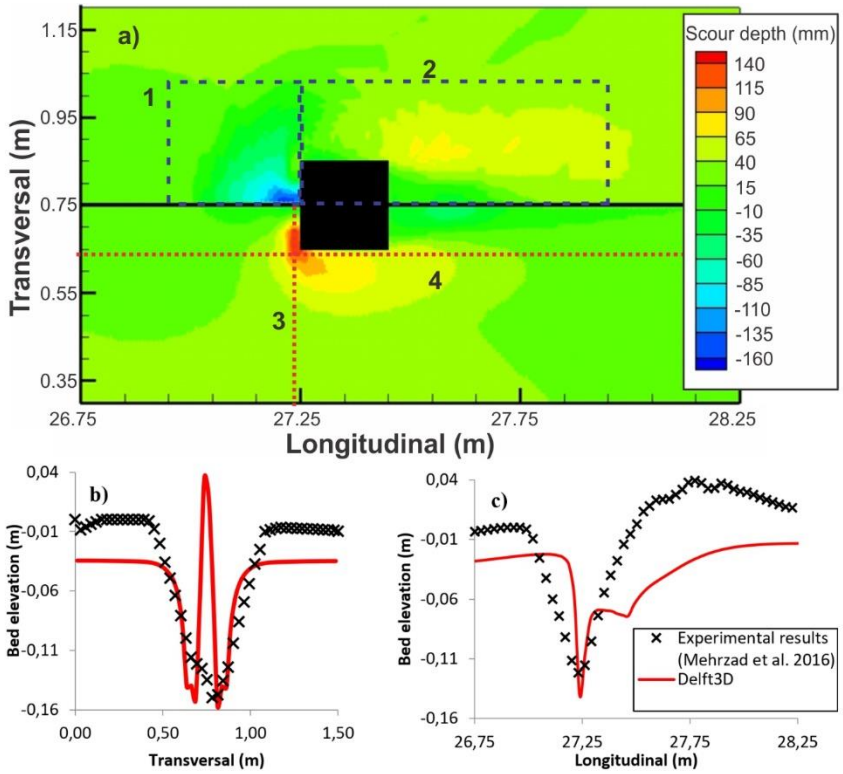

Figure 3.7: a) Top: Difference between Experimental Results and Delft3D Results Bottom: Delft3D Results using Standard k-ε Turbulence Model b) Transversal Profile of the Final Bed Elevation at Cross-section 3 c) Longitudinal Profile of the Final Bed Elevation at Cross-section 4

Figure 25, 26 and 27 show the plan and cross sectional views of the bed elevation after the completion of each numerical run from all the models. In Figure 25 a) and Figure 26 a) to d), the figures' top half shows the difference between the experimental results and numerical model results, obtained by subtracting the elevation of the experimental bed level from the numerical one. A positive value indicates that the numerical model resulted in more scouring than the experimental results, and vice-versa for negative values. The bottom half shows the numerical models scouring result only. The color scale in the bottom half is indicating the scour depth. Lines 3 and 4 in Figure 25 a) are the cross sections shown in Figure 25 b), Figure 25 c), Figure 27 a) and Figure 27 b). Zones 1 and 2 are areas where the Root Mean Square Error (RMSE) was calculated and compiled in Table 3.1. Zone 1 is extending 300 mm upstream from the structure and 300 mm

on each side of the centerline. Zone 2 is a 700 mm by 600 mm rectangle starting at the upstream face of the structure, extending 500 mm downstream of the column and is centered in the *y* direction. RMSE was calculated with the elevation difference at every centimeter in both horizontal directions.

When using the Delft3D model, the results matched the maximum scour depth of 160 mm measured in the experiment. The maximum scour depth occurred at the front corner of the structure, as opposed to the middle of the upstream face in the case of the physical experiment. The numerical model as shown in Figure 7 a) poorly reproduced the shape and spatial extent of the upstream scour hole. Scour was not present in the numerical results at the same location where the deepest scour occurred in the experimental results. In fact, sediment accumulation in the structure's front area was observed in the Delft3D model. This difference is also confirmed by the RMSE in zone 1 with a value of 41.12 mm (see Table 3.1). Scouring on the side of the structure continued much further downstream comparted to the experimental results. Even though Delft3D poorly reproduced the spatial extent of the front scour hole, it had the least amount of error of all models in zone 2 with an RMSE of 38.36 mm.

Table 3.1: Scour RMSE for the regions defined in Figure 3.7

Models	RMSE Zone 1 (mm)	RMSE Zone 2 (mm)
Delft3d	42.12	38.36
FLOW-3D standard k-ε	17.30	58.47
FLOW-3D RNG k-ε	19.84	58.47
FLOW-3D k-ω	17.30	56.27
FLOW-3D LES	19.75	48.41
FLOW-3D LES - Nielsen	15.42	43.77

Very steep slopes were found in the scour hole, particularly in the region in front of the structure where slopes up to 75 degrees were measured. The steep slopes may be due to the lack of consideration of the slope stability calculation in the version of Delft3D used. In fact, no indication of slope stability is present in the Delft3D-FLOW manual (Deltares, 2011). If a slope stability calculation was applied, the accumulation at the structure front would experience slope failure, leading to more realistic slopes of the scour hole. Also, the hydrostatic assumption prevented the formation of an upstream vertical vortex (see Figure 3.6) The only substantial vertical velocities observed in the model were found in the first column of cells upstream of the structure. The cells beyond the first set of vertical cells are virtually not affected by the downward or upward velocity next to the column which led to no vertical vortex being generated. The poor reproduction of this phenomenon is preventing the occurrence of the downward acceleration of the flow, which is responsible for most of the scouring at the front of the structure. Overall, the scouring results given by Delft3D were judged to be unsatisfactory.

3.4.2.2 FLOW-3D Results

Using FLOW-3D, the scour pattern improved notably compared to using Delft3D. Figure 8 a) shows scouring using the same turbulence model (standard *k-ε*) as Delft3D. Major scouring was generated in front of the structure, with maximum scouring occurring at the front corners of the

structure. The shape and magnitude of the upstream scour hole is well replicated with little vertical error (RMSE = 17.30 mm) by the Flow3D model. However, the numerical scour hole developed too far downstream and, hence, the RMSE in zone 2 was 58.47 mm. This pattern was observed in Delft3D as well, but with a lesser magnitude. Downstream scouring was correctly modeled, but too much sediment was removed downstream of the column. FLOW-3D shows better results than Delft3D when it comes to replicating scour in front of the structure. The non-inclusion of the hydrostatic pressure assumption has greatly helped in FLOW-3D to recreate the effects of the upstream vortex on the upstream scouring.

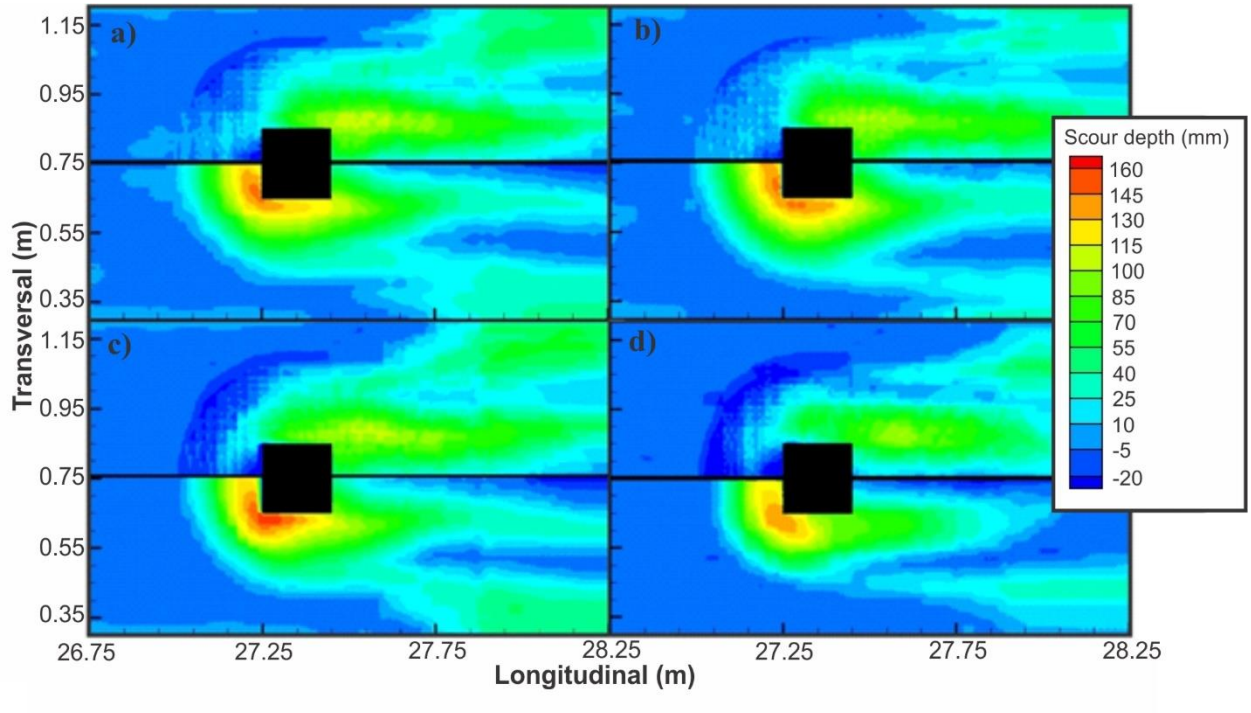

Figure 3.8: a) FLOW-3D standard k-ε turbulence model results b) FLOW-3D k-ω turbulence model results c) FLOW-3D RNG k-ε turbulence model results d) FLOW-3D LES turbulence model results // top: difference between experimental results (Mehrzad et al., 2016) *and FLOW-3D results // bottom: FLOW-3D results*

All turbulence models yielded scour results with some commonalities after calibration as both the shape and magnitude of the final scour were close to the experimental results. The maximum scour depth found at the upstream corners as opposed to the center in the physical model. *k-ω* and standard *k-ε* have the least amount of scouring difference at the front, closely followed by the other two turbulence models. The local scouring at the corners is most prevalent in the case of RNG *k-ε*.

When comparing the cross-sections shown in Figure 9, some difference was observed between the results provided when using the investigated turbulence models. The upstream scour was well replicated when all the turbulence models were used but have poorly represented the downstream end. Figure 3.9 b) reinforces the previously made observation that RNG *k-ε* performed worse than the other turbulence models. The final scour hole obtained with this model had very steep side slopes compared to the results of the other models, resulting in greater impact on the transversal profile of the RNG *k-ε* model showed in Figure 3.9 b). In Figure 3.9 a), only LES provided some

difference from the results of the other models investigated. Downstream of x=27.6 m, less scouring occurred and the erosion profile was closer to the experimental measurements.

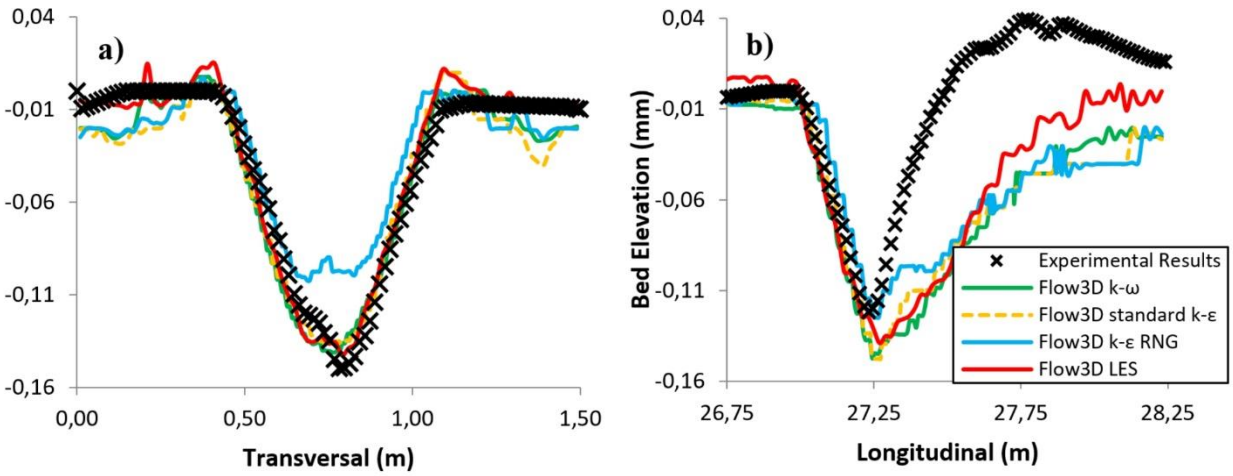

Figure 3.9: Comparison of numerical and experimental data (Mehrzad et al., 2016)*: a) transversal profile of the final bed elevation at cross-section 3 b) longitudinal profile of the final bed elevation at cross-section 4*

Downstream scouring, in the case of all turbulence models, continued far downstream when compared to the experimental results. More specifically, very similar scour shapes was observed for all the turbulence models. This indicates a problem that may be common to all of them. This issue may stem from the employment of Van Rijn's (1984) sediment transport model. LES replicated the experimental results best and especially the downstream bed elevation, with an RMSE of 48.41 mm in zone 2. The scour hole when using LES was shorter and shallower than the other turbulence models. This suggests that the non-time averaging method of this turbulence model is better at cancelling the turbulence and local flow acceleration and preventing erosion propagation downstream. The downstream sediment accumulation was also better represented with LES. The accumulation reached the back of the column and widens sooner than when using the other models employed. The size of the accumulation was still lower than what was observed in the physical model, but performance was the best among all turbulence models.

3.4.2.3 FLOW-3D Sediment Transport Model Comparison

While keeping the same turbulence model (LES), an additional sediment transport model was tested in FLOW-3D to investigate its performance. Nielsen's (1992) model was tested and compared to that using the Van Rijn (1984) formula used in the previous sections. Results were similar; however, using Nielsen's model showed some improvement in both the frontal scour depth and length (Figure 3.10 a) and b)). In the cross-sections shown in Figure 3.10 c) and d), marginal differences between the two sediment transport models can be observed, but, when using the Nielsen model, sediment accumulation at the downstream end of the scour hole occurs earlier. This accumulation still occurred much further downstream than that observed in the physical experiment.

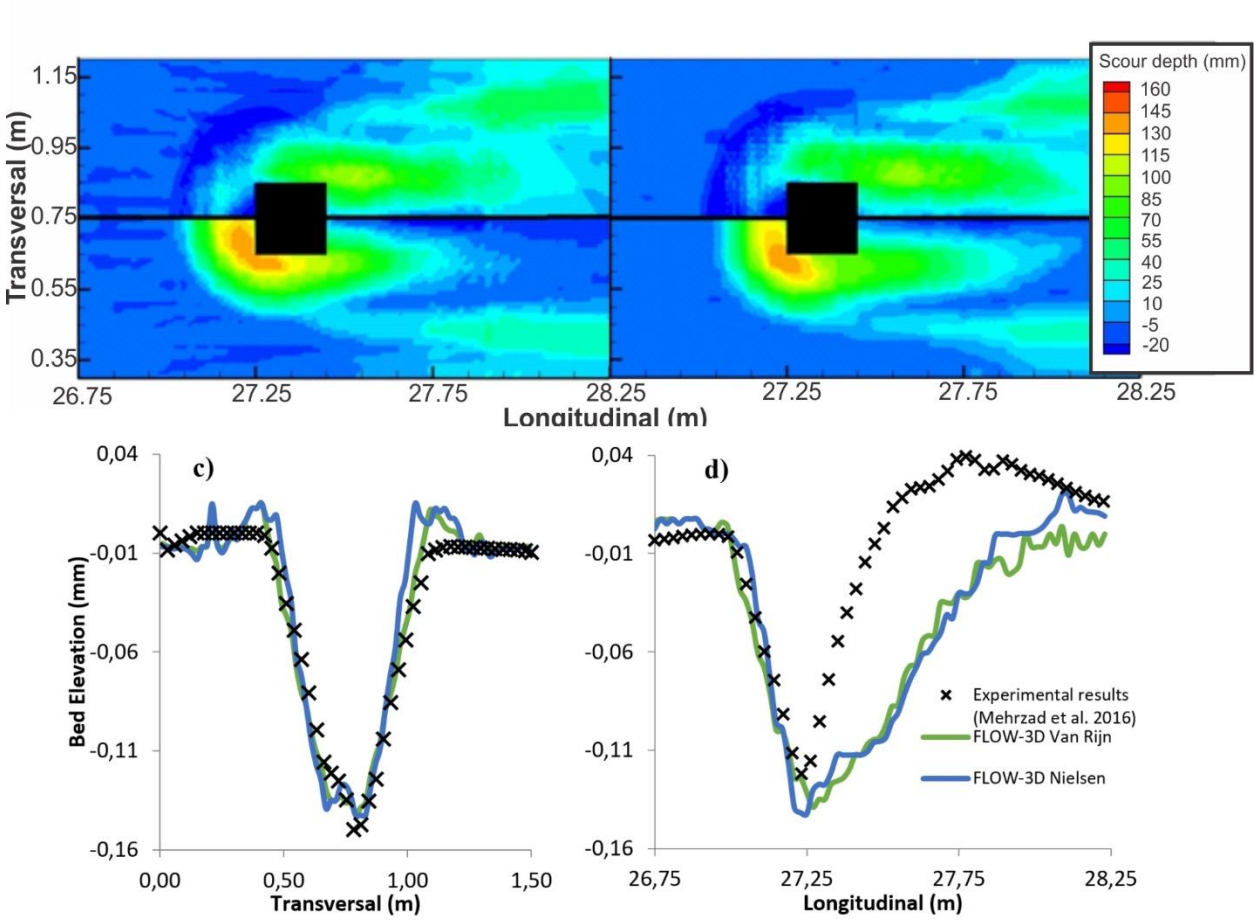

Figure 3.10: Nielsen (1992) and Van Rijn (1984) sediment transport model comparison in FLOW-3D using LES turbulence model a) plan view of bed elevation results of Nielsen (1992) sediment transport model b) plan view of bed elevation results of Van Rijn (1984) sediment transport model c) transversal profile of the final bed elevation at cross-section 3 d) longitudinal profile of the final bed elevation at cross-section 4

3.5 Discussion

In the following lines, the possible explanation behind the difference in the results are discussed. The differences in the hydrodynamic and scouring performances of both numerical models are discussed, as well as the difference between the turbulence models tested. These reasoning explain the final choice of model combination for this tsunami study's next steps.

3.5.1 Hydrodynamic Performances

Both models, Delft3D and FLOW-3D, replicated well the hydrodynamic properties of the dambreak bore. In the bore tip, significant vertical acceleration and turbulence occurs and these two features represent a challenge for numerical models, especially for the hydrostatic ones, such as the case of Delft3D. The only differences were observed at the very tip of the bore and this is due to the different grid coarseness.

Closer to the structure, replicating the vertical vortices proved to be difficult for hydrostatic-type models due to the vertical flow acceleration. In Delft3D, some vertical velocities at the structure front was observed, but to a lesser degree then that reproduced by FLOW-3D. The maximum vertical velocity measured in the center longitudinal plane was -1.7m/s for FLOW-3D, and -0.4m/s for Delft3D (Figure 3.6). In Delft3D, the flow was mainly directed horizontally; resulting in the absence of a vertical vortex formation. The location of the maximum vertical velocity was against the column. The horizontally forced flow caused significant horizontal flow acceleration at the upstream corners of the structure, leading thus to increased concentrated scour on the sides and upstream corners of the structure. In FLOW-3D, the maximum velocity occurred near the bed, a few cells away from the column, and a clear circular flow motion was observed. Therefore, the fact that FLOW-3D applies the Navier-Stokes momentum equation in the vertical direction helps to predict the vertical vortices at the structure front. FLOW-3D's final grid was more refined than the Delft3D's after the sensitivity analysis was performed. However, when Delft3D's grid resolution was increased to match FLOW-3D's grid resolution in the vicinity of the column, no major hydrodynamic change was observed in Delft3D.

3.5.2 Scouring Performances

Large discrepancies in the results were noted between FLOW-3D and Delft3D. FLOW-3D was more capable than Delft3D at reproducing the scour pattern in front of the structure. Although the maximum scour depth was reached using Delft3D, no scouring occurred at the middle of the structure front, where the maximum scour depth was observed in the physical model. Possible sources for such differences could be the absence of both the vertical vortex and the slope stability calculation in Delft3D. The absence of the vertical vortex, stemming from the hydrostatic assumption, is more likely to be the greatest source of error. The reason being that, in steady flow modeling, a local scour around a square column is badly replicated by models that fail to generate a proper horseshoe vortex since it is the main driving force for sediment transport (Khosronejad, Kang, and Sotiropoulos, 2012). Therefore, the use of a non-hydrostatic modeling is important for properly replicating local scour. The profiles from cross-sections 3 and 4 are shown in Figure 3.11 to better compare the results from the two models.

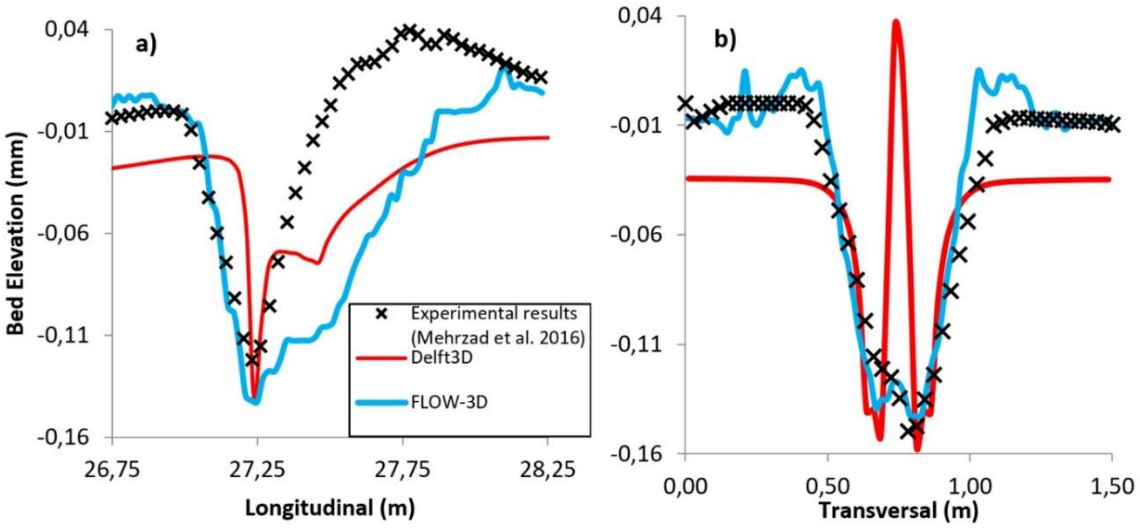

Figure 3.11: Comparison of FLOW-3D and Delft3D a) transversal profile of the final bed elevation at cross-section 3 b) longitudinal profile of the final bed elevation at cross-section 4

Two sediment transport models proposed by Van Rijn (1984) and Nielsen (1992) available in FLOW-3D were tested to verify which of them reproduced best the experimental results. Nielsen's model showed good performance for both the upstream and side scouring formation and the RMSE was reduced by 22% and 9% for zones 1 and 2, respectively. Since Nielsen's and Van Rijn's models have the same formulations for calculating the suspended sediments in FLOW-3D and their bedload equations are based on Shields' parameter, the scour results can be expected to be similar. The difference between the results is mainly attributed to the fact that the excess shear stress is to the power of 2.1 in the formulation of bedload transport in Van Rijn (1984) (equation 3.7) compared to an exponent of 1 for Nielsen (1992). This difference causes the Van Rijn model to overestimate transport where flow is accelerated along the column sides, leading a longer scour hole.

In Mehrzad et al. (2016), it was observed that, at the end of the runs, sand was depositing in the scour hole, reducing the final scour depth by up to 20% compared to the maximum recorded value. Therefore, scouring showed in Figure 3.2 is scouring after scour slope collapse had occurred and is not representative of the previously occurring maximum scour hole. Only FLOW-3D showed some minimal post-bore deposition. The maximum scour depth was reduced by up to 5% in those cases. The version of Delft3D used, on the other hand, does not account for slope stability, explaining why this model exhibited scour side slopes of up to 75 degrees. This indicates that Delft3D does not account for a slope stability limit. If such a concept was included, it is possible that Delft3D could be performing to a satisfactory level. Strong scouring at the upstream corners seems to be correct (Mehrzad, Nistor, and Rennie, 2016) and, over time, will lead to slope failure in the middle of the column, increasing scouring at the structure front. In FLOW-3D, scouring started at the corners and then spread to the center of the column. The maximum scour depth was found at the corners (see Figure 3.8). This explains why field observations of scouring at vertical structures is maximum at the corners or sides (Kato, Sato, and Yeh, 2000; Lavictoire, Nistor, and Rennie, 2014; Nakamura, Kuramitsu, and Mizutani, 2008).

3.5.3 FLOW-3D Turbulence Models Comparison

Scouring results from all turbulence models were similar in geometry and depth after calibration. Several observations were made: the scour hole was well represented upstream of the column, the scour hole extended too far downstream, and the downstream accumulation did not describe the correct triangular shape observed in the experimental teste. The calibration factors for the turbulence models used were very different. The entrainment coefficient used for calibration was increased to 0.15, 0.3, 0.3 and 0.6 for LES, k-ω, standard k-ε and RNG k-ε turbulence models, respectively. This difference can be attributed to the difference in excess shear stress calculated by those models. The driving factor for the upstream scour was the vertical vortex at the upstream face of the structure. Since the rapid velocity change at the upstream end of the structure was critical, a model capable of representing rapidly changing flow is key. LES showed the greatest downward velocity in the vertical vortex at the structure front. The vertical velocity was larger for LES than for the RANS turbulence models because LES does not average velocities over time, increasing the model's capacity to reproduce strong flow curvature and unsteady flows (Roux et al., 2005).

Some differences were observed between the results of the standard *k-ε* and RNG *k-ε* models. The RNG *k-ε* model performed worse in terms of the front scouring. One of the major differences between these two models is the swirl modification factor found in RNG *k-ε*, resulting in the swirling effect not being dependent on the flow behavior. The result is a reduction in turbulence viscosity in rapidly strain flows which should increase the flow velocity (Yeoh, and Tu, 2009). The increase in velocity was similarly observed in this case, but the associated quantity of transported sediment was lower than standard *k-ε* model. Therefore, the difference likely stems from the coefficient difference. However, previous researchers have concluded that most *k-ε* models have a tendency to poorly reproduce highly swirling flows, such as those observed at the upstream face of the column (Clayton, and Morsi, 1986; Escue, and Cui, 2010; Firth, and Duggins, 1985).

When comparing the models using the k-ω and k-ε turbulence models, no major scour differences were observed. Only scouring at the very front of the column was different, and a slight difference in RMSE in zone 2 with a 2.2 mm difference. *k-ω* was more accurate with respect to the experimental results. Adverse pressure present at the toe of the column may generate difficulties for *k-ε*-type models to accurately simulate the experimental results, a notable problem with *k-ε* models. Near-boundary flows are also usually better represented by *k-ω*, explaining the calibration factor and better representation of the upstream scouring (Patel, Rodi, and Scheuerer, 1984; Wilcox, 1988). *k-ω* and *k-ε* showed similar results in free flows (Menter, 1993). Therefore, the small difference in the results indicates that the scour was driven more by the flow swirling than the near-boundary shear stress.

3.6 Conclusions

Several conclusions were drawn from this comparative study of scour simulation performance using Delft3D and FLOW3D. The two numerical models were applied with the objective of finding the most suitable model to simulate dambreak-type bore-induced scouring around structures. Both models were successfully calibrated against Chanson (2009) analytical dambreak bore profiles and Mehrzad (2016) scouring results. Both models well replicated the dambreak bore profile. However, only FLOW-3D was able to simulate the vertical vortices at the structure toe.

FLOW-3D performed better than Delft3D in the critical scouring area (structure front). However, the computation time was much longer for the former and the results for side and downstream scour still need improvement. In Delft3D, the absence of the slope stability calculation and the non-hydrostatic solving of Navier-Stokes reduced the accuracy of the hydrodynamic and scouring results. Other differences between the models, such as the resolution of vertical turbulence may also have contributed to the differences in scour results. Although little difference was found between the performances of the FLOW-3D turbulence models results, LES was found to perform slightly better. The RMSE in the downstream region was 34% less indicating that LES simulated best the complex vortices around the column. A 13% reduction in bed profile RMSE was obtained when using Nielsen (1992) against Van Rijn (1984) sediment transport model. Both defined zones, upstream and downstream of the column, indicate better results when using Nielsen (1992). In addition, the scour hole was shortened.

Chapter 4: Effect of Lateral Spacing of Structures on Tsunami-Induced Scour

4.1 Abstract

Tsunamis are a devastating force, a statement supported by the extreme tsunamis which struck the Indian and Pacific Ocean over the past two decades: the 2004 Indian Ocean Tsunami, the 2010 Chile Tsunami and the 2011 Tohoku Japan Tsunami. In those events, flood-induced scouring was found to be an important phenomenon which often led to infrastructure damage. Past research has focussed on scouring around single columns and other isolated horizontal structures to attempt to understand the complex processes characterizing this phenomenon. However, given that coastal cities are often comprised of complex arrangements of multiple, often crammed, structures, tsunami inundation flow often finds concentrated paths in between such structures; these flow concentrations increase the resulting scouring. This research is an attempt to inform the scientific community on the potential of augmented scour due to flow concentration due to the lateral spacing of structures and compare it with non-concentrated flow-induced scour. The authors employed the FLOW-3D numerical model for this study. This model was first calibrated using a physical model experiment performed in the Dambreak Flume of the University of Ottawa, Canada. Results from this study demonstrate that flow concentration due to the lateral spacing of structures leads to greater scouring than for the case of an isolated structure and that the magnitude of the scour, for most cases studied, was larger than what is prescribed by the latest building codes.

4.2 Introduction

With the increase in world population, coastal communities are expanding. Living in the proximity of oceans comes with socio-economic benefits. However, it also places the inhabitants of these communities at a high risk to extreme hydrodynamic events such as hurricanes and associated storm surges, and/or tsunamis. To cope with such risks, infrastructure design codes were developed to design structures capable of withstanding effects and loading caused by tsunamis. Codes written in mandatory language for the design of tsunami-resistant buildings have only recently been elaborated and rely a limited data. One of the least understood mechanisms leading to structural failure is scouring induced by the tsunami flooding. In the latest version of the *Chapter 6 - Tsunami Loads and Effects* in the *ASCE 7 –6 Minimum Design Loads and Associated Criteria for Buildings and Other Structures* standard developed by the American Society of Civil Engineering (ASCE) , the only factor considered in determining the maximum design scour depth (d_s) is the tsunami inundation depth (y) (ASCE, 2016a). This standard was based on a limited amount of field measurements obtained after the 2011 Great Japan Tsunami (Tonkin, Francis, and Bricker, 2014). The standard states that a vertical structure at a given location shall be designed for scouring with depths equal to 1.2 times the predicted flow depth at that location ($d_s = 1.2y$), up to a maximum scour depth of 3.6 m. The latest proposed change for pile scour design is to consider a vertical scouring to projected element width ratio of 1.3 times the Froude number ($d_s/b = 1.3Fr$) up to a Froude number of 1. The d_s/b ratio remains constant at 1.3 for flows with a Froude number above 1 (Nistor, 2020). However, sediment characteristics, flow properties other than flow depth, obstacle geometry and structure configurations (which represent the focus of this study) influence

scour depth in steady flow (Ettema *et al*., 1998; Kothyari *et al*., 1992, 1993; Melville and Chiew, 1999); however the ASCE 7 Chapter 6 does not consider them at this stage.

Most studies aiming to explain tsunami-induced scouring were performed through field investigations of areas affected by tsunamis or by using physical experiments (Jayaratne *et al*., 2016; Kato, Sato, and Yeh, 2000; McGovern *et al.*, 2019; Moon, Tan, and Lau, 2014; Nouri *et al*., 2010; Palermo *et al.*, 2013; Rueben *et al.*, 2015; Sarjamee, Nistor, and Mohammadian, 2017; Thomas, Killian, and Bridges, 2015; Tonkin *et al.*, 2003; Yeh and Li, 2008; Yoshii, Tanaka, and Matsuyama, 2017). Results from those experiments suggest that flow properties, the structures' position relative to the shore, and their geometry and dimensions significantly influence the development of the scour.

To date, few numerical investigations have been successfully performed for tsunami-induced scouring. The ones that have succeeded in this endeavor combined physical experiments with a numerical model, which was proven to be a good method to gather additional measurements after the latter was calibrated with experimental data (Chen *et al.*, 2016; Larsen *et al.*, 2017, 2018; Nakamura, Kuramitsu, and Mizutani, 2008; Rahman, Schaab, and Nakaza, 2005; Sulianto and Murakami, 2015; Wei *et al.*, 2016). A similar methodology was employed in this research to study parameters affecting tsunami-induced scouring. The parameter investigated herein is flow concentration due to the lateral spacing of structures. The effect of flow concentration due to the presence of two closely positioned structures increases flow velocity around the designed structure. Scouring induced by this flow concentration during tsunami inundation is also referred to as channelization scouring (Tonkin, Francis, and Bricker, 2013). This phenomenon was documented in field investigations of tsunami affected zones (Chock et al., 2013), but this topic lacks adequate documentation (Wilson, Davenport, and Jaffe, 2012).

The example documented by Yeh, Sato, and Tajima (2013) and Chock *et al.* (2013) is considered here. Prior to the 2011 Great Japan Tsunami, two tsunami-resistant hospital buildings were constructed in the proximity of each other in the Town of Onagawa, with an unobstructed corridor between them (Figure 4.1). During the 2011 Tsunami inundation, the two neighbouring buildings concentrated the flow in the narrow spacing between them, leading to the creation of a scour hole between them whose depth exceeded 3.5 m. Conclusions from recent physical experiments indicate that the final scour depth is lesser than the maximum scour depth generated by a tsunami due to sediment settlement and slope failure (Mehrzad, Nistor, and Rennie, 2016; Tonkin *et al*., 2003). Therefore, this scour hole most likely reached a maximum scour depth which was deeper than the maximum scour depth prescribed in the ASCE7 Chapter 6.

Figure 4.1: Deep scour hole between two hospital buildings in Oganawa caused by the 2011 Great Japan Tsunami

The two adjacent buildings focussed the flow in between them, which subsequently led to this deep scouring. In steady flow conditions, the distance between two vertical structures placed on the same transversal plane to the flow is referred to as spacing (Arneson et al., 2012; Beg, 2010; Elliott and Baker, 1985). Beg (2010) experimentally investigated the effects of two structures installed transversely on the flow in a clear-water conditions. The addition of a second vertical pier increased the maximum scour depth at the structure up to a spacing equal to 7 times the width of the structure. Scour depth increased by 21% when the columns were placed at a distance equal to the piers' diameter. Results from Elliott and Baker (1985) show that the approach flow characteristics influence the scour, increasing the effects of structures' lateral spacing: the higher the intensity of the flow (approach velocity to sediment's critical velocity for transport), the greater the influence of the structures' lateral spacing.

In the past decade, researchers have studied the hydrodynamic changes due to the interaction of multiple buildings and tsunami-like flows. Nouri *et al.* (2010) experimentally investigated the effects of the flow constriction on hydrodynamic loading of structures located downstream of the constriction. The constriction was built by attaching wooden blocks to the flume's walls, upstream of a vertical column, to constrict the flow of a dambreak bore. The constriction resulted in a 10% increase in the flow velocity in the worst case and, hence, an increase in the impact force exerted on the downstream structure. Thomas, Killian, and Bridges (2015) investigated the effect of flow

constriction in a wide flume. They used square shaped blocks installed upstream of the structure of interest to constrict the flow produced by a paddle wave maker. In the worst case observed, the force experienced by the structure of interest was double their baseline (which was a standalone monitored block). The bore front velocity was amplified by a factor of 25% when the blocks were placed at an upstream angle varying between 20 and 35 degrees. The maximum measured velocity increase was of 40%. However, no significant effect on runup was observed. These two experimental studies were used to inform the ASCE 7 Chapter 6 recommendations on flow amplification due to constriction.

Other studies have used a numerical-based approach to study dambreak bores. Multiple studies confirmed that the bore hydrodynamics can be accurately reproduced by various hydrodynamic models while using different turbulence closure models (Brufau and Garcia-Navarro, 2000; St-Germain *et al.*, 2014; St-Germain, Nistor, and Townsend, 2012; Xia *et al.*, 2010). St-Germain *et al.* (2014) utilized a weakly compressible smoothed-particle hydrodynamic model with large eddy simulation (LES) turbulence model to simulate a dambreak bore advancing onto a free standing single square column. Water levels at the column were accurately simulated except for the peak in water height recorded at bore impact. Sediment transport on a flat and uneven bed were well replicated by multiphase Lagrangian-type models (Yeh and Li, 2008). Pan and Huang (2012) applied a 2D unstructured numerical model to replicate the experimental results on tsunami scour performed by Tonkin *et al.* (2003). The Eulerian-type model closely matched the hydrodynamic properties of the wave attacking the structure and replicated the final scour hole reasonably well. However, Pan and Huang (2012) concluded that the use of a 2D numerical model was limiting the quality of their results and a 3D model should be used instead.

The goal of the present research is to numerically investigate the potential for scour augmentation between two laterally spaced structures in tsunami-like flows. The numerical model FLOW-3D was utilized for this endeavour. Its selection was motivated by its capacity to reproduce scouring caused by complex flows (Alemi and Maia, 2018; Chen et al., 2016; Omara et al., 2019; Vasquez and Walsh, 2009). Additionally, FLOW-3D was shown to accurately replicate scouring due to a dambreak bore in the first phase of this study (April Le Quéré, Nistor, and Mohammadian, 2020).

4.3 Methods

In order to study the effect of laterally spaced neighbouring structures in tsunami-like flows on scouring, the following steps were implemented:

- The FLOW-3D numerical model was calibrated to the experimental results from the physical tests of Mehrzad, Nistor, and Rennie (2016) – details of the experimental test are briefly described in the next section. The numerical model calibration is described in detail in the first phase of the study April Le Quéré, Nistor, and Mohammadian (2020). The resulting calibration was verified by comparing the model to additional experimental results from the same experiment.
- Using the calibrated model, the scouring around single and two-columns arrangements were tested with different lateral spacing between the columns (S), different impoundment depths (h0) used to generate the dambreak waves and two column widths (b).
- The effect of the additional lateral structure on scour was analyzed.

- The hydrodynamic properties of the flow around the structures was subsequently investigated to explain the scouring results and to further discuss the potential scour risks.

4.3.1 Experimental data

The calibration of the FLOW-3D numerical model was performed using the scour results from a physical experiment conducted by Mehrzad, Nistor, and Rennie (2016). The experiment was conducted in the Dambreak Flume of the University of Ottawa, Canada. Their experiment consisted of a comprehensive experimental program, which investigated the spatial and temporal evolution of scour generated by a turbulent bore with different characteristics flowing around a single column model installed in sand bed. The turbulent bore was in the form of a dambreak wave generated by the rapid release of a volume of water impounded behind a swing gate. Their flume was 30 m long, 1.5 m wide and 0.8 m deep. The rapid opening of the gate resulted in dambreak wave with hydrodynamic properties similar to those of a tsunami broken wave advancing inland on a flat coastal plain (Chanson, 2005, 2006, 2009; Madsen, Fuhrman, and Schäffer, 2008). A single square column was installed downstream of the swing gate in a movable bed section consisting of uniform sand with a median diameter (d_{50}) of 0.001 m. The rest of the flume floor was made of concrete covered with similar sand grains glued on the flume surface to ensure uniform bed roughness. In the numerical model, the identical flume configuration was reproduced for the calibration exercise and for the column spacing tests. Figure 4.2 shows a conceptual side and plan view of the flume.

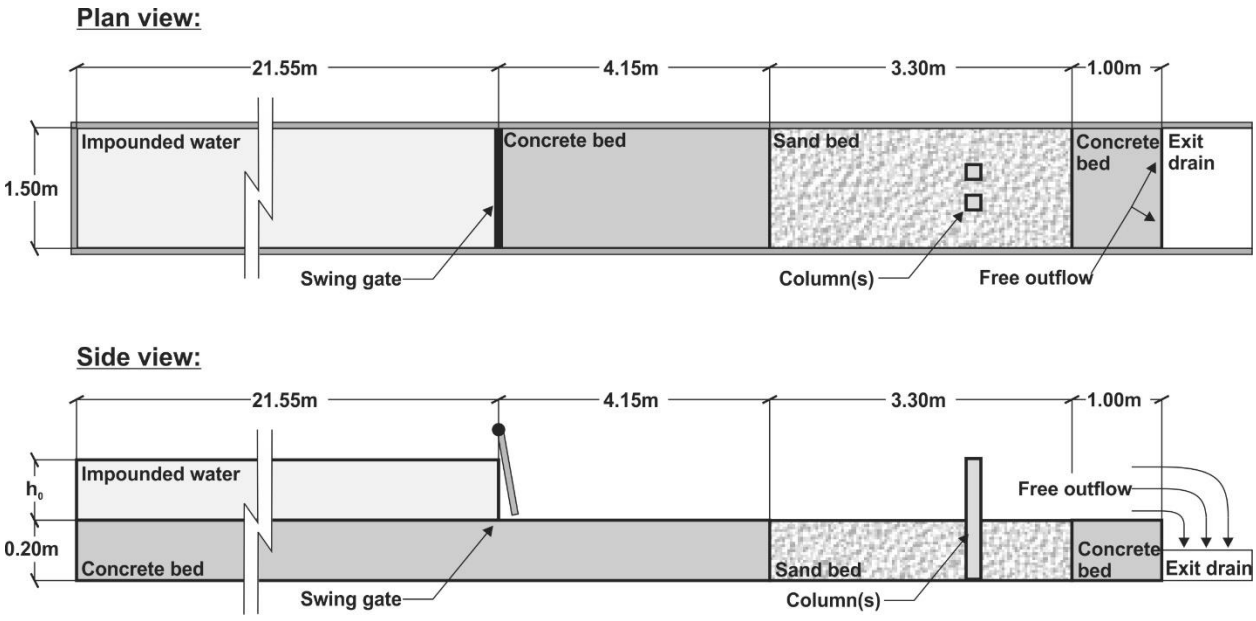

Figure 4.2: Experimental flume setup

At the end of each experimental test, the bed scour was measured using a Leica Disto TM laser altimeter, which has an accuracy of ±0.001 m. The results from the elevation measurements was an accurate 3D representation of the bed topography measured at the end of each test series. The resulting bed topography was utilized for the validation of the numerical model.

4.3.2 Numerical model

In this study, a commercially available numerical model (FLOW-3D) was applied to test the potential for scouring enhancement caused by building spacing in tsunami-like flows (Flow Science, 2018). This model was selected because of its capacity to simulate scouring around complex geometries (Alemi and Maia, 2018; Vasquez and Walsh, 2009), tsunami induced scour behind dike-like horizontal structures (Chen et al., 2016) and was also found to capably represent tsunami-induced scouring around a single square column when using Large Eddy Simulation (LES) and Nielsen (1992) sediment transport formula (April Le Quéré, Nistor, and Mohammadian, 2020). The numerical model setup and its main equations are described in this section.

4.3.2.1 Computational grid

The computational grid consisted of four nested grids of approximatively cubic cells. The cells were not all cubic to allow the solid boundaries and nested grid boundaries to follow cell segments instead of crossing them. This arrangement allowed the geometry of the experimental features to be correctly modeled by FAVOR (Flow Science, 2018) and to allow a smooth transition between the nested grids. The average cell size varied from $\Delta_1 = 0.02$ m in most of the flume to $\Delta_4 = 0.0075$ m near the columns for a total of approximatively 4 million cells (Figure 4.3). A sensitivity analysis of the grid resolution was performed and showed that there was no scouring change when a finer grid is used. The time step was optimized by the FLOW-3D algorithm throughout the simulation to ensure convergence and stability. The time step was reduced when the Courant number was greater than 1.0 and increased when it was unnecessarily low. This method allowed a balance between computational efficiency and accuracy.

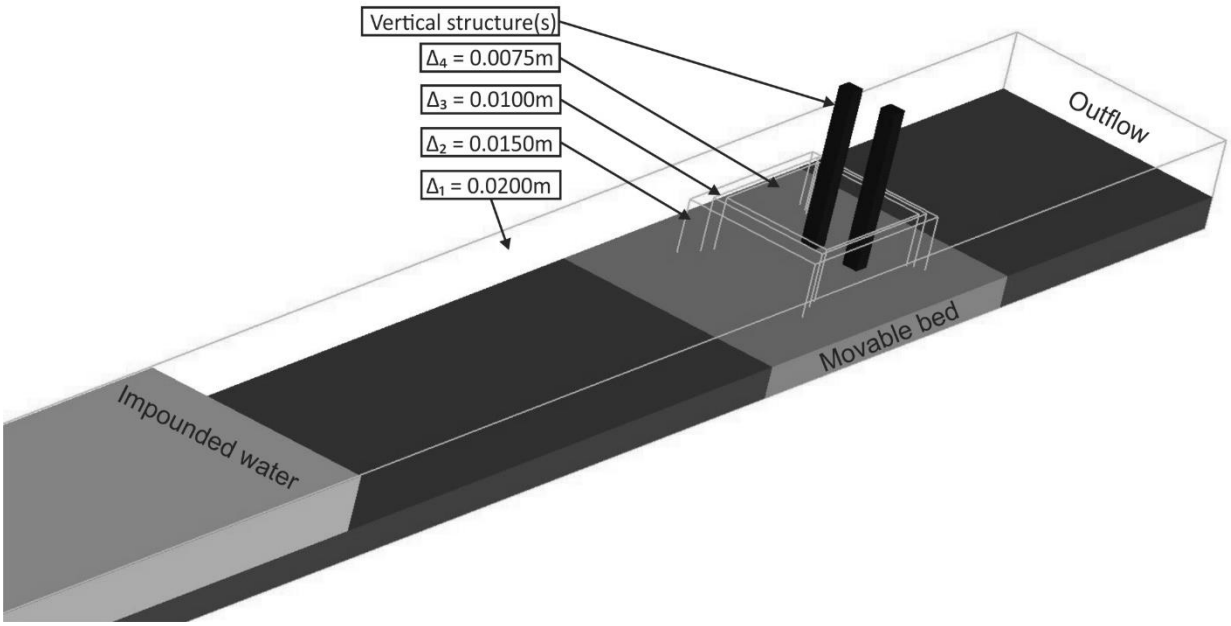

Figure 4.3: Numerical Model Mesh in FLOW-3D

4.3.2.2 Boundary conditions

All boundaries in the model were defined as symmetric pressure in order to simulate walls, except for the downstream boundary, which was defined as a negative pressure boundary. Defining the

downstream boundary in this manner allowed for an unhindered outflow of water, replicating the experimental flume outlet. This method resulted in no wave reflection or any outflow effect at the column. A roughness height of 0.001 m was defined for the fixed portion of the flume bed, in order to adequately model the sand glued to the fixed portion of the flume bed in the experimental setup.

4.3.2.3 Governing equations

FLOW-3D solves the Navier-Stokes momentum equation in all directions, allowing for a fully non-hydrostatic solving of the flow. LES was used for closing the Navier-Stokes equations, which is described in the Turbulence model section. The fully non-hydrostatic model help capture the vertical vortices forming in the vicinity of the column, which is crucial for properly modelling local scour (Khosronejad, Kang, and Sotiropoulos, 2012). The continuity and momentum equations, which are solved in all Cartesian directions, are expressed as:

$$\frac{\partial u_i}{\partial x_i} = 0 \tag{4.1}$$

$$\frac{\partial u_i}{\partial t} + \frac{\partial u_i u_j}{\partial x_j} = -\frac{1}{\rho}\frac{\partial P}{\partial x_i} + \frac{\partial}{\partial x_j}\left[(\nu)\left(\frac{\partial u_i}{\partial x_j} + \frac{\partial u_j}{\partial x_i}\right)\right] + F_i \tag{4.2}$$

where u_i and u_j are the velocity vectors, t is the time, x_i and x_j are the position vectors, P is the pressure, ρ is the fluid density, ν is the eddy viscosity coefficient and F_i represent the external forces applied to the fluid such as the gravity.

The FAVOR method was employed to represent the geometry of elements in the experimental model. Geometric shapes were approximated with the intersection between the grid faces and the user defined geometry, such as the columns and flume bed. This procedure allows for a cubic grid to model complex geometries by partially blocking certain cells. The Volume-of-fluid (VOF) method was used for the tracking of the free surface (Vasquez and Walsh, 2009; Flow Science, 2018).

4.3.2.4 Turbulence model

The turbulence model used in the numerical model calculations was LES, which is a spatially averaged model. In the resolution of the turbulence, LES removes small eddies and replaces them by local viscosity increases based on the assumptions that larger eddies carry more energy and that small eddies are similar to local energy sinks. In the preliminary study accomplished by the authors (April Le Quéré, Nistor, and Mohammadian, 2020), it was shown that the use of this model resulted in a better representation of the bed scouring compared to time-averaged models such as k-ε and k-ω. The better performance of LES was due to the fact that spatially-averaged models allow for rapid flow fluctuation, making it more accurate for simulating flow separation and strong flow curvatures (Pope, 2004; Roux et al., 2005; Spalart et al., 2006) such as the complex vortices generating local scour (Istiarto, 2001; Melville and Raudkivi, 1977; Omara et al., 2019). To apply LES, the length scale is found using a geometric mean of the grid cell dimensions: δx, δy and δz (Smagorinsky, 1963):

$$L_s = (\delta x \delta y \delta z)^{\frac{1}{3}} \tag{4.3}$$

LES scales velocity fluctuation with the magnitude of L_s multiplied by the mean shear stress. The LES kinematic eddy viscosity is hence:

$$\nu_T = (cL_s)^2 \sqrt{2e_{ij}2e_{ij}} \tag{4.4}$$

where c is a constant with typical values varying between 0.1 and 0.2 (taken as 0.1 in this study) and e_{ij} are the strain rate tensor components.

The kinematic eddy viscosity is then added to the fluid's viscosity (ν) in the momentum equation (Equation 4.2).

4.3.2.5 Sediment transport model

The calculation for sediment transport was performed by considering separately the bedload sediment transport and the suspended sediment transport. The bedload transport was simulated using the sediment transport model proposed by Nielsen (1992), which was developed for coastal-type conditions. This model was based on the principle that excess shear stress causes transport, based on the Shields (1936) parameter:

$$|q_{b,i}| = 12\left[g\left(\frac{\rho_s - \rho_w}{\rho_w}\right){d_i}^3\right]^{1/2}\left[\theta'_{b,c}\right]^{0.5}\left(\theta'_{b,c} - \theta_{b,cr}\right) \tag{4.5}$$

where $q_{b,i}$ is the bed load transport rate in units of volume per bed width per time, g is the gravitational acceleration, ρ_s and ρ_w are the density of the sediment and water, respectively, d_i is the grain diameter, $\theta'_{b,c}$ is the local shields and $\theta_{b,cr}$ is the critical shields parameter calculated using the Soulsby-Whitehouse equation (Soulsby, 1997).

$$\theta'_{b,c} = \frac{\tau}{(\rho_s - \rho_w)d_i\|g\|} \tag{4.6}$$

$$\theta_{b,cr} = \frac{0.3}{1 + 1.2d_*} + 0.055[1 - exp(-0.02d_*)] \tag{4.7}$$

$$d_* = d_i\left[\frac{\rho_w(\rho_s - \rho_w)\|g\|}{{\mu_w}^2}\right]^{\frac{1}{3}} \tag{4.8}$$

where τ is the bed shear stress calculated from the law of the wall and the quadratic law of bottom shear stress for 3D turbulent flow, d_* is the dimensionless grain size and μ_w is the dynamic viscosity of water.

The bedload transport rate was then used to calculate the change in bed elevation (Z_b) based on the packing fraction (p'), taken as 0.64:

$$p'\frac{\partial Z_b}{\partial t} = \frac{\partial q_{b,i}}{\partial x_i} + D - E \tag{4.9}$$

where D is the downward sediment flux and E is the upward sediment flux.

For the suspended sediment, the formulation of Mastbergen and Van Den Berg (2003) was applied. The entrainment lift velocity of sediment ($u_{lift,i}$) was used to compute the amount of sediment converted into suspension, adding the suspended sediment in the flow over the movable bed. Equation 4.10 describes the entrainment lift velocity of the sediment:

$$u_{lift,i} = \alpha_i n_s {d_*}^{0.3}\left(\theta'_{b,c} - \theta_{b,cr}\right)^{1.5}\sqrt{\frac{\|g\|d_{50}(\rho_s - \rho_w)}{\rho_w}} \tag{4.10}$$

where $u_{lift,i}$ is the entrainment lift velocity of sediment, α_i is the entrainment coefficient used as calibration coefficient (taken as 0.15) and n_s is the outward pointing normal to the packed bed interface.

For additional details on the numerical model's equation, the reader is directed to the FLOW-3D user manual (Flow Science, 2018).

4.3.3 Numerical model calibration and verification

The model was calibrated by adjusting the entrainment coefficient in the sediment transport model, which has a default value of 0.018 (Mastbergen and Van Den Berg, 2003). This coefficient is multiplied to the excess shear stress calculation and enhances the sediment pick-up rate (see Equation 4.10). Values ranging from 0.01 to 0.6 were used in the calibration exercise and, with a final value of 0.15, the maximum scour depth in the numerical model was identical to the one in the experimental results from Mehrzad, Nistor, and Rennie (2016). For additional details on the calibration exercise, the reader is referred to April Le Quéré, Nistor, and Mohammadian (2020). The final bed profile and comparison with experimental data for the calibration run (b = 0.2 m, h_0 = 0.25 m) are shown in Figure 4.4.

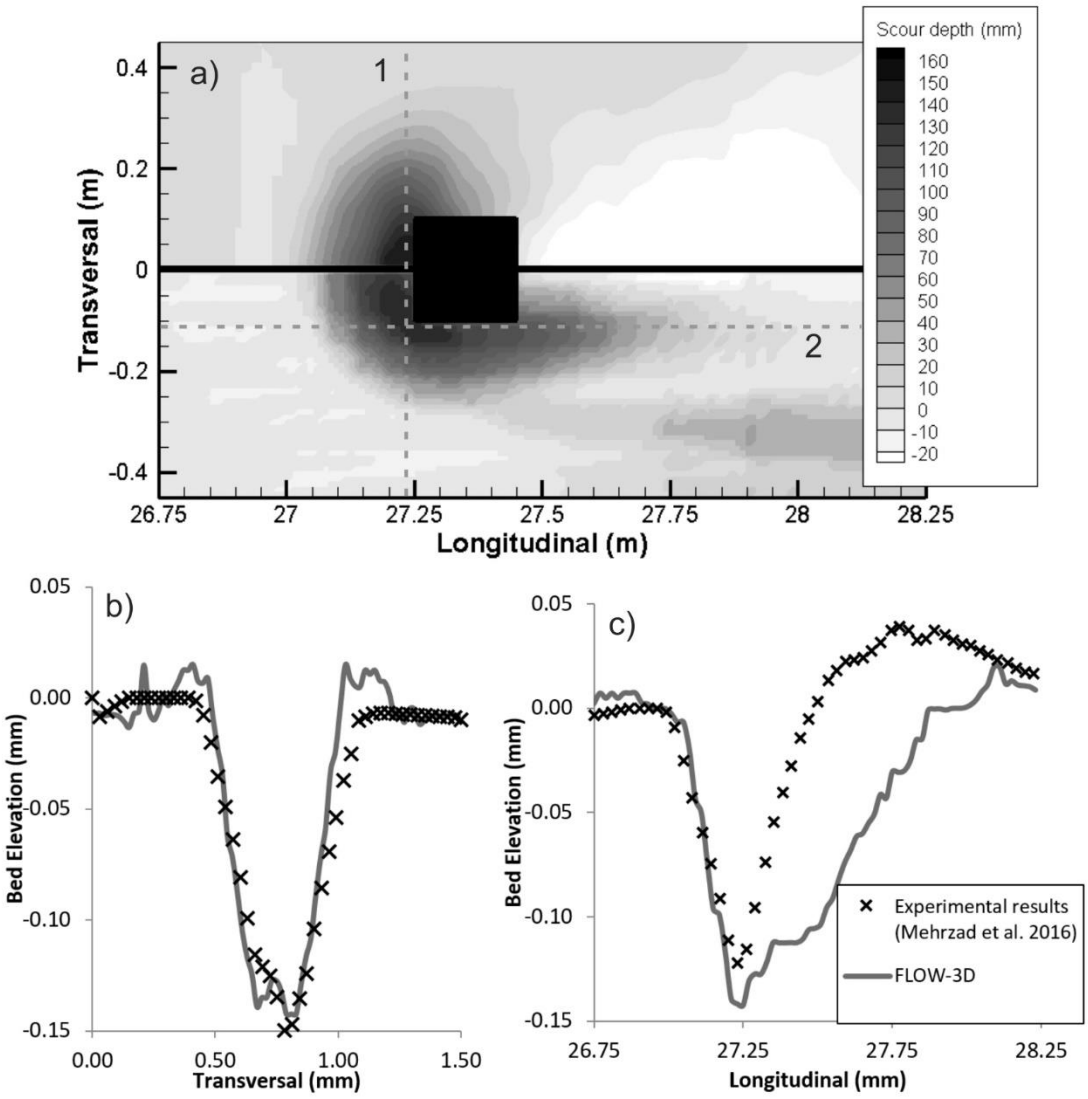

Figure 4.4: FLOW-3D calibration results with b = 0.2m and a bore generated by a h_0=0.25m impoundment depth; a) top plate: plan view of the experimental final bed surface) and bottom plate: plan view of the numerical model final bed surface; b) bed elevation at cross-section 1; c) bed elevation at cross-section 2

Scouring upstream of the structure was replicated with reasonable accuracy. In a rectangular area extending 0.3m upstream of the column and 0.3 m on either side of its centerline covering the upstream scour hole area, a root mean square error (RMSE) of 15.42 mm was calculated. The RMSE for the back of the column was calculated in a rectangular area between *x* = 27.25 m and x = 27.65 m with a width 0.6 m centered on the centerline. The resulting RMSE for the second area was 43.77 mm, indicating larger discrepancies in the side and downstream area of the scour hole.

A verification of the calibration was performed by comparing the calibrated numerical model results to an additional topography result from the same study. In this verification setup, a column width of 0.3m and an impoundment depth of 0.2 m were used. The remainder of the setup was identical to the one performed in the calibration. Figure 4.5 shows a comparison between the final bed elevations calculated using FLOW-3D and the one measured in the experiment. The resulting

scour profile shows similar trends as the calibration run (b = 0.2 m, h_0 = 0.25 m). Scouring in the numerical model extends further downstream compared to the experimental results. The location of the deepest scour in the numerical model is situated at the upstream corners as opposed to the front of the column in the physical experiment. In the case of the larger column, the experimentally measured maximum scour depth is upstream of the front corners instead of in the middle of the upstream segment, making it closer to the numerically calculated maximum scour location. The maximum scour depth was well replicated: 125 mm for FLOW-3D vs 130 mm for the physical experiment.

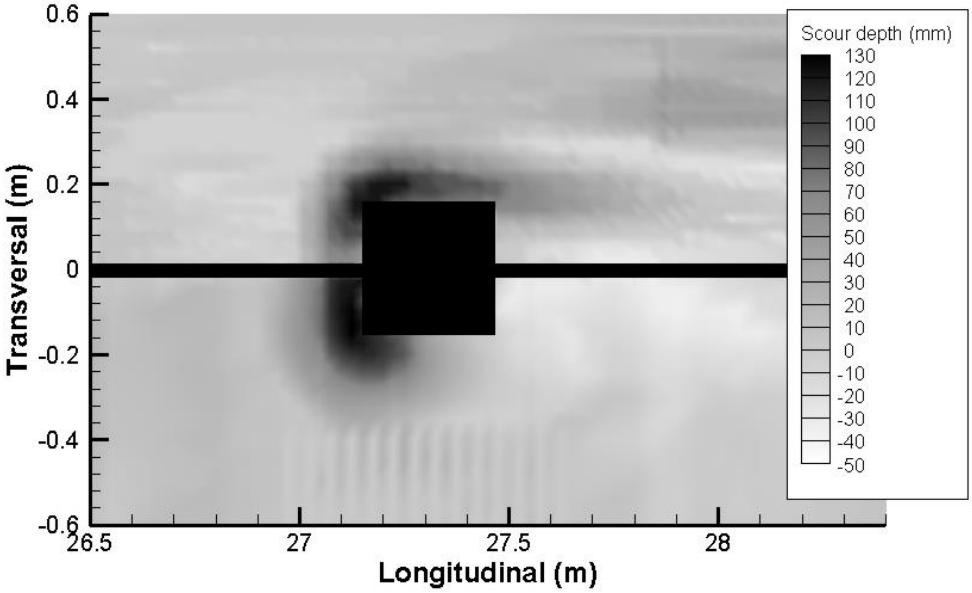

Figure 4.5: Numerical model verification using a 30 cm column and a bore generated by a 20 cm impoundment depth; top: FLOW-3D results // bottom: experimental results

Single column runs were simulated when investigating the effect of the lateral spacing between the structures in order to obtain a baseline for the increase effect. The numerically calculated final profile's maximum scour depth was compared to the results in Mehrzad, Nistor, and Rennie (2016) when the same conditions were used (Figure 4.6). The model was initially calibrated using a 20cm wide column and an impoundment depth of 25 cm, which explains why the numerical model matched accurately the experimentally-obtained value. The other three setups returned a maximum scour depth with a relative error between 3% and 4%. These results indicate that the calibrated model is robust enough to correctly evaluate the maximum scour depth when different impoundment depths and obstruction widths are used.

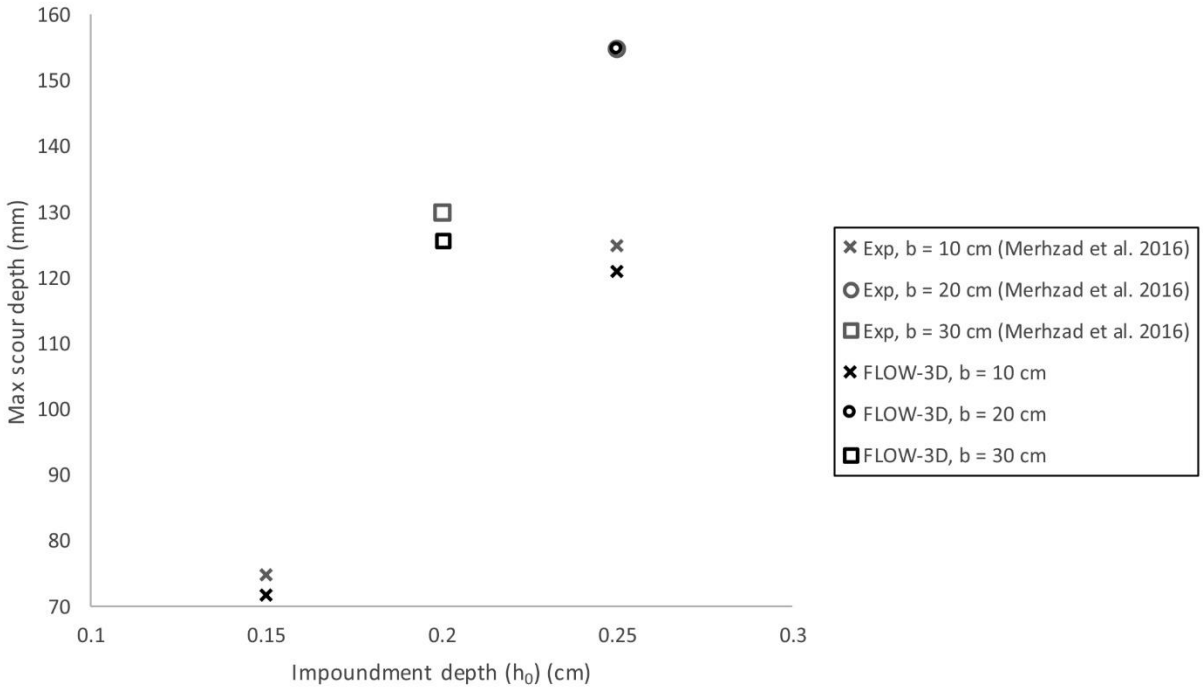

Figure 4.6: Maximum scour depth comparison for varying impoundment depths (h_0) and column widths (b)

4.3.4 Numerical test setup

In the numerical test runs, a second column was added in the same transversal plane as the column of interest to study the effect that lateral spacing between the structures has on scouring (Figure 4.7). The column width was reduced to 0.1 m for most runs to reduce wall effects at higher spacing ratios. A series of tests were performed with a 0.2 m wide column to test the effects of the model scale and structure width. The lateral spacing (S), defining the distance between the inner side of the two columns, was varied from S = 0 m to S = 0.3 m. Beyond a distance of S = 0.3 m, the space between the walls and the columns would be smaller than S, which would result in greater flow concentration between the walls and the columns than between the columns themselves. Single column runs were performed to obtain a reference maximum scour depth, which was used to compare the changes caused by the addition of the second column. Three impoundment depths (h_0 = 0.15 m, 0.25 m and 0.35 m) were used to generate the bore and to evaluate the significance of the approach flow momentum on the lateral spacing effect.

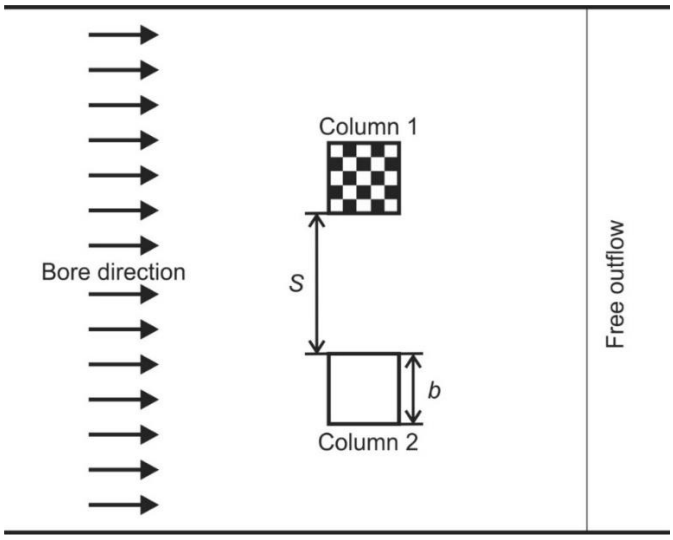

Figure 4.7: Plan view of the laterally-spaced columns setup in the numerical model

4.3.5 Model scaling

The numerical simulations followed a Froude scale of 1:80 model to prototype ratio, which guarantees the dynamic similarity of the gravitational forces. This scaling method comes at the expense of ignoring viscosity and roughness scaling. Firstly, the surface tension effects can be negligible at such scale given that it relates to air entrainment. Some relative roughness effects will be experienced in the early and late stages of the bore as the flow is lesser, but turbulence in most of the flow duration reduces Reynolds effect in tsunami-like flows (Foster, Rossetto, and Allsop, 2017). However, overlooking Reynolds number similarity may lead to a poor representation of the horseshoe vortex, resulting in a poor representation of near-structure scouring (Huang, Yang, and Xiao, 2009).

The three impoundment depths used in this study (0.15 m, 0.25 m and 0.35 m) generated bores with the properties shown in Table 4.1. At a Froude scale of 1:80, the prototype flow properties compare well to tsunami events such as the 1993 Hokkaido-Nansei-Oki tsunami (Jaffe and Gelfenbuam, 2007; Titov and Synolakis, 1997) or the 2010 Chilean Tsunami (Earthquake Engineering Research Institute, 2010; Fritz et al., 2011b).

Table 4.1: Hydraulic properties of the dambreak bore at prototype scale following an 80:1 Froude similarity

	Model scale			Prototype Scale		
Impoundment depth (h_0) (m)	0.15	0.25	0.35	12	20	28
Maximum flow depth (m)	0.080	0.146	0.182	6.40	11.2	14.4
Maximum depth averaged velocity (m/s)	0.72	0.90	1.35	6.44	8.05	12.1
Inundation period (s)	50	50	50	450	450	450

The median grain size (d_{50}) used in the physical experiment and in the numerical model calibration exercise was of 0.001 m. The grain size, in Mehrzad, Nistor, and Rennie (2016), was selected following the dimensionless shear stress proportion. However, the exact proportions could not be reached due to the ripple forming behaviour of smaller grain size. For the numerical model, smaller grain size could be used to respect the dimensionless shear stress proportion without experiencing rippling effects or cohesion forces due to the built-in formulas for sediment transport. However, the numerical model results could not be verified with a physical model if such a small grain size were to be used. Therefore, the authors chose to keep the same grain size of 0.001 m in the numerical model. Keeping this size of sand allowed the tests to represent prototype scale scour process linked to the sediment size. The reasoning behind this statement is that the size of uniform sediments does not affect the scour depth unless the ratio of column width to grain size (b/d_{50}) is smaller than 50 (Melville and Chiew, 1999). In the case of the smaller column used (0.1 m), the proportion b/d_{50} is 100, which is theoretically sufficient to prevent sediment scale effects. As shown later in this study, local scour is the governing process for scouring, not channelization. Therefore, the single column theory remains applicable in this case.

4.4 Results

Results from the FLOW-3D simulations are presented in this section. These results include both scouring and hydrodynamic changes caused by the addition of a laterally spaced column of the same size.

4.4.1 Scour results

First, the bed elevation change results for the single column (b = 0.1 m) and for the different column lateral spacing are presented (Figure 4.8) for scour generated from a bore produced by the release of water with one specific impoundment depth (h_0 = 0.25 m). The 0.1 m wide single column shows a different scour pattern than that calculated for case of the 0.2 m column. The maximum scour depth still occurred in front of the upstream face of the column, but a much larger scour area extended downstream, along the structure's sides (see Figure 4.8 a). The scour wrapped around to the back of the column and prevented sediment accumulation to occur at the downstream face of

the column. Once an adjacent column was added (with a lateral spacing ratio (*S/b*) = 0), the scour depth increased by 48% due to the doubling of the structure's effective width. The maximum scour depth was located just upstream of the front face due to the circular nature of the strong horseshoe vortex. Unlike for the single column case, sheltering from the two virtually adjacent set columns allowed sediment accumulation to occur at the downstream face. The scour pattern that formed around the two 0.1m adjacent columns was very similar to that of the 0.2 m single column. A small amount of scouring extended downstream at a 45-degree angle.

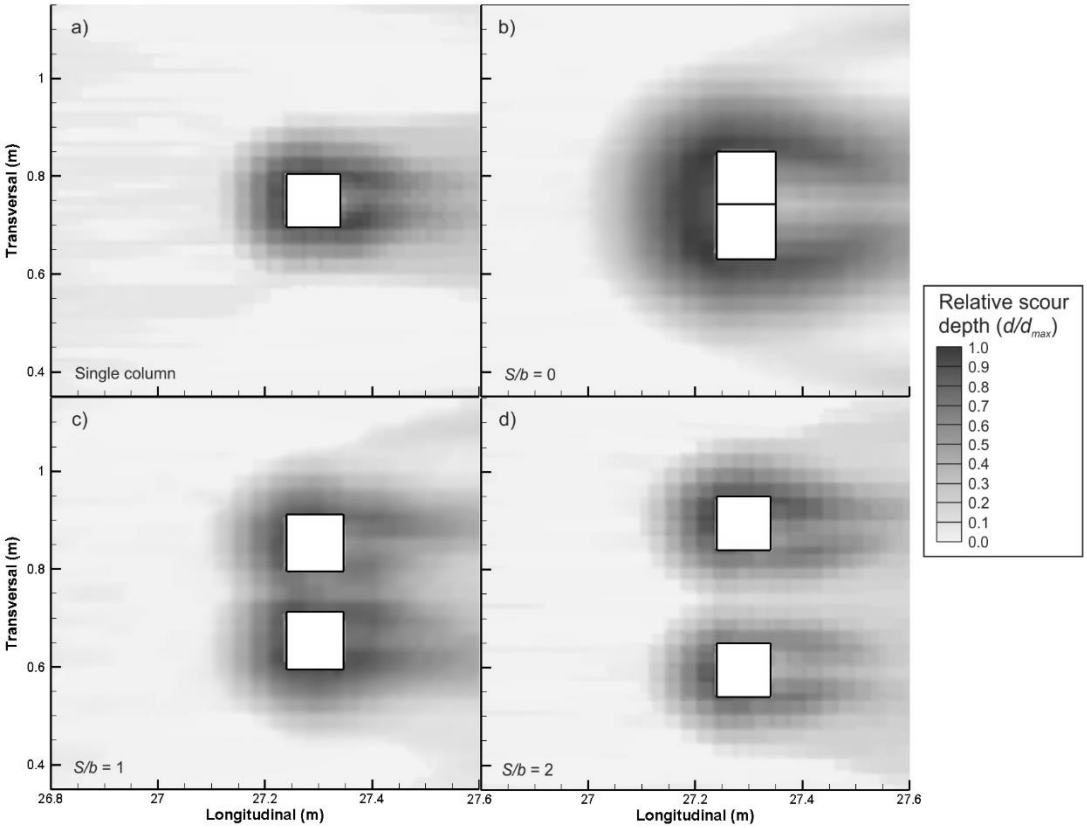

Figure 4.8: Plan view of the relative scour bed elevation for a single column (a) and for spacing ratios varying from 0 (b) to 2 (d); due to a bore generated by an impoundment depth, h_0 = 0.25m and a column width, b = 0.10m

For a lateral spacing ratio *S/b* = 1, the separation between the columns allowed some flow between them. The scouring was found to be greater than that observed in the single column test. The maximum scour depth occurred at both of the upstream corners and the scour between the columns was lesser than observed at the upstream corners (Figure 4.9). The scour extended further downstream than in the single column test, which may be caused by an acceleration of the flow around the structures. A downstream angled scour, similar to *S/b* = 0, was observed for all the two-column configurations. At *S/b* = 2, the scour hole around each column was similar to the single column pattern, but with a slightly longer scour tail and a deeper maximum depth at the outside upstream corners. Indeed, the upstream bed elevation cross-sections at *S/b* = 2 and *S/b* = 3 were only marginally different from that observed for the case of the single column (Figure 4.9), implying that the effect of the adjacent column becomes negligible for *S/b* = 2 and above for these particular hydrodynamic conditions.

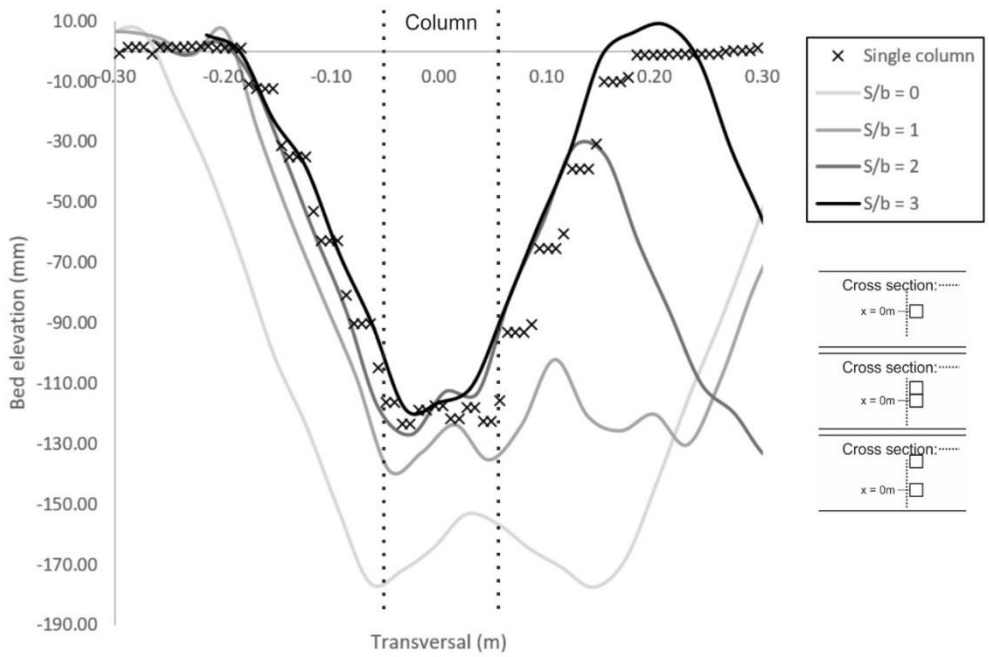

Figure 4.9: Transversal vertical cross-section of the final bed elevation upstream of the columns; centered on the midpoint of the right column due to a bore generated by an impoundment death, with h_0 = 0.25m and a column width, b = 0.10m

Interestingly, symmetry was not observed in the formation of the scour. This is the result of using a spatially averaged turbulence model (LES). Symmetry is typically not preserved with this type of model because the turbulence is not time-averaged, causing rapid variation of both the flow direction and flow velocity.

Figure 4.10 shows the resulting relative scour depth (maximum scour depth of the test divided by maximum scour depth in single column test (d_s/d_{s0})) of the 15 numerical setups grouped by the same impoundment depth (h_0). When the two columns were placed next to each other (S/b = 0), the relative maximum scour depth increased for bores generated by the higher impoundment depths released from the reservoir. The same trend of scour augmentation was observed for every spacing ratio, indicating that the spacing effect varies depending on the approaching flow properties. At S/b = 1, the relative scour depth sharply reduced compared to the adjacent columns cases. At S/b = 3, the relative scour depth was approximately 1.0 for h_0 = 0.15 m and h_0 = 0.25 m, meaning that the adjacent column had a negligible effect on the maximum scour depth starting at that spacing. For the highest impoundment depth (h_0 = 0.35 m) used, the second column had a greater effect on the maximum scouring and up to the highest spacing tested. With the 0.2m column, the effect of spacing on scour reduced as spacing increased. When the spacing ratio was 1.5, a different behaviour was observed. The relative scour depth sharply reduced to 1.04, which is similar to the results found when the two adjacent 0.1m columns were spaced by 2 or 3 diameters. This difference may indicate that the flow depth is limiting the lateral size of the column related vortices, preventing the interaction of the turbulence generated by each column at lower flow depths.

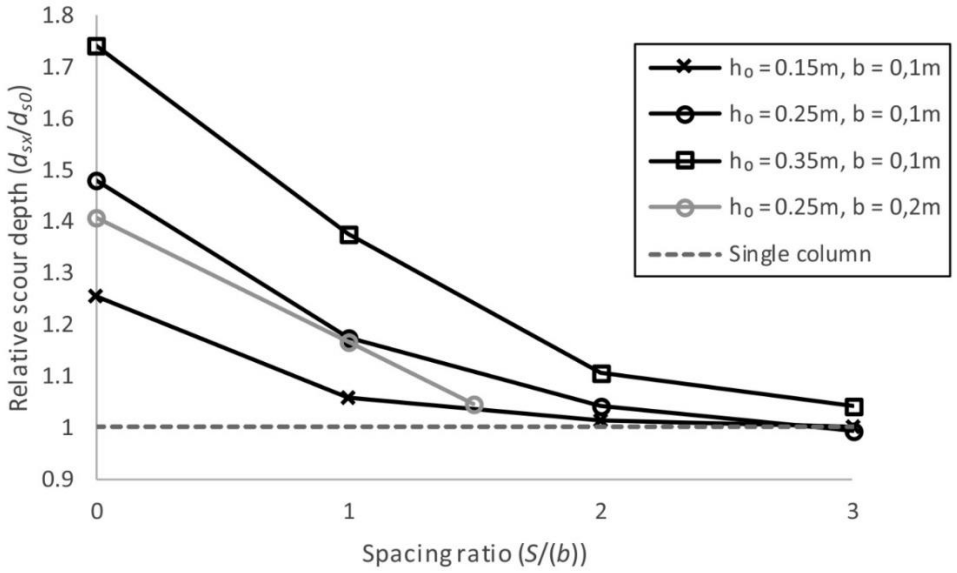

Figure 4.10: Maximum scour depth variation with the lateral spacing ratio (S/b) and the bore-generating impoundment depth (h_0)

To account for the variation of lateral spacing effect with an increase in the impoundment depth, the lateral spacing ratio was adjusted for the approach flow depth (y) (defined as the adjusted spacing ratio ($S'=(S+b)/(by)$) and plotted against the relative scour depth in Figure 4.11. A linear trend seemed to appear when the adjusted spacing ratio (S') was less than $S'<17.2$. To build the trend line, the value of 2.0 was used as an intersection point on the vertical axis. This value was considered as a theoretical maximum for the relative scour depth, since it is the maximum value for the relative scour depth occurring for two columns placed transversally in steady flow (Beg, 2010). This maximum occurs when the lateral spacing is equal to zero, which effectively doubles the projected width of the structure, explaining the intersection with the y-axis. The best fit linear regression for the results with an adjusted spacing ratio of $S'<17.2$ had a negative slope of 0.058 and was crossing the vertical axis at $d_s/d_{s0} = 2$ (described by Equation 4.11). A coefficient of determination (R^2) of 0.922 was calculated for the curve described by Equation 4.11. The relative scour depth associated with an adjusted spacing ratio of S'>17.2 was found to be close to 1.0, with a maximum difference of ±0.04. A conservative envelope is proposed in Equation 4.13 to account for lateral spacing when designing structures in tsunami risk area. However, this curve was only developed with a limited amount of numerical tests, with one grain size and one structure shape.

$$\text{For } S' = \left[\frac{(S+b)}{(by)}\right] < 17.2 \qquad \frac{d_s}{d_{s0}} = 2 - 0.058\left[\frac{(S+b)}{(by)}\right] \tag{4.11}$$

$$\text{For } S' = \left[\frac{(S+b)}{(by)}\right] > 17.2 \qquad \frac{d_{sx}}{d_{s0}} = 1 \tag{4.12}$$

$$\text{For } S' = \left[\frac{(S+b)}{(by)}\right] < 27 \qquad \frac{d_s}{d_{s0}} = 2 - 0.037\left[\frac{(S+b)}{(by)}\right] \tag{4.13}$$

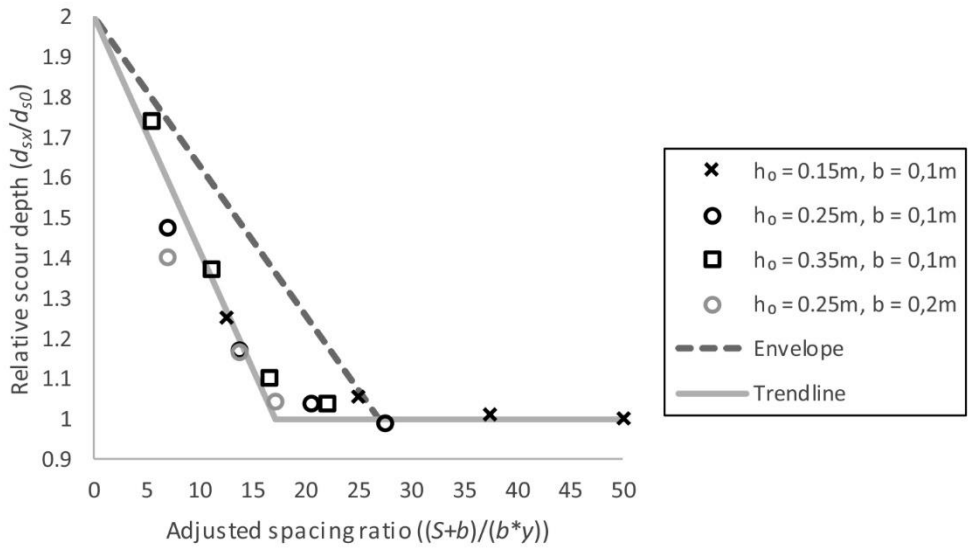

Figure 4.11: Maximum scour depth increase as a function of the adjusted spacing ratio (S'=(S+b)/(by))

4.4.2 Hydrodynamic results

It is recognized in the scientific community that the horseshoe vortex is the main hydrodynamic structure responsible for local scouring (Ettema, Kirkil, and Muste, 2006), meaning that the associated scour depth will be proportional to this vortex's strength. One likely source of the increase in maximum scour depth is the change in the horseshoe vortex strength associated with the addition of a second column in the vicinity of the first one. Figure 4.12 shows a longitudinal *x*-*z* cross-section of the flow upstream of the mid-point of one of the two columns for all the column spacings. A specific instant (t = 30 s) was chosen because the horseshoe vortex was well formed by this time, which was also the moment before the approaching flow depth started to decrease. Expected flow direction fluctuations linked to the calculation of turbulence by LES were observed in the model results. However, those single instants were indicative of an observed trend. A large vertical vortex was present at the structure toe in all the model arrangements. The vorticity of the horseshoe vortex was much larger at S/b = 0 (Figure 4.12 b) than in the case of the single column (Figure 4.12 a). Generally, when a second column was included, the vorticity at the structure toe was always larger than that calculated in the case of the single column. As the spacing increased, the intensity of the vortex reduced, but the vorticity was still larger than in the single column case. The augmentation of the vortex strength associated with the increase in the effective structure width, which further intensified the erosion process, is consistent with the literature for steady flow (Dargahi, 1989).

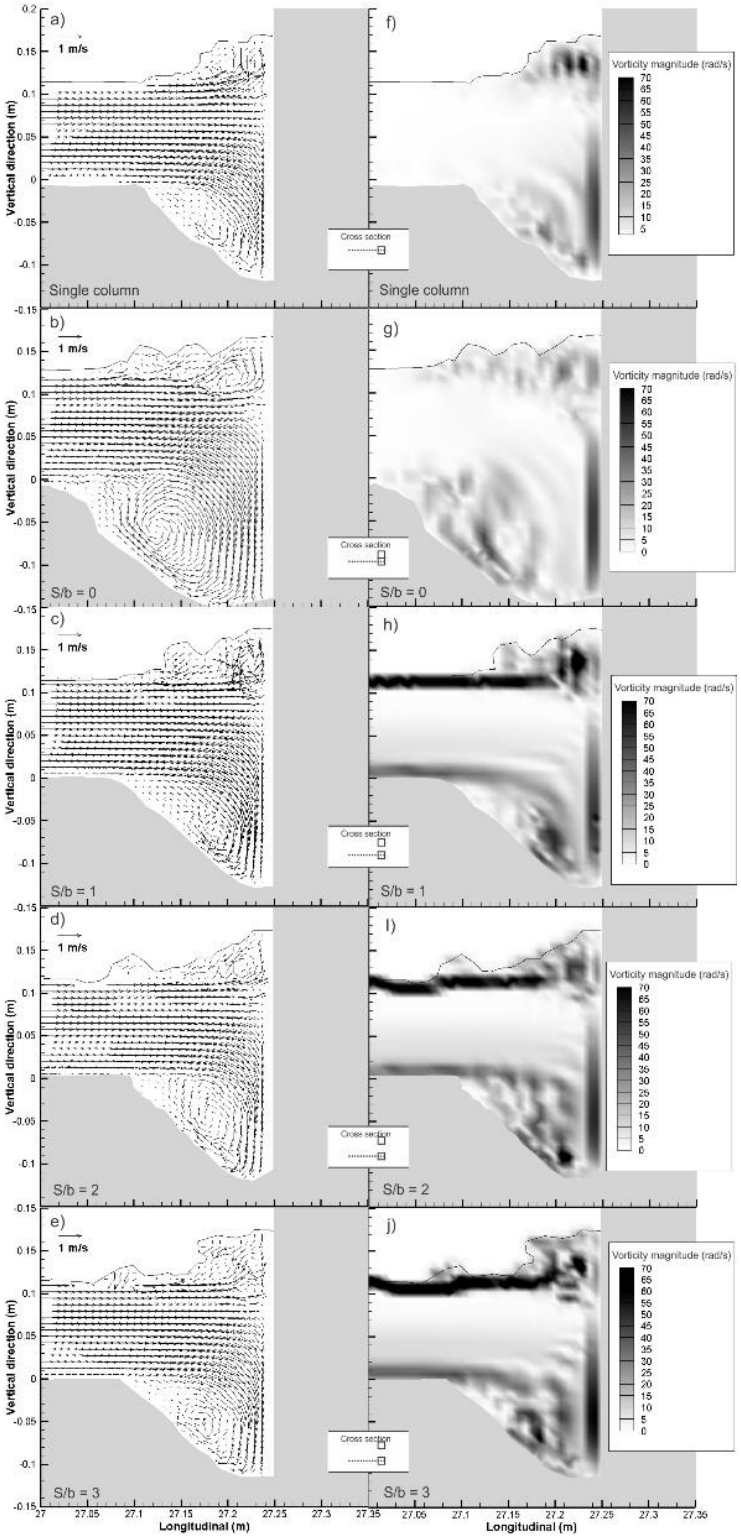

Figure 4.12: Horseshoe vortex and vorticity at the midpoint of the column(s) upstream face at t = 30s with column width, b = 0.1m and the impoundment depth, h_0 = 0.25m; a), b): single column b) to e) and g) to j): spacing ratio varying from 0 to 3

4.5 Discussion

In this section, the scouring and hydrodynamic changes caused by the addition of a laterally spaced column is compared to previous findings from literature. In addition, the significance of these results for the design of structures in tsunami-prone areas are discussed.

4.5.1 Scouring

The final bed elevation profiles showed lengthier scour holes that extended further downstream as the spacing between the columns reduced. These long scour holes may not be fully accurate as during the calibration and verification exercises, it was noted that the length of the scour holes was overestimated in the FLOW-3D simulations. In the field observations made in Oganawa (Yeh, Sato, and Tajima, 2013), the scour hole was present only in between the buildings and no scouring was reported along the side walls nor downstream of the structures. However, soil protection in the form of concrete and an asphalt layer was observed at the site and this may have prevented the formation of lengthier scour holes at those locations.

When compared to the scouring increase due to lateral spacing in steady flow, similarities can be noted. The relative scour depth generated by a bore resulting from an impoundment depth of 0.35m was close to the one found by Beg (2010) whose experimental tests were conducted in steady flow conditions, especially for the spacing ratios of 2 and 3. In their investigation, the relative scour depth was 1.95 for S/b = 0, 1.21 for S/b = 1, 1.1 for S/b = 2 and 1.05 for S/b = 3. In the present experiments, the maximum scour depth did not double when the columns were side by side, as with the case observed in steady flow (Breusers, Nicollet, and Shen, 1977). This observation is consistent with findings of Mehrzad, Nistor, and Rennie (2016) who found that the doubling of the column's effective width did not result in a doubling of the scour depth in tsunami-like flows. One possible reason of the difference between steady and unsteady flow is that, in unsteady flow conditions, such as the ones occurring during tsunami inundation, the flow duration is not sufficiently long to reach the equilibrium scour depth. The variation of impoundment depth did not affect the duration of the flow, but the larger flow momentum associated with bores generated by the higher impoundment depths was crucial in the effect induced by the lateral spacing. Similarly, in steady flow conditions, the approaching flow properties influence scour enhancement caused by lateral spacing (Elliott and Baker, 1985).

4.5.2 Hydrodynamic changes

In the numerical model, the addition of a second structure on the same transversal plane increased the strength of the horseshoe vortex as shown in Figure 4.12. This change may suggest that the process responsible for the scour augmentation at the structures was not only channelization (see Figure 4.13 for a depiction of the flow structures dictating the scour process). Instead, there are hypothesis that the local scouring process was enhanced by the column-induced blockage, as explained in the following. The channelization scouring, in steady flow, is caused by the flow momentum increase caused by the narrowing of a flow path (Briaud *et al.*, 2005; Sturm, Ettema, and Melville, 2011) and scouring caused by this process is observed between the obstructions. Whereas in the case discussed in this study, the scouring was mostly present at the upstream face and corners of the columns. The fact that the horseshoe vortex was the main driver of scouring

may explain why the 0.2 m column had a relative scour depth similar to the 0.1 m column at a lateral spacing ratio of 0 and 1, but was much lower when the spacing ratio was of 1.5. As shown in Figure 4.10, the reservoir impoundment depth and the subsequent bore generated by its rapid release significantly influenced the effect of the lateral spacing effect on scouring. The authors suggest that the flow depth at the column location(s) limited the lateral expansion of turbulence around them; this resulted in a more significant influence of the lateral spacing at deeper flow depths, associated with deeper impoundment depths. It also means that the stronger turbulence generated by the wider 0.2 m columns was transversally limited in size, reducing the interaction between the structures. This hypothesis explains the more rapid decrease in the influence of the lateral spacing in the case of the wider column (0.2 m).

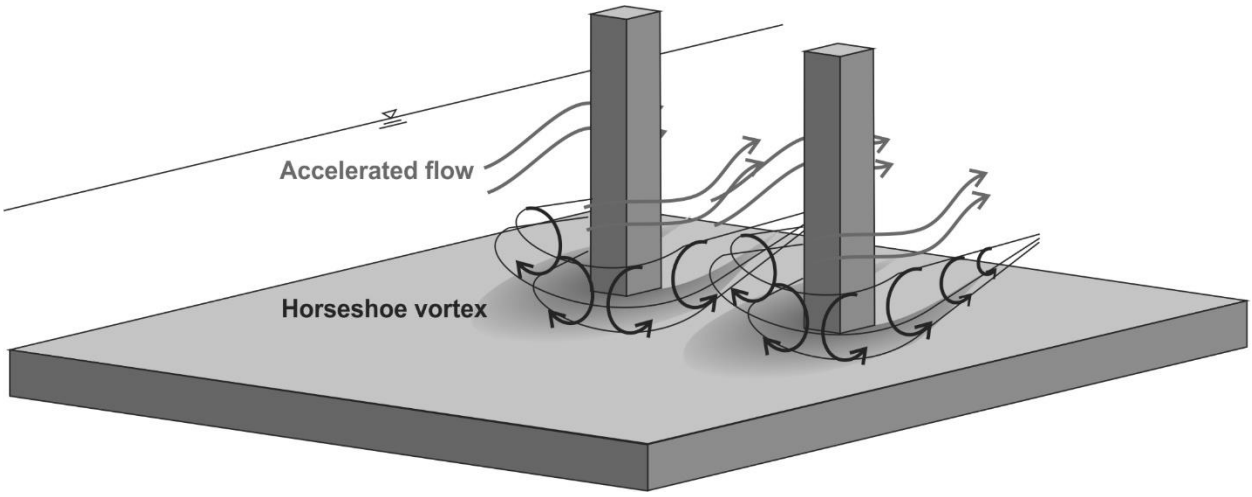

Figure 4.13: Schematic representation of the flow structures creating scour around the columns

4.5.3 Comparison to ASCE 7 design considerations

When comparing the numerical model results to the latest recommendations by ASCE 7 - Chapter 6, it is apparent that further investigations on the topic of scour is necessary. The newer recommendations for tsunami-induced scour around columns are based on experiments used for the calibration of the present numerical model and on additional experiments performed in the same dambreak flume at the University of Ottawa (Lavictoire, Nistor and Rennie, 2014; Mehrzad, Nistor, and Rennie, 2016). Since design considerations in ASCE 7 – Chapter 6 are only provided for the case of single columns, the numerical model results were considered as single column when inputting the column width. On the other hand, the column width in the numerical tests with a spacing of 0m was considered as two times the column width, which corresponds to the effective width of the two columns. For the lowest impoundment depth, the resulting vertical scour to column width ratio (d_s/b) was well below the envelope proposed by ASCE 7 (Figure 4.14). However, for the bores generated by the impoundment depths h_0 = 0.25 m and h_0 = 0.35 m, some of the results were situated above the proposed envelope. In fact, even the single column test was above the envelope when the impoundment depth was of 0.35 m. Some consideration of structure spacing should be included in the design of structures prone to experiencing tsunami-induced scouring, especially at higher flow momentums.

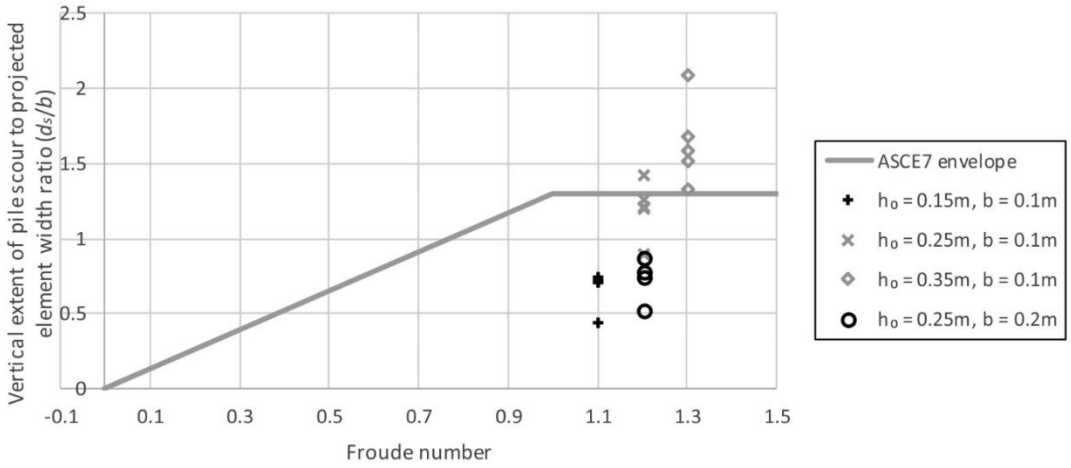

Figure 4.14: Vertical extent of pile scour to projected element width ratio (d_s/b)

4.6 Conclusions

Several conclusions from this numerical investigation using FLOW-3D were drawn. (1) The lateral spacing between two columns does affect the scour depth around them. This increase in scour depth, similar to the case of steady flows, is inversely correlated with the distance between the columns and directly proportional with the strength of the flow momentum. (2) The increase in horseshoe vortex strength is believed to be responsible for this scouring augmentation, leading the authors to believe that the flow depth may be a controlling factor for effect the lateral spacing between the columns because it limits the lateral size of structure-associated highly turbulent zone. (3) Some of the scour depths calculated by the numerical model were found to be exceeding the scour design envelope proposed by ASCE 7 Chapter 6. Equations 4.11, 4.12 and 4.13 are preliminary proposed to help calculate scour around column elements that are close to each other. However, the authors point to the strict limitations of these equations, indicating that, prior to proposing them as practical tools for design as they are only based on numerical model results. More experimental and numerical investigations need to be performed to validate these numerical results and equations.

Physical modeling is planned by the authors in the near future to help confirm the phenomenon of increased tsunami-induced scouring caused by lateral spacing.

Chapter 5: Hydrodynamics and associated scour around a free-standing structure due to turbulent bores

5.1 Abstract

Forensic engineering field surveys conducted in the aftermath of large-scale tsunamis documented the presence of deep local scour holes around structures caused by the extreme inundation occurring during such events. The mechanisms leading to scour in extreme flows are still not well understood as several physical phenomena influencing the spatio-temporal extent of scour have not been adequately investigated. The authors have conducted an experimental test program that has employed a large square column in the Large Wave Flume of the Coastal Research Center, Germany, while they also used a state-of-the-art numerical model (FLOW-3D) to numerically reproduce the experimental results. An investigation of the turbulent flow structures observed around the impacted structure showed that these flow structures are largely responsible for the sediment transport during the runup phase, but the turbulent energy was far less intense during the drawdown phase. The weakness of the turbulent structures observed during drawdown indicates that a different physical phenomenon than the one corresponding to the inflow phase is responsible for the sediment transport experienced during inundation drawdown. Due to the rapid lowering of the flow depth during the drawdown phase of tsunami inundations, a loss of excess pressure occurs because of the upward pressure gradient forming within the soil. However, the pore pressure measurements taken inside the soil in the physical experiment indicate no sign of upward pressure gradient on the inshore side of the column, which is an observation that is incongruent with previous similar studies and previous theoretical concepts. This difference was explained by a layer of soil that remained with a low water content throughout the test because the column was installed on dry sand with low permeability, a condition never tested before for pore pressure change caused by tsunami-like waves.

5.2 Introduction

Over the past few decades, large tsunami events have impacted coastal communities along the coastlines of many countries (see e.g. Krautwald et al., 2021; Stolle et al., 2020; Suppasri et al., 2013), resulting in infrastructure failures (Chock et al., 2013; Ghobarah et al., 2006; Jayaratne et al., 2016; Palermo et al., 2013; Shibayama et al., 2013; Stolle and Goseberg, 2020; Yeh et al., 2013), lives lost and various forms of pollution, some in the form of floating debris (J. Stolle et al., 2019; Jacob Stolle et al., 2020; Stolle et al., 2018). To this day, the scientific community has a limited understanding of tsunami inundations and their resulting impacts on structures. This lack of knowledge is partly because it is challenging to predict the occurrence of this type of extreme hydrodynamic phenomenon, leading to a lack of "live" field observations and measurements of tsunami events. Scouring around buildings is one of the least understood effects of the tsunami inundation. Not only is the scouring around structures in the field still not predicted to an adequate level of accuracy, but the transient nature of tsunamis is adding its complexity. Parameters such as the grain size (Lavictoire et al., 2014), structure width (Mehrzad et al., 2016), flow depth (Tonkin et al., 2013), number of wave (Chen et al., 2013; Larsen et al., 2018, 2017), wave period, and flow velocity (D. J. McGovern et al., 2019) were found to influence scour when examining the tsunami

effects using a physical model. However, many other parameters which may influence scour are yet to be investigated.

To simulate tsunamis at reduced scale, various generation methods have been utilized to recreate either the surge or the highly turbulent tsunami bore advancing inland (Fritz et al., 2011a; Takahashi et al., 2011). Solitary waves (Nakamura et al., 2008; Nistor et al., 2017b, 2017a), N-waves (Yeh and Li, 2008), cnoidal waves (Antuono and Brocchini, 2011), and dam break waves (Lavictoire et al., 2014; Mehrzad et al., 2016; Nouri et al., 2010; St-Germain et al., 2014, 2012) have all been used by scientists to study tsunami behaviors in laboratory. A more detailed review of tsunami generation methods using experimental facilities was provided by Goseberg et al. (2013). These wave proxies present different challenges and can lead to an inappropriate representation of some of the tsunami wave properties. Indeed, Tonkin et al. (2003) showed, through the use of solitary wave experiment, that the wave drawdown leads to a large sediment erosion around the inland face of structures.

Sediment transport associated with the drawdown process is, in part, caused by the pore pressure variation within the soil, which leads to an increase in scouring because of momentary liquefaction. In the case of tsunamis and other similar extreme flow events, the inundation generates infiltration in the sediment bed, which causes an increase in pressure within the voids of the soil skeleton to balance the pressure generated by the water on the soil surface. Once the drawdown process is initiated, the overburden pressure exerted by the inundation lowers rapidly, resulting in greater excess pressure within the soil than that applied to the sediment bed surface and this difference in pressure causes an upward pressure gradient within the soil skeleton. This pressure gradient results in a net upward force exerted on the bed particles, which effectively reduces their submerged weight (Mason and Yeh, 2016; Sumer, 2014; Sumer et al., 2011). Physical experiments showed that the drawdown sheet flow results in the greatest quantity of sediment transport and this phenomenon was strongest at the location of the still water level; these were both explained by the rapid generation of upward pressure gradient within the sediment bed skeleton (Sumer et al., 2011). The locations near a structure where a decrease of excess shear stress was forming during the drawdown phase corresponded to areas where the greater scouring occurred (Nakamura et al., 2008). Therefore, representing this return phase of the wave is highly important when studying the full extent of the phenomenon of tsunami-induced scour.

Few researchers have studied the variation of pore pressure in sediment beds caused by tsunami-like waves using numerical models, with many lacking comparison with physical experiments (Guo et al., 2019; Scholtès et al., 2015) and with little success when they did (Xiao et al., 2010; Yeh and Mason, 2014). However, all those models were performed on flat beaches and the pore pressure effect on the prediction of scour around a structure caused by tsunami-like waves is yet to be investigated.

Previous authors have shown the accuracy of numerical models to simulate tsunami-like flows (Motley et al., 2016; St-Germain et al., 2014, 2012), and their capabilities and limitations to calculate the resulting scour induced by that flow (April Le Quéré et al., 2020; Chen et al., 2016; Jiang et al., 2015; Larsen et al., 2018, 2017; Liu et al., 2019; Pan and Huang, 2012; Xiao et al., 2010). In this study, a state-of-the-art numerical model (FLOW-3D) was applied to investigate the possible scour error around structures induced by the lack of pore pressure considerations in sediment transport models. The selection of this numerical model was motivated by its proven capability to model scouring generated by complex and transient flows (Alemi and Maia, 2018;

April Le Quéré et al., 2020; Chen et al., 2016; Omara et al., 2019; Vasquez and Walsh, 2009). The numerical model was calibrated and compared with results from experiments performed at the Large Wave Flume (GWK) at the Coastal Research Center (FZK) in Hannover, Germany. The primary objectives of this study are to:

1. Numerically simulate the hydrodynamics of a turbulent bore resulting from a broken solitary wave advancing onto a sloped sandy beach;
2. Discuss the differences between the experimental and numerical scour results and how those differences relate to the spatio-temporal variation in pore water pressure;
3. Investigate the change in turbulence structures around the structure and how it influences the associated scour.

The scope of this study is bounded by the fact that authors present a portion of the results of a comprehensive experimental program which is novel in its scale and whose results were used to validate the numerical model and explain the scour results of the latter. This study does not address the full extent of the experimental program. The primary focus of the study is on the presentation of the numerical model results, which include a first comparison of the turbulence structures forming around a structure during runup and rundown of tsunami-like inundation. Its second focus is on discussing the effects of the experimental pore pressure measurements, which showed a different pattern compared to previous studies on the scour induced by tsunami-like wave.

5.3 Methodology

The novel set of physical experiments, performed at FZK, Hannover, Germany, with unique new experimental conditions allowed for high-quality observations, an accurate understanding of the phenomenon of scour and selected experimental runs all of which were further used to calibrate the numerical model, FLOW-3D (Flow Science, 2019). Further in-depth analysis of the experimental campaign will be the subject of future publications. The numerical model, which was already used to inform and instruct the research planning of this experimental program, supplemented the authors with additional measurements to gain a greater understanding of the flow behavior and increase confidence in the numerical solutions.

5.3.1 Physical experiment

The experiments described in this study were performed in the GWK of the Leibniz Institute Hannover in Germany. This flume is 307 m long, 5 m wide and 7 m deep, which makes it one of the largest of its kind in the world. The specifics of this experimental facility, its wave generating capabilities and technology are described in previous publications (see e.g. Fernández et al., 2014; Gieschen et al., 2021; Rupprecht et al., 2017; Sriram et al., 2016).

5.3.1.1 Experimental setup

Figure 5.1 shows the experimental setup with the installations placed in the flume to perform the experiments. A mobile bed with a slope (1:20), composed of sand with properties listed in Table 5.1, was built at one end of the flume, at a distance of 170 m away from the wave maker's zero position. The beach slope utilized in this experiment was built with the same slope gradient used in the extensive solitary wave runup investigation performed by Synolakis (1987) and as that used in the tsunami scour experiments conducted by Tonkin et al. (2003) and Kato et al. (2000). A

square column manufactured of acrylic material, fixed to a concrete base located 1.5 m below the sand level, with square cross-section and a width (*b*) of 0.6 m was installed into the dry portion of the beach to simulate the scour around a structure at prototype scale. This size of the structure was decided to maximize the realizable scale of the structure, but such that the blockage ratio would not lead to the occurrence of wall effects (Melville and Raudkivi, 1977). During the experiment, the water in the basin was kept at a constant water level (*d*) and a piston-type wave maker produced a solitary wave.

Table 5.1: Sand slope sediment properties

	Value
Hydraulic conductivity (*K*) (cm/s)	0.333
Median grain size (d_{50}) (mm)	0.34
Porosity	0.435
Sorting coefficient ((d_{75}/d_{25})$^{0.5}$)	1.39
Span (d_{90}/d_{10})	3.24

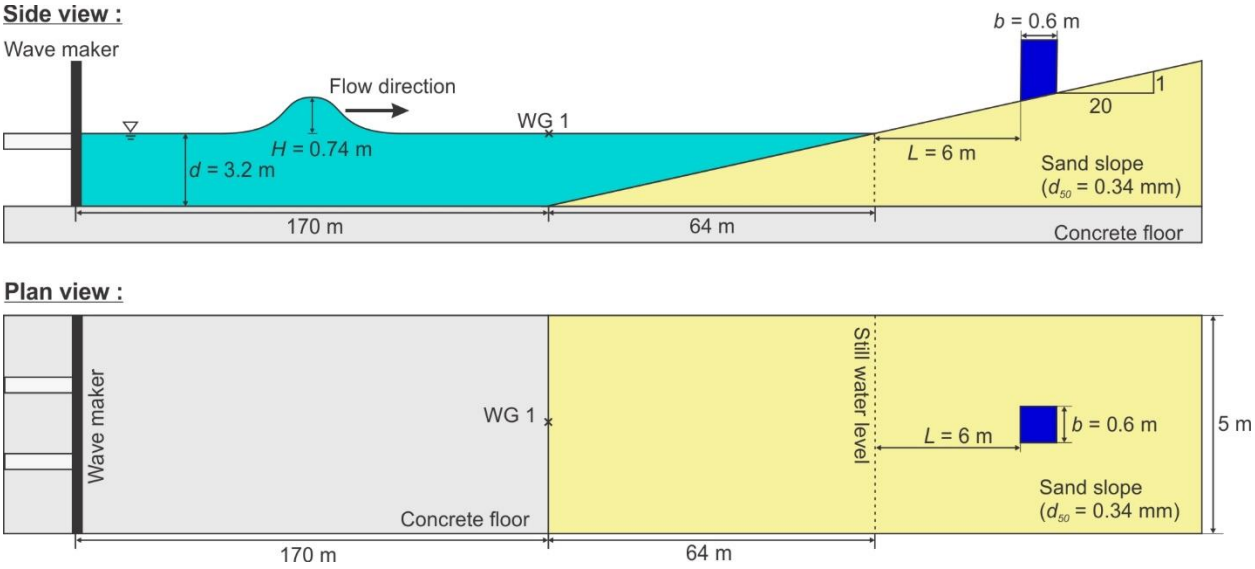

Figure 5.1: Experimental setup with side and plan view, waves propagating from left to right - Large Wave Flume, Hannover, Germany, a joint research facility run between Technische Universität Braunschweig and Leibniz University Hannover

5.3.1.2 Experimental protocol

This paper has a specific focus on numerical modelling and the comparison of the numerical model results with the experimental ones obtained as part of the comprehensive experimental program. A more detailed description of the whole experimental program is presented in a different study, and, as such, only details of some of the experimental tests used in here are presented. The height (*H*) of the solitary wave generated for the validation case was 0.74 m. The undisturbed water depth

(d) in the deep section of the flume was set to 3.2 m, which resulted in a non-linearity parameter (H/d) of 0.231 (within the range of values suggested by Madsen et al., 2008). In order to test the repeatability of the results of the experiments, the test was repeated once and the examination of the time histories of water surface elevations measured by the ultrasonic scanners and scour depth along the column faces yielded standard deviations of 19.9 mm and 8.64 mm, respectively. After each run, the water level in the flume was lowered to allow for a full reconstruction of the beach slope using heavy machinery while the area around the column model and walls was formed manually. The accuracy of the reconstruction work, as well as for a reference data set, the bathymetry and topography of the beach and the square column was measured with a 3D laser scanner (type: Faro Focus 3D, FARO Europe GmbH, Korntal-Münchingen, Germany). After the water level was reset to the appropriate level for the following test, a minimum of 12 hours interval before performing the subsequent test was set to allow the water table in the soil to reach a near equilibrium level before every test series.

5.3.1.3 Scale effects

Scaling the dimensions of the wave and the column with a ratio of 1:20 using the Froude scale (Eq. (5.1)), a value which is a commonly used in the past to scale tsunami experiments (Yoshii et al., 2017), and by using the Dean's scale (Eq. (5.2)) for the sediment size, which is based on the sediment's fall velocity (Dean, 1985; Hughes, 1993; Hughes and Fowler, 1990), results in the experiment being of similar magnitude to real tsunami events such as the 1993 Hokkaido-Nansei-Oki Tsunami (Jaffe and Gelfenbuam, 2007; Titov and Synolakis, 1997) or the 2010 Chilean Tsunami (Earthquake Engineering Research Institute, 2010; Fritz et al., 2011b) (see Table 2). The Froude number (Fr), with the flow depth as characteristic length, an element which is one of the important characteristics of the tsunami inundation at the location of the structure, had a value between 0.5 and 1.5, typical for tsunami inundation (Bricker et al., 2012; Matsutomi et al., 2010). Fr is also used for the determination of many critical cases in tsunami design and can be easily determined in a tsunami prone area using the Energy Grade Line (EGL) method proposed in Chapter 6 (Tsunami Loads and Effects) of the American Society of Civil Engineers (ASCE) 7-16 standard (Robertson, 2020).

$$\frac{L_P}{L_M} = \left(\frac{V_P}{V_M}\right)^2 \tag{5.1}$$

$$\frac{L_P}{L_M} = \left(\frac{V_P}{V_M}\right)^2 = \left(\frac{D_{SP}}{D_{SM}}\right)^2 \tag{5.2}$$

Where L_P and L_M are lengths at prototype and model scale respectively, V_P and V_M are velocities at prototype and model scale respectively, and D_{SP} and D_{SM} are particle grain size at prototype and model scale respectively.

Table 5.2: Solitary wave bore and sediment parameters at prototype scale following a 1:20 Froude scale and Dean's scale

	Model scale	**Froude scale 1:20**	**Dean scale 1:20**
Wave height (H) (m)	0.74	14.8	14.8
Maximum flow depth (h_{max}) (m)	0.50	10	10

Maximum depth averaged velocity (V_{max}) (m/s)	1.5-2	6.7-8.9	6.7-8.9
Median grain size (d_{50}) (mm)	0.34		1.5
Inundation period (T) (s)	20	90	90

During moments when the flow depth was largest, the Reynolds number (*Re*), defined with the structure width as the characteristic length, was between 0.7 x 10^6 and 1.0 x 10^6. Due to the transient nature of the inundation flow, a range of values needed to be defined for *Re*. However, during the early part of the runup and when the rundown was fully developed, which corresponds to the instances when the majority of the scour occurred, *Re* was sufficiently large to mitigate surface tension, viscosity scale effects (Bricker et al., 2015) and the formation of near-structure vortices (Larsen et al., 2017). However, the inundation period, when scaled up to prototype, was an order of magnitude lower than that of a typical tsunami. The Keulegan-Carpenter (KC) number for this case was 45. The KC number calculated from field measurements ranges from 50 to 1500) (D. J. McGovern et al., 2019). At low KC numbers, the flow field around the structure may not exist long enough to contribute to the scour process and the bed requires more time to reach equilibrium. However, the expected flow structures formed around the structure, indicating that the KC number is large enough to be a factor for the scour development. Therefore, the experiment and the numerical model may not have properly reproduced some features, such as the magnitude of the scour depth of *in-situ* sites visited after tsunami events, but the above-mentioned considerations ensure that the mechanisms governing the scour are well represented. In addition, as the numerical model showed good capability to reproduce the experimental scouring observations, the authors are confident that the model can be further used to simulate larger durations in future work.

5.3.1.4 Instrumentation

Three Mic+340/IU/TC Ultrasonic sensors (US) by Microsonic (Microsonic GmbH, Dortmund, Germany) were used to measure the time-history of the water surface elevation at representative locations along the sloped beach, which allowed for the estimation of the flow depth at the structure's location over time. Two US sensors were installed at the same longitudinal axis as the velocity measuring equipment (0.9 m inshore and offshore of the column) while one was installed at the same longitudinal location as that of the center of the column (Figure 5.2(a)). In addition, a 2D scanner (Sick Group, Düsseldorf, Germany, LMS511-20100) was used to monitor the water surface elevation along the beach. A wave gauge (WG) (custom-made, in-house wire-resistance type, FZK, Germany) was installed at the beach toe to monitor the time-history of the water surface elevation (shown in Figure 5.1).

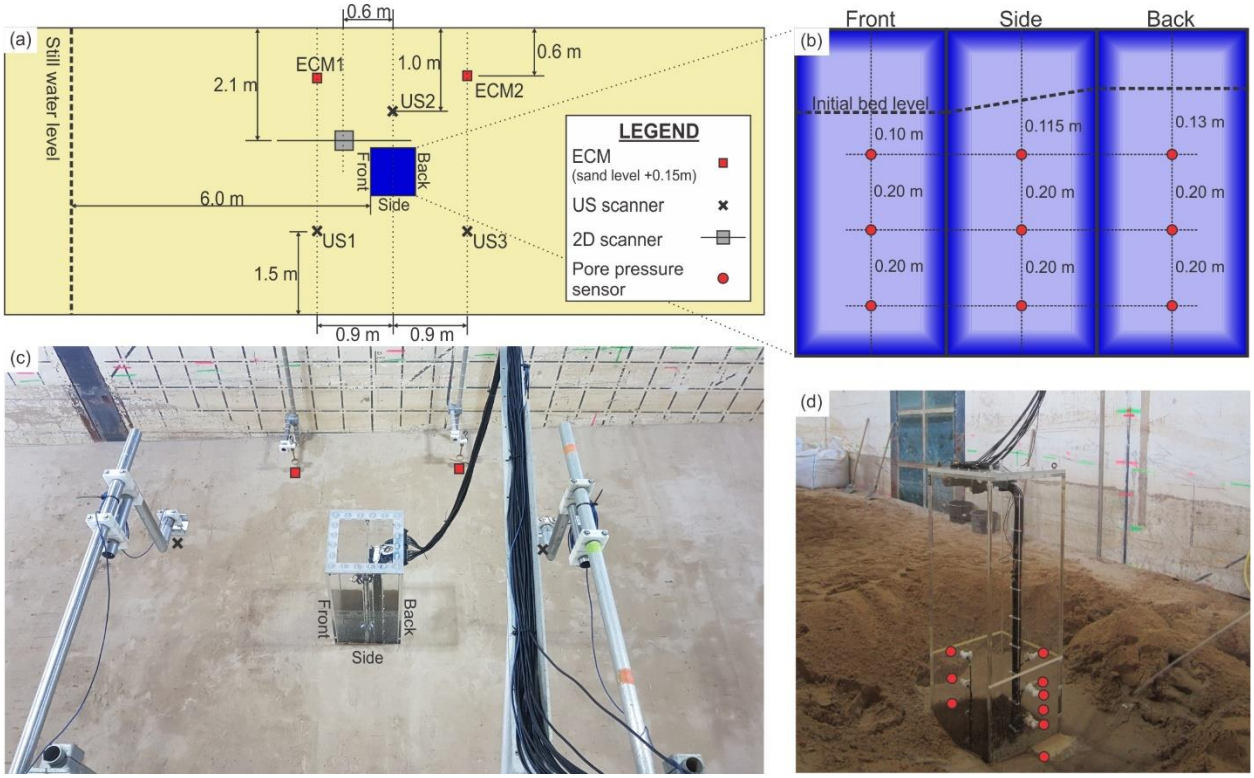

Figure 5.2: (a) Location of the measuring instrumentation; (b) location of the pore pressure sensors on the column faces; (c) photograph of the measuring instrumentation around the column; (d) photograph of the exposed pore pressure sensors during the bed construction

Two electromagnetic current meters (ECM) (HS Engineers, D-18107 Lichtenhagen, Germany, type: ISM-2001) were placed 0.15 m above the initial sand surface. The ECMs were installed 0.9 m upstream and downstream of the longitudinal location of the column's center, at a distance of 0.6 m away from the flume walls.

Fifteen pressure sensors (General Electric, 1830 Druck High Performance Level Pressure Sensors, Fairfield, United States) were installed on the three of the column faces (front, side and back) to monitor the pore pressure change in the sand bed around the structure. On each face, pressure sensors were installed every 0.2 m, with the first one installed 0.10 m, 0.115 m and 0.13 m below the initial surface of the sand for the front, side and back faces, respectively (see Figure 5.2(b)).

The three US, the two ECM and the pressure sensors were all synchronized with the use of an in-house custom made data acquisition system. The sampling rate of all these instruments was set at 1000 Hz.

Throughout the tests, bed elevation change along the walls of the column model was monitored using two cameras (GoPro, United States, type: Hero 8, sampling frequency: 60 Hz) installed inside the column. The two cameras were installed below the initial sand bed level. The two cameras were sufficient to spatially cover three faces of the column (front, one longshore side and back) when recording. After the completion of each run, bed elevation around the column was scanned from several positions using the 3D scanner (FARO Europe GmbH, Korntal-Münchingen, Germany, type: Faro Focus 3D). These measurements resulted in a 3D representation of the final bed topography.

5.3.2 Numerical model

In this study, the FLOW-3D numerical model (Flow Science, 2019) was used to investigate the turbulent structures occurring around a column subjected to tsunami-like flows. The model was also used to evaluate the scour induced by the turbulent flow around the structure and to also evaluate the need to account for pore pressure when estimating scour caused by transient tsunami-like flows. The use of the large eddy simulation (LES) turbulence model in combination with Nielsen's (1992) sediment transport model were found to be accurate for calculating scouring caused by tsunami-mimicking flows around a square columns (April Le Quéré et al., 2020). The numerical model setup and its main equations are further described in this section.

5.3.2.1 Governing equations

FLOW-3D is a non-hydrostatic numerical model that solves the Navier-Stokes momentum equation along the three principal Cartesian directions to simulate flows occurring within its boundaries. The non-hydrostatic solution helps to capture the complex vortex structures such as the ones forming at vertical elements, which are crucial for accurately modelling local scour (Imran et al., 2017; Khosronejad et al., 2012). The continuity and momentum equations were resolved with an implicit method of second order of accuracy (Hirt, 1979). The free surface condition was modelled using the volume of fluid (VOF) method (Hirt, 1981).

5.3.2.2 Sediment transport model

The calculations for the sediment transport were performed by considering separately the bedload sediment transport, using the Nielsen's (1992) model, and the suspended sediment transport, with the formulation of Mastbergen and Van Den Berg (2003). First, the bedload transport model proposed by Nielsen (1992) was developed for coastal-type conditions and was constructed on the principle of that excess shear stress causes sediment transport and is based on Shields parameter. The formulation of Mastbergen and Van Den Berg (2003) was applied to model the suspended sediment transport rate.

5.3.2.3 Computational domain

The computational domain consisted of four consecutive meshes consisting of cubic cells with different grid size (see Figure 5.3). A size ratio of two was applied between consecutive meshes, which was found to minimize the errors when the flow was transitioning from one mesh to the other. The cell size varied from $\Delta_1 = 0.10$ m in the offshore section to $\Delta_3 = 0.025$ m near the column for a total number of approximatively 6 million cells. The offshore limit of the mesh extended to the toe of the sand slope. The computational domain extended onshore to the maximum longitudinal position of the wave runup. The faces of the cells of mesh #3 were chosen to follow the surfaces of the column, which allowed the geometry of the experimental features to be correctly modeled by FAVOR (Flow Science, 2019). The circular dots shown in Figure 5.3 indicate the location of data collection points, which corresponded to the location of the experimental measuring tools described in the Instrumentation section.

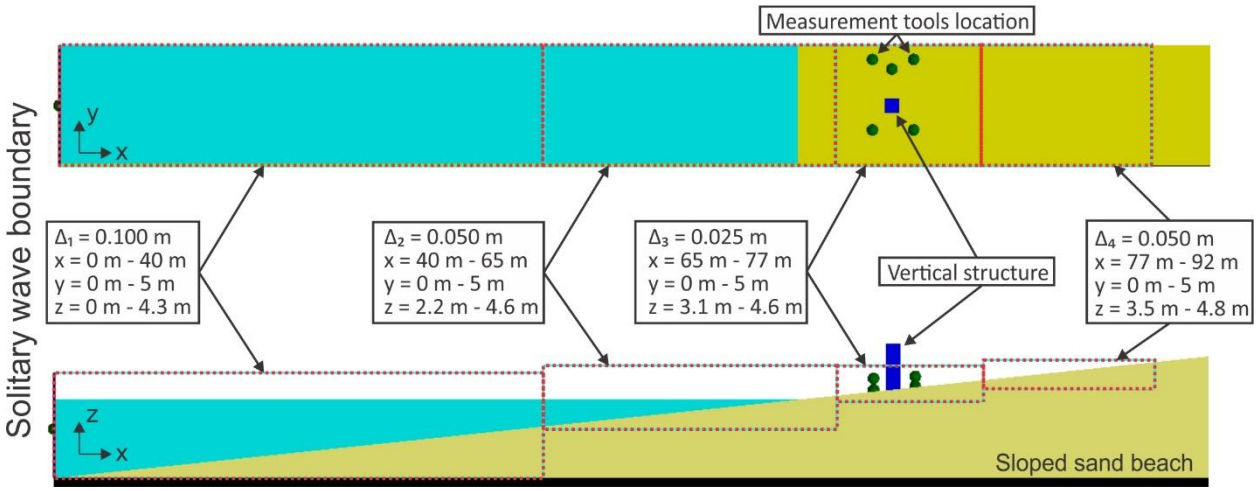

Figure 5.3: Computational domain showing the four regions and their specific grid dimensions

5.3.2.4 Initial and boundary conditions

The initial conditions for the model were based on the parameters of the physical experiment. The still water level in the basin was set to 3.2 m and the solitary wave height was 0.74 m. The slope of the sand bed was of 1:20 with the particle size of the bed material being 0.34 mm, the same as the median grain size (d_{50}) of the sand used in the experiment. The critical Shields parameter selected for the sand used was of 0.036 based on the formulations of Soulsby (1997).

All boundaries in the model, except for the offshore one, as well as the beach slope, were defined as free slip boundaries in order to simulate solid walls. The offshore boundary was defined as a solitary wave boundary, where the free surface elevation and flow velocity imposed at that boundary were calculated with the equation of McCowan (1891) for solitary wave. The beach slope was defined as a rough no-slip boundary with a roughness height of 0.0003 m, which led to an accurate representation of the inundation hydrodynamics.

5.3.2.5 Turbulence model

A large eddy simulation (LES) approach was employed in this study, whereby the turbulence is resolved for eddies larger than the cell size and smaller eddies are replaced by local viscosity based on the assumption that large eddies carry more energy and that smaller ones are similar to local sinks of energy. For additional details on the numerical model's equations, the reader is directed to the FLOW-3D user manual (Flow Science, 2019).

5.3.2.6 Mesh sensitivity analysis

The required mesh sensitivity analysis was performed in a two-step process. The first step was to find the coarsest mesh that does not lead to a change in the results of the wave runup on the sand beach or decay of the offshore wave. This analysis was performed with a 2D vertical mesh without the presence of the column and the model domain was extended 200 m offshore similar to the experimental flume setup (see Figure 5.1). The cell size was varied from 0.2 m to 0.05 m with 0.05 m increments. The results indicated no decay of the offshore wave through numerical diffusion and the time -history of the water surface elevation along the beach from the 0.1 m mesh and the 0.05 m were nearly identical, with an average RMSE of 0.00756 m at the three US locations. However, a 0.05 m mesh was chosen for the beach section to reduce the error induced

by the transition between two meshes in highly turbulent areas. The second step consisted of varying the cell size near the column. The calculated final bed topography was compared between the different simulations to test mesh sensitivity. The cell size near the column was varied between 0.05 m and 0.015 m with increments varying between 0.01 m and 0.005 m. Additional mesh blocks were defined between the 0.05 m meshes and the mesh near the column to reduce the mesh transition induced error. The sensitivity analysis showed that a mesh with a cell size of 0.025 m was optimal for the domain near the column, since the final maximum scour depth was different by 4% and the standard deviation of the scour depth in the vicinity of the column was 0.002 m.

No sensitivity analysis was performed for the time step for this model. However, the time step was automatically varied, based on stability, during the simulation from a maximum of 0.035 s, when the wave was propagating over the basin, to a minimum of 0.0002 s at the instant the broken wave bore collided with the column. The reduction of the time step throughout the simulation was done to allow for a convergence of pressure and to keep the Courant number below 1.0 (Courant et al., 1967), leading to model stability. When possible, the model automatically increased the time step to minimize the total run time.

5.3.2.7 Calibration procedure

The first calibration was performed by adjusting the entrainment coefficient (α_i), which influences the pickup rate of the bed particles in the sediment transport model. The authors elected to tune this coefficient to adjust the scour since it is recommended to use for calibration purposes by the developers of FLOW-3D (Flow Science, 2019) and, as such, this coefficient was varied between 0.012 and 0.15. The coefficient was modified until the maximum final scour depth in the numerical model was of equal magnitude to the one measured in the experiment, with no discrimination for the location of this maximum scour depth. α_i = 0.014 was found to be the most appropriate value in this case.

5.4 Results

The results presented in this section include both experimental measurements and numerical calculations of the flow hydrodynamic and bed elevation changes, and comparisons of those results with analytical solutions.

5.4.1 Offshore wave profile

First, the offshore water surface displacement caused by the solitary wave, calculated by the numerical model and measured in the experiment model, was compared with that obtained using Goring's approximation of the Boussinesq solution (Goring, 1978), which is described by Equations 5.3 through 5.5:

$$\eta = Hsech^2\left(\frac{\beta(ct-x)}{2}\right) \tag{5.3}$$

$$\beta = \sqrt{\frac{3H}{d^3}} \tag{5.4}$$

$$c = \sqrt{g(H+d)} \tag{5.5}$$

where η is the free surface displacement, H is the solitary wave height, β is the wave number, c is the wave celerity, t is the time, x is the longitudinal position and d is the still water depth. The solitary wave in the experimental model was generated by the method of Goring (1978) as described in Schimmels et al. (2016) and the water surface displacement at the wave boundary in the numerical model was calculated using the McCowan's (1891) solution.

The evolution of the water surface displacement presented in Figure 5.4 was taken at WG1, which was located at the toe of the sloped sand beach. Time (t) = 0 s (reference time for the remainder of this manuscript) in Figure 5.4 corresponds to the instant at which the broken bore reaches the location of US1. The results showed that the numerical model represented well the physical model and analytical solution. It also confirms that the paddle wave maker generated the solitary wave appropriately and the wave height decay through viscous dissipation and surface friction in the experimental flume was minimal.

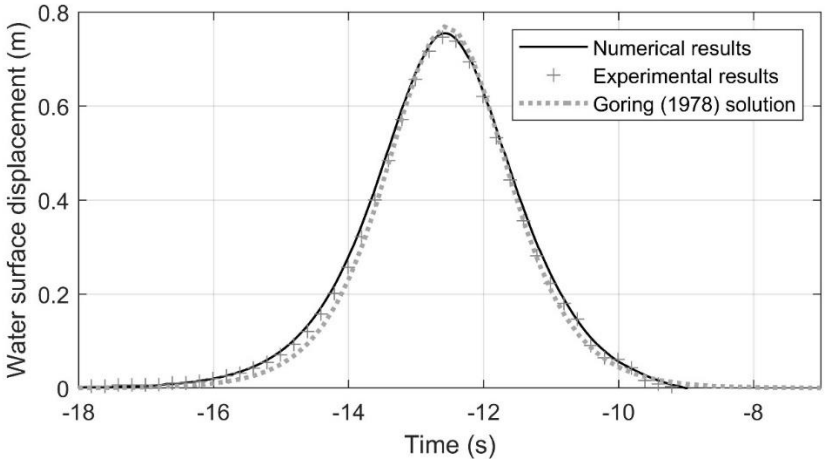

Figure 5.4: Time-history of the water surface displacement caused by the solitary wave at WG1

5.4.2 Post-wave breaking time-history of the water surface

In Figure 5.5, the temporal variation of the water surface elevation on the beach was compared between the observed experimental data, the numerical results and the analytical solution for solitary wave runup on a sloped beach proposed by Peregrine and Williams (2001). Their analytical solutions for the water surface displacement, which equals to the flow depth since the soil was dry at the location of measurement, and the near-bed velocity are Equation 5.6 and Equation 5.7, respectively:

$$\eta = \frac{1}{9gcos\theta}\left(2\sqrt{gA} - \frac{1}{2}gt^{*}sin\theta - \frac{x^{*}}{t^{*}}\right)^{2} \tag{5.6}$$

$$\bar{u} = \frac{1}{3cos\theta}\left(2\sqrt{gA} - 2gt^{*}sin\theta - \frac{2x^{*}}{t^{*}}\right) \tag{5.7}$$

where (θ) is the angle of the bed slope, A is half of the runup maximum vertical reach (taken as 0.62 m), x^* is the longitudinal location with respect to the location of the bore collapse, t^* is the time zeroed at the instant when the bore collapsed.

When the broken wave reached the US positions, large spikes were measured between t = 0 s and t = 3 s, which were caused by the splash induced by the impact of the wave on the column. Since these spikes were judged as non-representative of the real water surface at the start of the wave runup they were removed from the data sets. After the spikes, the flow depth rapidly reached its maximum. At the column location (Figure 5.5(b)), the maximum flow depth reached 0.45 m and 0.48 m in the experiment and the numerical model, respectively. Following the flow depth peak (t = 3 s), flow depth reduced until approximately t = 6 s. Then, the average flow depth plateaued until the final rapid flow depth reduction at t = 15 s. The flow reversal, estimated at t = 7.5 s, represents the instant when the flow velocity at ECM2 reached zero and the flow initiated an offshore movement at that location. The flow depth measured by US1 and US3 showed a noticeably different flow behavior. The presence of the plateau was nonexistent at US1 (Figure 5.5(a)), while its length was enhanced at US3 (Figure 5.5(c)). The total inundation time at the column location was approximately 20 s in both the numerical model and the experimental measurements. Previous studies of solitary wave runup reported similar results of runup flow depth evolution over time (Pujara et al., 2015; Sumer et al., 2011; Tonkin et al., 2003).

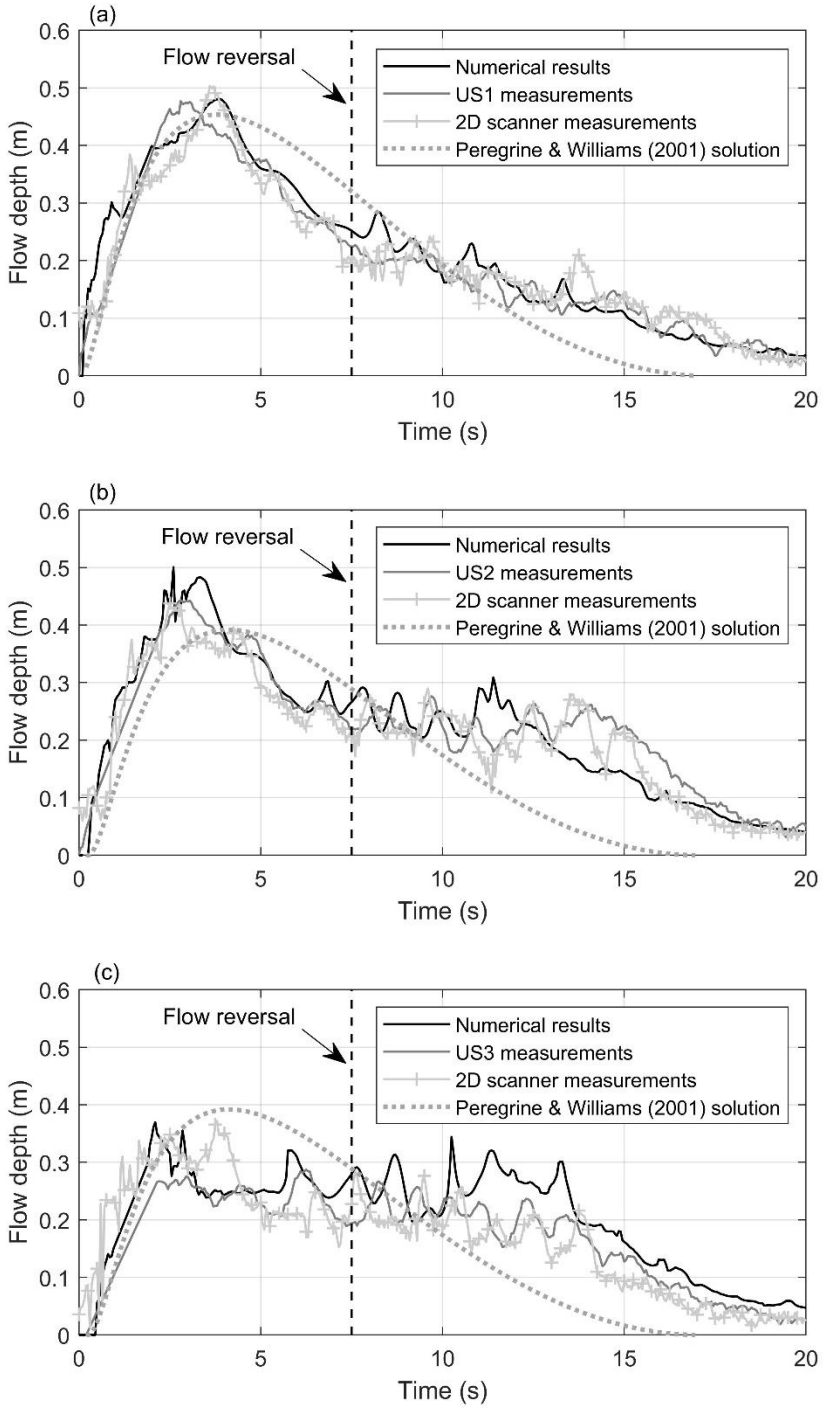

Figure 5.5: Comparison of the numerical model and experimental results of the flow depth at the three ultrasonic sensors: (a) US1 (b) US2 (c) US3

Both the experimental results and the numerical ones showed good agreement with the analytical solution in the early stages of the wave, especially at the location of US1. However, flow depth reduced quicker in the analytical solution after the flow depth has reached its maximum. In addition, the plateau found at US2 and US3 is not found in the analytical solution. The presence

of the structure and the movable bed, which dissipated some of the flow energy, may explain the generation of this plateau. This flow depth plateau can also be observed in the results discussed in Tonkin et al. (2003), indicating that the structure and sediment bed may be causing this flow behavior.

The numerical and experimental flow depth results along the sloped beach showed good agreement. The maximum flow depth and the general wave profile were similar at all three locations. Some ripples produced by the wave-structure interaction were observed in US2 (Figure 5.5(b)) and US3 (Figure 5.5(c)), which were well replicated by the model. The ripples did not completely match, but their period and magnitude were similar between the two. The RMSE was used as a quantitative measure for the difference between the numerical and the US scanners results, which was calculated between t = 3 s and t = 20 s to remove the section with the spikes. The RMSE was of 0.0285 m, 0.0462 m and 0.0485 m for the US1, US2 and US3 respectively.

5.4.3 Post-wave breaking time-history of the flow velocity

In Figure 5.6, the velocity measured by the two ECMs was compared to the velocity calculated by the numerical model at their sampling locations and to the analytical solution of Peregrine and Williams (2001) (Eq. (7)). A delay was observed before the moment at which the first velocity measurement was taken because the sampling location of the ECMs was 0.15 m above the initial bed level to eliminate the bed influence on the measurements. This elevation of the sampling location also explains why the velocity calculated in the numerical model decreased to zero at t = 14 s when the flow depth reduced below 0.15 m. Only a section of the ECM experimental measurements was retained due to the high fluctuations and noise observed in the measurements outside of the interval presented herein. These fluctuations and the inherent lack of accuracy during the measurements during these instants was attributed to the high turbulence in the initial flow and the entrained air in the bore. More significant such fluctuations were measured by ECM1 compared to ECM2, and the interval of low noise data of the former was shorter. However, when comparing those velocity intervals with the numerical model's measurements, good agreement was observed both in the scale of the measurements and the timing of the flow reversal.

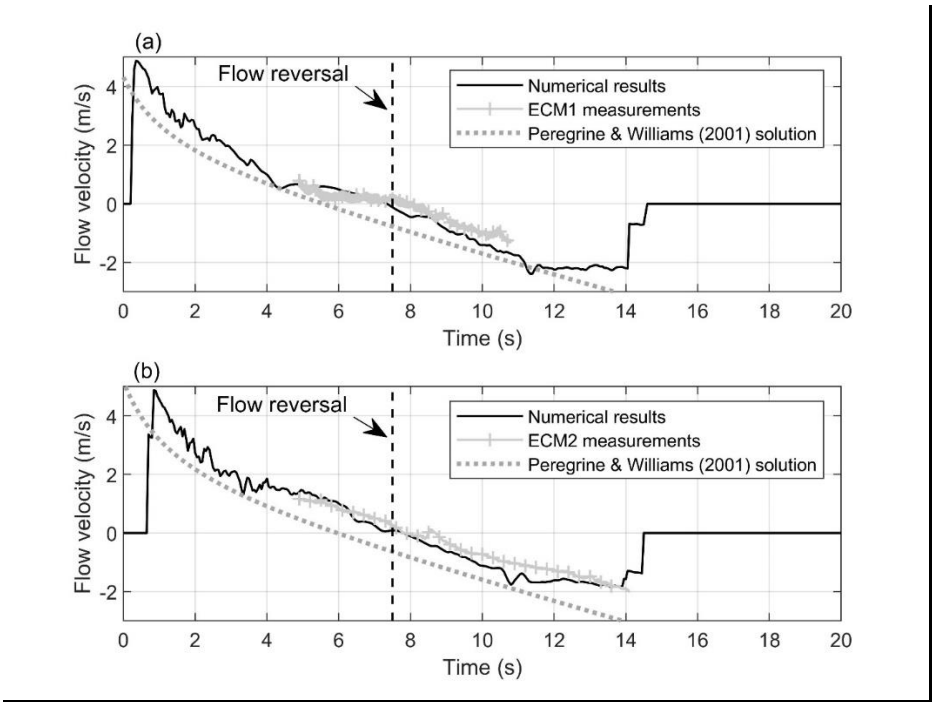

Figure 5.6: Comparison of the flow velocity results in the numerical model and in the experiment at (a) ECM1 and (b) ECM2

Owing to the good agreement between the numerical and experimental results, velocity calculations obtained through the numerical model could be used to gain a better understanding of the hydrodynamic behavior of the wave runup at the structure's location. The maximum velocity calculated from the numerical model occurred when the wave first reached the ECM level. Then, the flow velocity reduced until its reversal at t = 7 s. At this point, the flow accelerated in offshore direction until a maximum velocity of 2.3 m/s and 2.0 m/s was reached for ECM1 and ECM2, respectively. The RMSE for ECM1 and ECM2 were of 0.396 m/s and 0.304 m/s respectively. Good agreement between the numerical, the experimental results, and the analytically calculated velocity was also noted. However, the analytical solution predicted the same velocity behaviors, but occurring about 1 to 2 seconds earlier, which may be due to the lack of energy loss considerations in the analytical solution.

Figure 5.7 shows the time-history of the Froude number (*Fr*) variation. The flow velocity measured by the ECM2 and the flow depth recorded by US3 (co-located longitudinally) were used to estimate *Fr* in the immediate vicinity of the structure's location. These sensors were located 0.9 m laterally inshore of the center of the column. For the numerical results, *Fr* was calculated using the depth-averaged velocity, which explains the larger interval of data than presented in Figure 5.6, at the location of US2. Although the flow and velocity measurements were not taken at the very same location, the temporal variation and magnitude of *Fr* were very similar and confirmed that using the measurements taken at the longitudinal location of ECM2 lead to an acceptable estimation of the *Fr* variation at the column location. This different sampling location also caused a slight shift in the *Fr* (Figure 5.7).

$$Fr = \frac{V}{\sqrt{gh}} \tag{4.8}$$

Where V is the flow velocity, g is the gravitational acceleration and h is the flow depth. The numerical model calculated the Fr for very shallow waters, which explains the very large spike at the wave arrival. After 3 s, the Fr decreased to a value of 0.8 and remained constant for 2 s. Then, Fr further decreased until flow reversal and then increased relatively linearly to a maximum of around 1.5 during the drawdown phase of the flow, a value sustained between t = 15 s and t = 18 s. This result indicates that the run-up phase of the flow can be characterized, for the current conditions, as deeper and relatively slower, while drawdown flow was shallower and faster, which is consistent with previous findings (Liu et al., 2019; Synolakis, 1987; Xiao et al., 2010).

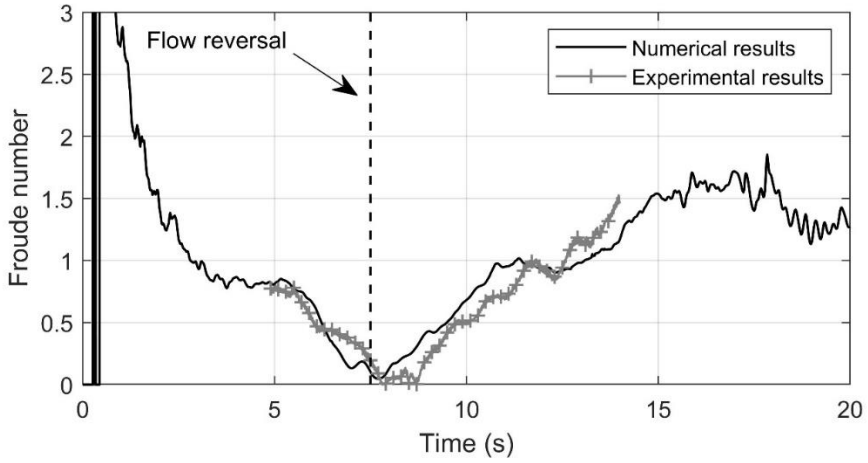

Figure 5.7: Time-history of the Froude number variation at the US2 location (Numerical results) and the ECM2 location (Experimental results)

5.4.4 Turbulent flow structures

The turbulent flow structures were studied for results from the numerical model by using the Q-criterion (Hunt et al., 1988), which is the relative dominance of the rotational vs strain components in a flow and used as a measure of vortical component. Figure 5.8(a) to Figure 5.8(c) show the turbulence structures around the column from three different angles of view at a given instance (t = 4 s) during the runup phase of the wave. Figure 5.8(d) to Figure 5.8(f) show the same, but at an instant (t = 10 s) selected during the drawdown phase. The results showed that the turbulence structures in the runup phase were greater in number, size and vorticity compared to the ones forming during the rundown phase. This highly turbulent energy, and its associated shear stress, were responsible for the rapid scour which occurred during the runup phase. During the drawdown phase, turbulent structures were fewer and lower in energy, which indicates that the scouring observed in the drawdown phase of the wave is associated with a different phenomenon.

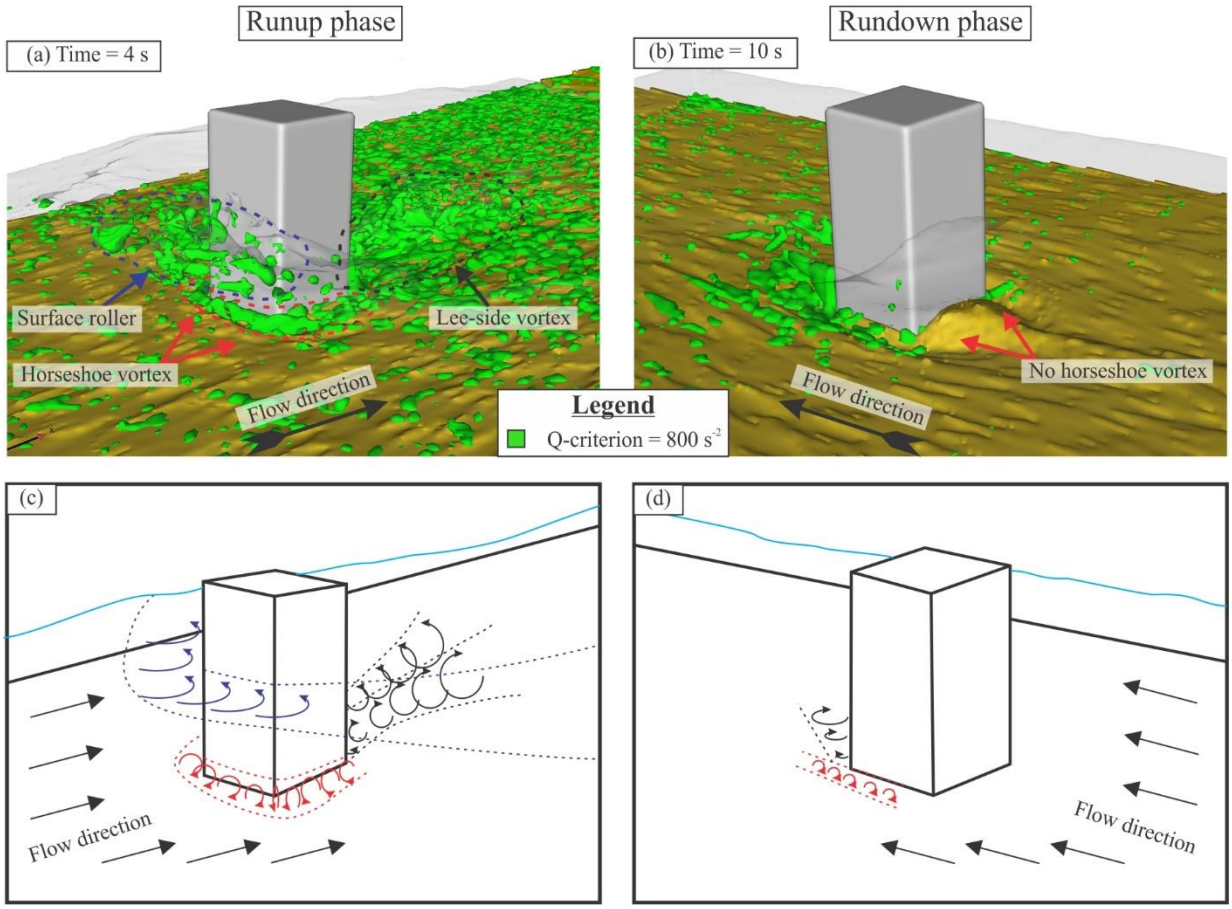

Figure 5.8: Evolution of the numerically-calculated turbulence structures (a,b) and sketches of the turbulence structures (c,d) around the column during the runup phase at 4.0 s (a,c) and the drawdown phase at 10.0 s (b,d)

Figure 5.9 shows stills taken from the GoPro video recordings taken from inside the column. Figure 5.9(a) and Figure 5.9(e) show the turbulent structures forming at the column during the runup, which occur at the same time as those shown in Figure 5.8(a) to Figure 5.8(c). Figure 5.9(c) and Figure 5.9(g) show the turbulent structures forming at the column during the drawdown, which corresponds to the same time as those shown in Figure 5.8(d) to Figure 5.8(f). In Figure 5.9(a), similarly to the numerical results, a horseshoe vortex formed along the bed while sand being suspended was observed at the front face. Vertical vortices (occurring within the blue circles) formed at the corners of the structure. These were also observed in Figure 5.9(c) and Figure 5.9(g) during the drawdown phase. The vertical vortices forming at the corners of the square structure were also observed by McGovern et al. (2019) and were attributed to the large sediment transport near the corners of the structure. The surface roller was observed forming along the front face during the runup (Figure 5.9(a)) and on the back side during drawdown (Figure 5.9(g)).

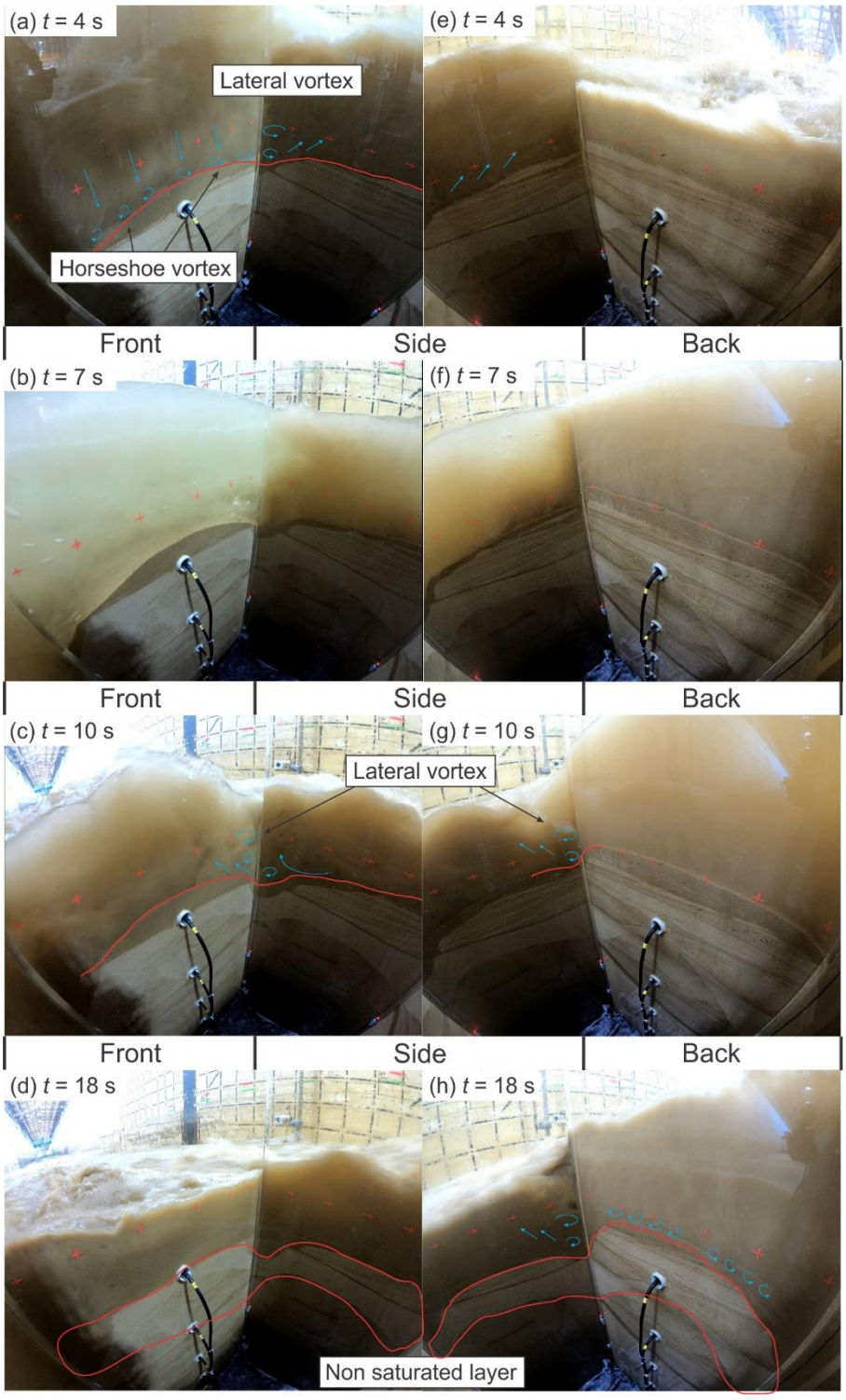

Figure 5.9: GoPro video stills from inside the column showing the front and side faces (a,b,c,d) and the side and back face (e,f,g,h) at 4.0 s (a,e), at 7.0 s (b,f) at 10.0 s (c,g) and at 18.0 s (d,h)

5.4.5 Scouring pattern and evolution

Three different representation of the scour results were compared between the numerical model and the physical experiment: (1) the final beach topography in close vicinity of the column, (2) the final bed elevation along the faces of the structure, and (3) the scour depth evolution over time at the center of the column faces.

The comparison of the final bed elevation change in both the experimental tests and the numerical model are shown in Figure 5.10(a) and Figure 5.10(b) respectively. The difference between the two topography results (numerical and experimental) is shown in Figure 5.10(c) (red indicates more scour in the numerical results and blue indicates more scour in the experimental results). The numerical results and the experimental results indicated similar patterns of erosion. The deepest scour was found at the front and back corners of the structure. Bed was eroded at all the faces of the structures, except for the center of the back face where accretion was observed. A large quantity of volume of accreted sand was found 0.5 m offshore and inshore of the column for both the numerical and experimental results, with more accretion in the case of the numerical one. The final maximum scour depth was matched in both, since it was used as a comparison point for the calibration exercise. However, the width of the scour was significantly larger in the experiment when compared to that observed in the numerical model, which may indicate that the rotational flow patterns at the onshore corners were less developed in the numerical model or indicate the presence of a different scour process. The accretions onshore of the column were much narrower in the numerical model, while the size and magnitude of the accretion offshore of the column were similar in both models. The numerical model showed an asymmetric scour pattern.

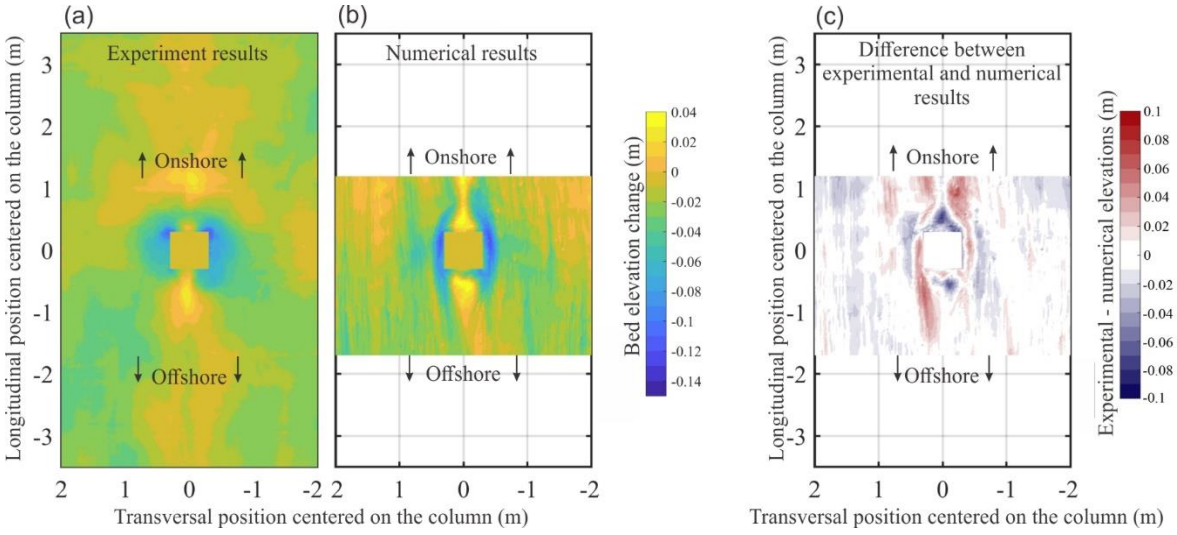

Figure 5.10: Comparison of the final bed topography: (a) experimental results, (b) numerical results and (c) the difference between the experimental results and the numerical ones (red – larger erosion of numerical calculation, blue – larger erosion of experimental

The final bed elevation change at three faces (front, side and back) of the column was compared between the numerical results and the experimental results in Figure 5.11. The results at the front (Figure 5.11(a)) showed a high agreement. The maximum difference between the two can be found near the corners, where the RMSE was 0.0107 m. For the sides (Figure 5.11(b)), the two lateral sides were shown for the numerical model, but only one side was measured during the experiment.

The two sides, in the numerical results, show again the asymmetry of the simulation. The experimental results followed a similar trend as the numerical results. The RMSE between the experimental results and the average of the two sides was 0.0131 m. The results at the back (Figure 5.11(c)) of the column point to significant differences between the numerical and experimental results. In fact, the bed in the experiment has reduced in elevation across the entire face length and the maximum scour depth was found at the corners of the back face. Contrary to this, accretion was shown to have occurred along most of the face in the numerical model. The RMSE between the two results was 0.0407 m, which indicates poor replication of the scour at the back face.

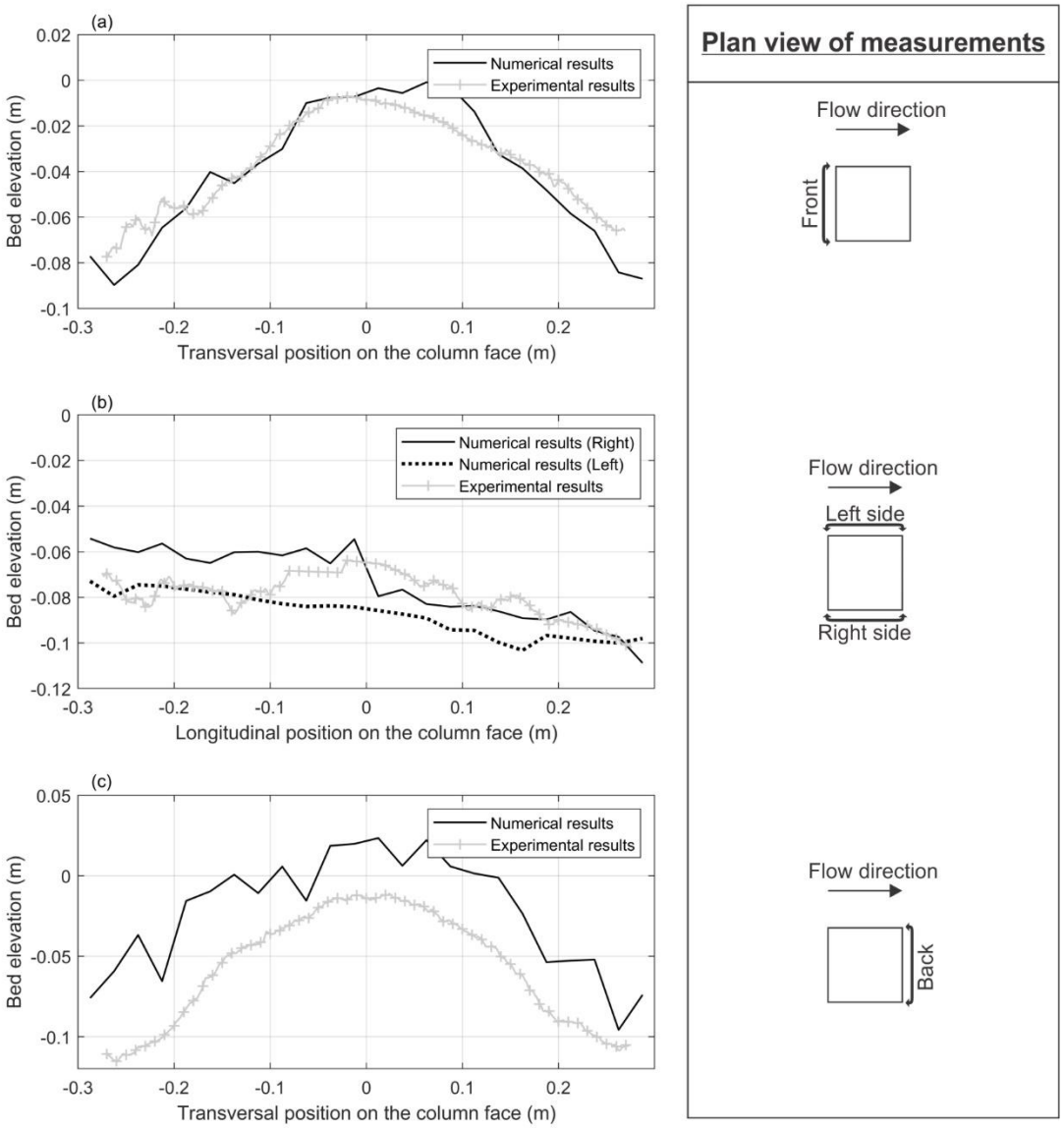

Figure 5.11: Final bed elevation comparison between the numerical and the experimental results at the (a) front face (b) side face (c) back face

The time-history of the scour evolution at the center of the structure's sides, where the pressure sensors were located, was monitored throughout the experiment to link it with the change in pore pressure over time (Figure 5.12). At the front face (Figure 5.12(a)), the pattern of bed elevation change was similar between the numerical results and experimental results. The bed rapidly scoured to an elevation of -40 mm and -35 mm in the numerical results and the experimental results, respectively. Then, the bed stabilized until the end of the drawdown phase, when material deposition led to an increase in bed elevation, which was lesser in the numerical model. A certain lag in the pressure sensor readings (see Figure 5.12(b)) indicated a downward pressure gradient during the runup and an upward pressure gradient during the drawdown (t = 5 s to 20 s), which would indicate a decrease in the effective stresses during drawdown. However, no scour linked with this reduction in effective stresses was observed during the drawdown at the front face.

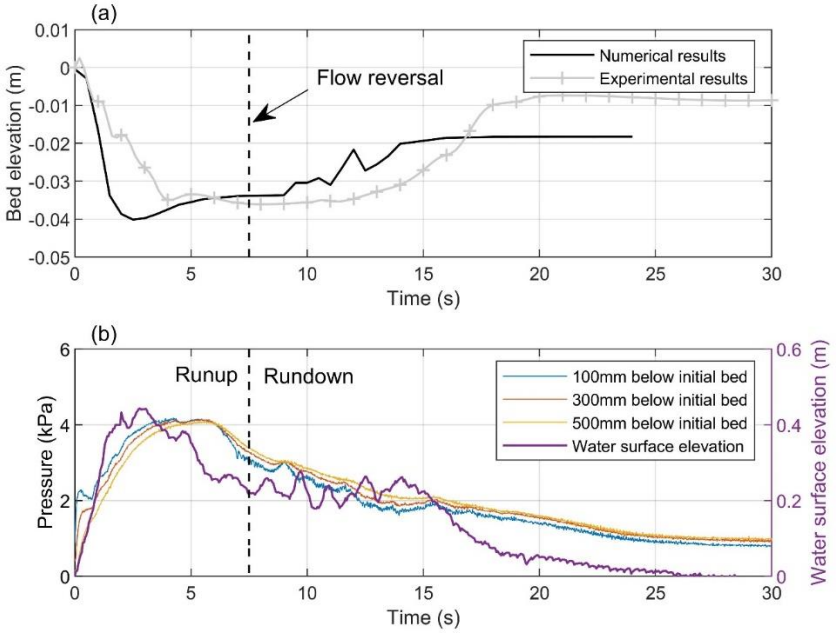

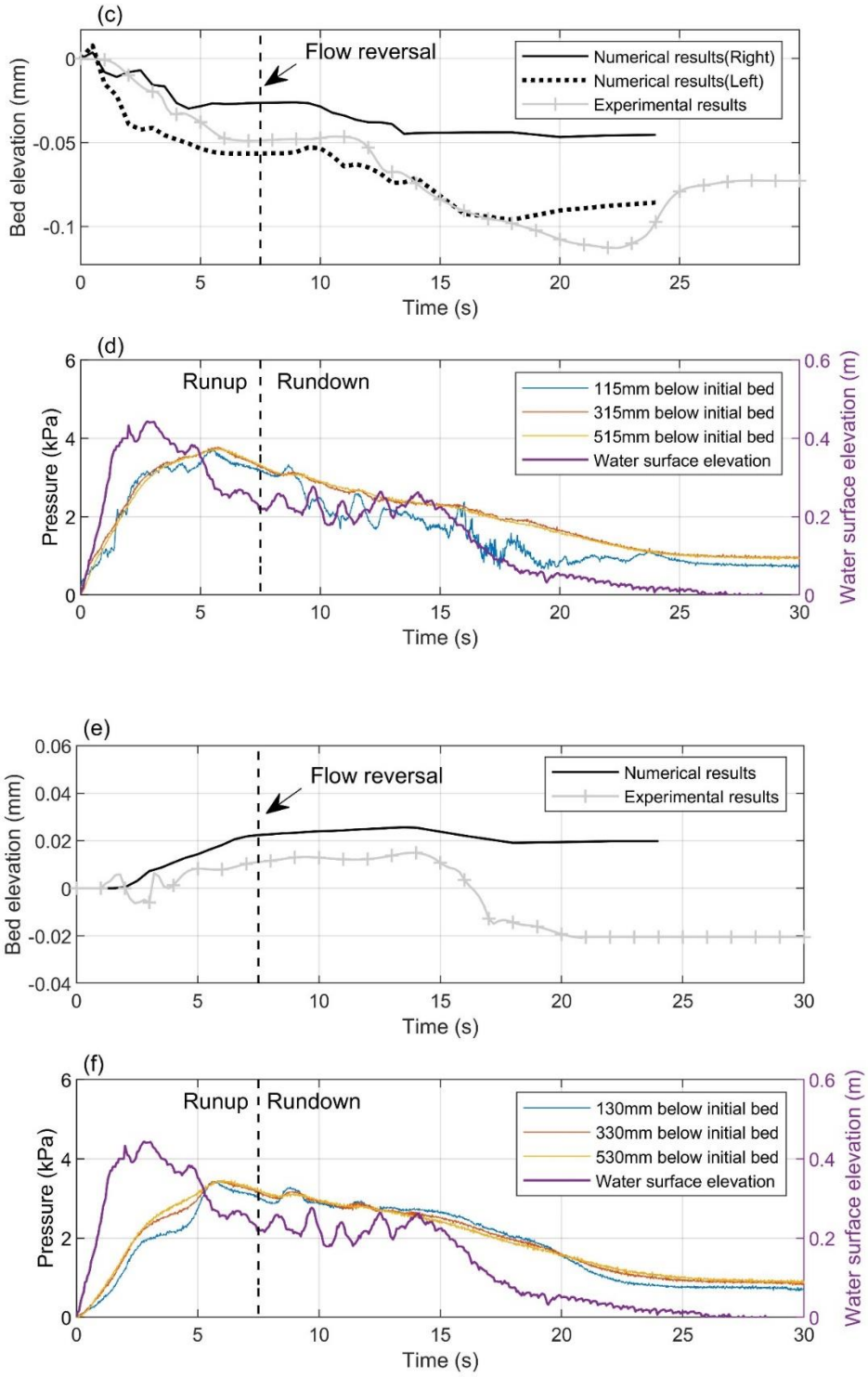

Figure 5.12: Temporal evolution of the bed elevation and the pore pressure at the center of the (a,b) front face (c,d) side face (e,f) back face

Similarly, on the sides, the pattern of scour evolution was well represented by the numerical model, especially when compared to the left side, but a certain difference of elevation was observed at the

end of the measurements (Figure 5.12(c)). Between t = 18 s and t = 24 s, some scour followed by a rapid deposition of sediment was observed in the experimental results, which led to the final scour depth to be lower than that calculated on the left side with the numerical model, but greater than that on the right side. This deposition occurred after the last data point for the numerical model, but no such deposition was observed when testing longer numerical test durations. The pore pressure variation (Figure 5.12(d)) was not as conclusive as on the front, and does not indicate any sign of significant decrease in effective stress. Also, the shallowest pressure sensor (115mm below the initial bed level) indicated fluctuations in the results which may be due to the fact that the bed level was approaching its sampling elevation.

On the back side of the structure (Figure 5.12(e)), before t = 14 s, the scour pattern was well replicated with a certain difference in magnitude from the experimental results. After this instant, the numerical model predicted a small erosion at the back face. On the other hand, the experimental results indicated rapid scouring for that same period. The rapid scouring experienced at that instant could be attributed to the presence of an upward pressure gradient in the soil generated by the rapid reduction in the flow depth. A phenomenon that was not accounted by the numerical model in the calculation of sediment transport. However, the experimental measurements of pore pressure did not point towards such an upward pressure gradient. In fact, the pressure at the shallowest pressure sensor remained greater than of the other two pressure sensors for the majority of the drawdown phase (t = 7 s to t = 20 s in Figure 5.12(f)). Therefore, if an upward gradient formed within the soil due to the rapid lowering in flow depth, its effects were not measured deep in the sand. A discontinuity in the pore pressure may have been created by the fact that the water infiltrated only a few centimeters in the soil and never reached the shallowest of the pressure sensors on the back side and the sides of the column. In Figure 5.9, it can be observed that a layer of sand remained unsaturated during the test. This is different than the experiment of Tonkin et al. (2003), where the soil was fully saturated because the column was installed at the still water level and a strong upward pressure gradient was noted during the drawdown of the wave.

5.5 Discussion

The accurate representation of the hydraulic bore by the numerical model helped to obtain good agreement of the scour results between the numerical results and the experimental ones on the front and sides of the structure. However, the magnitude of the final maximum scour depth (0.15 m) was much lower than the one predicted by the ASCE 7-16 Chapter 6 (0.528 m) for this situation (see Figure 5.G12-20 in Robertson (2020)). As expected, it indicates that the short inundation period, which was an order of magnitude shorter than that for a typical tsunami, has most probably led to less sediment scour than would be experienced during a tsunami inundation at a prototype scale. However, by exclusively considering the flow depth, and ignoring factors such as inundation duration and grain size scaling, when predicting the scour, the method proposed by Robertson (2020) was developed conservatively.

In addition, the scour at the back of the structure was significantly underestimated by the numerical model. The sediment transport model was only considering flow patterns when calculating the sediment transport because the calculations are based on shear stresses calculated at the bed level. During the runup phase, the flow near the structure was characterized by strong turbulent eddy structures, which allowed for a more accurate calculation of the sediment transport in the numerical model since the latter accounted for it when calculating sediment transport. However, during

drawdown, most of the turbulent structures were found on the lee side of the structure and exhibited lesser turbulent energy, which has not led to sediment transport on the back side, as was however observed in the experiment.

The lack of scour produced during the drawdown on the back side of the structure indicates that a different mechanism, not considered by the numerical model, was influencing the sediment transport during this phase of the wave. The rapid lowering of the flow depth created a reduction in overburden pressure on the surface of the soil and should have led to an upward pressure gradient in the soil skeleton during the drawdown phase, especially at the back side of the structure. However, the measurements from the pressure sensors within the soil (as seen in Figure 5.12(f)) do not support this observation made during the comprehensive physical experiment conducted by Tonkin et al. (2003). Although similar, the present experiment and the experiment of Tonkin et al. (2003) have a few differences. Both experiments studied erosion around a vertical column on a sloped sand beach using tsunami-like solitary wave as a forcing hydrodynamic event. However, some of the conditions in the current experiments were quite different from those of Tonkin et al. (2003), and they may have affected pore pressure measurements:

1. The shape of the column was different (squared column in the present experiments, compared to a round column).
2. The incident wave height was 2.5 times higher than the one used by Tonkin et al. (2003), which should have led to an increase in pore pressure gradient (Abdollahi and Mason, 2020) because the resulting increased flow depth over the shore increases the pressure on the soil surface.
3. The column used in the present study was placed on the beach at a distance of 6 m from the still water level, instead of being installed at the still water level. The placement of the column further up the shore translates into reduced flow depth at the column and the associated hydrostatic pressure on the soil surface, which should have decreased the chances of an upward pressure gradient forming in the soil (Sumer et al., 2011).

The authors judged that the fact that the column placed on dry land, in combination with the smaller grain diameter, were the key differences that led to the upward pore pressure gradient not forming deep in the soil. In fact, it was noted that a layer of sand remained unsaturated in the soil (see Figure 5.9(d) and Figure 5.9(h)) and the water only infiltrated a small distance in the soil due to the low hydraulic conductivity of the soil skeleton. This layer of unsaturated soil was not present in the experiment of Tonkin et al. (2003) since the column was installed at the still water level. In addition, to the authors' knowledge, most previous studies that explain theoretically the phenomenon of momentary liquefaction caused by tsunami have done so with the assumption that there is an uniformity in water content within the soil pores and that this water content is high (Guo et al., 2019; Mason and Yeh, 2016; Scholtès et al., 2015; Xiao et al., 2010; Yeh and Mason, 2014). Although this layer of unsaturated soil prevented the pore pressure to increase deep in the soil, an upward pore pressure gradient may have occurred near the bed surface. Due to the placement of the pore pressure sensors in the unsaturated layer of soil, this could not be observed.

This phenomenon, however, was not accounted for in the numerical model as the latter is modelling the soil as one single phase, effectively neglecting an important process. There is further need to couple the fluid domain (at least one-way) to a model that is capable of solving the soil-governing processes.

5.6 Conclusions

A numerical model was successfully applied to simulate the results of a large-scale experiment of a solitary wave impacting a vertical structure installed on a sloped sand beach. The numerical model showed an accurate representation of the flow characteristics of the wave runup on the sloped beach. The calculation of the final scour accurately represented the experimental results on the sides and front of the structure, but the numerical model failed to predict the deep scour holes that formed near the back corners or the structure. This discrepancy was found to be due to the lack of pore pressure gradient consideration in the calculation of sediment transport in the numerical model. The latter used the shear stresses to model the scour of the bed by the flow and the associated turbulent structures. This resulted in the numerical model accurately representing the scour during the runup phase of the wave. However, during the rundown phase, when the back of the structure has shown significant scour, the model failed to predict it. This was hypothesized that it is partly due the fact that the significant influence of the decrease in effective shear stress of the surface's soil is not taken into account in the numerical model.

Chapter 6: Influence of Macroroughness on Tsunami Scour of Coastal Structures

6.1 Abstract

The extreme tsunamis of the past two decades (e.g., the 2004 Indian Ocean Tsunami, the 2010 Chile Tsunami, and the 2011 Tohoku, Japan Tsunami) have proven the devastating force of such extreme hydrodynamic events. Flood-induced scouring leading to infrastructure damage has been found to be an important phenomenon during post-tsunami forensic investigations, and previous research focused on investigating the complex process of tsunami-induced scouring utilized around isolated single columns or horizontal structures. However, given that coastal cities often have complex arrangements of multiple structures, and narrow, often-crammed paths between edifices, the channels between these structures concentrate the flows, which results in an enhancement of scour risk compared to isolated structures. This research is an attempt to inform the scientific community regarding the amplification of scour due to flow concentration due to the presence of macroroughness elements offshore of the design structure. The authors employed a comprehensive physical experimental method for this study. The experiments were performed in the new Dambreak Flume at the University of Ottawa, Canada. The results from this study demonstrate that factors such as the flow conditions and the distance between the macroroughness elements influence the effect of the macroroughness elements upstream on the increase of scour at the design structure.

6.2 Context and research needs

Post-tsunami forensic investigations over the past few decades have highlighted the devastating impacts of such extreme hydrodynamic events. To reduce the impacts of similar natural phenomena in the future, scientists have studied these waves, their hydraulic properties, and their effects on structures. The focus of this study is on one of those effects: scouring. At present, many parameters that dictate scour that are linked with extreme inundations, such as tsunamis, are still unknown. One parameter for scour that has yet to be investigated by the scientific community is the effects of neighbouring structures around the design structure. Field examples of multiple structures, focusing on the flow between them, which leads to enhanced scour, can be found in existing forensic tsunami investigations (Chock et al., 2013; Wilson et al., 2012; Yeh et al., 2013).

Yeh et al. (2013) documented a case of two large tsunami-resistant hospital buildings that generated local flow concentrations between them which led to failure of all the structures on the onshore side of the gap between the buildings. These two large buildings can be considered as "macroroughness elements" that concentrated the flow both between and downstream of them. Although hydrodynamic forces were likely responsible for the failure of most of the structures on the onshore side of the hospital buildings, the authors hypothesized that there was a greater risk for scour at the location of the failed structures due to the two neighboring tsunami-resistant buildings.

Tonkin et al. (2013) separated tsunami-induced scour into four different categories: (1) local scour, which occurs near a vertical structure; (2) generalized scour, which occurs over a large area; (3)

overtopping scour, which occurs when a flow overtops a horizontal structure; and (4) channelized scour, which occurs when a flow is concentrated or redirected. The specific case of upstream macroroughness elements focusing the flow onto a downstream single structure is investigated in the present study. This case can be argued as being a combination of both local scour (1), because of the shape of the columns, and channelized scour (4), because of the focused flow between the two upstream macroroughness elements.

Steady flow studies have highlighted the risk of increased scour due to the narrow spacing between structure elements (Beg, 2010; Hamidi and Siadatmousavi, 2018; Hosseini and Amini, 2015; Kim et al., 2014; Zhang et al., 2017). Hosseini and Amini (2015) and Hannah (1978) found that columns that are placed in a staggered arrangement lead to an increase of up to 25% in scour depth at the downstream column when subjected to a steady flow. Meanwhile, Zhang et al. (2017) investigated the case of two upstream macroroughness elements concentrating a flow onto a downstream column of similar size, and their results show that while this arrangement leads to less scouring around the downstream column when the columns are close to one another, it leads to increased scour when the distance between the columns is set at 3 times their diameter. These observations give clues that upstream macroroughness elements are likely to lead to an increase in scouring around a downstream structure when subjected to a tsunami-like wave.

Channelized scour, also referred to as constriction scour, has been researched in steady flow conditions, in contrast to tsunami flow situations. Channelized scour occurs when abutments spanning a long section of a river reduce the effective width of that river (Gill, 1981; Laursen, 1963). The flow's streamlines are concentrated in the contraction, leading to more shear stress across the entire width of the bed (Ettema et al., 2010; Sturm et al., 2011); however, if the river is wide, only local flow accelerations and scour are observed near the sides of the constricted reach (Lim and Cheng, 1998). Channelized scour is also contingent on the assumption that the transition between river reaches with different widths is "long". When the transition occurs over a short distance, large scouring at the abutments can be observed, which is driven more by turbulence than by unidirectional flow acceleration (Ballio, 2004; Ettema et al., 2010; Melville, 1997). This turbulence indicates that a local scour process is responsible for the displacement of bed material, rather than channelized scour (Ettema et al., 2006b, 1998). Differentiating between the two scour processes is important when analysing the case studied here.

Most tsunami scour research has been performed with observations from post-tsunami forensic investigations and using laboratory experiments or applying numerical models. When investigating the scouring mechanisms of tsunamis using the latter two methods, the majority of cases considered structure-less beaches, horizontal structures (such as seawalls), or individual vertical structures.

Only a limited number of studies have investigated the interaction between multiple structures subjected to tsunami flows. Nouri et al. (2010) investigated the amplification of the flow velocity and hydrodynamic forces on a standing column caused by an upstream contraction. The contraction in this case was built out of wood studs attached to the sidewalls of a flume, which rapidly reduced the flume's effective width. Thomas et al. (2015) similarly investigated the amplification of flow energy due to an upstream contraction by using a series of vertical square columns to channel the flow onto a downstream column of the same size. In both cases, an increase in flow velocity and hydrodynamic force was noted downstream of the contraction. Furthermore, Thomas et al. (2015) noted a sheltering effect leading to a reduction in flow velocity and force

when the wake clearance angle (β) between the macroroughness elements and the downstream column was less than 10º. The results of these two studies were used to inform the design considerations for tsunami flow amplification caused by the constriction effect of shoreward structures, as found in ASCE 7-16 Chapter 6, Tsunami Loads and Effects (Robertson, 2020). However, no constriction effect relating to tsunami scour is mentioned in this building standard.

Le Quéré et al. (2021) utilized a numerical model to investigate the effect of lateral spacing of two columns on local scouring induced by a tsunami-like wave, and their results indicated that the addition of a second column installed on the same transversal plane leads to an increase in scouring. The increase in scouring was attributed to the increase in strength of the near-column flow turbulence, as well as because the effect of the second structure was greater when the spacing between the columns was smaller and when the flow depth at the columns was greater. No additional studies have investigated the effect of neighboring structures on tsunami-induced scouring.

The objectives of this research were to recreate tsunami flows in a novel hydraulic flume setup and to investigate the effects of upstream constriction on scouring around a downstream-positioned column. In addition, the effects on scour amplification of the spacing between upstream macroroughness elements (W_c), the longitudinal distance between the macroroughness elements and the design column (L), and the incoming wave properties (h_0) caused by upstream constriction were investigated.

6.3 Methodology

The authors elected to study the phenomenon of scour caused by upstream macroroughness elements through a comprehensive physical experiment. This section describes the method used in the experiment as well as the equipment used, the setup tested, and the scaling considerations by the authors.

6.3.1 Dambreak flume

The comprehensive experimental program discussed herein was carried out in the newly-built dambreak flume of the Hydraulic Laboratory of the University of Ottawa, Canada (see Figure 6.1). The dimensions of the flume were 30.3 m in length, 1.5 m in width, and 1.5 m in depth. A large piston-activated swing gate was utilized to retain water upstream of the flume (see Figure 6.2(a)). The gate was then opened rapidly to obtain a sudden release of water in order to generate the dambreak bore. Although it is not physically feasible to achieve an instant release of impounded water, the gate's opening time was below the gate removal time proposed by Lauber and Hager (1998) ($T_0 = t_0\sqrt{g/h_0} < 1.41$), which has been widely used to evaluate the rapidity of gate-opening in previous dambreak experiments. Where T_0 is the non-dimensional gate opening time, t_0 is the dimensional gate opening time, and g is the gravitational acceleration. Three wave absorbers were installed in the flume upstream of the swing gate in order to attenuate the inevitable negative wave generated after the dambreak bore rushed up the approach slope. Their porosity was 0.5, and a thick fabric was attached to the upstream-most wave absorber to further reduce the wave energy.

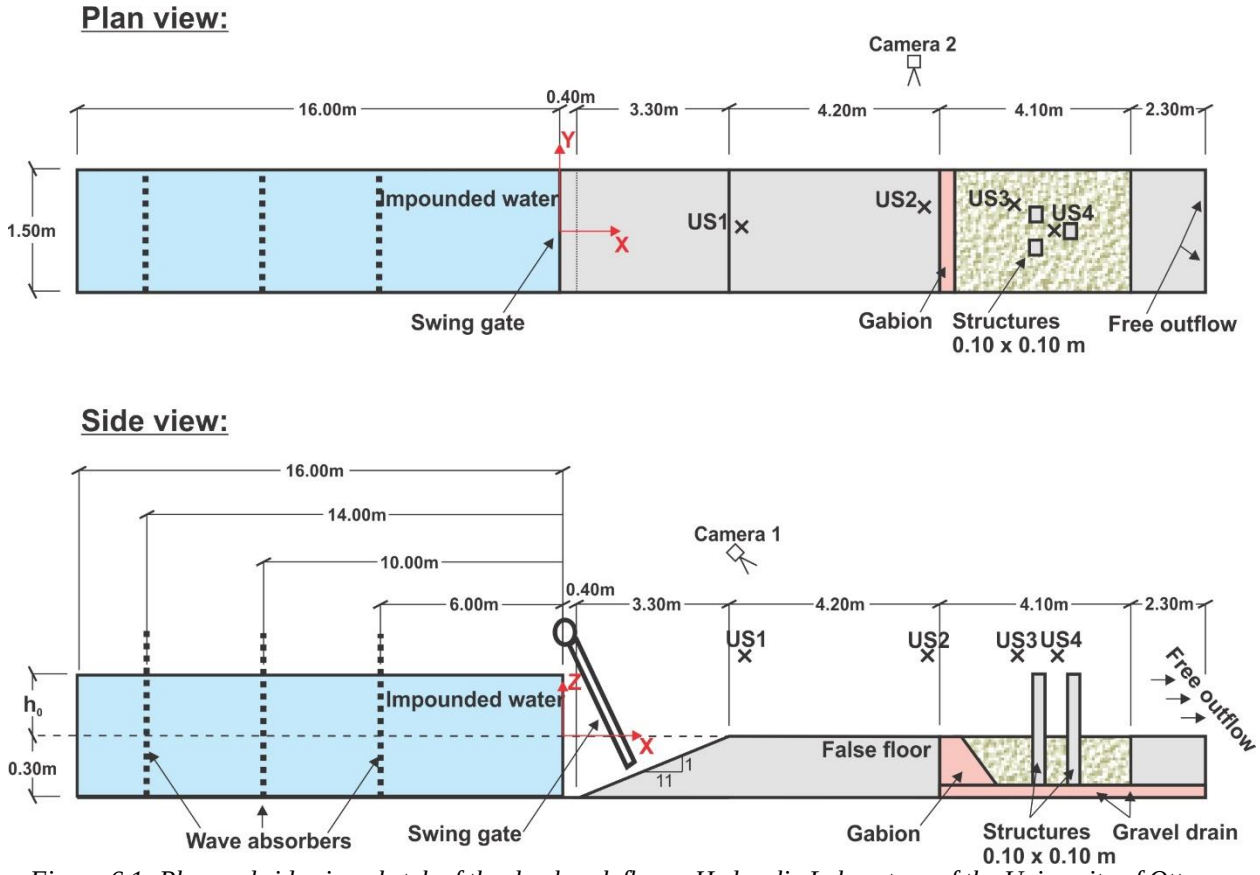

Figure 6.1: Plan and side view sketch of the dambreak flume, Hydraulic Laboratory of the University of Ottawa, Canada

In order to install a sand bed area to evaluate scour, the bed of the flume was raised by the installation of a false floor section downstream of the swing gate. Starting from the upstream end of the false floor, a 3.30 m-long approach slope (11:1) section was followed by a 4.20 m-long horizontal section. This section of the false floor was constructed with steel plates supported by cinder blocks. The sand bed section was protected at the upstream end by a 0.20 m-long gabion to reduce the inevitable scour that would occur at the transition between the solid false floor and the sand section. The sand bed section ($d50$ = 0.1 mm) was 3.9 m in length and was retained at the downstream end by a concrete weir. A gravel drain was installed below the sand bed and the downstream weir to allow for the drainage of excess water that would infiltrate the sand bed during the tests.

Figure 6.2: Pictures of experiment installation: a) swing gate system; b) false floor installation; c) measurement equipment and column support system

6.3.2 Instrumentation

Four (4) ultrasonic sensors (MassaSonic, M5000, Hingham, United States; accuracy: 1 mm, range: 0.1 m to 1.0 m) were installed at strategic locations along the flume to monitor the water surface elevation. The locations of the sensors were as follows: (US1) at X = 4.5 m; (US2) at X = 7.5 m to monitor the flow behavior on the horizontal section; (US3) at X = 10.0 m to monitor the flow behavior just before the macroroughness elements; (US4) at X = 10.85 m to monitor the runup at the upstream face of the design column. The positions of the ultrasonic sensors were as shown in Figure 6.1.

Analog voltage signals from the ultrasonic sensors were converted to digital format with a data acquisition system (HBM, MX1601B, Darmstadt, Germany, rate = 200 Hz) which offered 16 individually configurable channels.
Two (2) cameras were used during the experimental campaign. Camera 1 (GoPro, HERO 7, San Mateo, United States; rate: 240 FPS, resolution: 720p) was used to evaluate the velocity of the bore front on the flat section of the false floor. The false floor was painted white, and black lines were drawn every 0.2 m to allow for tracking of the bore front position. The times of the bore passage at each line were used to determine the speed. Camera 2 (Apple, iPhone 7, Cupertino, United States; rate: 240 FPS, resolution: 720p) was used to estimate the water surface velocity by the use of hollow plastic balls 5 mm in diameter released in the reservoir prior to each test. The difference between their passage time at the lines with positions of X = 7.40 m and X = 7.60 m was used to estimate the velocity of the balls at the location of US2. The velocity measurements from the camera were synchronized with the data from the ultrasonic sensors by estimating the time of arrival of the bore front at the location of US2. The positions of the two cameras were as shown in Figure 6.1.
A Terrestrial Laser Scanner (Leica, ScanStation P50, Heerburgg, Switzerland; accuracy: 1.2 mm @ 120 m) was employed to scan the bed elevation before and after the bore passage. The difference between those two measurements was used to evaluate the scour produced by the dambreak bore. The three columns utilized were square and were constructed with Plexiglas. Square columns were used as they represent well the shape of a typical building. Their dimensions were 0.10 m x 0.10

m x 1.50 m, and the walls of the columns were 0.01 m thick. The columns were secured in place by their upper sections by using a system of wooden studs and clamps in order to allow sturdy anchoring and to simplify changes in location between tests (Figure 6.2(c)). All sides of the columns were painted with matte black paint to prevent the laser scanner from measuring the bed elevation through them, which would induce measurement errors due to light refraction when the laser passed through the Plexiglas walls.

6.3.3 Experimental test program

A 3-column arrangement was utilized in the present experimental program. The experimental program conducted by Thomas et al. (2015) inspired the disposition of the columns in the present study. A square column of width (b) = 0.10 m, referred to as the design structure, was placed at the transversal center of the flume, and two macroroughness elements of the same dimensions as the design structure were installed upstream of the design structure. Figure 6.3 shows a plan view of the columns' arrangement. The longitudinal distance between the macroroughness elements and the design column (L_D) was varied between 2b and 4b, and the distance between the two macroroughness elements (W_c) was varied between 0b and 4b. The impoundment depth (h_0) was varied between 0.15 m and 0.35 m. In addition, three single-column tests, one for each h_0, were performed to allow for a baseline comparison. Table 6.1 shows all the tests that were performed to examine the dependency of the scour amplification due to constriction on the three above-mentioned measurements. The test number designates the dimensions of the h_0, W_c, and L_D in each particular test. The first letters in the test number describe the arrangement type ("Sg": single column; "C": constriction). The number immediately following "h" is the wave condition ("1": h_0 = 0.15 m; "2": h_0 = 0.25 m; "3": h_0 = 0.35 m). The numbers immediately following "w" and "L" refers to the magnitudes of W_c and L, respectively.

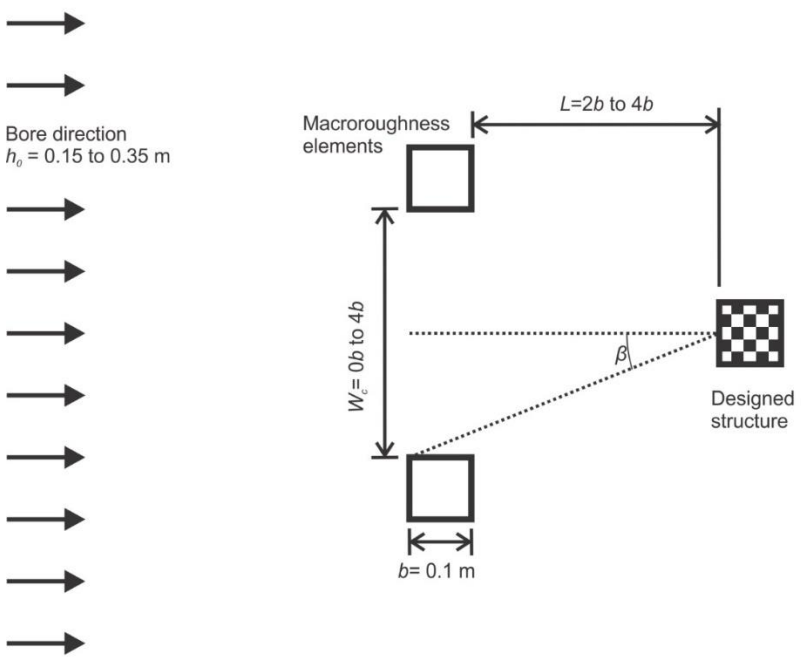

Figure 6.3: Plan view of the three columns' arrangement and the relevant measurements

Test no	Impoundment depth (h_0) (cm)	Obstacle spacing (W_c)	Downstream distance (L_D) (cm)	Clearance angle (β)
Sg_h1	15	N/A	N/A	N/A
Sg_h2	25	N/A	N/A	N/A
Sg_h3	35	N/A	N/A	N/A
C_h1_w0_L2	15	0	2	0.0
C_h1_w1_L2		1	2	9.5
C_h1_w2_L2		2	2	18.4
C_h1_w3_L2		3	2	26.6
C_h1_w4_L2		4	2	33.7
C_h2_w0_L2	25	0	2	0.0
C_h2_w1_L2		1	2	9.5
C_h2_w2_L2		2	2	18.4
C_h2_w3_L2		3	2	26.6
C_h2_w4_L2		4	2	33.7
C_h3_w0_L2	35	0	2	0.0
C_h3_w1_L2		1	2	9.5
C_h3_w2_L2		2	2	18.4
C_h3_w3_L2		3	2	26.6
C_h3_w4_L2		4	2	33.7
C_h2_w0_L3	25	0	3	0.0
C_h2_w1_L3		1	3	7.1
C_h2_w2_L3		2	3	14.0
C_h2_w3_L3		3	3	20.6
C_h2_w4_L3		4	3	26.6
C_h2_w0_L4	25	0	4	0.0
C_h2_w1_L4		1	4	5.7
C_h2_w2_L4		2	4	11.3
C_h2_w3_L4		3	4	16.7
C_h2_w4_L4		4	4	21.8

Table 6.1: Detailed list of the experimental program tests

6.3.4 Scaling considerations

The comprehensive experiments presented herein do not represent a particular case at the prototype scale. Nonetheless, the implications of scaling must be considered when planning such experiments for them to appropriately represent similar physical phenomena at such a scale. In general, experiments using hypothetical scales ranging from 1:40 to 1:80 compare well to recent large-scale tsunamis such as the 1993 Hokkaido-Nansei-Oki Tsunami (Jaffe and Gelfenbuam, 2007; Titov and Synolakis, 1997) and the 2010 Chilean Tsunami (Earthquake Engineering Research Institute, 2010; Fritz et al., 2011b).

The Froude number (*Fr*), one of the most important characteristics of a tsunami inundation, has a value between 0.5 and 1.5 (Bricker et al., 2012; Matsutomi et al., 2010). In the experiments presented herein, *Fr* was found to be between 1.0 and 1.5 for the majority of the inundations. Therefore, the *Fr* was similar to real-life observations of tsunamis. Melville and Chiew (1999) proposed that when $b/d_{50} < 50$, the local scour depth is influenced by the sediment size. In the present experiment, this ratio is of 1000, which suggest that the sediment size should not have affected local scour measured in the present study.

The Reynolds number should also be considered when scaling hydrodynamic phenomena. The flow can be separated into two phases: impact phase (t = 0 s to 10 s in Figure 6.5) and the quasi-steady-flow phase (t = 10 s to 45 s in Figure 6.5). The Reynolds number (*Re*) associated with the structure width for those phases is between 2 x 10^5 and 3.2 x 10^5, and 1 x 10^5 for the impact phase and the quasi-steady-flow phase, respectively. These values are similar to, or marginally smaller than, typical prototype scale tsunamis (reaching Re = 3 x 10^8 (Tihn et al. 2022)). However, the current values of *Re* indicate that the flow was fully turbulent, mitigating surface tension, viscosity scale effects (Bricker et al., 2015) and allowing the formation of near-structure vortices (Larsen et al., 2017), especially during the impact phase when most of the scour occurs.

The Keulegan-Carpenter numbers ($KC = UT/b$) for the waves of the present experiments were between 1200 and 1600. Where U is the maximum value of the outer oscillatory flow velocity, T is the inundation period and b is the column width. These values compare well with previous dambreak experiments but are greater than in other studies of tsunami-like experiments using other types of waves and field measurements (50 to 1500) (McGovern et al., 2019). These high values of KC number indicate that the inundation was sufficiently long to allow for the appropriate formation of turbulent structures at the column.

6.3.5 Test repeatability

Multiple tests with the same hydrodynamic conditions were performed. Figure 6.4 shows the flow depth measured by US2 during 9 tests: 3 performed with each h_0 (0.15 m, 0.25 m, and 0.35 m). A good agreement was achieved in all three flow conditions. The normalized standard deviations were 3.9%, 5.1%, and 4.4% for the tests with h_0 = 0.15 m, h_0 = 0.25 m, and h_0 = 0.35 m respectively. In addition, 5 tests were repeated with the same column arrangement in order to test the repeatability of the bore-induced scouring. The normalized standard deviation for the maximum scour depth was 2.9%, which indicates appropriate test repeatability.

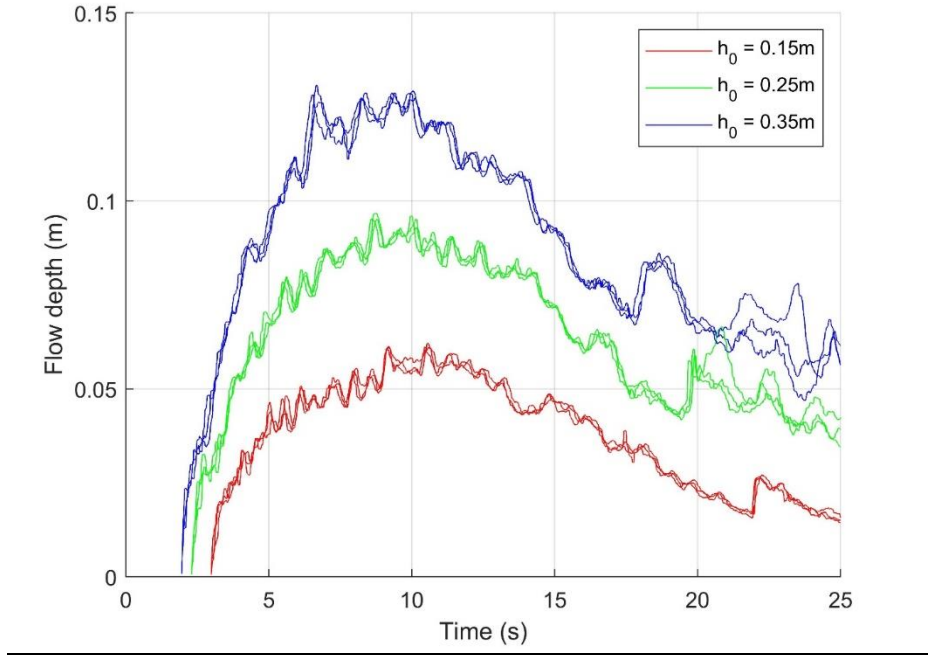

Figure 6.4: Repeatability of dambreak bore water surface elevations at US2, comparing 3 tests for 3 different impoundment depths

6.4 Results

The results section presents the experimental results in three categories: (1) hydrodynamic properties of the undisturbed bore; (2) hydrodynamic changes in the dambreak bore caused by the presence of the columns; and (3) the scouring results.

6.4.1 Bore hydrodynamic properties

Figure 6.5 shows the time series of the hydrodynamic data collected during the single column tests. In this figure, the water surface elevation variations at two locations along the flume measured by US2 and US3 (Figure 6.5b, Figure 6.5c), the surface velocity variations over time estimated with Camera 2 (Figure 6.5d), and the Froude numbers at US2 (Figure 6.5e) are shown. In addition, the runup at the upstream face of the design column for the single column tests, measured by US4, is shown in Figure 6.5a. At all the measurement points, the bore water surface saw a rapid increase in water depth followed by a gradual decrease in depth after the maximum flow depth was reached (t = 10 s to 12 s). As well, the maximum velocity was reached at the time of the bore's arrival and decreased as the wave progressed. The Froude number rapidly reached its maximum value at the wave's arrival and progressively decreased over time. A typical Froude number value for this flow was found to be between 1.0 and 1.5, which occurred between t = 10 s and t = 30 s for all impoundment depths. The Froude number was slightly overestimated for these experiments because the surface velocity was utilized instead of the depth-averaged velocity. However, the turbulence of the dambreak bore and the low friction of the false floor surface should have reduced the vertical gradient of the horizontal flow velocity. This velocity uniformity results in the surface

velocity being more representative of the depth-averaged velocity compared to flows with greater vertical gradient of velocity.

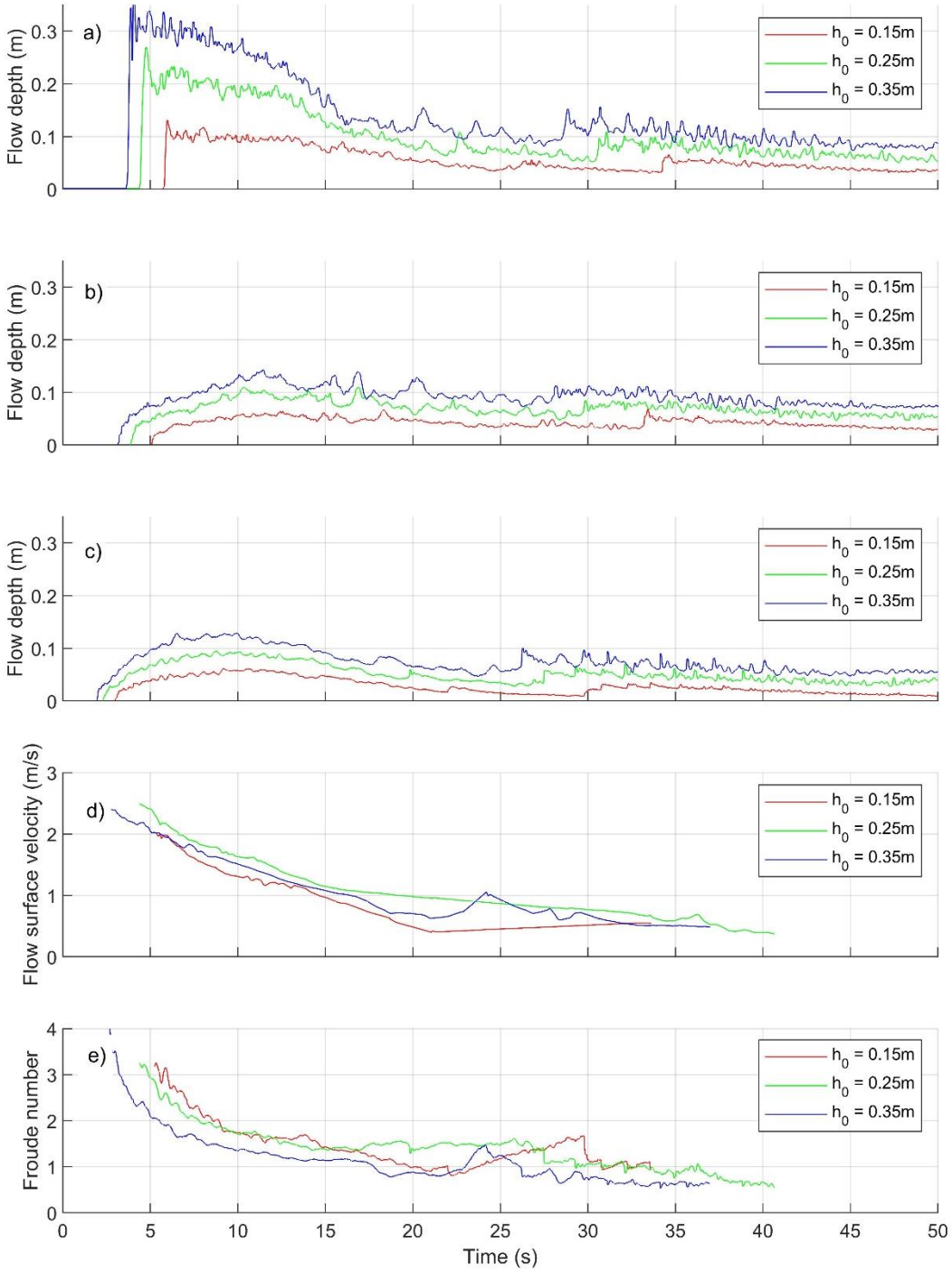

Figure 6.5: The time series data of the single column tests: (a) the runup at the upstream face of the column (US4); (b) the water surface elevation of the flow approaching the column (US3); (c) the water surface elevation just upstream of the sand bed (US2); (d) the surface flow velocity at US2; (e) the Froude number at US2

A secondary reflection wave was noted in the measurements. This wave resulted in the flow depth increasing by < 0.02 m and was accompanied by surface ripples. This wave was generated by the upward forcing of the water when the bore reached the approach slope. After the bore reached the top of the approach slope, a differential in water surface was generated between the top of the false floor and the location of the gate. This surface elevation gradient generated an upstream movement of energy in the form of a wave which moved in the upstream direction, reached the end of the flume, and was reflected towards the columns. The installation of the three wave absorbers reduced the wave height by 70%, and surface ripples were generated by the partial reflection of the wave from the wave absorbers. This wave was inevitable due to the presence of the false floor. The authors judged that this was a good compromise between the absorption of the return wave while not largely impeding the free movement of the dambreak wave.

The analytical solution from Ritter (1892) for dambreak bores advancing on a horizontal surface (Equation 6.1) was compared to the free surface elevation measurements taken by US2 (see Figure 6.6). Although not all of the flume's false floor was fully horizontal, the bore was compared to Ritter's solution since it represents tsunami bores advancing on flat coastal plains (Chanson, 2009, 2006, 2005).

$$\frac{H}{h_0} = \frac{1}{9}\left(2 - \frac{x}{t * \sqrt{g * h_0}}\right)^2 \tag{6.1}$$

where H is the flow depth, x is the horizontal distance between the dambreak gate and the particular location of measurement, t is the time starting at the instant the impounded water was released, and h_0 is the impoundment water depth. The impoundment depth in Ritter's solution was augmented by 0.1 m in order to achieve the best fit for the bore front (t < 10 s). With this adjustment, a good agreement between the experimental results and the theoretical solution was reached. This adjustment was necessary due to the fact that this is a theoretical equation and physical phenomena such as friction and turbulence were not accounted for when it was developed. In addition, h_0 in this paper is the elevation of water in the reservoir that exceeded the level of the false floor. However, in reality, a bore of h_0 + (false floor height) was produced and lost energy as it rushed up the approach slope. In this case, it can be concluded that the energy loss does not correspond to the gain in gravitational potential from t = 0 s to the moment the bore reached the top of the false floor. Therefore, the wave carries more energy than the height of impounded water exceeding the elevation of the bed would account for.

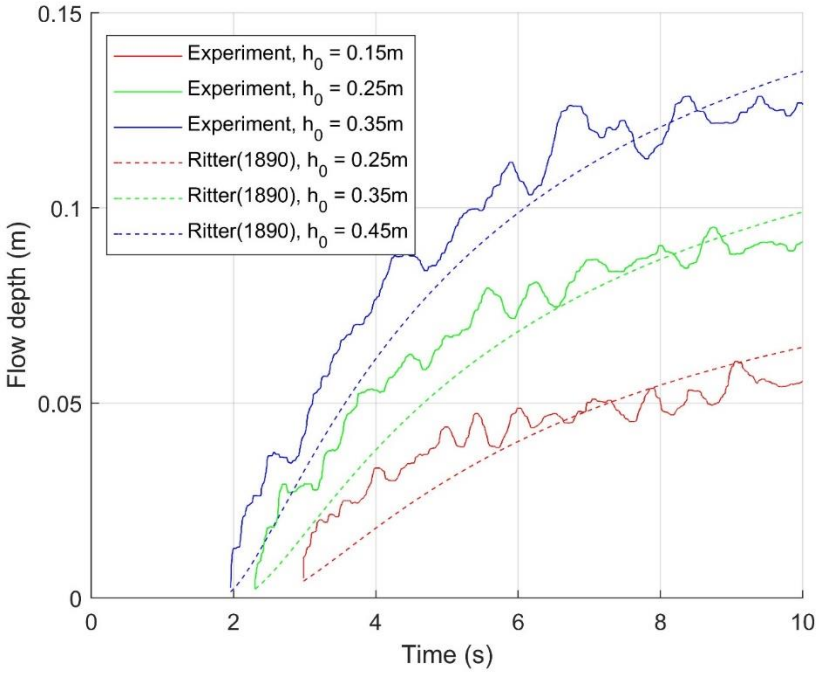

Figure 6.6: Water surface time histories from US2 compared to the bore surface solution proposed by Ritter (1892)

Figure 6.7 shows the bore front speed as it progressed over the horizontal section of the false floor. The time the tip of the bore reached the lines painted at 0.2 m increments on the false floor was used to estimate the bore front's speed. The average bore front speed over three tests was used to construct the data displayed in Figure 6.7. The bore entered the section monitored by Camera 2 (X = 4.5 m) with its highest velocity; then, the front's speed decreased and was approximatively constant for the last 1.5 m of the monitored section (X = 6.5 m to X = 8.0 m). When comparing the results to Equation 6.2, proposed in FEMA P-646 (2012), the bore speed at the end of the horizontal section was in good agreement with this theoretical solution.

$$U = 2\sqrt{g * H_{max}} \tag{6.2}$$

where U is the bore front speed and H_{max} is the maximum flow depth (taken at US2). This equation was developed for estimating tsunami velocity based on the flow depth. A similar equation was proposed by Ritter (1892) and emphasized by Chanson (2005), but using h_0 used instead of H_{max}. The bore front speed resulting from Ritter's (1892) and Chanson's (2005) methods resulted in velocities far greater than those obtained with H_{max}. The use of h_0, as proposed by Ritter (1892) and Chanson (2005), was based on theoretical approach that neglected real-life physical phenomena such as friction and turbulence, and may not be the most appropriate in this context.

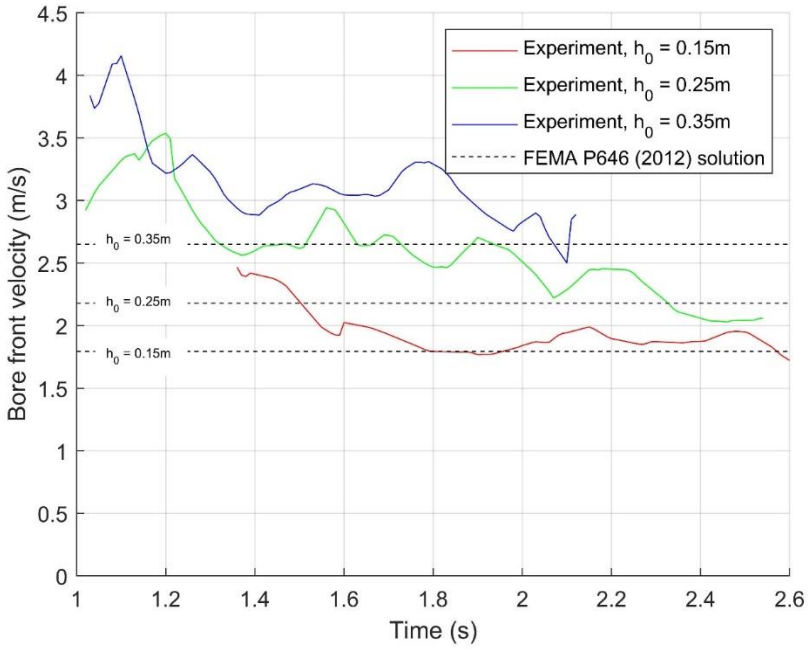

Figure 6.7: Comparison of the bore front velocity along the horizontal section of false floor with the theoretical solution proposed by FEMA P-646 (2012)

6.4.2 Water surface change with macroroughness elements

Figure 6.8 shows still shots of the water surface around the columns at t = 10 s taken from three points of view ((a) side, (b) angled view from upstream, (c) in-flume top view). Although Figure 6.8 shows the surface from only one test (C_h2_w4_L4), the flow structures depicted were found in all setups with $W_c \geq$ 2b. The intensity and dimensions of the flow structures varied between setups. When the flow reached the front face of the columns, the vertical face of the column redirected the flow in the vertical direction, generating a surface roller (indicated in blue) which directed the water to the sides of the columns to generate wakes. The wakes generated by the columns met in the center between the columns, which created a local flow acceleration. The junction of these two wakes generated a strong flow with a slight downward trajectory advancing towards the design column (see red arrows in Figure 6.8a). This intensified flow resulted in a larger roller and wake in front of the design column. The downward component of the flow may also have contributed to an intensification of the horseshoe vortex that drives sediment transport around columns (H N C Breusers et al., 1977; Ettema et al., 2006b). The exaggeration of the horseshoe vortex is only speculated by the authors, but the surface flow acceleration between the columns and the scour amplification at the design column presented later in the paper gives clues into this horseshoe vortex intensification. As W_c was reduced, the roller forming at the design structure was less exaggerated by the constriction effect of the upstream columns. When W_c = 1b, the flow between the columns decelerated and was highly turbulent. The surface roller at the design column was remarkably less intense than at the macroroughness elements. Similarly, when W_c = 0b, no flow passed between the columns. The turbulence on the lee side of the macroroughness elements reached the design column and formed disorganised turbulent flow patterns. No strong visual difference in flow structures was noted when L was changed.

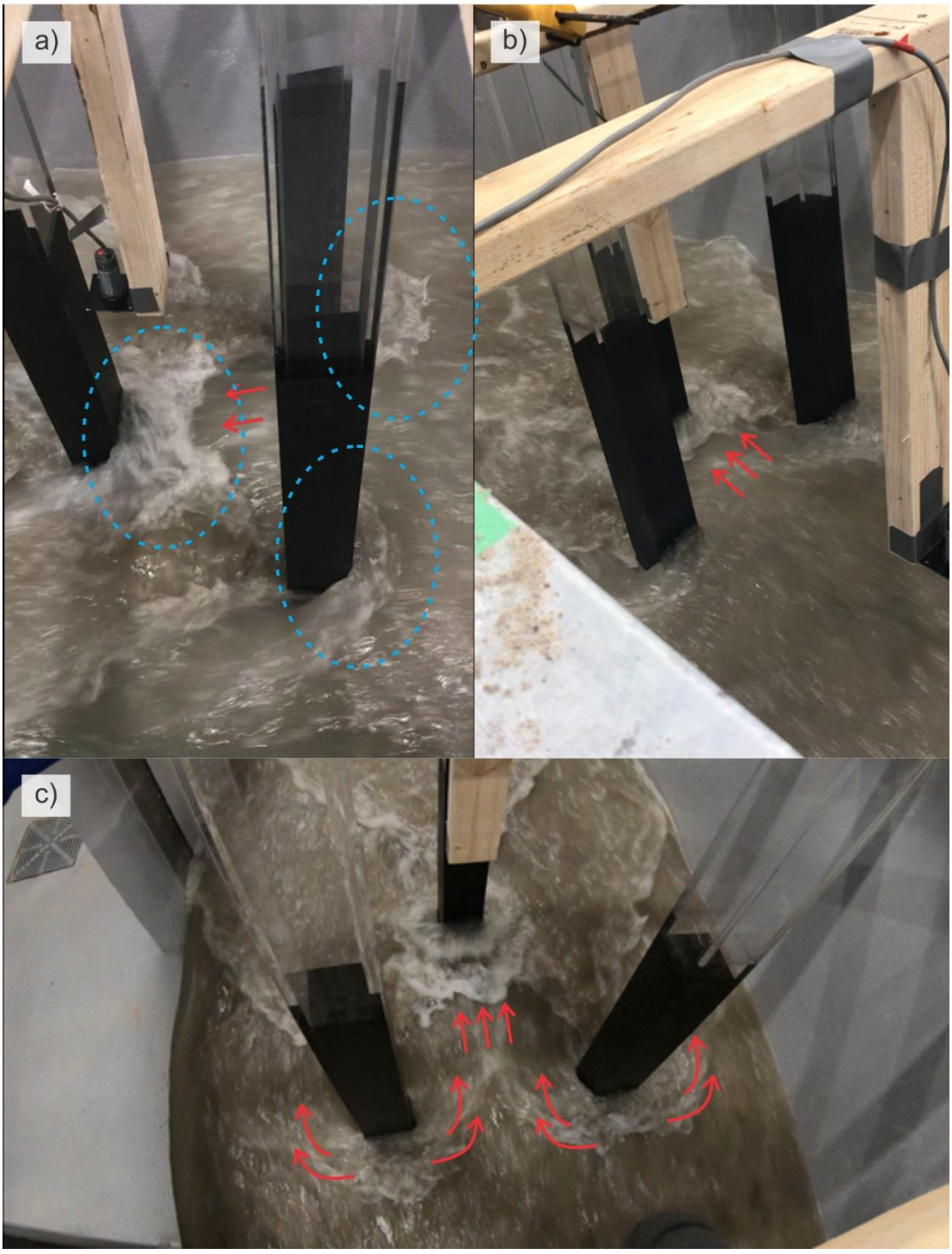

Figure 6.8: Images of flow surface reaction to the presence of the three vertical structures at t = 10 s: a) side view; b) angled view from upstream; c) in-flume top view (test: C_h2_w4_L4). Blue circles indicate surface rollers and red arrows indicate flow direction

The runup at the design column was monitored by US4. A comparison of the maximum runups for all setups (R_i) and the one for the single column tests (R_0) is plotted against β in Figure 6.9. Although the flow was accelerated between the macroroughness elements, the runup at the design

column was lower in all tests than that for the single column tests. A very strong correlation between β and the runup was observed. However, little difference was noted when L_D was varied. The h_0 = 0.25 m and h_0 = 0.35m tests yielded very similar results, except when β = 0b. The h_0 = 0.15m tests showed less reduction of runup linked with the presence of macroroughness elements. This reduction in runup was caused by a combination of a sheltering effect from the macroroughness elements and an amplification of the scour depth at the design column, which led to a lowering of the bed level at the column.

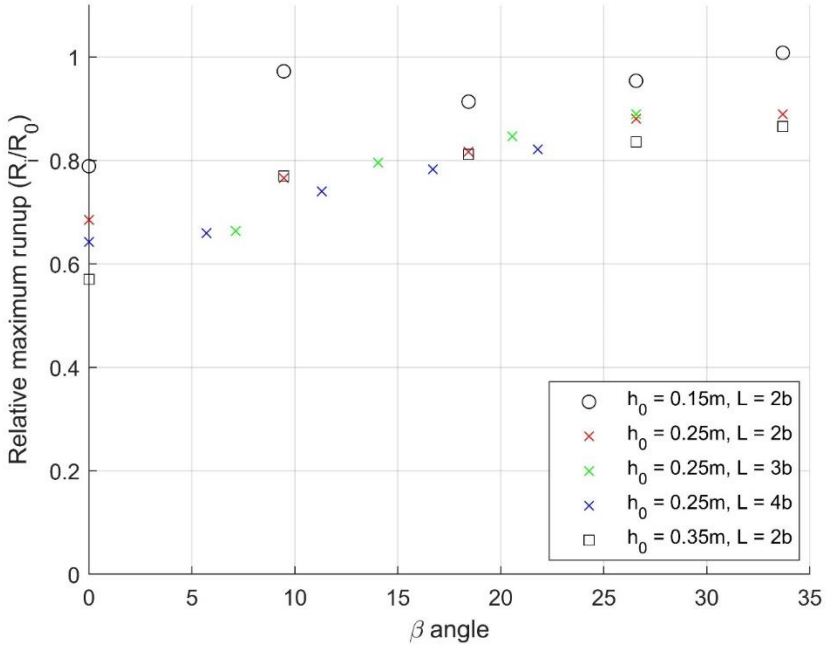

Figure 6.9: Influence of upstream constriction on the runup at the design column (US4)

6.4.3 Scour results

Figure 6.10 shows the bed topography after the passage of the bore for all the structure arrangements. The majority of the scouring was found upstream of the front face, in a bowl shape, and accumulation was found downstream of the design column. The deepest scouring was found at the corners of the structures, except for the tests where W_c = 0b. In those tests, the maximum scour depth was found in a depression near the center of the front face or along the sides of the column. As the impoundment depth was increased, the scouring also increased. In runs with h_0 = 0.35 m and in some of the h_0 = 0.25 m runs with deeper scouring, the scour hole wrapped around the column and scoured the soil at the back face of the column.

With all arrangements with $W_c \geq$ 2b, the scouring was greater around the design column compared to the single column tests with the same impoundment depth. This scour amplification was similar to the flow acceleration observed between the macroroughness elements as described in Figure 6.8. L was found to be inversely correlated with the scour depth at the design column. In tests with h_0 = 0.35 m, the scour holes associated with the three columns were wide enough to connect with each other and form one scour hole with irregular topography. Arrangements with $W_c \leq$ 1b led to

a sheltering effect from the two macroroughness elements and a great reduction in scouring at the design column.

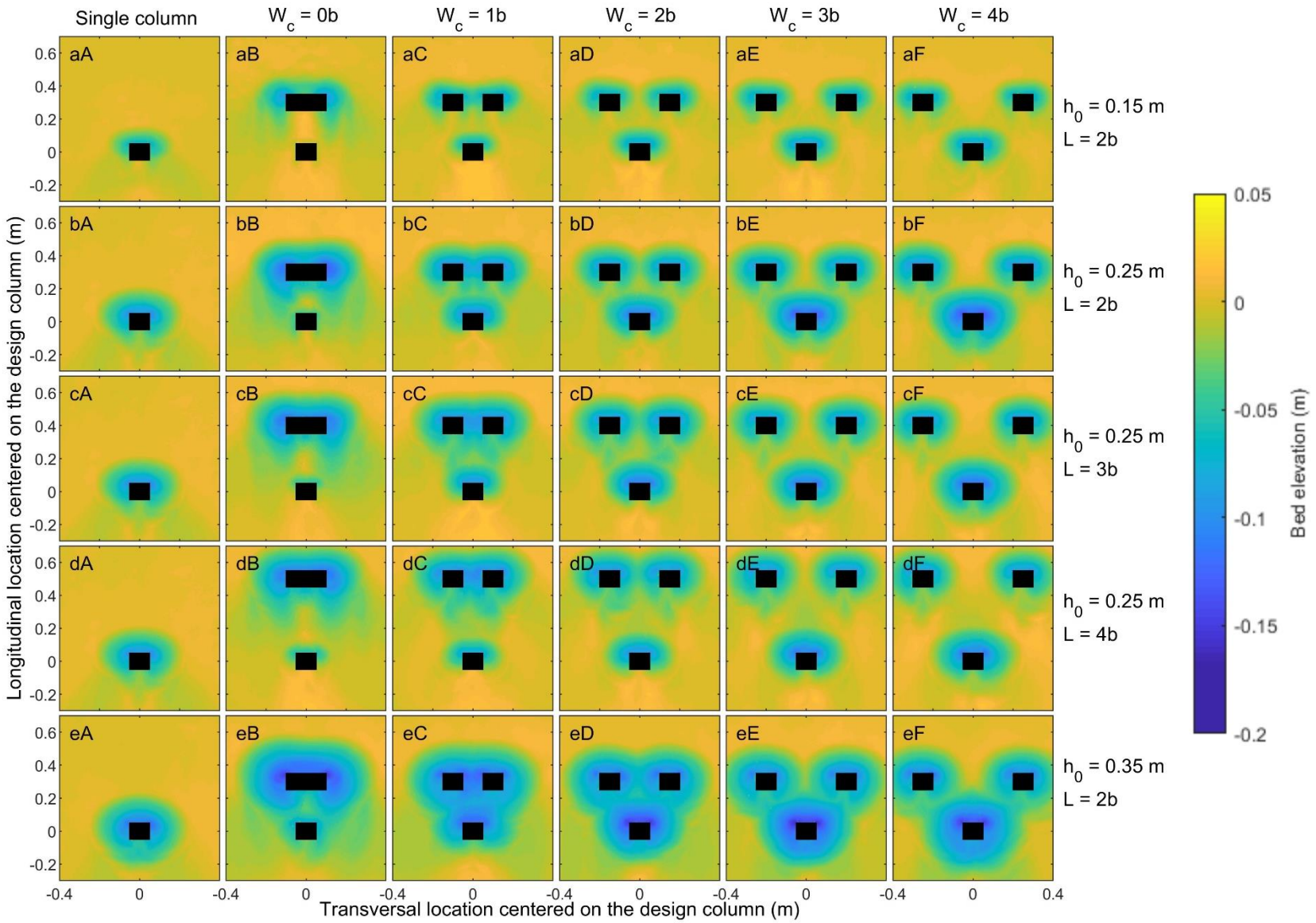

Figure 6.10: Post-bore passage sand topography: (a) h_0 = 0.15 m, L = 2; (b) h_0= 0.25 m, L = 2; (c) h_0= 0.25 m, L = 3; (d) h_0 = 0.25 m, L = 4; (e) h_0 = 0.35 m, L = 2 // (A) single column; (B) W_c = 0; (C) W_c = 1; (D) W_c = 2; (E) W_c = 3; (F) W_c = 4

A comparison of the maximum scour for all setups (d_{si}) and the one for the single column tests (d_{s0}) is plotted against the macroroughness spacing (W_c/b) in Figure 6.9. As illustrated in Figure 6.11, the tests with $W_c \leq 1b$ led to a reduction in maximum scour depth at the design column, while the contrary was observed for the tests with $W_c > 2b$. When observing the dependency of the scour amplification on h_0, the tests with $h_0 = 0.15$ m had a lower maximum scour depth amplification, but the sheltering effect at low W_c was greater. The contrary was observed for the runs with $h_0 = 0.25$ m and with $h_0 = 0.35$ m. The tests with $L_D = 2b$ and $h_0 = 0.35$ m and $h_0 = 0.25$ m showed a very similar maximum scour amplification in all arrangements, except for one test (C_h3_w4_L2), which could be considered as outlier. The change in L_D was only tested for $h_0 = 0.25$ m. The distance L_D was found to be inversely proportional to the constriction effect with regard to maximum scour depth. The constriction effect increased as W_c increased without reaching an upper limit. In the flume utilized in this study, the distance between the macroroughness elements could not be increased further without encountering a high risk of wall effects. Since the distance between the macroroughness elements and the walls would be less than the distance between the macroroughness elements when $W_c \geq 4.33b$, therefore the upper limit of the constriction effect on scour was not found in this study.

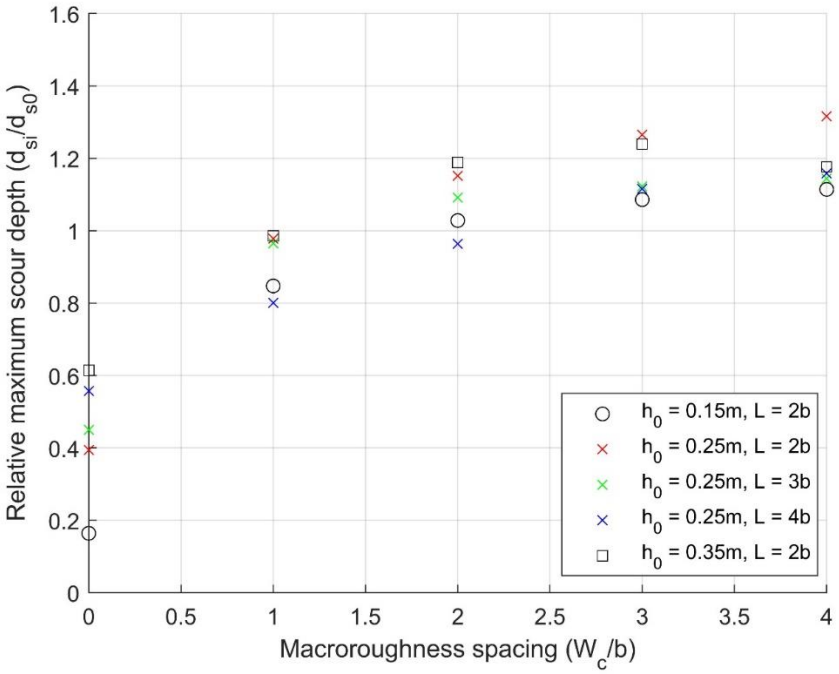

Figure 6.11: Relative maximum scour depth with varying macroroughness spacing

The use of the wake clearance angle (β) to compare the test results for all the setups allows for simultaneously incorporating W_c and L_D in the analysis. In addition, this angle is already present in the ASCE standard for calculating flow velocity amplification caused by upstream constriction (ASCE, 2016b). Macroroughness elements installed with $\beta < 13^o$ sheltered the design column and reduced the maximum scour depth at the column. When $\beta > 13^o$, the constriction effect of the macroroughness elements increased the scouring at the design column, and the best-fit curve in Figure 6.12 illustrates this correlation.

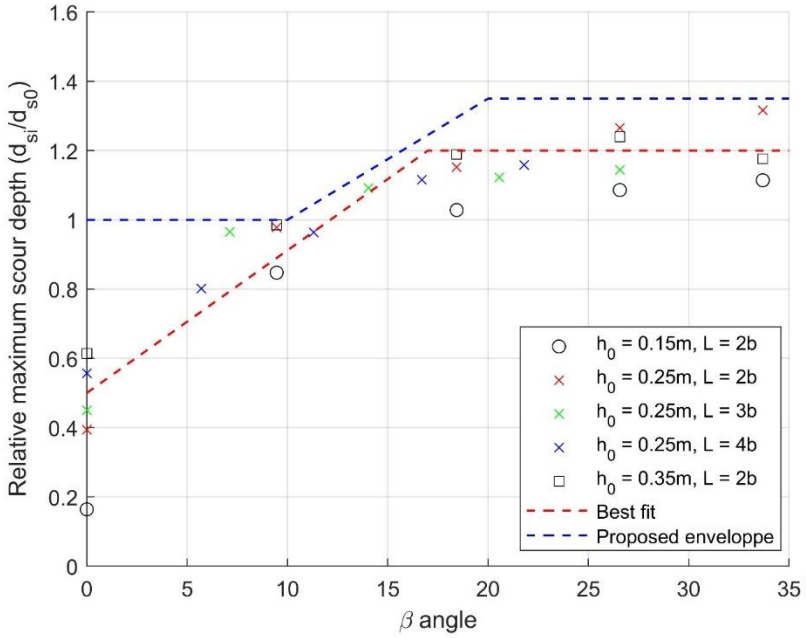

Figure 6.12: Relative maximum scour depth increase with varying of angle β

In addition, the authors proposed a design envelope in Figure 6.12 which conservatively includes all the test results. When compared to the velocity curve from ASCE7, both have similar features (see Table 6.2). When considering onshore flow constrictions, there are no changes to the existing scour or velocity predictions when structures are present at $\beta < 10^o$. When $10^o < \beta < 20^o$, the scour amplification factor is a linear function bounded by 1.0 at the lower limit ($\beta = 10^o$) and 1.35 at the upper limit ($\beta = 20^o$). When $20^o < \beta < 35^o$, an amplification factor of 1.35 should be applied to the maximum scour depth calculated with the equations from ASCE7. For $\beta > 35^o$, no experimental data are available, which is a limitation of this study. Since the envelope for $\beta < 35^o$ is very similar to the velocity amplification and because the scour is closely related to flow velocity (Ettema et al., 1998; Melville, 1985), the authors believe that the scour amplification would be highly similar to the velocity amplification when $\beta > 35^o$. Therefore, it is proposed that the scour amplification factor for $35^o < \beta < 55^o$ should be a linear function with 1.35 and 1.0 at the lower and upper limits respectively. Structures found at $\beta \geq 55^o$ are not expected to generate any flow constriction that would lead to scour amplification.

Effective wake clearance angle (β)	0º	10º	20º	35º	>55º
Flow speed amplification factor (ASCE, 2016b)	1	1	1.25	1.25	1
Scour depth amplification factor (proposed)	1	1	1.35	1.35	1 (unknown)

Table 6.2: Flow speed and scour depth amplification factors with respect to β

The scour results were plotted against the approach flow depth at US2 (Figure 6.13) and against the Froude number at US2 (Figure 6.14), and compared with the curves in Figures 6.12-1 and 6.12-2 from ASCE7 (Robertson, 2020). The h_0 was positively correlated with flow depth, and the produced bore generated a deeper scour hole. The Froude number, on the other hand, did not show a significant dependency on scour depth since its magnitude was very similar in all 3 impoundment depths. In addition, it is challenging to define a singular value for the Froude number due to the transient nature of the studied flow. However, the Froude number (Fr) exceeded 1.0 in all tests for the majority of the tests' duration. The 6.12-2 envelope is constant beyond Fr = 1. Therefore, according to Figure 6.12-2 from ASCE7, the ratio of scour depth to the column width should be 1.3 in all the tests in this study.

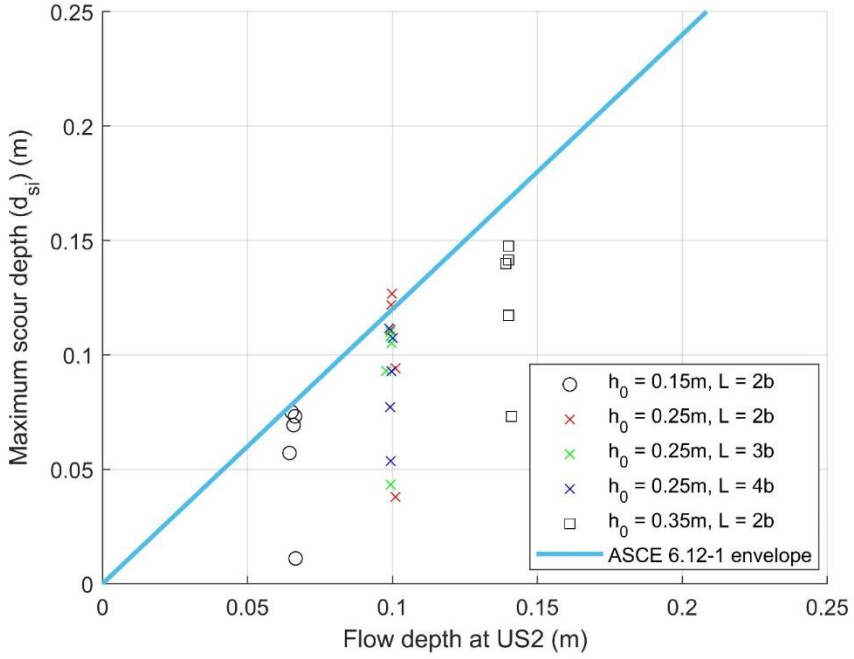

Figure 6.13: Maximum scour depth at design structure with respect to the flow depth at US2

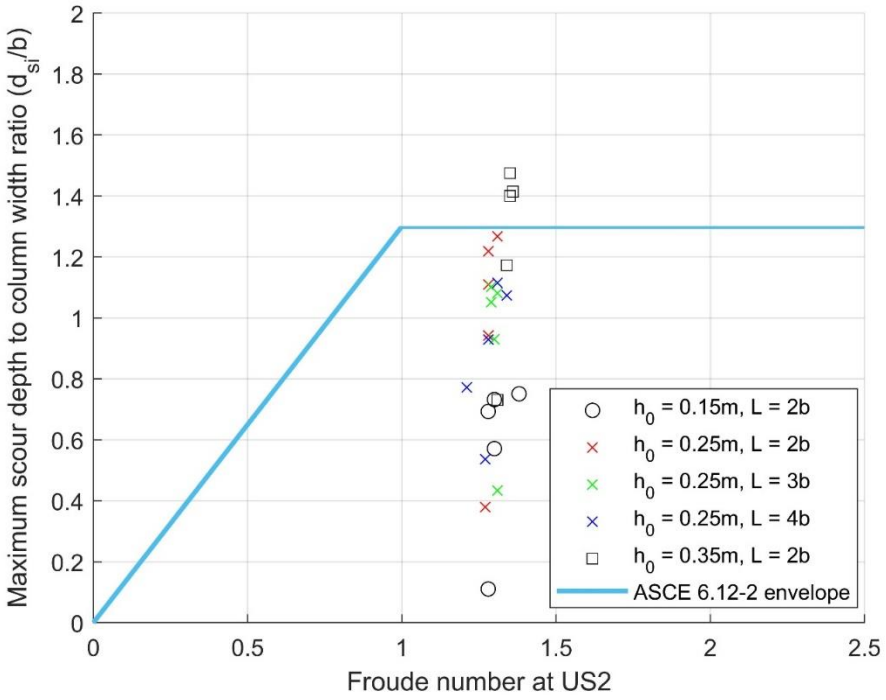

Figure 6.14: Maximum scour depth to column width ratio against the Froude number at US2

When observing Figure 6.13 and Figure 6.14, 2 and 3 data points, with h_0/b = 3.5, for each figure respectively exceeded the conservative envelope of the ASCE standard. The curve in Figure 6.13 was developed by field observation, but the sloped portion of the envelope was developed theoretically by Tonkin et al. (2013). The envelope in Figure 6.14, on the other hand, was developed conservatively with results from dambreak experiments (Lavictoire et al., 2014; Mehrzad et al., 2016). A comparison between the single column from the present study and the studies used for the development of the ASCE7 6.12-2 envelope is illustrated in Figure 6.15. The nature of the waves used in the experiments was similar; however, Lavictoire et al. (2014) used circular columns, and wider columns were used in most of their experiments, which led to a lower ratio of maximum scour depth to column width compared to the present study. Mehrzad et al. (2016) performed three tests with the same shape and size of columns (square base, b = 0.10 m) as in the present study, and in their tests, the resulting maximum scour depths surpassed by 10 to 20% the ones measured in the present study for similar conditions. This dissimilarity may be due to the difference in inundation periods resulting from the dambreak waves produced in the two studies. The scales of the flumes were highly similar, but the length of the impoundment was 23 m in Mehrzad et al.'s (2016) study compared to 16 m in the present study. The longer water reservoir led to a greater total amount of water rushing toward the columns and a longer inundation period, and thus theoretically more scour (Kothyari et al., 1993; Zhang et al., 2017). Applying an increase of 20% to the scour results of the present study in order to account for the different flume conditions used to develop the ASCE 6.12-2 envelope resulted in 12 data points surpassing the ASCE 6.12-2 envelope.

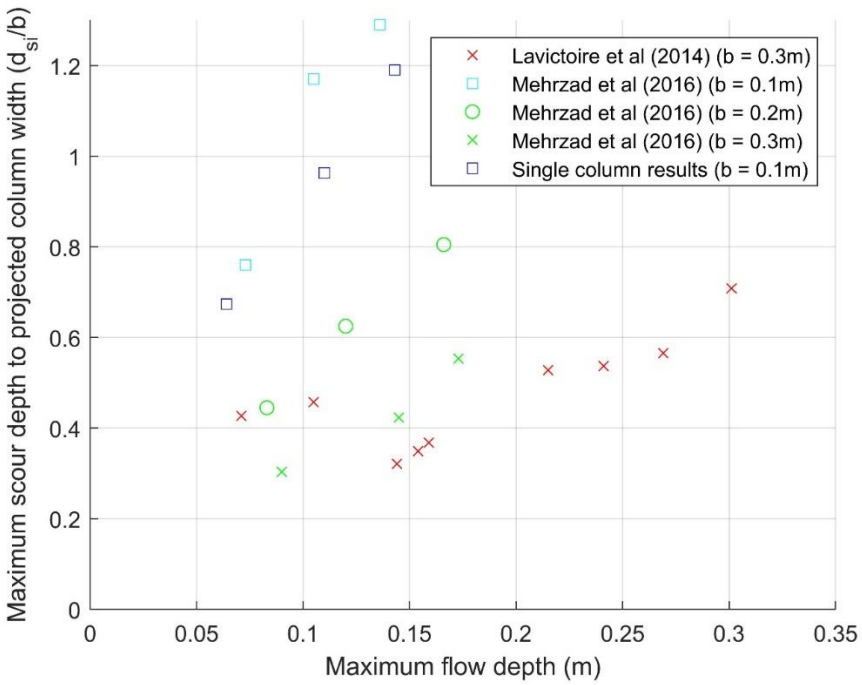

Figure 6.15: Single column results compared with the results from the experiments by Mehrzad et al. (2016) and Lavictoire et al. (2014)

6.5 Discussion

Although neighboring structures redirected the flows and enhanced the scour at the design columns, the authors argue that local scour, and not channelized scour, was responsible for the soil transport. The flow accelerated between the columns, but only minimally scoured the soil between the columns and just downstream of them. Scouring was very concentrated at the columns' front faces, and highly turbulent eddies were found to be present at the columns. Therefore, this study showed an example of the amplification of local scour caused by flow acceleration, as opposed to channelized scour.

The resulting scour amplification factor showed a dependence on the three factors examined: spacing between macroroughness elements (W_c); longitudinal distance between design structure and macroroughness elements (L_D); and flow conditions (h_0). W_c was positively correlated with the amplification factor, and L was negatively correlated with the scour amplification factor. The two were combined to generate the β angle, which showed high similarities with the flow amplification factor given in the ASCE7 standard (Table 3). However, due to flume width limitations, β was only 33.7º at its maximum. This limitation prevented the authors from observing at what point the clearance angle was too open to influence scour at the design structure. The lower impoundment depth led to a lower scour amplification, but h_0 = 0.25 m and h_0 = 0.35 m waves resulted in highly similar scour amplification factors for the same β angle. According to these observations, once the extreme hydrodynamic event reaches a certain size, the factor for scour amplification caused by upstream constriction remains constant for all wave sizes. However, the scale of the experiment constitutes a limitation.

The present study employed a dambreak type setup to produce waves similar to tsunami inundations. This setup has the advantage of correctly replicating tsunami inundation periods, but at the cost of not simulating the drawdown phase of the waves, as in the case of solitary wave-type setups. The scour produced by the runup phase is associated with highly turbulent eddies formed around the columns (D. J. McGovern et al., 2019; Tonkin et al., 2003), while the scour produced by the drawdown phase is linked to pore pressure softening of the soil (Abdollahi and Mason, 2020; Mason and Yeh, 2016; Tonkin et al., 2003; Yeh and Mason, 2014). Knowing that the scour amplification caused by upstream constrictions is linked with flow velocity, the effect of surrounding macroroughness will be very important during the runup phase and less during the drawdown phase. During the latter phase, the flow velocity may be exaggerated by the presence of surrounding macroroughness elements, but the pore pressure change, the main driver of sediment transport in this phase, should be affected to a much lesser extent. Therefore, this study should appropriately represent a worst-case scenario for scour amplification due to onshore flow constrictions. In addition, only edifices present on the upstream side of a building should be considered when using the scour amplification factor.

6.6 Conclusions

In this study, the influence of upstream macroroughness elements on tsunami-induced scouring was investigated, and a process of local scour amplification at a design structure was observed. The wakes from two upstream macroroughness elements met midway to generate a strong plunging flow that resulted in scour amplification at the design structure in some arrangements. The maximum scour at the design column was found to exceed the ASCE guidelines.

The resulting scour amplification factor showed a dependence of the scour amplification on the three factors investigated. An increase in scour was noted when the distance between the macroroughness elements (W_c) was greater than 1. The longitudinal distance between design structure and macroroughness elements (L_D) was inversely correlated with scour amplification at the design column, while impoundment depth (h_0) was positively correlated with the scour amplification.

A reduction in maximum scour depth was noted for macroroughness elements with $W_c \leq 2b$, and with $\beta < 10^o$. When $\beta > 10^o$, the upstream macroroughness elements strongly influenced the scour at the design structure. A curve for scour amplification was proposed based on the scour results. There was a high similarity between the scour amplification due to upstream constriction found in this study and the velocity amplification found by Thomas et al. (2015). The link between scour and velocity has often been mentioned in the literature for steady flows, but the same cannot be said for dambreak bores. Many other factors influence the velocity of extreme flows, such as bed slope and roughness elements; however, their explicit links with scour in extreme flow contexts are still mostly undiscussed.

Chapter 7: Structures Sheltering and Lateral Spacing Effects on Tsunami-Induced Scour

7.1 Abstract

Post-event field investigations of the 2004 Indian Ocean Tsunami and the 2011 Great Japan Tsunami highlighted the risk of damage to structures caused by adjacent hydraulic scouring. Since inhabited coastal regions often have large numbers of constructed edifices in close proximity, flows are often found to be either focused or diminished in intensity by the presence of these structures, and these flow concentration and dissipation areas influence the resulting scour around the structures. The American ASCE building standard only provides guidance for limiting scour around a single isolated structure. Hence, the current study is an attempt to investigate, through the use of a comprehensive physical model, scouring around two arrangements in order to test the effects of sheltering and lateral spacing of columns on tsunami-induced adjacent scour formation. The experiment consisted of varying the incoming flow properties and different setup dimensions to measure their impact on the produced scour. The wave runup and scour at a sheltered column were found to be always lower than those around a single column. Tighter lateral spacing of columns led to an increase in scour; however, in contrast to steady flow conditions, wider spacing led to a decrease in scour.

7.2 Introduction

Tsunamis of the past few decades have been proven to be highly destructive, and have led to great amounts of structure damage and loss of life (Chock et al., 2013). The difficulty of forecasting such events and the short reaction time after a wave is generated present a great challenge for engineers. In addition, post-tsunami forensic investigations from the 2011 Great Japan Tsunami proved that the building standards were underestimating the potential impact of such natural extreme hydrodynamic events, and updating those standards by the scientific and engineering communities is still in progress. One standard that is still lacking details involves recommendations for scour. Only a limited number of field observations were used to construct the present recommendation in the ASCE7 standard for local scour caused by tsunami waves, and the magnitude of the forecasted scour depth is based on flow depth alone (Robertson, 2020). Many additional factors that affect scour in steady flow are considered in the HEC-18, but have not yet been fully investigated for transient flows such as tsunami waves. These factors include structure shapes, flow attack angles, bed forms and materials, flow depths, and column spacing, to name a few (Melville and Coleman, 2000; Richardson et al., 2001). Among these factors, many involve the presence of nearby structures.

To give a real-life example, the case of two tsunami-resistant buildings constructed near one another in Onagawa, Japan which were impacted by the 2011 Great Japan Tsunami illustrates well the importance of neighboring structures (Yeh et al., 2013). Figure 7.1(a) shows a picture taken in the onshore direction of the gap between two tsunami-resistant buildings, and Figure 7.1(b) shows an aerial photograph of the same area. A deep scour hole surpassing 3.5 m in depth formed between the edifices which was caused by the flow acceleration due to the close proximity of the two buildings. In addition, structures in the onshore shadow of the tsunami-resistant buildings were

found to be still standing after the passage of the tsunami, while the edifices directly onshore of the gap between the buildings had failed. Therefore, the tsunami-resistant buildings had sheltered the structures that were still standing from the impact of the tsunami. The phenomena of scour amplification caused by the tight lateral spacing between the buildings and the sheltering caused by upstream structures have yet to be investigated for a tsunami flow.

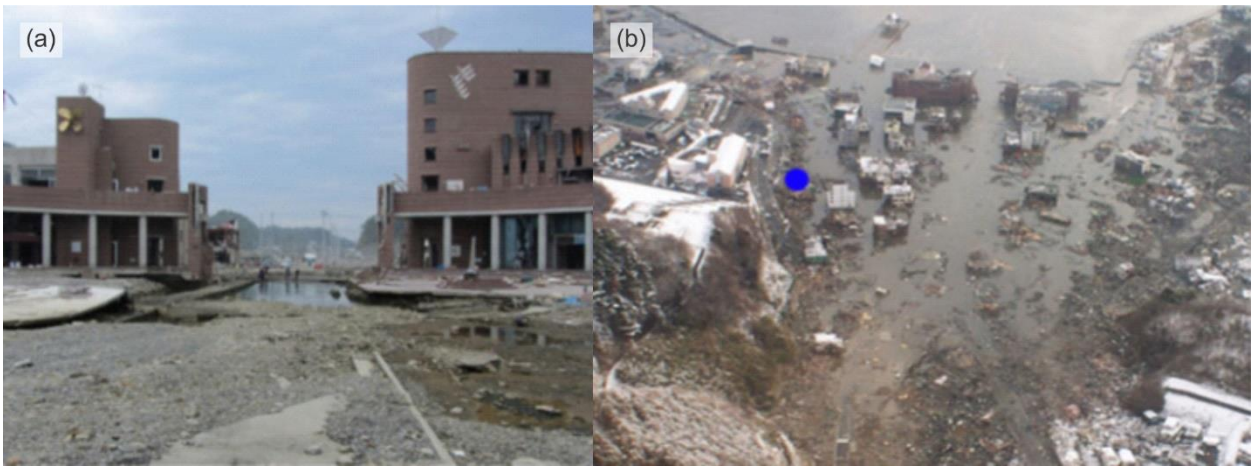

Figure 7.1: Post-tsunami examples of sheltering and spacing effects, 2011 Great Japan Tsunami, Onagawa (Yeh et al., 2013)

Although this field example gives clues into the stresses induced by tsunami inundations, only a very limited number of studies have investigated the hydrodynamic differences caused by the presence of multiple structures in such inundations (Nouri et al., 2010; Thomas et al., 2015). To the knowledge of the authors, at the time of this writing, only one study has considered the lateral spacing effect on tsunami-induced scour (Le Quéré et al., 2021), whereas other studies on tsunami-induced scour have focused on flat beaches, horizontal structures, or isolated vertical structures. In contrast, for steady flows, scouring around groups of columns (piers), sometimes quite complex, has been of great interest (Alemi and Maia, 2018; Amini et al., 2012; Ghaemi et al., 2013; Hannah, 1978; Hosseini and Amini, 2015; Vasquez and Walsh, 2009), but steady-flow scouring around simpler column systems, such as two columns placed one behind the other or side-by-side has also been explored in order to investigate the effects on scour of sheltering and spacing, respectively.

First considering two columns placed one behind the other, a reduction of scour around the downstream column occurs when the angle between the flow direction and the line of the columns is below 15^{o} (Hannah, 1978; Memar et al., 2018). In this case, the upstream column shelters the downstream column by reducing the velocity of the flow advancing onto the latter, thereby reducing the intensity of the horseshoe vortex (Ataie-Ashtiani and Beheshti, 2006; Hosseini and Amini, 2015). In addition, deposition from the upstream column changes the flow patterns around the sheltered column, as the presence of the upstream column generates suspended sediments in the flow, and the flow acts like it is in a live-bed condition at the downstream column (Ataie-Ashtiani and Beheshti, 2006). The combination of these three physical mechanisms leads to less scour at the downstream column compared to that around a single column subjected to the same test conditions (Ataie-Ashtiani and Beheshti, 2006; Keshavarzi et al., 2018).

However, there is one exception to the rule that a sheltered column experiences less scour, i.e., when the width of the upstream column is greater than that of the downstream one (Beg and Beg,

2015). In these cases, the scour depth at a downstream (sheltered) column may surpass that for a single column, because the scour holes forming around the two columns join and the scour depth of the upstream column dictates the depth of scour at the sheltered column.

The scouring around the sheltered column occurs at a much slower rate than around the upstream column (Keshavarzi et al., 2018). This difference is very important particularly in transient flows such as tsunami inundations, because the equilibrium scour depth is often not reached by the time the flow subsides.

When the angle between the lines of the columns and the direction of the flow is greater than 15^{o}, an accentuation of scour occurs at the downstream column due to vortices shedding from the upstream column (Hannah, 1978). This accentuation of scour is present even when the columns are placed laterally to the flow (Memar et al., 2018). Beg (2010) found that the presence of a second, laterally spaced column increased the width, length, and depth of the scour holes around each column, but only up to the point where the columns were spaced apart (S) to 7 times the columns' widths (b). The maximum amplification of scour depth occurs when $S = 0$. In this case, the two columns act similarly to a single column of twice the width. The increase in scour at low S is caused by the compression of the flow between the columns, which compresses the horseshoe vortex (Hosseini and Amini, 2015) and increases the sediment transport (Yang et al., 2020). As S increases, the scour amplification caused by the presence of the second column decreases (Ataie-Ashtiani and Beheshti, 2006).

Elliott and Baker (1985) found that the flow intensity (the ratio of flow velocity to the critical flow velocity necessary for sediment transport) was positively correlated with the scour amplification linked with lateral spacing. Similarly, Yang et al. (2020) found that the Froude number affected the scour hole forming around column groups. Therefore, considering tsunami-induced scour, the flow conditions may have an effect on the sheltering and spacing effects.

Scour around isolated columns in tsunami flows has been researched with post-tsunami field campaigns, numerical models, and experimental models (Jayaratne et al., 2016; Kato et al., 2000; D. J. McGovern et al., 2019; Moon et al., 2014; Nouri et al., 2010; Palermo et al., 2013; Rueben et al., 2015; Sarjamee et al., 2017; Thomas et al., 2015; Tonkin et al., 2003; Yeh and Li, 2008; Yoshii et al., 2017). Through the use of physical models of tsunami-like waves, parameters such as sediment grain size (Lavictoire et al., 2014), structure width (Mehrzad et al., 2016), flow depth (Tonkin et al., 2013), number of waves (Chen et al., 2013; Larsen et al., 2018, 2017), and wave periods (D. J. McGovern et al., 2019) have been found to influence tsunami-induced scour. Similar to steady flow conditions, turbulent eddies forming around vertical structures are responsible for the transport of bed materials around columns (April Le Quéré et al., 2020; Larsen et al., 2018, 2017; D. J. McGovern et al., 2019), and also like in steady flow conditions, these flow structures may be affected by the addition of a second column.

Le Quéré et al. (2021) showed the risk of tsunami-induced scour amplification due to lateral column spacing with the use of a numerical model, and both the flow conditions and the spacing were found to affect the amplification caused by the addition of a second column. These observations are yet to be confirmed with a physical model.

Based on the literature reviewed, the hypotheses presented here are that the presence of an upstream structure will reduce the scour at a design column, and that a structure spaced

transversely to the design structure will result in an amplification of scour. The objectives of this study were:

1- To verify that the produced dambreak bores had hydrodynamic properties similar to real-life tsunamis;
2- To study the effect of the presence of a sheltering structure on scour around the design structure;
3- To study the effect of the presence of a laterally spaced structure on scour around the design structure; and
4- To propose comprehensive design guidelines based on the results of the present study in order to improve on current tsunami scour predictions.

7.3 Methodology

To accomplish the above-mentioned objectives, the authors elected to conduct a comprehensive physical experiment. The new dambreak flume at the University of Ottawa, Canada, was utilized for this endeavour. Different column setups and flow conditions were tested to fully investigate the influence of sheltering and lateral spacing on tsunami-induced scour.

7.3.1 Experimental setup

The dambreak flume was 30.3 m in length, 1.5 m in width and 1.5 m in depth. The flume floor was horizontal and did not allow for the installation of a sand bed, and therefore a false floor composed of four subsections was constructed in order to raise the existing floor and allow the installation of a sand bed section. The four subsections were established as follows (see Figure 7.2 for more details on the experimental setup):

1) Approach slope: This section was constructed with a steel plate supported by several cinder blocks, and caulking was used to ensure a tight seal around the edges.
2) Horizontal false floor: This section was built completely out of cinder blocks, and a steel plate covered the section to create a uniform surface. This section was painted in white, and black lines were drawn at 0.2 m intervals to allow for estimates of the bore front velocity and flow surface velocity.
3) Sand bed: The median grain size (d_{50}) of the sand was 0.1 mm, and a gabion was installed at the upstream end of this section in order to reduce the inevitable scour occurring at the sand bed-false floor interface. A drain component constructed of uniform gravel covered with a geotextile material was installed below the bed to allow excess water to drain out of the test area.
4) Concrete weir: The concrete weir was constructed with cinder blocks installed on the gravel drain.

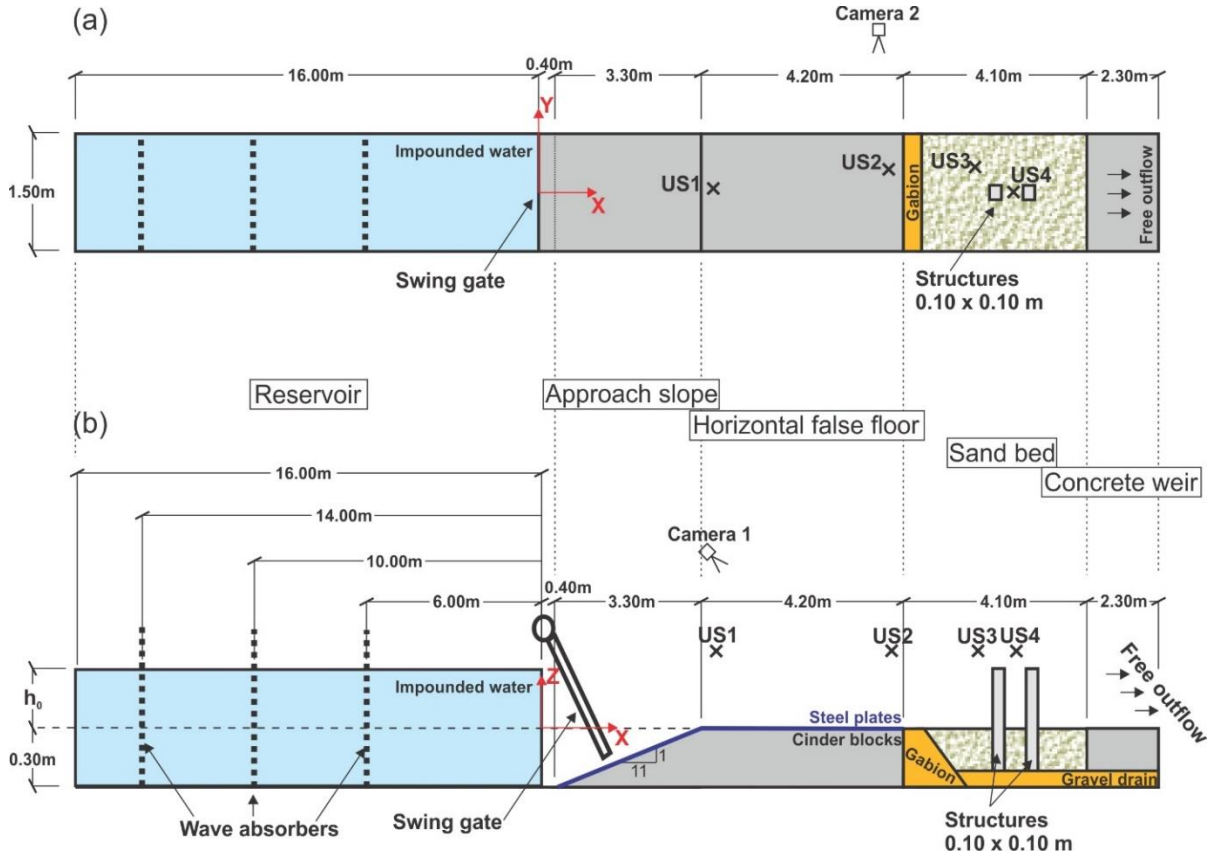

Figure 7.2: Flume setup and equipment location: (a) plan view; (b) side view

The dambreak wave was produced by releasing water impounded behind a piston-activated swing gate (Figure 7.3(b)). The rapid opening of the swing gate led to a near-instantaneous release of the impounded water. The gate-opening time satisfied the standards used in previous dambreak research for the free release of impounded water (Lauber and Hager, 1998; Jacob Stolle et al., 2020, 2019). The flume downstream of the gate was dry along its full length. The runup of the dambreak wave on the false floor generated a negative wave that propagated upstream, which was reflected onto the structural setup, and therefore three wave absorbers with a porosity of 0.5 were installed in order to reduce the action of the negative wave. In addition, a thick fiber mat was installed on the upstream-most wave absorber to further damper the action of the reflected wave. The negative wave is described in more detail in the *Bore hydrodynamic properties* section.

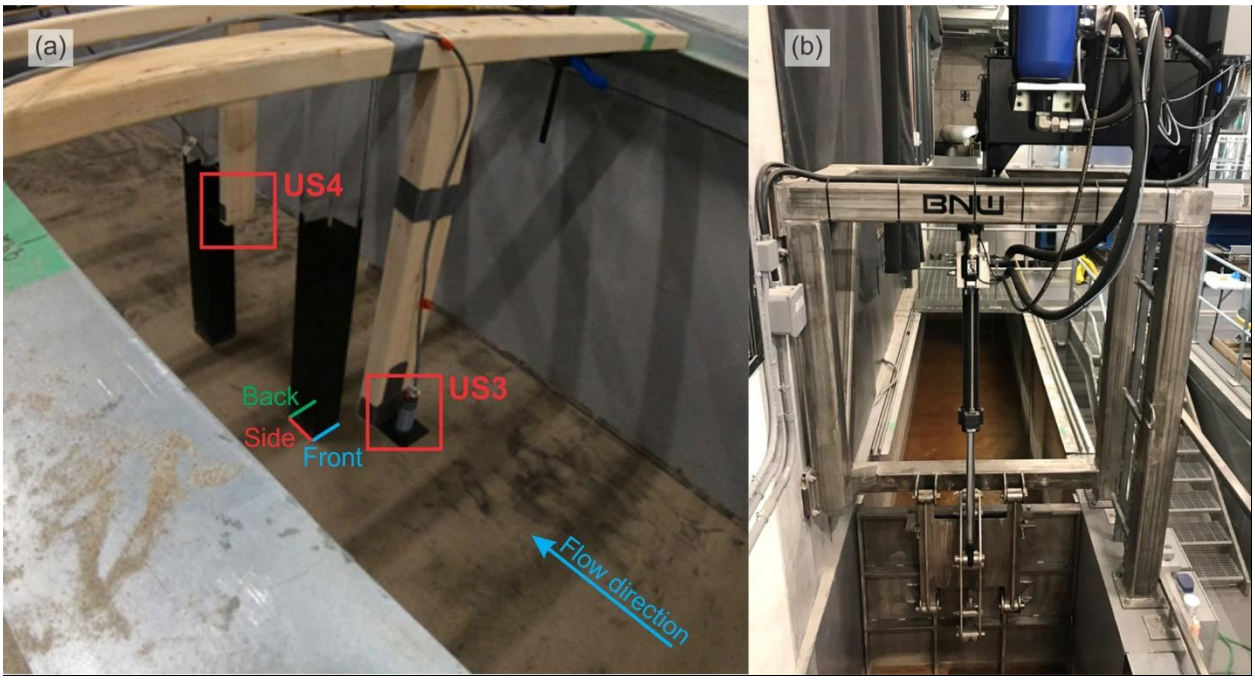

Figure 7.3: (a) Column and ultrasonic sensor disposition; (b) the piston-activated swing gate

7.3.2 Equipment

Four ultrasonic sensors (MassaSonic, M5000, Hingham, United States; accuracy 1 mm, range 0.1 m to 1.0 m) were installed at strategic locations along the flume to monitor the progress of the surface of the dambreak wave. The *X*,*Y* positions of the ultrasonic sensors, in meters, were: US1 (4.5, 0); US2 (7.5, 0.2), to monitor the flow behavior on the horizontal false floor section; US3 (10.0, 0.2), to monitor the undisturbed flow behavior just before the columns; and US4 (10.85, 0), to monitor the runup at the front face of the design column. The locations of the ultrasonic sensors were as described in Figure 7.2.

A data acquisition system (HBM, MX1601B, Darmstadt, Germany; rate = 200 Hz) with 16 individually configurable channels was utilized to convert the analog voltage signals from the ultrasonic sensors to digital format.

Two cameras were used during the experiments. Camera 1 (GoPro, HERO 7, San Mateo, United States; rate = 240 FPS, resolution = 720p) was installed above the flume and looking down at the horizontal false floor section, with an *X*,*Y* position of (4, 0). Camera 1 was used to evaluate the bore front velocity as it progressed on the horizontal false floor section. The black lines on the horizontal false floor section were used to track the bore front position, with the times of the bore passage at each line being used to determine its velocity. Camera 2 (Apple, iPhone 7, Cupertino, United States; rate = 240 FPS, resolution = 720p) was positioned on top of the flume sidewall (see Figure) looking down at the position of US2 (7.5, 0.8). Hollow plastic balls 5 mm in diameter were released in the reservoir prior to each experiment, and the times of their passage over the lines with position X = 7.40 m and X = 7.60 m were used to estimate the velocity of the balls near US2, which is served to estimate the flow surface velocity. A visual representation of the positions of the two cameras can be found in Figure 7.2.

A Terrestrial Laser Scanner (Leica, ScanStation P50, Heerburgg, Switzerland; accuracy = 1.2 mm @ 120 m) was utilized to scan the bed elevations before and after the bore passage. The difference between the two measurements was used to evaluate the scour caused by the dambreak bore. The laser scanner was positioned at a minimum of three locations around the columns to scan the whole bed. Stitching of the scans generated a three-dimensional representation of the bed topography. For the sheltering runs with two upstream columns, one scan had to be performed outside the flume in order to measure the whole bed. The authors adjusted the data from these scans to account for light refraction through the Plexiglas wall of the flume.
Three square columns with a width (b) of 0.10 m were employed in the experimental campaign (see Figure 7.3(a)). The walls of the columns were constructed out of 0.01 m-thick Plexiglas. All sides of the columns were painted with matte black paint to prevent the laser scanner from measuring the bed elevation through them, which would have induced measurement error due to light refraction when the laser passed through the column walls.

7.3.3 Test procedures

Two setups were used to test the sheltering effect and the lateral spacing effect. For the sheltering setup (Figure 7.4), three distances were varied in order to test the dependency of the scour on those distances: the longitudinal distance between the upstream macroroughness element and the design column (L_D), the elevation Z of water in the reservoir prior to the dambreak (h_0), and the width of the upstream macroroughness element (b_{Sh}). This entailed 10 different tests, as detailed in Table 7.1. The test numbers in Table 7.1 accord with the particular test settings. The first two letters refer to the type of setup (Sh: sheltering setup; Sp: spacing setup; Sg: single column). The numbers immediately following h, L, and b refer to the scale of h_0 (1: 0.15 m; 2: 0.25 m; 3: 0.35 m), the scale of L (2: 2b; 3: 3b; 4: 4b), and the scale of b_{Sh} (1: 1b; 2: 2b), respectively.

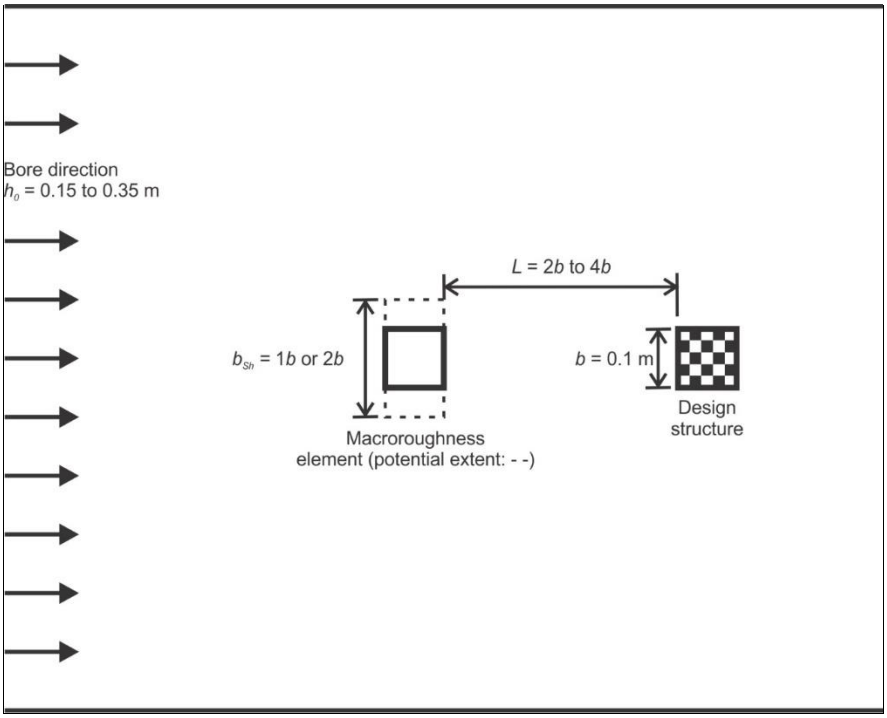

Figure 7.4: Plan view of sheltering setup column arrangements tested

Test no.	Type of setup	Impoundment depth (h_0) (m)	Downstream distance (L_D)	Width of macroroughness element (b_{Sh})
Sh_h1_L2_b1	Sheltering	0.15	2b	1b
Sh_h1_L2_b2	Sheltering		2b	2b
Sh_h2_L2_b1	Sheltering	0.25	2b	1b
Sh_h2_L2_b2	Sheltering		2b	2b
Sh_h3_L2_b1	Sheltering	0.35	2b	1b
Sh_h3_L2_b2	Sheltering		2b	2b
Sh_h2_L3_b1	Sheltering	0.25	3b	1b
Sh_h2_L3_b2	Sheltering		3b	2b
Sh_h2_L4_b1	Sheltering	0.25	4b	1b
Sh_h2_L4_b2	Sheltering		4b	2b

Table 7.1: Sheltering setups utilized

For the spacing setups, two columns were installed on the same transversal line. To test the influence of the macroroughness element column on the scour depth at the design column, two settings were varied (Figure 7.5): the elevation Z of water in the reservoir prior to the dambreak (h_0), and the distance between the macroroughness element column and the design column (S). In total, 15 tests were carried out (Table 7.2). The numbers in Table 7.2 summarize the test setups, where the first two letters refer to the type of setup (Sh: sheltering setup; Sp: spacing setup; Sg: single column). The numbers immediately following h and S refer to the scale of h_0 (1: 0.15 m; 2: 0.25 m; 3: 0.35 m) and the scale of S (0: 0b; 1: 1b; 2: 2b; 3: 3b; 4: 4b), respectively.

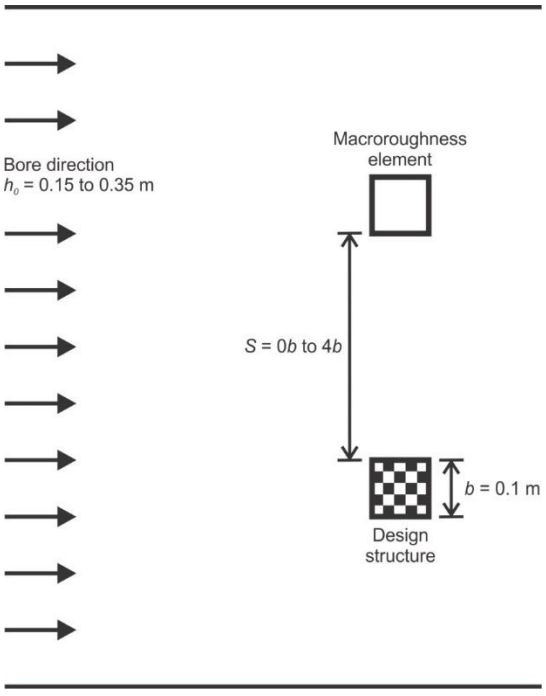

Figure 7.5: Plan view of lateral spacing setup column arrangements tested

Test no.	Type of setup	Impoundment depth (h_0) (m)	Spacing ratio (S)
Sp_h1_S0	Spacing	0.15	0b
Sp_h1_S1	Spacing		1b
Sp_h1_S2	Spacing		2b
Sp_h1_S3	Spacing		3b
Sp_h1_S4	Spacing		4b
Sp_h2_S0	Spacing	0.25	0b
Sp_h2_S1	Spacing		1b
Sp_h2_S2	Spacing		2b
Sp_h2_S3	Spacing		3b
Sp_h2_S4	Spacing		4b
Sp_h3_S0	Spacing	0.35	0b
Sp_h3_S1	Spacing		1b
Sp_h3_S2	Spacing		2b
Sp_h3_S3	Spacing		3b
Sp_h3_S4	Spacing		4b

Table 7.2: Lateral spacing setups utilized

Although not shown in this article, in the spacing tests, a third column was present downstream of the two laterally spaced columns in order to test the effect of flow constriction on scour formation at the downstream column. The two laterally spaced columns were utilized as macroroughness elements to amplify the flow at the downstream column and amplify the scouring at the latter. However, the downstream column was found to have a negligible effect on scour-hole formation around the laterally spaced upstream columns. The effect of the downstream column was tested by running tests with and without the column and comparing the scour depths. The standard deviation divided by the mean of the maximum scour depth of the two setups was 3.7%, which was judged to be negligible, especially when compared to the normalized standard deviation of the maximum scour depth for the single-column tests (3.3%).

In addition, a single-column test was conducted for each h_0 in order to obtain a baseline to test the effects of lateral spacing and sheltering on scouring (see Table 7.3).

Test no.	Type of setup	Impoundment depth (h_0) (m)
Sg_h1	Single column	0.15
Sg_h2	Single column	0.25
Sg_h3	Single column	0.35

Table 7.3: Single column setups utilized

Between each test, a delay of at least 22 hours was allowed to ensure a similar soil water content prior to the next test. Before each run, the bed was leveled with a flat wooden stud, and horizontal polystyrene guides installed along the flume walls helped in ensuring a horizontal, level bed. Depressions in the sand bed were filled and compacted by hand. Immediately after each test, the swing gate was closed and any water present between the approach slope and the swing gate was

pumped out. The three-dimensional scans of the flume were performed 1 hour after each test to allow residual water in the sand bed to exit through the gravel drain.

7.4 Repeatability

Repeatability of the present experiment was tested by comparing the transversal cross-sections of final bed elevation at X = 10.89 m (0.01 m upstream of the columns) for three repetitions of the test Sp_h2_S3. The normalized standard deviation of the bed elevation along the whole cross-section for the three tests was of 0.96% (Figure 7.6). In addition, the three single-column tests were performed at least twice each, and the normalized standard deviation for the maximum scour depth of those tests was 3.3%. Therefore, it was concluded by the authors that the present experimental series is highly repeatable.

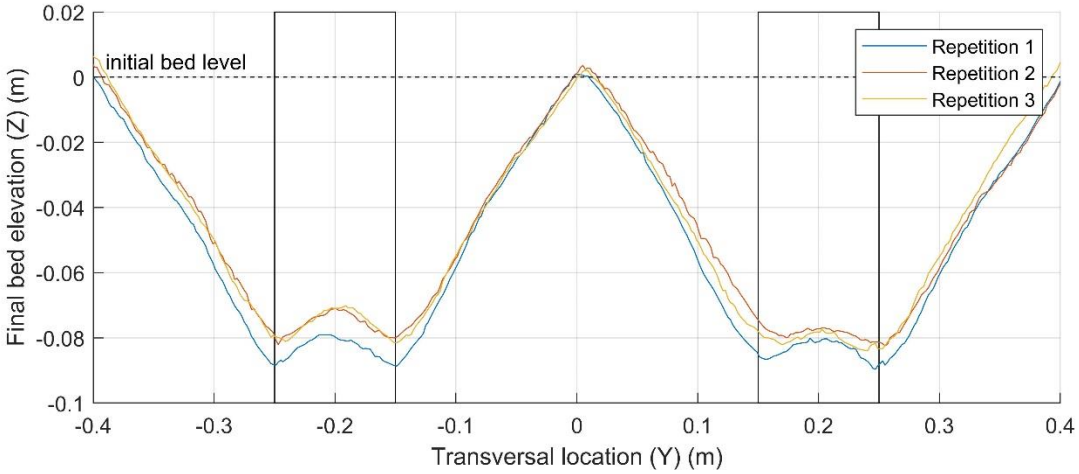

Figure 7.6: Scour repeatability of Sp_h2_S3 test

7.5 Results

The current section of this article reports the main results of the above-described experiments. It is divided in four subsections: (1) the hydrodynamic properties of the dambreak bore; (2) the flow behaviour around the columns arranged in a sheltering setup; (3) the effects on scouring of two columns placed in a sheltering setup; and (4) the hydrodynamic and sediment transport results associated with the spacing setups.

7.5.1 Bore hydrodynamic properties

The bore hydrodynamic properties at US2 are illustrated in Figure 7.7. By the time the bore reached US2, the bore had run up on the approach slope and passed over the majority of the horizontal false floor (see Figure 7.2 for reference). The longitudinal position of US2 was chosen in order to display the hydrodynamic properties of the bore because the bore had not yet reached any columns, nor did the movable bed section and the painted horizontal floor at that location allow for an estimation of the flow velocity. Figure 7.7(a) shows the flow depth measured at US2. In the initial stage of the bore (t = 0 s to t = 10 s), the flow depth rapidly increased to its maximum, and then

the flow depth gradually decreased until the return wave reached US2, which was accompanied by numerous surface ripples. The authors dampened this return wave by installing three wave absorbers, which reduced its height by 70% and produced surface ripples from the partial reflection of the return wave by the wave absorbers. The authors judged that this wave absorber setup was a good compromise between reducing the energy of the return wave and mitigating the impact of the absorbers on the free flow of the impounded water. Greater h_0 led to greater flow depth.

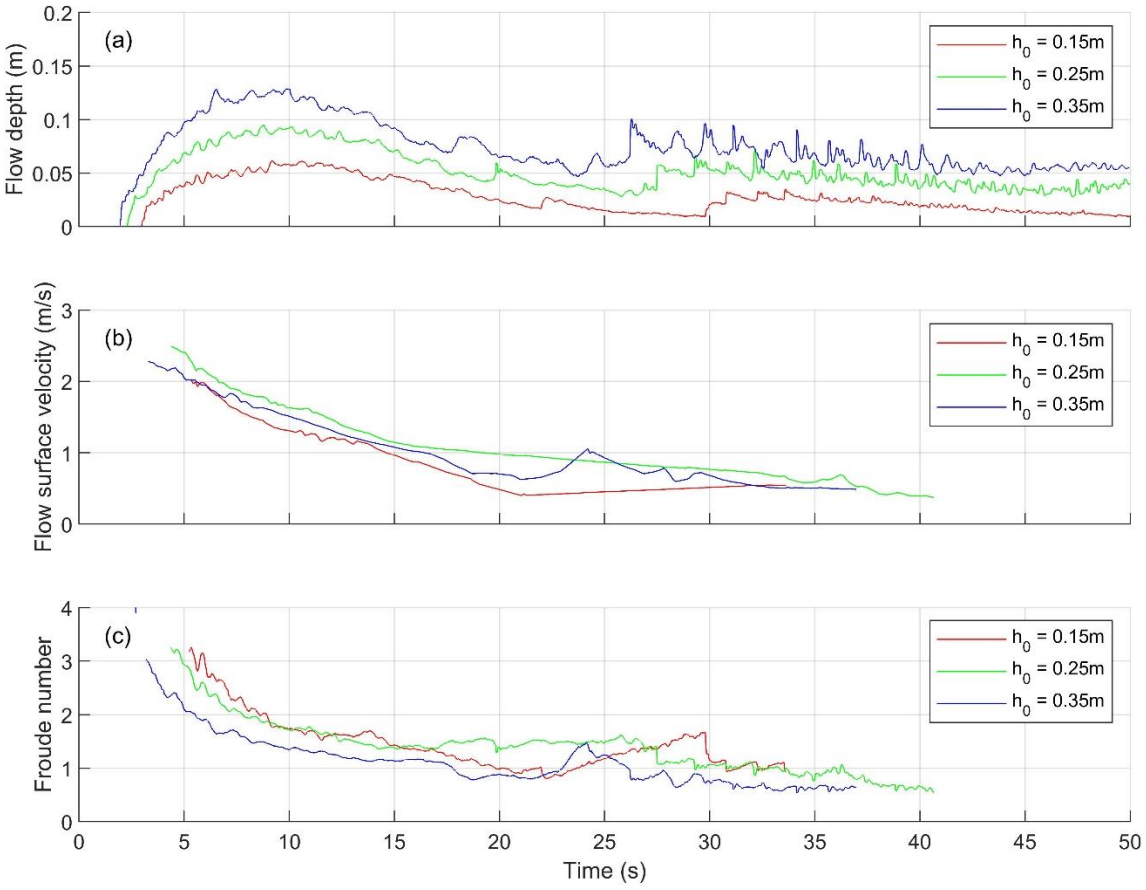

Figure 7.7: Hydraulic properties of flow at US2: (a) flow depth; (b) flow surface velocity; (c) Froude number

In Figure 7.7(b), the flow surface velocity as measured with the floating plastic particles is shown. The greatest surface velocity was measured at the beginning of the bore. The surface velocity then gradually decreased with time. In contrast to the flow depth, no strong correlation was found between the surface velocity and h_0. The Froude number for the undisturbed dambreak bore was calculated by using the flow depth and the surface velocity (Figure 7.7(c)). The utilization of the surface flow velocity may lead to a slight overestimation of the Froude number, since it does not represent the depth-averaged velocity that is normally used in this relationship. However, the relatively smooth false floor and the turbulent nature of the dambreak bore reduced the vertical gradient of the longitudinal velocity, and so therefore, in this case, the surface velocity was a good representation of the flow velocity. The Froude number was found to be at its maximum at the arrival of the bore front, and then rapidly decreased to a value between 1.0 and 1.5. The magnitude of the Froude number remained in this range for most of the inundation. Similar to the situation with the velocity, no strong correlation between the Froude number and h_0 was found.

7.5.2 Sheltering effects on flow behavior

Figure 7.8 shows a still shot of the test Sh_h3_L2_b1 at t = 7 s. Although this is just an example at one instant during one test, this figure gives an example of the flow structure that formed around the columns in every sheltering setup. The flow around the upstream macroroughness element acted similarly to the flows during the single-column tests. Due to the supercritical nature of the flow, the design column did not affect the flow around the upstream macroroughness element. However, it should be mentioned, in a general case, the design column may affect the flow around upstream macroroughness when the distance between the two structures is short. At the front face of the macroroughness element, a strong surface roller formed due to the flow being redirected vertically. The water from the roller was then pushed laterally to form a V-shaped wake. The water then wrapped around the macroroughness element and generated disorganized turbulence at the back face. This turbulent flow then reached the design column and started transporting the soil around it. Weak rollers formed on the sides of the design column, but no distinct structured eddies were present. This disorganized turbulent flow means that a horseshoe vortex did not form and scour the soil in a way similar to that in a single-column test. A reduction in scour at the design column can be expected because of the absence of a horseshoe vortex. Downstream of the design column, a small section of strong turbulence was observed, followed by a V-shaped wake.

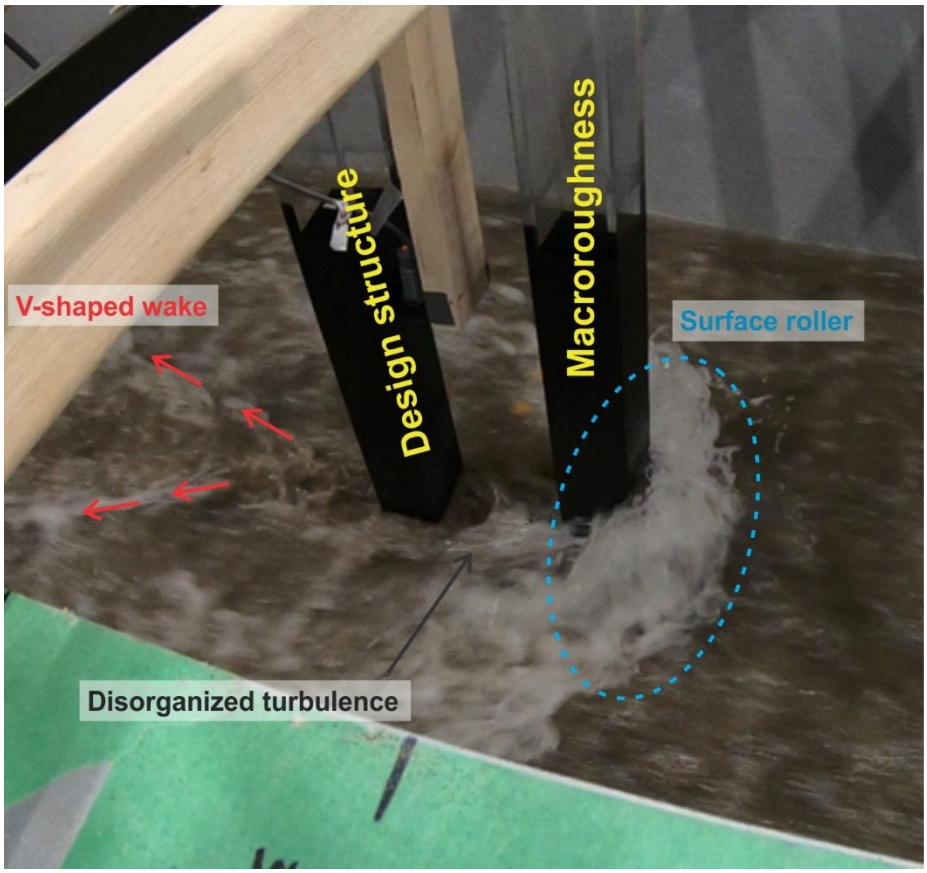

Figure 7.8: Turbulent flow structures around two structures placed in a sheltering setup (Sh_h3_L2_b1 at t = 7 s)

The maximum runup was measured for all setups by US4 (Figure 7.9). All setups resulted in a reduction in maximum runup at the design column compared to the single-column tests with the

same h_0. The minimum reduction for the tests was 24% for Sh_h2_L4_b1 and a maximum of 49% for Sh_h3_L2_b2. In the setups tested, L_D did not have a definitive influence on runup. The width of the upstream macroroughness element (b_{Sh}) was found to have a strong influence on the runup at the design column. An average reduction of 9% of the runup at the design column was measured when b_{Sh} was increased from 1b to 2b. Lastly, an increase in h_0 resulted in an inverse correlation with the relative maximum runup at the downstream column. This influence of h_0 was likely caused by the magnitude of highly turbulent area around the structures. The higher h_0 resulted in a deeper flow at the structures, which allowed for larger eddies to form. Since L was not changed when h_0 was increased, the scale of the eddies associated with the greater h_0 was greater in comparison with the scales of the columns and L.

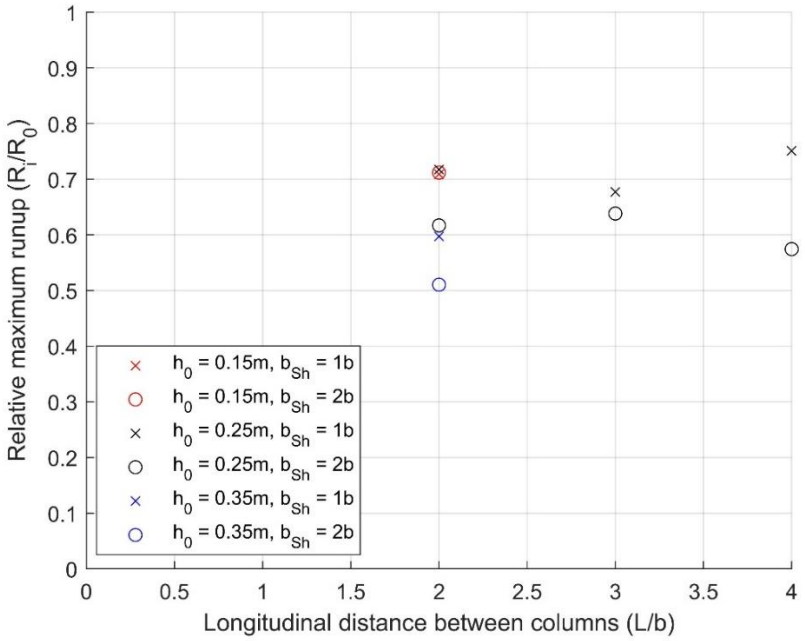

Figure 7.9: Relative maximum runup (maximum runup of the test (R_i) divided by the maximum runup of the single-column test (R_0)) with respect to the longitudinal distance between columns

7.5.3 Sheltering effects on scour

Figure 7.10 shows a two-dimensional representation of the post-bore bed topography for all the sheltering setups. The scour holes forming at the upstream macroroughness element were bowl-shaped, and maximum scouring was found at the front corners. At the back face of the macroroughness element, accumulation was noted except for the setups where h_0 = 0.35 m and when h_0 = 0.25m and b_{Sh} = 2b, because the scour hole induced by the eddies forming at the upstream corners extended past the sides of the macroroughness element and to the back face. However, when h_0 < 0.35m, accumulation occurred between the columns and downstream of the design column. When h_0 = 0.35m, the scour hole forming around the macroroughness element extended downstream until it reached the design column, and one non-uniform scour hole was formed. The combination of the accumulation between the columns and the disorganized flow reaching the design column led to far less scouring at the design column compared to the single-column tests. The scouring at the design column was greatly reduced when b_{Sh} was increased from

1*b* to 2*b*. The locations with the deepest scour were found either at the corners of the front face or in the middle of the front face.

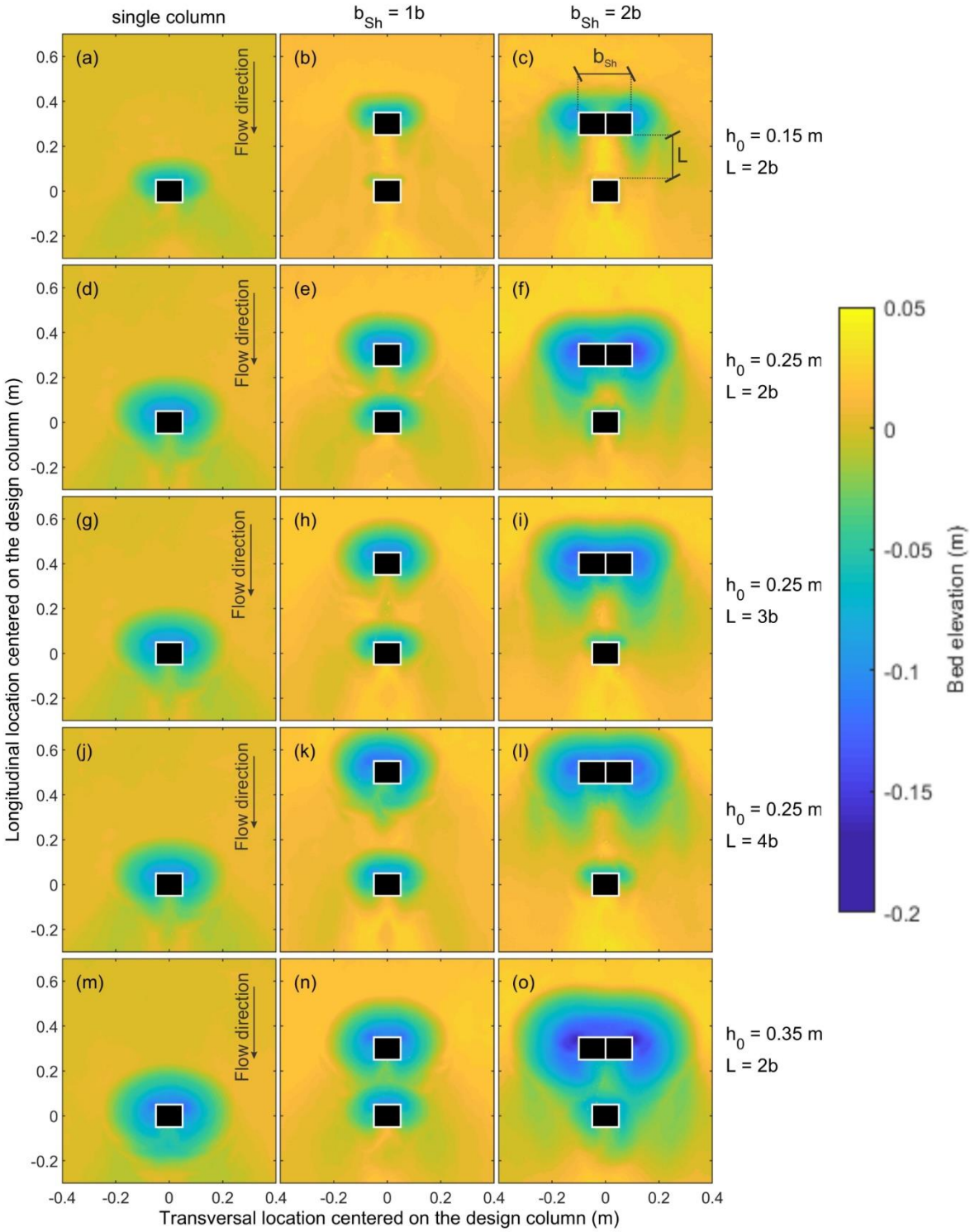

Figure 7.10: Post-bore topographies

The maximum scour reduction for all the different setups is presented in Figure 7.11. All three distances (h_0, b_{Sh}, and L_D) in the tests were found to influence the maximum scour depth at the design structure. h_0, only tested for $L_D = 2b$, was found to be inversely correlated with the sheltering effect of the upstream macroroughness element, meaning that the upstream macroroughness element reduced the scour forming around the design column more with lower h_0. The greater effect at low h_0 may be caused by the fact that the shear stress the inundation induced on the sand was low and that the energy loss caused by the upstream macroroughness element reduced the excess shear stress more than when h_0 was greater. In addition, accumulation between the columns may have caused some filling in the scour hole in the latter stages of the inundation. On the other hand, at h_0 = 0.35 m, the scour hole around the upstream macroroughness element reached the design column, which enhanced the scour depth at that column.

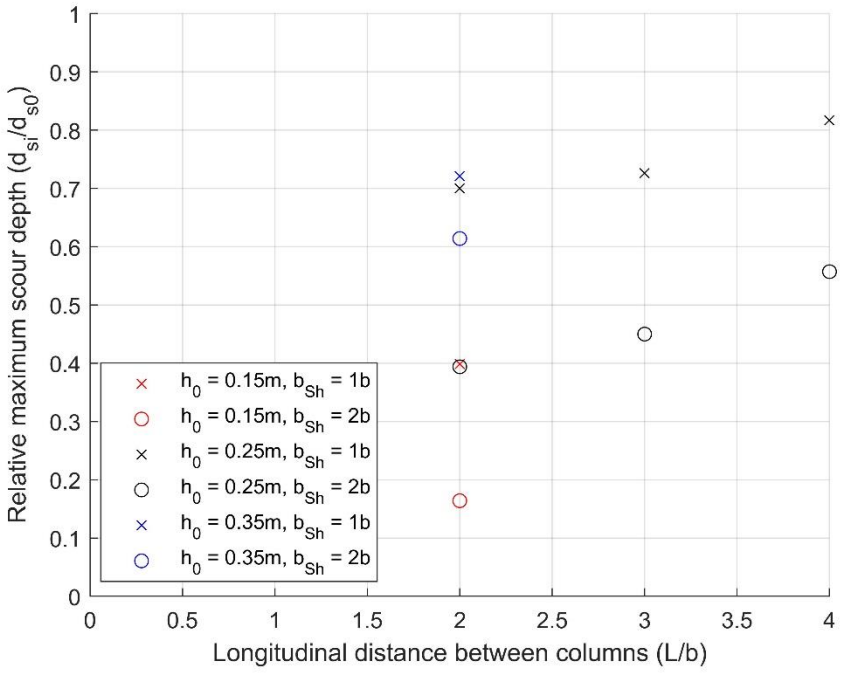

Figure 7.11: Relative maximum scour depth (maximum scour depth of the test (d_{si}) divided by the maximum scour depth of the single column test (d_{s0})) with respect to the longitudinal distance between columns (L_D/b)

As L was increased, the sheltering effect decreased, and the turbulence of the rooster tail behind the upstream macroroughness element decreased as it moved downstream. This resulted in a more uniform flow, which in turn allowed for more developed eddies to form around the design column and scour the soil. The formation of developed eddies is apparent when comparing Figure 7.10(f) and Figure 7.10(l). In the former, most of the scouring was found on the sides of the design structure and did not resemble the typical scour hole around a single column. In the latter case, the scour hole shape was very different. The scouring was found at the corners of the front face, which was similar to the single-column cases, where the flow prior to impacting the column is undisturbed and developed eddies form at the upstream corners.

b_{Sh} was found to be positively correlated with the sheltering effect, and Figure 7.12 shows its influence on the relative maximum scour depth. The reduction in relative maximum scour depth at the design column was found to be as high as 25% when b_{Sh} was increased from 1b to 2b. This

reduction was because of the increased blockage from the upstream macroroughness element. The smaller difference in the tests with h_0 = 0.35 m was caused by the fact that the scour hole around the upstream macroroughness element reached the design structure and enhanced the scouring there.

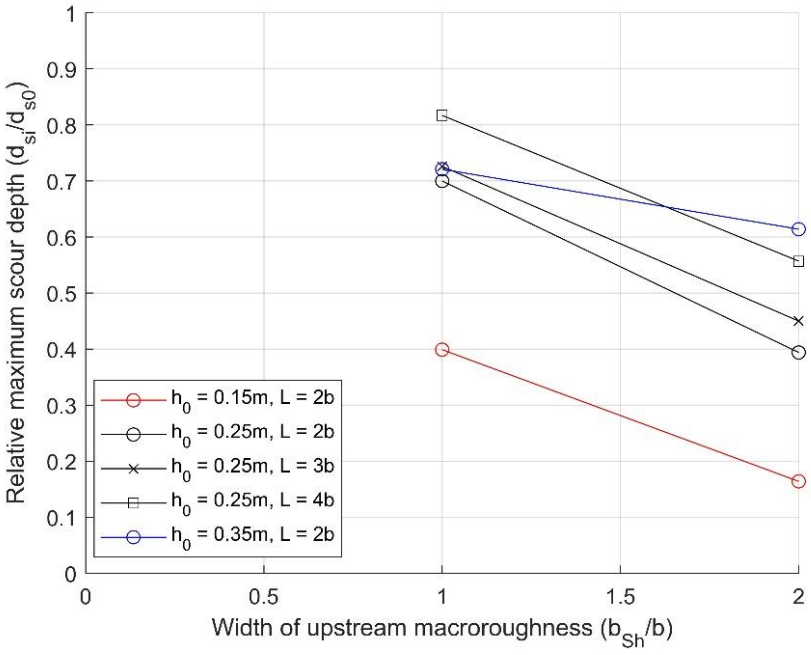

Figure 7.12: Relative maximum scour depth with respect to distance between columns (b_{sh}/b)

7.5.4 Spacing effects

Figure 7.13 shows the flow structures forming around the two columns of the Sp_h1_S2 test at four different times. At t = 7 s, a strong surface roller formed at the front face of both structures, and there was no apparent interaction between these two flow structures except for between the two columns where the two waves merged. At that location, the rollers around each column were rotating in opposite directions. This led to strong surface turbulence, which may have led to the difference in scouring between the columns. Downstream of the columns, two defined V-shaped wakes, one for each column, formed. The size and strength of those two turbulent structures decreased rapidly with time. These flow structures were noted to be very similar to the flow structures that formed around a single column, except for the interaction between the columns.

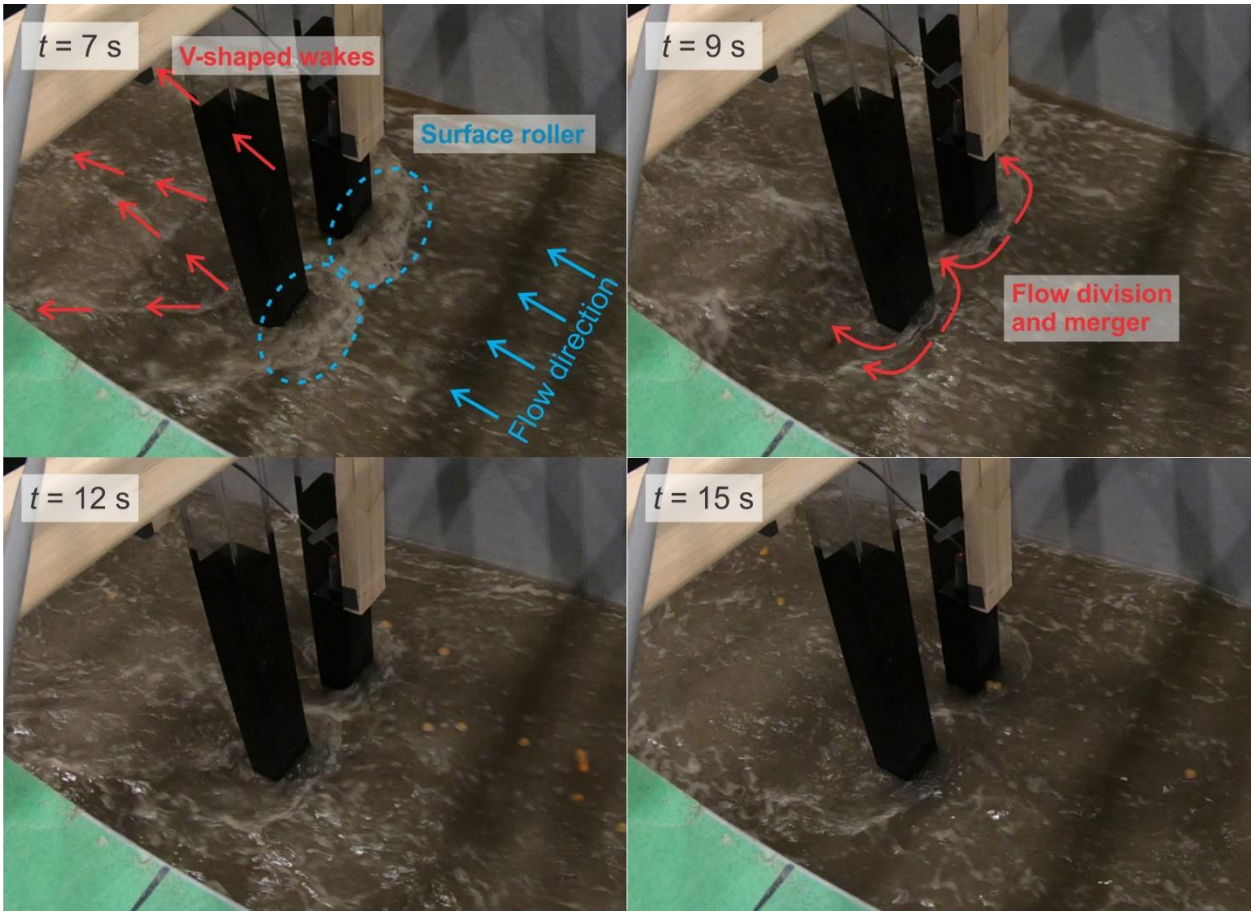

Figure 7.13: Turbulent flows around two laterally spaced structures (Sp_h1_S2)

As in the single-column tests, the scour holes formed around the laterally spaced columns were bowl-shaped, with the maximum scour occurring at the front corners due to the shape of the eddies around each column (see Figure 7.14). In most setups, the scour hole reached the back corners. When h_0 = 0.25 m or 0.35 m, the scour hole reached the center of the back face. For all setups with $S \leq 2$, the scour holes that had formed around each column joined together (Figure 7.14(d) to Figure 7.14(l)) and for Sp_h3_S3 (Figure 7.14(o)).

As noted in the *Test procedures* section, a third column was present downstream at a distance of $L = 2b$ in all of the spacing tests (Figure 7.14(d) to Figure 7.14(r)). However, its influence was found to be negligible when compared with the tests without this column. The upstream limit of the scour hole forming around the downstream column can be seen in Figure 7.14(o), Figure 7.14(q), and Figure 7.14(r). Because of the supercritical nature of the flow, the presence of the downstream column had no influence on the eddies at the front face of the laterally spaced columns which drove the sediment transport, since the presence of that column prevented sediment accumulation from forming directly downstream of the laterally spaced columns. However, the focus of this paper is on the scour holes forming around the columns, not on sediment accretion downstream of them.

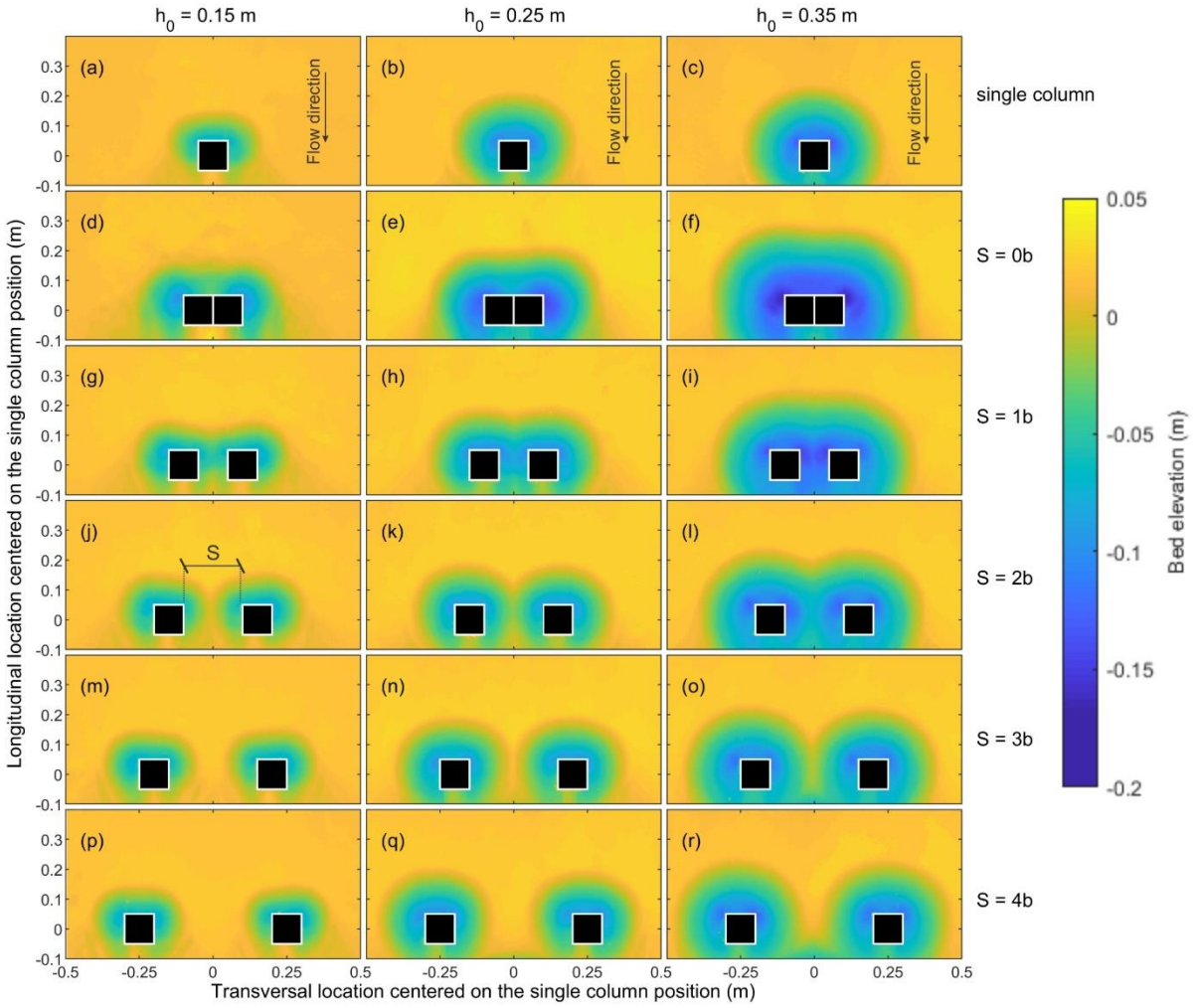

Figure 7.14: Spacing setup post-bore topographies (includes single columns)

The maximum scour depth was found at the front corners of the structures, and more particularly, when $S = 1b$, the centermost front corners showed the deepest scour, while when $S = 0$ or $S > 1b$, the locations of the deepest scour were at the outermost front corners. In addition, the edges of the scour holes in most setups were not symmetrical around the transversal center of each column. Also, the scour holes were larger and extended farther upstream on the outer-most sides. Figure 7.14(j) best illustrates the formation of the non-symmetrical scour holes. These skewed scour holes were due to a compression of the horseshoe vortex between the columns (Hosseini and Amini, 2015), caused by the presence of the additional laterally spaced column.

Figure 7.15 illustrates the transversal cross-sections for each test 0.01 m upstream of the two laterally spaced columns. The zero on the x-axis represents the center of the leftward column. The second column would be located on the negative side of the x-axis, with the spacing as described in the legend. In 7 of the 9 setups with $S > 1b$, the scouring was deeper near the outside corners (at 0.05 m on the x-axis). In addition, in most of the setups with $S > 1b$, less scouring was noted compared to the single-column setup.

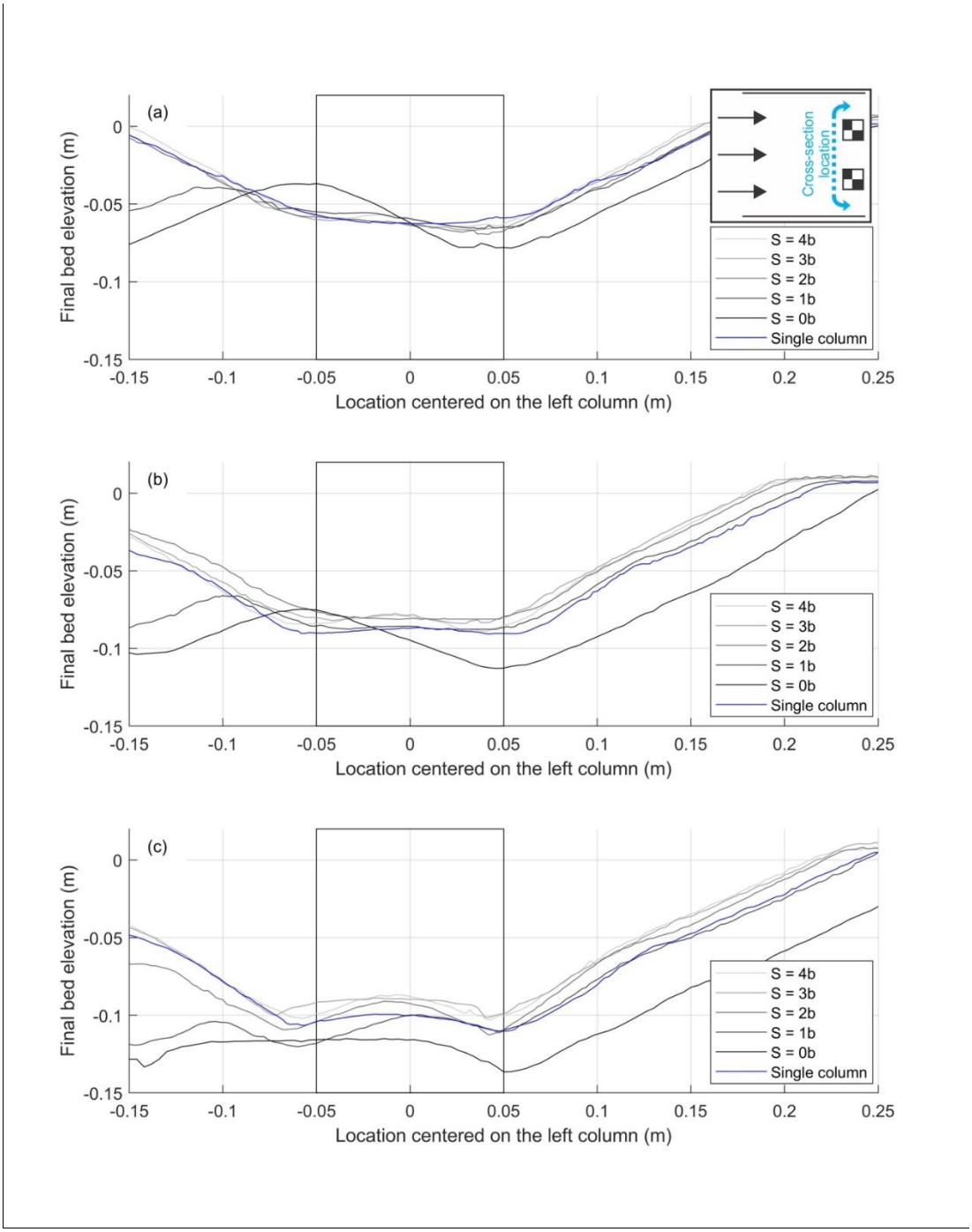

Figure 7.15: Cross-section of bed 0.01m upstream of columns, centered on the left column

When comparing the maximum scour depths of the dual-column tests to those of the single-column tests, the tests with $S = 0b$ and $S = 1b$ and Sp_h1_S2 showed an increase in maximum scour depth (Figure 7.16). The rest of the tests showed a decrease in maximum scour depth of up to 14%. The tests with $S = 0b$ showed an average scour amplification of 19%, with no strong correlation between h_0 and the relative maximum scour depth. This column disposition is similar to doubling the effective width of a single column, since water does not flow between the two columns. As S increased, the relative maximum scour depth decreased. When $S \geq 2b$, the maximum scour depth

decreased and was lower than that for the single-column tests. Therefore, the mechanism governing the scouring was negatively impacted by the presence of the second column, and/or a greater amount of deposition was caused by the presence of the second column. If only the latter phenomenon took place, the vortices around the structures would lead to the same sizes and shaped of the scour holes, but accumulation at the bottom of the holes would increase the bed elevation. In this case, the width of the scour holes would be the same as in the single column case, and either the slopes of the scour holes would be milder or the bottoms of the holes would be flat because of deposition. However, when observing the cross-sections between x = 0.05 m and x = 0.25 m in Figure 7.15, it is apparent that when S was greater, the width of the scour hole decreased. The authors concluded from this observation that deposition was not responsible for this reduction in maximum scour depth, and instead, a reduction in the strength of the vortices forming around the structures was responsible for the reduction in scour.

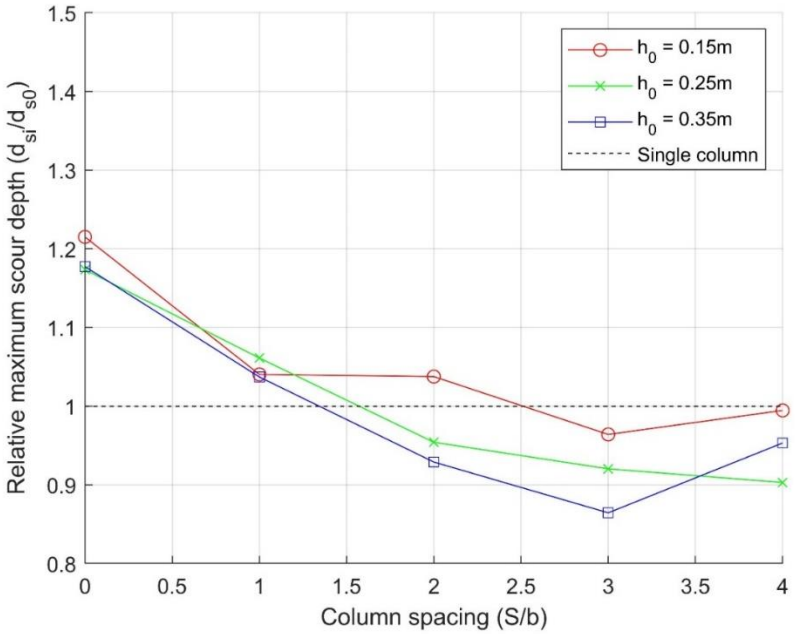

Figure 7.16: Relative maximum scour depth variation (maximum scour depth of the test (d_{si}) divided by the maximum scour depth of the single column test (d_{s0})) with the lateral spacing ratio and the bore-generating impoundment depth (h_0)

7.6 Discussion

7.6.1 Column Sheltering

Sheltering effects on runup and scour led to the expected results, i.e., the setups with greater upstream macroroughness element widths (b_{Sh}) increased the sheltering effect, while the setups with a shorter distance between the macroroughness element and the design structure (L_D) increased the sheltering effects. In both cases, the eddies around the design structure became more disrupted by the upstream macroroughness element as b_{Sh} increased and L_D decreased. This led to the turbulent flow patterns influencing the formation of scour at the design column.

h_0 also influenced the sheltering effect on runup and scouring at the design column. h_0 was positively correlated with runup and negatively correlated with scour reduction. The lower flow momentum associated with low h_0 resulted in less energy loss from the upstream macroroughness element, leading to a flow with sub-critical velocity at the design column and hence a decreased scour depth. In addition, sediment accumulations on the lee side of the macroroughness element increased the bed elevation near the design structure.

Runup is determined as the flow depth added to the bed elevation at the location of measurement. Therefore, in cases with deeper scouring but a similar flow depth, the runup was lower. In cases with h_0 = 0.35 m, the scour depth was greater in proportion to the flow depth compared to the other wave conditions, and so the resulting runup for those tests was lower due to the deeper scour hole. Tests without a movable bed would perform better at isolating the runup at the structure and in representing a worst-case scenario. Therefore, in this study, the effect of the scouring on the runup is too great to allow a conclusion on the effect of sheltering on runup alone.

7.6.2 Discussion of Lateral Column Spacing

The results from the spacing setup were compared to two previous studies which also dealt with the amplification of scour caused by column spacing: the steady flow physical experiments by Beg (2010) and the dambreak numerical investigation by Le Quéré et al. (2021). The physical experiments by (Beg (2010) differ from those in this study because of the different flow conditions and because in their study, the columns were circular instead of square. In addition, only a steady flow condition was used in the study by Beg (2010), which would reflect an example of an endless flow, which in turn would provide an infinite period for the scour to reach equilibrium. This situation contrasts with the present study and the study by Le Quéré et al. (2021), which allowed comparisons of flows with similar properties, such as maximum flow depths and Froude numbers. Also, in the study by Le Quéré et al. (2021), the numerical FLOW-3D model was applied for the same spacings, sizes, and shapes of columns as in the present study, and the impoundment water depths were the same. However, the flume utilized in their numerical model differed; i.e., the length of the impoundment was 23 m compared to 16 m in the present study, leading to a longer inundation time, and the flume floor was completely horizontal.

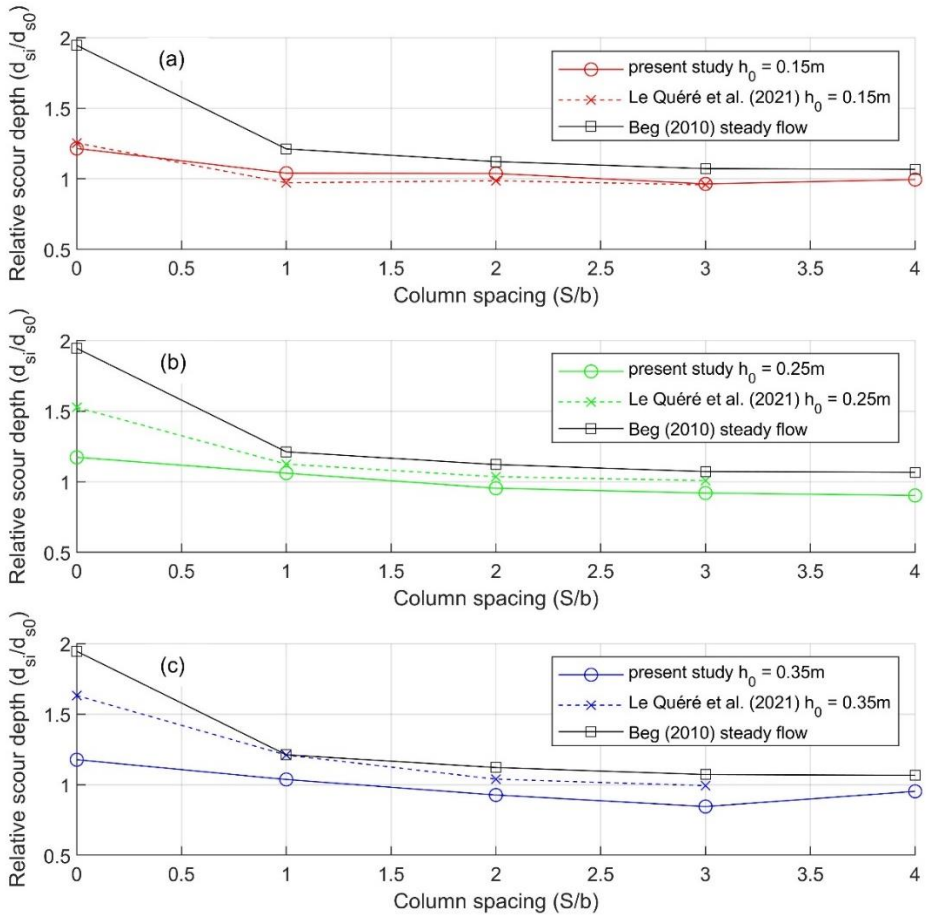

Figure 7.17: Comparison of present study to previous studies numerical results and steady flow results (a) h_0 = 0.15 m (b) h_0 = 0.25 m (c) h_0 = 0.35 m

In Figure 7.17(a), it can be seen that the results from h_0 = 0.15 m from the present study were very comparable to the numerical results from Le Quéré et al. (2021). However, the relative maximum scour depths for the dambreak setups in the present study and Le Quéré et al.'s (2021) study were much lower than those for the steady flow in Beg's (2010) study. The longer flow period in the case of the steady flow amplified the effect of the lateral spacing.

In Figure 7.17(b), a difference can be seen between the present study's experimental results, Le Quéré et al.'s (2021) numerical results, and Beg's (2010) steady flow results. In the numerical results, no reduction in relative maximum scour depth was noted when $S \geq 2b$; however, the difference in inundation periods may have caused this result. The maximum scour depths for the single-column tests in the present study were up to 20% lower in magnitude than in the numerical results by Le Quéré et al. (2021). The spacing effect may have similarly been affected by the flow period.

In Figure 7.17(c), with h_0 = 0.35 m, an even larger difference can be seen between Le Quéré et al.'s (2021) numerical results and those of the present study. The experimental results of the present study with h_0 = 0.35 m were similar to those with h_0 = 0.25 m, but Le Quéré et al.'s (2021) numerical results showed an exaggeration of the spacing effect when a greater impoundment depth was used. The results of the latter were similar to those with the steady flow for some S. This

exaggeration of the spacing effect with a greater h_0 was attributed to the greater flow depth and longer flow period in Le Quéré et al. (2021); however, the same effect was not observed in the present study. This discrepancy may have been caused by numerical errors induced by the difficulty of numerical models to simulate unsteady flows. The comparison of the present study and the steady flow results from Beg (2010) highlights the importance of the inundation time on the spacing effect.

The dambreak setup used in this experiment comes with the advantage of properly replicating the long period of a natural tsunami, unlike the solitary waves often utilized in some tsunami-related experiments (Madsen et al., 2008). However, only the runup phase of the tsunami inundation was simulated, not the drawdown phase. One disadvantage of not modeling the drawdown phase is that some of the scour processes, exaggerated by soil-softening due to an upward pressure gradient in the soil, are not included in the experiment. Although changes in the horizontal pressure gradient linked with a sheltering-type column setup was hypothesized by previous authors (Yeh and Li, 2008; Yeh and Mason, 2014), a verification of this phenomenon is still needed. In addition, the drawdown exposes the design column to an undisturbed flow, and therefore a larger quantity of sediment may be transported compared to what was found in this study.

7.7 Conclusions

A comprehensive experimental program was carried out to investigate scouring related to various two-column setups. Scouring patterns around two columns installed on the same longitudinal line (sheltering setup) and around two columns installed on the same transversal line (spacing setup) were found to be different, as well as differing from the scouring patterns around a single column. When two columns were placed in a sheltering setup, a reduction in wave runup was found at the design (downstream) column that was positively correlated with the impoundment depth (h_0) and the width of the upstream macroroughness element (b_{Sh}). Scouring at the design column was also reduced by the addition of the upstream macroroughness element. A reduction of up to 83% was measured in one test (Sh_h1_L2_b2, see Table 7.1). The longitudinal distance between the design structure and the macroroughness element (L_D), as well as h_0, were negatively correlated with scour reduction, while b_{Sh} was positively correlated with scour reduction.

When two columns were placed on the same transversal line, the maximum scour depth was amplified by 20% at a spacing (S) of 0. A maximum amplification of 7% was measured at the lowest spacing ($S = 1b$), which indicates that the second column slightly amplified the development of scour, contrary to that in a steady flow condition. For tests with $S > 1b$, only one test (Sp_h1_S2, see Table 7.2) showed an amplification of scour, while the other tests showed a reduction in maximum scour depth. The authors hypothesized that the formation of a horseshoe vortex around the columns was disrupted by flow structures forming around the second column, which reduced the capacity to transport sediment. Tests with a longer period, such as in the case of the numerical model presented in Le Quéré et al. (2021) and for the steady flow in Beg (2010), allow more time for the horseshoe vortices to gather more energy compared to flow structures around single columns.

From the results of this experimental program, the authors were unable to produce clear and safe design guidance for the construction of future structures in tsunami-prone areas. The authors therefore propose that more flow conditions should be tested for both setups, including some that

allow for the rundown phase of the wave. Also, the columns were placed only at two angles to the flow direction (0º and 90º), and more angles should be tested to further investigate scour amplification caused by surrounding structures. Different sediment diameters and experiment scale should also be considered for future studies.

Chapter 8: Conclusions and Recommendations for Future Work

8.1 Conclusions

The work presented in this thesis examined the processes governing the scour around structures caused by flows similar to tsunamis inundation. A series of numerical modelling studies and two experimental programs conducted at Leibniz University Hannover, Germany, and at the newly constructed Dambreak Wave Flume in the Hydraulic Lab at the University of Ottawa were conducted. The following conclusions were drawn from this study:

- Numerical investigation of scour around a single column and two laterally spaced columns (Chapter 3-4):
  - Tsunami-induced scour is a complex phenomenon influenced by several parameter, which were identified in the literature review. Based on this study, the approach flow depth, the inundation time, the structure size, and the presence of surrounding structures should be considered when predicting the scour at a vertically standing structure.
  - Applying numerical models showed the importance of non hydrostatic solving of the RANS equations when evaluating local scour induced by tsunami-like waves. This approach allows for a solving of the momentum equation in the vertical direction and allows for the generation of vertical eddies responsible for scour at the toe of a structure subjected to tsunami flows.
  - The numerical model FLOW-3D in combination with the LES turbulence model (Smagorinsky, 1963) and Nielsen (1992) sediment transport model was found to accurately simulate the scour hole forming at the upstream face of structure subjected to a dambreak bore. The correct resolution of scour forming at this location is crucial since the deepest scour was forming at the upstream corners. However, the scour past the front face was poorly simulated by this model.
- Combined numerical and experimental investigation of scour around a single column in Hannover, Germany (Chapter 5)
  - The FLOW-3D model was successfully applied to a large-scale experiment with solitary waves to simulate a tsunami wave. The turbulence forming around the square column was found to be much stronger during the runup phase compared to the drawdown phase of the inundation. However, discrepancies in the scour depth results on the onshore side of the structure, which formed during the drawdown phase, point towards a scour mechanism not taken into account by the numerical model.
  - In the literature, the soil softening caused by an upward pore pressure gradient the soil should be the mechanism enhancing the scour during the drawdown process of the wave. However, pore pressure measurements performed during the experiment does not support the presence of this upward pore pressure gradient.
- Experimental study of scour around multiple arrangements of columns in Ottawa, Canada (Chapters 6-7)

- The study of lateral spacing of columns using both a numerical model and a series of physical experiments showed a change in scour (increase or decrease, depending on the test) at the columns depending on the lateral distance between the columns and the incoming flow properties (flow depth and Froude number). However, the magnitude of scour changes due to the column's lateral spacing was very different between the numerical model calculations and experiment measurements. The numerical results showed an amplification of scour in all tests compared to single column tests, while the physical experiments showed a small amplification of scour at low spacing, but a decrease in scour compared to single column tests at higher spacing. The results were judged not conclusive enough to provide design guidance.
- The experimental study of the effect of sheltering on scour showed a decrease in runup and scour at the downstream column when the latter was placed directly in the shadow of an upstream positioned column. The upstream column width, the longitudinal distance between the two column, and the incoming flow properties (flow depth and Froude number) were found to influence the runup onto the face of the column and the scour depth at the downstream column. However, no exact correlation between these measurements was drawn, which would lead to appropriate design guidelines.
- The presence of upstream columns was found to be influencing scour at a column placed downstream of the gap between them. The width between the upstream columns, the distance longitudinal between the downstream column and the upstream columns, and the incoming flow properties (Froude number and flow depth) were found to influence the scour around the sheltered column. A design scour amplification factor was proposed to account for the effect of upstream flow constriction on scour.

8.2 Recommendation for Future Work

The studies presented herein focused on the scour induced by tsunami-like inundation around single column and multi-columns arrangements. The scope of the work had limitations described in Chapter 1 and the candidate suggests the following potential avenues for future research to further enhance the body of knowledge on tsunami-induced scour:

- The investigation of the effects of different parameters, found to influence scour in steady flow, in tsunami flow conditions. Those parameters include, but are not limited to: structure geometry, sediment properties, flow velocity, shore slope, and inundation time.
- The need to compare the scour generated by the two main tsunami-like inundation mechanisms used in lab experiments: the dambreak bore and the broken solitary wave. These two flow conditions were used to model tsunami waves in scaled experiments. However, no study has directly discussed their different resulting scour at similar scale.
- The investigation of scour changes with the experimental scale. Studies have previously varied the height of the incoming wave/bore and column size and demonstrated their importance on scour formation. However, none tested the scale effect by simultaneously changing the size of wave, structure and movable bed particles. Studying the scale effects would test the assumptions that scaling rules used to investigate scouring in steady flow conditions also apply for tsunami-like flows.

- A prototype scale investigation of local scour induced by a tsunami wave has yet to be done. A prototype study could help confirm the validity of the scaling methods used in small scale experiments to investigate tsunami scour.
- More numerical investigations should be performed to improve the accuracy of simulations of dam-break-induced scour around structures. Although the numerical results of dam-break-induced scour presented in this thesis are accurate in the critical section of the scour that occurs in the close front face of a square column, the difference in scour at the back and sides of the column should be improved.
- The numerical investigation of the turbulent flow patterns forming around multi-column arrangements when subjected to tsunami flows. The differences in the turbulence characteristics associated with multiple columns positioned close to one-another, when compared to a singular structure may explain the reason for the change in scour associated with the addition of columns.
- Investigation of two-columns setup placed at different orientation angles with respect to inflow direction should be performed. Two-column setups in this study were performed at two angles: 0º (sheltering setup) and 90º (spacing setup). Additional angles between the two columns and the incoming flow direction will provide more detail on the scour change caused by surrounding columns.
- A possible investigation of tsunami-induced scour forming around multi-column arrangements when a setup that allows for drawdown to occur would be worthwhile. In the present study, the scour amplification caused by the presence of multiple structure was only studied using a dambreak wave. The use of a solitary wave or a long wave would allow the investigation of the drawdown effects on the scour processes.

References

Abdollahi, A., Mason, H.B., 2020. Pore Water Pressure Response during Tsunami Loading. J. Geotech. Geoenvironmental Eng. 146, 1–11. https://doi.org/10.1061/(ASCE)GT.1943-5606.0002205

Alemi, M., Maia, R., 2018. Numerical Simulation of the Flow and Local Scour Process around Single and Complex Bridge Piers. Int. J. Civ. Eng. 16, 475–487. https://doi.org/10.1007/s40999-016-0137-8

Amini, A., Melville, B.W., Asce, M., Ali, T.M., Ghazali, A.H., 2012. Clear-Water Local Scour around Pile Groups in Shallow-Water Flow. J. Hydraul. Eng. 138, 177–185. https://doi.org/10.1061/(ASCE)HY.1943-7900.0000488

Antuono, M., Brocchini, M., 2011. Swash Zone Dynamics due to Impulsive Waves. J. Waterw. Port, Coastal, Ocean Eng. 137, 192–203. https://doi.org/10.1061/(ASCE)WW.1943-5460.0000080

April Le Quéré, P., Nistor, I., Mohammadian, A., 2020. Numerical Modeling of Tsunami-Induced Scouring around a Square Column: Performance Assessment of FLOW-3D and Delft3D. J. Coast. Res. https://doi.org/10.2112/JCOASTRES-D-19-00181.1

Arabi, M.G., Sogut, D.V., Khosronejad, A., Yalciner, A.C., Farhadzadeh, A., 2019. A numerical and experimental study of local hydrodynamics due to interactions between a solitary wave and an impervious structure. Coast. Eng. 147, 43–62. https://doi.org/10.1016/j.coastaleng.2019.02.004

Arneson, L.A., Zevenbergen, L.W., Lagasse, P.F., Clopper, P.., 2012. Evaluating Scour at Bridges, Hydraulic Engineering Circular 18. Washington, D.C.

ASCE, 2016a. Chapter 6: Tsunami Loads and Effects.

ASCE, 2016b. Chapter 6: Tsunami Loads and Effects Commentary.

Ataie-Ashtiani, B., Beheshti, A.A., 2006. Experimental Investigation of Clear-Water Local Scour at Pile Groups. J. Hydraul. Eng. 132, 1100–1104. https://doi.org/10.1061/(ASCE)0733-9429(2006)132

Ballio, F., 2004. Local and contraction scour at bridge abutments. Jt. Conf. Water Resour. Eng. Water Resour. Plan. Manag. 2000 Build. Partnerships 104. https://doi.org/10.1061/40517(2000)403

Bardina, J.E., Huang, P.G., Coakley, T.J., 1997. Turbulence Modeling Validation, Testing, and Development, NASA Technical Memorandum 110446.

Beg, M., 2010. Characteristics of Developing Scour Holes around Two Piers Placed in Transverse Arrangement. Int. Conf. Scour Eros. 2010 32, 491–500.

Beg, M., Beg, S., 2015. Scour hole characteristics of two unequal size bridge piers in tandem arrangement. ISH J. Hydraul. Eng. 21, 85–96.

https://doi.org/10.1080/09715010.2014.963176

Breusers, H. N. C., Nicollet, G., Shen, H.W., 1977. Local Scour Around Cylindrical Piers. J. Hydraul. Res. 15, 211–252. https://doi.org/10.1080/00221687709499645

Breusers, H N C, Nicollet, G., Shen, H.W., 1977. Local Scour Around Cylindrical Piers. J. Hydraul. Res. 1686. https://doi.org/10.1080/00221687709499645

Briaud, J.L., H. Chen, Y.L., Nurtjahyo, P., Wang, J., 2005. SRICOS-EFA method for contraction scour in fine-grained soils. J. Geotech. Geoenvironmental Eng. 131, 1283–1294.

Bricker, J.D., Francis, M., Nakayama, A., 2012. Scour depths near coastal structures due to the 2011 Tohoku Tsunami. J. Hydraul. Res. 50, 637–641. https://doi.org/10.1080/00221686.2012.721015

Bricker, J.D., Gibson, S., Takagi, H., Imamura, F., 2015. On the need for larger Manning's roughness coefficients in depth-integrated tsunami inundation models. Coast. Eng. J. 57. https://doi.org/10.1142/S0578563415500059

Briere, C., Giardino, A., Van der Werf, J., 2011. Morphological Modeling of Bar Dynamics With Delft3D: the Quest for Optimal Free Parameter Settings Using an Automatic Calibration Technique. Coast. Eng. Proc. 1, 60. https://doi.org/10.9753/icce.v32.sediment.60

Brufau, P., Garcia-Navarro, P., 2000. Two-dimensional dam break flow simulation. Int. J. Numer. Methods Fluids 33, 35–57. https://doi.org/10.1002/(SICI)1097-0363(20000515)33:1<35::AID-FLD999>3.0.CO;2-D

Chacón-Barrantes, S., 2018. Effectiveness of N-waves for predicting morphological changes due to tsunamis. Appl. Ocean Res. 74, 217–226. https://doi.org/10.1016/j.apor.2018.03.006

Chanson, H., 2009. Application of the method of characteristics to the dam break wave problem. J. Hydraul. Res. 47, 41–49. https://doi.org/10.3826/jhr.2009.2865

Chanson, H., 2006. Tsunami Surges on Dry Coastal Plains: Application of Dam Break Wave Equations. Coast. Eng. J. 48, 355–370. https://doi.org/10.1142/S0578563406001477

Chanson, H., 2005. Analytical Solution of Dam Break Wave With Flow Resistance. Application To Tsunami Surges. 31st IAHR Bienn. Congr. 3341–3353.

Chen, J., Huang, Z., Jiang, C., Deng, B., Long, Y., 2013. Tsunami-induced scour at coastal roadways: A laboratory study. Nat. Hazards 69, 655–674. https://doi.org/10.1007/s11069-013-0727-6

Chen, J., Jiang, C., Yang, W., Xiao, G., 2016. Laboratory study on protection of tsunami-induced scour by offshore breakwaters. Nat. Hazards 81, 1229–1247. https://doi.org/10.1007/s11069-015-2131-x

Chock, G., Roberson, I., Kriebel, D., Francis, M., Nistor, I., 2013. Tohoku Japan tsunami of March 11, 2011 – Performance of structures under tsunami loads.

Ciofalo, M., 1996. Large-eddy simulations of turbulent flow with heat transfer in simple and complex geometries using Harwell-FLOW3D. Appl. Math. Model. 20.

Clayton, B.R., Morsi, Y., 1986. Determination of principal characteristics of turbulent swirling flow along annuli: Part 3: Numerical analysis. Int. J. Heat Fluid Flow 7.

Courant, R., Friedrichs, K., Lewy, H., 1967. On the Partial Difference Equations of Mathematical Physics. IBM J. Res. Dev. 11, 215–234. https://doi.org/10.1147/rd.112.0215

Dames, Moore, 1980. Design and Construction Standards for Residential Construction in Tsunami-prone Areas in Hawaii.

Dargahi, B., 1989. The turbulent flow field around a circular cylinder. Exp. Fluids 8, 1–12.

Dean, R.G., 1985. Physical modelling of littoral processes, in: Dalrymple, R.A. (Ed.), Physical Modelling in Coastal Engineering. Rotterdam, Netherlands, pp. 119–139.

Deltares, 2011. Delft3D-FLOW.

Di Risio, M., De Girolamo, P., Bellotti, G., Panizzo, A., Aristodemo, F., Molfetta, M.G., Petrillo, A.F., 2009. Landslide-generated tsunamis runup at the coast of a conical island: New physical model experiments. J. Geophys. Res. Ocean. 114, 1–16. https://doi.org/10.1029/2008JC004858

Earthquake Engineering Research Institute, 2010. The Mw 8.8 Chile Earthquake of February 27, 2010.

Ehteram, M., Mahdavi, A., 2015. Journal of Computational and Applied Numerical modeling of scour depth at side piers of the bridge. J. Comput. Appl. Math. 280, 68–79. https://doi.org/10.1016/j.cam.2014.11.039

Elliott, K.R., Baker, C.J., 1985. Effect of pier spacing on scour around bridge piers. J. Hydraul. Eng. 111, 1105–1109. https://doi.org/10.1061/(ASCE)0733-9429(1985)111:7(1105)

Escue, A., Cui, J., 2010. Comparison of turbulence models in simulating swirling pipe flows. Appl. Math. Model. 34, 2840–2849. https://doi.org/10.1016/j.apm.2009.12.018

Ettema, R., Kirkil, G., Muste, M., 2006a. Similitude of Large-Scale Turbulence in Experiments on Local Scour at Cylinders. J. Hydraul. Eng. 132, 33–40. https://doi.org/10.1061/(ASCE)0733-9429(2006)132

Ettema, R., Kirkil, G., Muste, M., 2006b. Similitude of Large-Scale Turbulence in Experiments on Local Scour at Cylinders. J. Hydraul. Eng. 132 (1), 33–40. https://doi.org/10.1061/(ASCE)0733-9429(2006)132

Ettema, R., Melville, B.W., Barkdoll, B., 1998. Scale Effect in Pier-Scour Experiments. J. Hydraul. Eng. 124, 639–642. https://doi.org/10.1061/(ASCE)0733-9429(1998)124:6(639)

Ettema, R., Nakato, T., Muste, M., 2010. Estimation of Scour Depth at Bridge Abutments. Natl. Coop. Highw. Res. Progr. NCHRP 24-2, 436 pp.

FEMA, 2008. Guidelines for Design of Structures for Vertical Evacuation From Tsunamis. Jetty.Ecn.Purdue.Edu 176. https://doi.org/10.1061/40978(313)7

FEMA P-646, 2012. Guidelines for Design of Structures for Vertical Evacuation From Tsunamis 3rd Edition, US deparment of homeland security.

Fernández, H., Sriram, V., Schimmels, S., Oumeraci, H., 2014. Extreme wave generation using self correcting method - revisited. Coast. Eng. 93, 15–31. https://doi.org/10.1016/j.coastaleng.2014.07.003

Firth, P.W.C., Duggins, R.K., 1985. Turbulence modelling for swirling flows, in: Numerical Methods in Laminar and Turbulent Flow; Proceedings of the Fourth International Conference. pp. 353–363.

Flow Science, 2018. Flow-3D User Manual v11.2.

Flow Science, I., 2019. FLOW-3D, Version~12.0.

Fluent Inc., 2001. Chapter 10. Modeling Turbulence.

Foster, A.S.J., Rossetto, T., Allsop, W., 2017. An experimentally validated approach for evaluating tsunami inundation forces on rectangular buildings. Coast. Eng. 128, 44–57. https://doi.org/10.1016/j.coastaleng.2017.07.006

Fourtakas, G., Rogers, B.D., 2016. Advances in Water Resources Modelling multi-phase liquid-sediment scour and resuspension induced by rapid flows using Smoothed Particle Hydrodynamics (SPH) accelerated with a Graphics Processing Unit (GPU). Adv. Water Resour. 92, 186–199. https://doi.org/10.1016/j.advwatres.2016.04.009

Fritz, H.M., Borrero, J.C., Synolakis, C.E., Okal, E.A., Weiss, R., Titov, V. V., Jaffe, B.E., Foteinis, S., Lynett, P.J., Chan, I.-C., Liu, P.L.F., 2011a. Insights on the 2009 South Pacific tsunami in Samoa and Tonga from field surveys and numerical simulations. Earth-Science Rev. 107, 66–75. https://doi.org/10.1016/j.earscirev.2011.03.004

Fritz, H.M., Petroff, C.M., CATALAN, P.A., CIENFUEGOS, R., WINCKLER, P., KALLIGERIS, N., WEISS, R., BARRIENTOS, S.E., MENESES, G., VALDERAS-BERMEJO, C., EBELING, C., PAPADOPOULOS, A., CONTRERAS, M., ALMAR, R., DOMINGUEZ, J.C., SYNOLAKIS, C.E., 2011b. Field Survey of the 27 February 2010 Chile Tsunami. Pure Appl. Geophys. 168, 1989–2010. https://doi.org/10.1007/s00024-011-0283-5

Ghaemi, N., Etemad-Shahidi, A., Ataie-Ashtiani, B., 2013. Estimation of current-induced pile groups scour using a rule-based method. J. Hydroinformatics 15, 516–528. https://doi.org/10.2166/hydro.2012.175

Ghobarah, A., Saatcioglu, M., Nistor, I., 2006. The impact of the 26 December 2004 earthquake and tsunami on structures and infrastructure. Eng. Struct. 28, 312–326. https://doi.org/10.1016/j.engstruct.2005.09.028

Gieschen, R., Schwartpaul, C., Landmann, J., Fröhling, L., Hildebrandt, A., Goseberg, N., 2021. Large-scale laboratory experiments on mussel dropper lines in ocean surface waves. J. Mar. Sci. Eng. 9, 1–20. https://doi.org/10.3390/jmse9010029

Gill, M.A., 1981. Bed erosion in rectangular long contraction. J. Hydraul. Div. 107, 273–284.

Goring, D.G., 1978. Tsunamis - the propagation of long waves onto a shelf, PhD thesis, University of California, Berkley. Keck Lab Rep. KH-R-38.

Goseberg, N., Wurpts, A., Schlurmann, T., 2013. Laboratory-scale generation of tsunami and long

waves. Coast. Eng. 79, 57–74. https://doi.org/10.1016/j.coastaleng.2013.04.006

Guan, D., Melville, B.W., Friedrich, H., 2015. Live-Bed Scour at Submerged Weirs. J. Hydraul. Eng. 141, 1–12. https://doi.org/10.1061/(ASCE)HY.1943-7900.0000954.

Guo, Z., Jeng, D.S., Zhao, H., Guo, W., Wang, L., 2019. Effect of seepage flow on sediment incipient motion around a free spanning pipeline. Coast. Eng. 143, 50–62. https://doi.org/10.1016/j.coastaleng.2018.10.012

Hamidi, A., Siadatmousavi, S.M., 2018. Numerical simulation of scour and flow field for different arrangements of two piers using SSIIM model. Ain Shams Eng. J. 9, 2415–2426. https://doi.org/10.1016/j.asej.2017.03.012

Hannah, C.R., 1978. Scour at pile groups. University of Canterbury.

Hirt, C.W., 1981. Volume of Fluid (VOF) Method for the Dynamics of Free Boundaries * 225, 201–225.

Hirt, C.W., 1979. Simplified Solution Algorithms for Fluid Flow Problems, in: PARTER, S. V (Ed.), Numerical Methods for Partial Differential Equations. Academic Press, pp. 193–211. https://doi.org/https://doi.org/10.1016/B978-0-12-546050-7.50011-3

Hosseini, R., Amini, A., 2015. Scour depth estimation methods around pile groups. KSCE J. Civ. Eng. 19, 2144–2156. https://doi.org/10.1007/s12205-015-0594-7

Huang, W., Yang, Q., Xiao, H., 2009. Computers & Fluids CFD modeling of scale effects on turbulence flow and scour around bridge piers. Comput. Fluids 38, 1050–1058. https://doi.org/10.1016/j.compfluid.2008.01.029

Hughes, S. a., 1993. Physical Models and Laboratory Techniques In Coastal Engineering. World Scientific Publishing, Singapore.

Hughes, S.A., Fowler, J.E., 1990. Midscale Physical Model Validation for Scour at Coastal Structures. Vicksburg, Miss. :U.S. Army Engineer Waterways Experiment Station ;

Hunt, J.C.R., Wray, A.A., Moin, P., 1988. Eddies, Streams, and Convergence Zones in Turbulent Flows, Center for Turbulence Research CTR-588.

Imran, J., Khan, S.M., Pirmez, C., Parker, G., 2017. Froude scaling limitations in modeling of turbidity currents. Environ. Fluid Mech. 17, 159–186. https://doi.org/10.1007/s10652-016-9488-6

Istiarto, I., 2001. Flow around a cylinder in a scoured channel bed. Ec. Polytech. Fed. Lausanne 2368, 431–444.

Jaffe, B.E., Gelfenbuam, G., 2007. A simple model for calculating tsunami flow speed from tsunami deposits. Sediment. Geol. 200, 347–361. https://doi.org/10.1016/j.sedgeo.2007.01.013

Jayaratne, M.P.R., Premaratne, B., Adewale, A., Mikami, T., Matsuba, S., Shibayama, T., Esteban, M., Nistor, I., 2016. Failure Mechanisms and Local Scour at Coastal Structures Induced by Tsunami. Coast. Eng. J. 58, 1640017. https://doi.org/10.1142/S0578563416400179

Jayaratne, R., Nicholas, M., Ghodoosipour, B., Magnaini, S., Nistor, I., Shibayama, T., 2018. TSUNAMI-INDUCED HYDRODYNAMICS AND SCOUR AROUND STRUCTURES.

Jiang, C., Chen, J., Yao, Y., Liu, J., Deng, Y., 2015. Study on threshold motion of sediment and bedload transport by tsunami waves. Ocean Eng. 100, 97–106. https://doi.org/10.1016/j.oceaneng.2015.03.011

Jones, W.P., Launder, B.E., 1972. The prediction of laminarization with a two-Equation Model of Turbulence 15, 301–314.

Kato, F., Sato, S., Yeh, H., 2000. Large-scale experiment on dynamic response of sand bed around a cylinder due to tsunami. Coast. Eng. 1848–1859.

Kawachi, I., Aida, J., Hikichi, H., Kondo, K., 2020. Disaster resilience in aging populations : lessons from the 2011 Great East Japan earthquake and tsunami. J. R. Soc. New Zeal. 50, 263–278. https://doi.org/10.1080/03036758.2020.1722186

Keshavarzi, A., Shrestha, C.K., Melville, B., Khabbaz, H., Ranjbar-Zahedani, M., Ball, J., 2018. Estimation of maximum scour depths at upstream of front and rear piers for two in-line circular columns. Environ. Fluid Mech. 18, 537–550. https://doi.org/10.1007/s10652-017-9572-6

Khosronejad, A., Kang, S., Sotiropoulos, F., 2012. Experimental and computational investigation of local scour around bridge piers. Adv. Water Resour. 37, 73–85. https://doi.org/10.1016/j.advwatres.2011.09.013

Kim, H.S., Nabi, M., Kimura, I., Shimizu, Y., 2014. Numerical investigation of local scour at two adjacent cylinders. Adv. Water Resour. 70, 131–147. https://doi.org/10.1016/j.advwatres.2014.04.018

Koike, K., 1996. The countermeasures against coastal hazards in Japan. GeoJournal 38, 301–312.

Kothyari, U.C., Raju, K.G.R., Garde, R.J., 1993. Temporal variation of scour around circular bridge piers 118, 1091–1106.

Kothyari, U.C., Raju, K.G.R., Garde, R.J., 1992. Live-bed scour around cylindrical bridge piers: Affouillement autour de piles de pont cylindriques dans un écoulement avec transport solide. J. Hydraul. Res. 30, 701–715. https://doi.org/10.1080/00221689209498889

Krautwald, C., Stolle, J., Robertson, I., Achiari, H., Mikami, T., Nakamura, R., Takabatake, T., Nishida, Y., Shibayama, T., Esteban, M., Goseberg, N., Nistor, I., 2021. Engineering Lessons from September 28, 2018 Indonesian Tsunami: Scouring Mechanisms and Effects on Infrastructure. J. Waterw. Port, Coastal, Ocean Eng. 147, 04020056. https://doi.org/10.1061/(asce)ww.1943-5460.0000620

Larsen, B.E., Arbøll, L.K., Kristoffersen, S.F., Carstensen, S., Fuhrman, D.R., 2018. Experimental study of tsunami-induced scour around a monopile foundation. Coast. Eng. 138, 9–21. https://doi.org/10.1016/j.coastaleng.2018.04.007

Larsen, B.E., Fuhrman, D.R., Baykal, C., Sumer, B.M., 2017. Tsunami-induced scour around monopile foundations. Coast. Eng. 129, 36–49. https://doi.org/10.1016/j.coastaleng.2017.08.002

Lauber, G., Hager, W.H., 1998. Experiments to dambreak wave: Horizontal channel. J. Hydraul. Res. 36, 291–307. https://doi.org/10.1080/00221689809498620

Laursen, E.M., 1963. An analysis of relief bridge scour. J. ydraulics Divition 83, 93–118.

Lavictoire, A., Nistor, I., Rennie, C.D., 2014. Bore-Induced Local Scour around a Circular Structure. University of Ottawa.

Le Quéré, P.A., Nistor, I., Mohammadian, M., 2021. Effect of Lateral Spacing of Structures on Tsunami-Induced Scour. J. Coast. Res. 37, 813–826. https://doi.org/10.2112/JCOASTRES-D-20-00144.1

Lebreton, L.C.M., Borrero, J.C., 2013. Modeling the transport and accumulation floating debris generated by the 11 March 2011 Tohoku tsunami. Mar. Pollut. Bull. 66, 53–58. https://doi.org/10.1016/j.marpolbul.2012.11.013

Lim, S.-Y., Cheng, N.-S., 1998. Prediction of Live-Bed Scour at Bridge Abutments. J. Hydraul. Eng. 124, 635–638. https://doi.org/10.1061/(asce)0733-9429(1998)124:6(635)

Liu, C., Liu, X., Jiang, C., He, Y., Deng, B., Duan, Z., Wu, Z., 2019. Numerical Investigation of Sediment Transport of Sandy Beaches by a Tsunami-Like Solitary Wave Based on Navier-Stokes Equations. J. Offshore Mech. Arct. Eng. 141, 1–16. https://doi.org/10.1115/1.4043504

Madsen, P.A., Fuhrman, D.R., Schäffer, H.A., 2008. On the solitary wave paradigm for tsunamis. J. Geophys. Res. Ocean. 113. https://doi.org/10.1029/2008JC004932

Mason, B.H., Yeh, H., 2016. Sediment liquefaction: A pore-water pressure gradient viewpoint. Bull. Seismol. Soc. Am. 106, 1908–1913. https://doi.org/10.1785/0120150296

Mastbergen, D.R., Van Den Berg, J.H., 2003. Breaching in fine sands and the generation of sustained turbidity currents in submarine canyons. Sedimentology. https://doi.org/10.1046/j.1365-3091.2003.00554.x

Matsutomi, H., Okamoto, K., Harada, K., 2010. Inundation flow velocity of tsunami on land and its practical use. Coast. Eng.

McCowan, J., 1891. VII. On the solitary wave. London, Edinburgh, Dublin Philos. Mag. J. Sci. 32, 45–58. https://doi.org/10.1080/14786449108621390

McGovern, D., Rossetto, T., Todd, D., 2019. Tsunami Scour and Forces at Onshore Structures. Coast. Struct. 506–515. https://doi.org/10.18451/978-3-939230-64-9_51

McGovern, D.J., Todd, D., Rossetto, T., Whitehouse, R.J.S., Monaghan, J., Gomes, E., 2019. Experimental observations of tsunami induced scour at onshore structures. Coast. Eng. 152, 103505. https://doi.org/10.1016/j.coastaleng.2019.103505

Mehrzad, S., Nistor, I., Rennie, C.D., 2016. Experimental modeling of supercritical flows induced erosion around structures. Proc. 6th Int. Conf. Appl. Phys. Model. Coast. Port Eng. Sci.

Melville, B.B.W., 1985. Live-bed scour at bridge piers 110, 1234–1247.

Melville, B.W., 1997. PIER AND ABUTMENT SCOUR : INTEGRATED APPROACH. J. Hydraul. Eng. 123, 125–136.

Melville, B.W., Chiew, Y., 1999. Time Scale for Local Scour at Bridge Pier 125, 59–65.

Melville, B.W., Coleman, S.E., 2000. Bridge Scour. Water Resources Publications, Highlands Ranch, Colorado.

Melville, B.W., Raudkivi, A.J., 1977. Flow characteristics in local scour at bridge piers. J. Hydraul. Res. 373–380. https://doi.org/10.1080/00221687709499641

Memar, S., Zounemat-kermani, M., Beheshti, A., De, G., 2018. Investigation of local scour around tandem piers for different skew-angles, in: River Flow 2018. E3S Web of Conferences 40, pp. 1–8.

Menter, F.R.., 1993. Zonal two equation k-w turbulence models for aerodynamic flows. 24th Fluid Dyn. Conf.

Moon, W.C., Tan, K.C., Lau, T.L., 2014. An Experimental Study on Wave Forces of Tsunami on Simplified Onshore Buildings at Penang Island, Malaysia. J. Civ. Eng. Res. 4, 164–172. https://doi.org/10.5923/c.jce.201402.29

Motley, M.R., Wong, H.K., Qin, X., Winter, A.O., Eberhard, M.O., 2016. Tsunami-Induced Forces on Skewed Bridges. J. Waterw. Port, Coastal, Ocean Eng. 142, 04015025. https://doi.org/10.1061/(ASCE)WW.1943-5460.0000328

Nakamura, T., Kuramitsu, Y., Mizutani, N., 2008. Tsunami-induced local scour around a square structure. Solut. to Coast. Disasters Tsunamis 106–117.

Nakamura, T., Mizutani, N., 2014. DEVELOPMENT OF FLUID-SEDIMENT-SEABED INTERACTION MODEL AND ITS APPLICATION, in: Coastal Engineering Proceedings.

Nielsen, P., 1992. Coastal Bottom Boundary Layers and Sediment Transport, Advanced series on ocean engineering. World Scientific, Singapore.

Nisizima, S., Yoshizawa, A., 1987. Turbulent channel and couette flows using an anisotropic k-ε model. AIAA J. 25, 414–420. https://doi.org/10.2514/3.9639

Nistor, I., Goseberg, N., Mikami, T., Matsuba, S., 2017a. Flood-induced debris dynamics over a horizontal surface.

Nistor, I., Goseberg, N., Stolle, J., 2017b. Tsunami-driven debris motion and loads: a critical review. Front. Built Environ. 3, 1–11. https://doi.org/10.3389/fbuil.2017.00002

Nistor, I., Palermo, D., 2015. Post-tsunami engineering forensics: tsunami impact on infrastructure - lessons from 2004 indian ocean, 2010 chile, and 2011 tohoku japan tsunami field surveys, in: Handbook of Coastal Disaster Mitigation for Engineers and Planners. Elsevier Inc., pp. 417–435. https://doi.org/10.1016/B978-0-12-801060-0.00020-4

Nouri, Y., 2008. The Impact of Hydraulic Bores and Debris on Free Standing Structures.

Nouri, Y., Nistor, I., Palermo, D., Cornett, A., 2010. Experimental investigation of tsunami impact on free standing structures. Coast. Eng. J. 52, 43–70. https://doi.org/10.1142/S0578563410002117

Omara, H., Elsayed, S.M., Abdeelaal, G.M., Tawfik, A., 2019. Hydromorphological Numerical

Model of the Local Scour Process Around Bridge Piers. Arab. J. Sci. Eng. 44, 4183–4199. https://doi.org/10.1007/s13369-018-3359-z

Palermo, D., Nistor, I., Saatcioglu, M., Ghobarah, A., 2013. Impact and damage to structures during the 27 February 2010 Chile tsunami. NRC Res. Press 758, 750–758. https://doi.org/10.1139/cjce-2012-0553

Pan, C., Huang, W., 2012. Numerical Modeling of Tsunami Wave Run-Up and Effects on Sediment Scour around a Cylindrical Pier. J. Eng. Mech. 138, 1224–1235. https://doi.org/10.1061/(ASCE)EM.1943-7889.0000406

Patel, V.C., Rodi, W., Scheuerer, G., 1984. Turbulence models for near-wall and low reynolds number flows : a review 23, 1308–1319. https://doi.org/10.2514/3.9086

Peregrine, D.H., Williams, S.M., 2001. Swash overtopping a truncated plane beach. J. Fluid Mech. 440, 391–399. https://doi.org/10.1017/S002211200100492X

Pope, S.B., 2004. Ten questions concerning the large-eddy simulation of turbulent flows. New J. Phys. https://doi.org/10.1088/1367-2630/6/1/035

Pujara, N., Liu, P.L.F., Yeh, H., 2015. The swash of solitary waves on a plane beach: Flow evolution, bed shear stress and run-up. J. Fluid Mech. 779, 556–597. https://doi.org/10.1017/jfm.2015.435

Rahman, M.M., Schaab, C., Nakaza, E., 2005. Experimental and Numerical Modeling of Tsunami Mitigation by Canals. J. Waterw. Port, Coastal, Ocean Eng. 0, 4016012. https://doi.org/doi:10.1061/(ASCE)WW.1943-5460.0000355

Richardson, E. V, Davis, S.R., others, 2001. Evaluating scour at bridges.

Ritter, A., 1892. Die Fortpflanzung der Wasserwellen. Vereine Deutcher Ingenieure Zeitswchrift 36, 947–954.

Robertson, I.N., 2020. Tsunami Loads and Effects, Tsunami Loads and Effects. American Society of Civil Engineering, Reston. https://doi.org/10.1061/9780784414972

Roux, S., Lartigue, G., Poinsot, T., Meier, U., Bérat, C., 2005. Studies of mean and unsteady flow in a swirled combustor using experiments , acoustic analysis , and large eddy simulations. Combustor and Flames 141, 40–54. https://doi.org/10.1016/j.combustflame.2004.12.007

Rueben, M., Cox, D., Holman, R., Shin, S., Stanley, J., 2015. Optical Measurements of Tsunami Inundation and Debris Movement in a Large-Scale Wave Basin. J. Waterw. Port, Coastal, Ocean Eng. 141, 04014029. https://doi.org/10.1061/(ASCE)WW.1943-5460.0000267

Rupprecht, F., Möller, I., Paul, M., Kudella, M., Spencer, T., van Wesenbeeck, B.K., Wolters, G., Jensen, K., Bouma, T.J., Miranda-Lange, M., Schimmels, S., 2017. Vegetation-wave interactions in salt marshes under storm surge conditions. Ecol. Eng. 100, 301–315. https://doi.org/10.1016/j.ecoleng.2016.12.030

Saatcioglu, M., Ghobarah, A., Nistor, I., 2005. Effects of the December 26 , 2004 Sumatra earthquake and tsunami on physical infrastructure. J. Earthq. Technol. 42, 79–94.

Saghatchi, R., Ghazanfarian, J., Gorji-bandpy, M., 2014. Numerical Simulation of Water-Entry

and Sedimentation of an Elliptic Cylinder Using Hydrodynamics Method. J. Offshore Mech. Arct. Eng. 136. https://doi.org/10.1115/1.4026844

Samarajiva, R., 2005. Mobilizing information and communications technologies for effective disaster warning: Lessons from the 2004 tsunami. New Media Soc. 7, 731–747. https://doi.org/10.1177/1461444805058159

Sarjamee, S., Nistor, I., Mohammadian, A., 2017. Large eddy simulation of extreme hydrodynamic forces on structures with mitigation walls using OpenFOAM. Nat. Hazards 85, 1689–1707. https://doi.org/10.1007/s11069-016-2658-5

Satake, K., Tanioka, Y., 1995. Tsunami Generation of the 1993 Hokkaido Nansei-Oki Earthquake. Pure Appl. Geophys. 145, 803–821.

Schimmels, S., Sriram, V., Didenkulova, I., 2016. Tsunami generation in a large scale experimental facility. Coast. Eng. 110, 32–41. https://doi.org/10.1016/j.coastaleng.2015.12.005

Scholtès, L., Chareyre, B., Michallet, H., Catalano, E., Marzougui, D., 2015. Modeling wave-induced pore pressure and effective stress in a granular seabed. Contin. Mech. Thermodyn. 27, 305–323. https://doi.org/10.1007/s00161-014-0377-2

Sharma, N., 2017. River System Analysis and Management, Springer. ed. Singapore.

Shibayama, T., Esteban, M., Nistor, I., Takagi, H., Thao, N.D., Matsumaru, R., Mikami, T., Aranguiz, R., Jayaratne, R., Ohira, K., 2013. Classification of Tsunami and Evacuation Areas. Nat. Hazards 67, 365–386. https://doi.org/10.1007/s11069-013-0567-4

Shields, A., 1936. Anwendung der Aehnlichkeitsmechanik und der Turbulenzforschung auf die Geschiebebewegung. [English title: Application of similarity principles and turbulence research to bed-load movement ; translated by W.P. Ott and J.C. van Uchelen]. Berlin, Germany.

Smagorinsky, J., 1963. General Circulation Expermients With the Primitive Equations. Mon. Weather Rev. 91.

Soulsby, R., 1997. Ch. 9: bedload transport, in: Dynamics of Marine Sand. Thomas Telford Publications, London.

Spalart, P.R., Deck, S., Shur, M.L., Squires, K.D., Strelets, M.K., Travin, A., 2006. A new version of detached-eddy simulation , resistant. Theor. Comput. Fluid Dyn. 181–195. https://doi.org/10.1007/s00162-006-0015-0

Sriram, V., Didenkulova, I., Sergeeva, A., Schimmels, S., 2016. Tsunami evolution and run-up in a large scale experimental facility. Coast. Eng. 111, 1–12. https://doi.org/10.1016/j.coastaleng.2015.11.006

St-Germain, P., Nistor, I., Townsend, R., 2012. Numerical modeling of tsunami-induced hydrodynamic forces on onshore structures using SPH. Coast. Eng. Proc. 1–15. https://doi.org/10.9753/icce.v33.structures.81

St-Germain, P., Nistor, I., Townsend, R., Shibayama, T., 2014. Smoothed-particle hydrodynamics

numerical modeling of structures impacted by tsunami bores. J. Waterw. Port, Coastal, Ocean Eng. 140, 66–81. https://doi.org/10.1061/(ASCE)WW.1943-5460.0000225

Stolle, J., Derschum, C., Goseberg, N., Nistor, I., Petriu, E., 2018. Debris impact under extreme hydrodynamic conditions part 2: Impact force responses for non-rigid debris collisions. Coast. Eng. 141, 107–118. https://doi.org/10.1016/j.coastaleng.2018.09.004

Stolle, Jacob, Ghodoosipour, B., Derschum, C., Nistor, I., Petriu, E., Goseberg, N., 2019. Swing gate generated dam-break waves. J. Hydraul. Res. 57, 675–687. https://doi.org/10.1080/00221686.2018.1489901

Stolle, J., Goseberg, C.K.I.N.N., 2020. Structural Response of Wood Structures Under Hydraulic Loading. Coast. Eng. Proc. 12. https://doi.org/10.9753/icce.v36v.structures.12

Stolle, J., Goseberg, N., Nistor, I., Petriu, E., 2019. Debris impact forces on flexible structures in extreme hydrodynamic conditions. J. Fluids Struct. 84, 391–407. https://doi.org/10.1016/j.jfluidstructs.2018.11.009

Stolle, J, Krautwald, C., Robertson, I., Achiari, H., Mikami, T., Nakamura, R., Takabatake, T., Nishida, Y., Shibayama, T., Esteban, M., Nistor, I., Goseberg, N., 2020. Engineering lessons from the 28 September 2018 Indonesian tsunami: debris loading. Can. J. Civ. Eng. 47, 1–12. https://doi.org/10.1139/cjce-2019-0049

Stolle, Jacob, Nistor, I., Goseberg, N., Petriu, E., 2020. Multiple Debris Impact Loads in Extreme Hydrodynamic Conditions. J. Waterw. Port, Coastal, Ocean Eng. 146, 04019038. https://doi.org/10.1061/(asce)ww.1943-5460.0000546

Sturm, T.W., Ettema, R., Melville, B.W., 2011. Evaluation of Bridge-Scour Research: Abutment and Contraction Scour Processes and Prediction, Evaluation of Bridge-Scour Research: Abutment and Contraction Scour Processes and Prediction. https://doi.org/10.17226/22841

Sulianto, A.A., Murakami, K., 2015. Study on local scouring of gravel mound due to tsunami overflow. Procedia Eng. 116, 195–202. https://doi.org/10.1016/j.proeng.2015.08.282

Sumer, B.M., 2014. Liquefaction Around Marine Structures. World Scientific. https://doi.org/10.1142/7986

Sumer, B.M., Fredsoe, J., Christiansen, N., 1992. Scour around vertical pile in waves. J. Waterw. Port, Coast. Ocean Eng. 118, 15–31.

Sumer, B.M., Sen, M.B., Karagali, I., Ceren, B., Fredsøe, J., Sottile, M., Zilioli, L., Fuhrman, D.R., 2011. Flow and sediment transport induced by a plunging solitary wave. J. Geophys. Res. Ocean. 116, 1–15. https://doi.org/10.1029/2010JC006435

Suppasri, A., Shuto, N., Imamura, F., Koshimura, S., Mas, E., Yalciner, A.C., 2013. Lessons Learned from the 2011 Great East Japan Tsunami: Performance of Tsunami Countermeasures, Coastal Buildings, and Tsunami Evacuation in Japan. Pure Appl. Geophys. 170, 993–1018. https://doi.org/10.1007/s00024-012-0511-7

Synolakis, C., Okal, E., Bernard, E., 2005. The Megatsunami of December 26, 2004. Bridg. 35, 26–35.

Synolakis, C.E., 1987. The runup of solitary waves. J. Fluid Mech. 185, 523–545. https://doi.org/10.1017/S002211208700329X

Takahashi, S., Kuriyama, Y., Tomita, T., Kawai, Y., Arikawa, T., Tatsumi, D., Negi, T., 2011. Urgent survey for 2011 great east japan earthquake and tsunami disaster in ports and coasts. Tech. note port Airpt. Res. Inst. 31–44.

Tang, A.K., 2011. Tohoku , Japan , Earthquake and Tsunami Of 2011. American Society of Civil Engineering, Reston, USA.

Thomas, S., Killian, J., Bridges, K., 2015. Influence of Macroroughness on Tsunami Loading of Coastal Structures. J. Waterw. Port, Coast. Ocean Eng. 141, 1–14. https://doi.org/10.1061/(ASCE)WW.1943-5460.0000268.

Tinh, Nguyen X., Hitoshi Tanaka, Xiping Yu, and Guangwei Liu. 2022. Numerical Study on the Turbulent Structure of Tsunami Bottom Boundary Layer Using the 2011 Tohoku Tsunami Waveform. J. of Marine Sc. and Eng. 10, no. 2: 173. https://doi.org/10.3390/jmse10020173

Titov, V. V, Synolakis, C.E., 1997. Extreme inundation flows during the Hokkaido-Nansei-Oki tsunami. Geophys. Res. Lett. 24, 1315–1318.

Tonkin, S., Yeh, H., Kato, F., Sato, S., 2003. Tsunami scour around a cylinder. J. Fluid Mech. 496, 165–192. https://doi.org/10.1017/S0022112003006402

Tonkin, S.P., Francis, M., Bricker, J.D., 2013. Limits on coastal scour depths due to tsunami, in: International Efforts in Lifeline Earthquake Engineering - Proceedings of the 6th China-Japan-US Trilateral Symposium on Lifeline Earthquake Engineering. pp. 671–678. https://doi.org/10.1061/9780784413234.086

Van Rijn, L.C., 1984a. Sediment transport, part I: bed load transport. J. Hydraul. Eng. - ASCE 110, 1431–1456.

Van Rijn, L.C., 1984b. Sediment transport, part II: Suspended load transport 110, 1613–1641.

Vasquez, J., Walsh, B., 2009. CFD simulation of local scour in complex piers under tidal flow. Proc. thirty-third IAHR Congr. Water Eng. a Sustain. Environ. 913–920.

Wang, D., Li, S., Arikawa, T., Gen, H., 2016. ISPH Simulation of Scour Behind Seawall Due to Continuous Tsunami Overflow. Coast. Eng. J. 58, 104–115. https://doi.org/10.1142/S0578563416500145

Wei, Z., Dalrymple, R.A., Rustico, E., Hérault, A., Bilotta, G., 2016. Simulation of Nearshore Tsunami Breaking by Smoothed Particle Hydrodynamics Method. J. Waterw. Port, Coastal, Ocean Eng. 142, 05016001. https://doi.org/10.1061/(ASCE)WW.1943-5460.0000334

Wilcox, D.C., 1988. Reassessment of the scale-determining equation for advanced turbulence models. AIAA J. 26, 1299–1310. https://doi.org/10.2514/3.10041

Wilson, R., Davenport, C., Jaffe, B., 2012. Sediment scour and deposition within harbors in California (USA), caused by the March 11, 2011 Tohoku-oki tsunami. Sediment. Geol. 282, 228–240. https://doi.org/10.1016/j.sedgeo.2012.06.001

Xia, J., Lin, B., Falconer, R.A., Wang, G., 2010. Modelling dam-break flows over mobile beds

using a 2D coupled approach. Adv. Water Resour. 33, 171–183. https://doi.org/10.1016/j.advwatres.2009.11.004

Xiao, H., Young, Y.L., Prévost, J.H., 2010. Hydro- and morpho-dynamic modeling of breaking solitary waves over a fine sand beach. Part II: Numerical simulation. Mar. Geol. 269, 119–131. https://doi.org/10.1016/j.margeo.2009.12.008

Yakhot, V., Orszag, S.A., 1986. Renormalization group analysis of turbulence. I. Basic theory. J. Sci. Comput. 1, 3–51.

Yan, X., Mohammadian, A., Rennie, C.D., 2020a. Numerical modeling of local scour due to submerged wall jets using a strict vertex-based, terrain conformal, moving-mesh technique in OpenFOAM. Int. J. Sediment Res. 35, 237–248. https://doi.org/10.1016/j.ijsrc.2019.12.007

Yan, X., Mohammadian, A., Rennie, C.D., 2020b. Numerical Modeling of Flow and Local Scour around Pipeline in Steady Currents Using Moving Mesh with Masked Elements. J. Hydraul. Eng. 146, 3–7. https://doi.org/10.1061/(ASCE)HY.1943-7900.0001740

Yang, Y., Qi, M., Wang, X., Li, J., 2020. Experimental study of scour around pile groups in steady flows. Ocean Eng. 195, 106651. https://doi.org/10.1016/j.oceaneng.2019.106651

Yeh, H., Li, W., 2008. Tsunami scour and sedimentation, in: Fourth International Conference on Scour and Erosion. pp. 95–106.

Yeh, H., Mason, H.B., 2014. Sediment response to tsunami loading: Mechanisms and estimates. Geotechnique 64, 131–143. https://doi.org/10.1680/geot.13.P.033

Yeh, H., Robertson, I., Preuss, J., 2005. Development of Design Guidelines for Structures that Serve as Tsunami Vertical Evacuation Sites 42.

Yeh, H., Sato, S., Tajima, Y., 2013. The 11 March 2011 East Japan Earthquake and Tsunami: Tsunami Effects on Coastal Infrastructure and Buildings. Pure Appl. Geophys. 170, 1019–1031. https://doi.org/10.1007/s00024-012-0489-1

Yeoh, G.H., Tu, J., 2009. Computational Techniques for Multiphase Flows. Butterworth-Heinemann. https://doi.org/10.1016/C2009-0-16604-7

Yoshii, T., Tanaka, S., Matsuyama, M., 2017. Tsunami deposits in a super-large wave flume. Mar. Geol. 391, 98–107. https://doi.org/10.1016/j.margeo.2017.07.020

Zhang, Q., Zhou, X.L., Wang, J.H., 2017. Numerical investigation of local scour around three adjacent piles with different arrangements under current. Ocean Eng. 142, 625–638. https://doi.org/10.1016/j.oceaneng.2017.07.045